THE UNIVERSITY *of* EDINBURGH

Water and Carbon in the Early Solar System

Ardith D. Bravenec

THE UNIVERSITY *of* EDINBURGH

Thesis submitted for the degree of

Doctor of Philosophy

The University of Edinburgh

School of GeoSciences

2021

Declaration

I declare that this thesis has been composed solely by myself and that it has not been submitted, in whole or in part, in any previous application for a degree. Except where stated otherwise by reference or acknowledgement, the work presented is entirely my own.

Ardith Bravenec, August 2021

Abstract

Hydrogen (H) is the most abundant element in the universe. The original budget and speciation of major volatiles, such as hydrogen and carbon (C), in the silicate material and atmospheres of rocky bodies in our Solar System was determined during their formation and early evolution. Nearly all the large rocky bodies in the Solar System are thought to have experienced at least one magma ocean phase as an outcome of formation processes. Highly reducing conditions well below the iron-wüstite buffer (IW) characterized by a low oxygen fugacity (fO_2) were likely prevalent during the differentiation stages of rocky bodies. Reducing conditions prevailed during the early stages of planetary evolution and magma ocean solidification, and whilst some bodies like Earth progressively oxidized, others have remained more reducing. The investigation of redox conditions not only has implications for primordial magma oceans, but also for solid terrestrial bodies. Current estimates for the prevalent redox conditions in the silicate reservoirs of Mercury, Venus, the Moon and Mars are more reducing than the Earth. Under highly reducing conditions, the effect of volatile speciation on the mineral/melt partitioning and on H solubility in major silicate minerals such as olivine is largely unknown. After three decades of interest, the influence of pressure, temperature, and composition is fairly well constrained for the storage capacity and solubility of H in olivine. However, considerably less work has been conducted on the effect of fO_2 on H solubility in olivine, especially at very low fO_2, and the few available reports on this topic show substantial inconsistency.

I present SIMS and Raman data to determine the H content and speciation of C-O-H volatiles in olivine and silicate glasses from experiments at (1-3.5 GPa) and temperature (1435-1750 °C). Using a Cr-Cr_2O_3 buffer and hydride-bearing starting material, the fO_2 is estimated to be ~ IW-4,

which can be directly compared to more oxidized experiments run at ~ IW+4. Results demonstrate the systematic variance of C-O-H speciation, solubility, and partitioning as function of fO_2, which can be further explored, but not sufficiently predicted, through C-O-H fluid models. The diminished H contents of olivine under reducing conditions indicates that future work concerning magma ocean crystallization or the reducing deep upper mantle of the Earth must consider the effects of low fO_2, high fH_2, and the existence of appreciable amounts of C.

Whilst there is a substantial body of literature on the nature and consequences of water incorporation in the Earth, we know comparatively less about the 'volatile' budgets of the other rocky planets. Mars is a particularly interesting body to investigate in this regard as there is evidence for the presence of a hydrosphere during its history, and it is also one of the few bodies we have direct (meteorite) samples from. Understanding the Martian H and C budget is crucial since such dissolved volatiles reduce the Martian mantle solidus, may act as drivers for volcanism, and are vital for the development of habitable surface environments. Concentrations of H and C were measured by SIMS in experimentally produced replications of synthetic Martian systems provided by Dr. Justin Filiberto with clinopyroxene, orthopyroxene, olivine, and coexisting silicate glass phases. Such nominally anhydrous minerals (NAMs) can contain significant amounts of H and, therefore, serve as important reservoirs for H within the silicate Earth and Mars. The determined values were used to calculate the mineral/melt partition coefficients (D values) for H and C. Experiments were conducted in nominally anhydrous conditions, and H partitioning values obtained here are significantly greater than those obtained in previous studies. Comparison with literature data indicate that melt H_2O content has an important additional control on H mineral/melt partitioning for clinopyroxene and orthopyroxene. Experimental

$D_H^{cpx/melt}$ values also differ from previous models for $D_H^{cpx/melt}$ that are based solely on clinopyroxene compositions and do not account for the activity of H_2O in the melt, especially at low activities. Combined with previous literature data on $D_H^{cpx/melt}$, a new empirically calibrated model for $D_H^{cpx/melt}$ is developed based solely on phase composition which allows estimation of $D_H^{cpx/melt}$ as a function of pressure and/or temperature. This model is applied to Martian meteorites, such as the nakhlites, which may contain low water contents. The nakhlite suite are augite-rich and minimally shocked meteorites, which are believed to have formed from lava flows from a single volcano, a shallow intrusion of basaltic magma, or a sill complex on Mars. Using the newly derived $D_H^{cpx/melt}$ model, the magmatic water contents of the nakhla parental melt was estimated, and subsequently used to calculate the Martian mantle source H_2O content by various equilibrium and fractional (accumulated) melting models. Both the parental magmatic and the mantle source H_2O contents can be compared to literature estimates for the Martian mantle derived from other methods. Results suggest the H_2O contents of the source regions for the nakhlites is significantly lower than most of Earth's upper mantle, but comparable to the primitive lunar mantle and the Martian depleted and enriched sources. Such limited data from Martian meteorites supports the presence of a partially hydrated Martian mantle, although one with a lower overall 'water' content than Earth, perhaps reflecting marked contrasts in geological processes on the two bodies. Finally, semi-empirical models derived from a thermodynamic starting point are used to further explore the available dataset on H solubility in olivine.

The second half of this thesis similarly concerns H and C at subsurface (elevated pressure and temperature) conditions but focuses on astrobiologically important hydrocarbons and organics. If molecular biotic evidence does exist on Mars, it is likely preserved within or below the crust where it would be

protected from surface radiation and photolytic decomposition. Extended UV exposure is expected to result in the eventual destruction of surface organics and diagnostic biomarkers. Molecular biosignatures may also have an advantage over morphological biosignatures (e.g., microfossils) in the subsurface environment. For instance, while micromorphology can potentially distinguish biotic from abiotic carbonates, carbonates experience significant loss of primary microfabric and destruction of fossil evidence due to pervasive recrystallization during diagenesis. Experimental studies of the interactions between bio-organics and minerals under conditions simulating the harsh Martian environment provide key insights into possible prebiotic processes and the search for life. In general, organic matter analysed from a geologic environment can fall into three categories: abiotic compounds that are not associated with biological organisms, biogenic compounds produced by biological organisms, and thermogenic compounds derived from the thermal decomposition of biologically generated compounds undergoing diagenetic processes. It is critical that biosignatures used to evidence past or present life on Mars are not only biogenic or thermogenic, but discernible from abiotic compounds despite significant diagenetic or fluid alteration processes. Additionally, assessing the evolution of organic molecules in subsurface environments has significant implications for evaluating plausible scenarios for the origins of life and prebiotic chemistry. Despite protection from UV and oxidative degradation, buried biosignatures may undergo diagenetic processes that decrease the concentration of organic matter, as well as other degradation mechanisms as a result of elevated temperatures, pressures, and mineral-organic interactions. I provide a fuller understanding of preservation potential by considering several variables, including pressure, temperature, and the mineral matrix environment. Results inform future *in situ* searches for life on Mars as well as the interpretation of organic analyses from past missions.

Lay Summary

How do rocky planets like Earth form?

What factors make these early planets able to support life?

How does water behave deep inside a planet?

What about a planet billions of years ago?

If life did exist on Mars millions of years ago, how would we know?

Could there be life or the precursors of life thriving underground on Mars?

These are some of the fundamental questions my thesis, a collection of scientific papers in planetary science and astrobiology, seeks to answer. As the title

"Water and Carbon in the Early Solar System" suggests, this body of work investigates these two important elements: hydrogen and carbon. In this thesis, H and C (hydrogen and carbon) are studied in two primary contexts: 1) within the deep interiors of rocky planets and especially Mars, and 2) within the shallow Martian surface. This thesis takes the opportunity to broadly study both H and C under the extreme planetary conditions of high-pressure and high-temperature.

It is thought that all rocky planets began as extremely hot worlds of molten rock, metal, and gas, appropriately named the magma ocean stage. This magma ocean may encompass the entire planet or only part. During this stage or soon after, it is likely that essential ingredients to life were accumulated: water and carbon. However, there are many unknowns regarding how both water and carbon behave in the magma ocean stage and not long after. Fortunately, it is possible to recreate such conditions in the laboratory and by mathematical modelling. By simulating these extreme conditions in the laboratory, I elucidate the empirical relationships and mechanisms that occur within newly born planets. Thermodynamics offers a powerful theoretical

starting point and was famously referred to by Einstein as "…the only physical theory of universal content concerning which I am convinced that within the framework of the applicability of its basic concepts, it will never be overthrown." Unfortunately, it is not always possible to obtain the required information (variables and parameters) from experimental data necessary for a rigorous thermodynamic analysis. Instead, it is useful to describe the observed behaviour of the system, e.g., if we increase pressure, is solubility affected and if so to what extent? The outcomes of this research include new estimates of how H and C exist in solidifying magma oceans and new models to calculate the water inside of Mars.

While the discussion of magma oceans and models of H and C are dominated by inorganics, this thesis also considers organics in the early Solar System. Evidence for previous life on Mars might be found in the form of biosignatures, which are organic remains providing evidence for present or previous signs of life. In this context, an organic compound is any chemical compound containing carbon-hydrogen bonds. As a result of carbon's ability to form chains with other carbon atoms, millions of organic compounds exist. These organics are pervasive on Earth and exist in the interstellar medium and on asteroids. However, if organics survive on Mars, they are unlikely to withstand the harsh surface conditions for any extended period of time but may exist within a hidden organic table below the surface. Again, it is necessary to discern the effects of pressure, temperature, and chemical environment, as well as other variables using high-pressure and high-temperature experiments. The results of this research are a wealth of data that suggests which compounds may or may not be indicative of life. The outcomes of this astrobiology investigation are directly useful to the search for life on Mars and interpretating the organic analyses from past missions.

Acknowledgments

I immensely grateful for the many people who have supported this research. First and foremost, thanks to the University of Edinburgh for providing funding via the Principal's Career Development Scholarship in tandem with the Global Research Award. Naturally, this work would not have been possible without the support of my primary supervisor Geoff Bromiley. Thank you for all the professional support, guidance, assistance in the lab, and for accompanying me on the Raman trip to Bristol. Thank you to my secondary supervisor, Tetsuya Komabayashi, and my advisor, Linda Kirstein, for their general support, advice, and specialized expertise.

I am grateful to my many collaborators. Exploring various facets and subdisciplines made my PhD research a multidisciplinary adventure and would not have been possible without subject matter experts. Many thanks to my astrobiology collaborators, including Claire Cousins, Wren Montgomery, Timothy Ward, and Sean McMahon. Thanks to my undergraduate alma mater Millsaps College and the Keck Center for Instrumental and Biochemical Comparative Archaeology Lab for use of facilities.

I am grateful for the expertise and troubleshooting assistance from Ian Butler, the Workshop staff, and the general support of EMMAC. Thank you to Emiko Komabayashi for the helpful discussions regarding Raman analysis. Thank you to Katriona Edlmann and Ali Hassanpouryouzband in the University of Edinburgh's Applied Geoscience Laboratory. Thank you to Nic Odling for assistance on the XRD and being a joy to teach undergraduate geochemistry labs with. Thank you to Paul Palmer for a wonderful teaching experience on the atmospheric composition course and an introduction to teaching with Jupyter notebooks.

Thanks to everyone in the experimental petrology group at Edinburgh (Tom, Sam, Sally, Nicci). A special mention goes to my peers in the Grant attic and especially those that shared the same booth as me over the years. Thank you to the School of GeoScience and Centre for Science at Extreme Conditions for the many wonderful seminars and conferences. Thanks to the postgraduate support team for helping coordinate finishing a PhD abroad during a pandemic.

Finally, many thanks to my family for providing emotional support from abroad; this endeavour would not have been possible without you.

Table of Contents

Chapter 1

Introduction

"As Arthur C. Clarke has observed: 'How inappropriate to call this planet Earth, when clearly it is Ocean.'"

James E. Lovelock
Gaia: A New Look at Life on Earth (1979)

1.1 Water, hydrogen, and carbon

Earth is a water-rich planet. Oceans of liquid water cover more than 70% of the planet's surface, but only comprise a miniscule proportion of the planet's mass. Liquid water is necessary for life as we know it and a mundane facet of our daily lives. Accordingly, the search for water has been a key driver for the exploration of our Solar System, whether through remote sensing observations, *in situ* exploration, or analyses of astromaterials. The science theme "Follow the Water" guided the Mars Exploration Program missions, including the 2001 Mars Odyssey, Mars Exploration Rovers, Mars Reconnaissance Orbiter, and the Mars Phoenix Lander. The necessity of water for the origin and development of life on Earth makes water, and by extension hydrogen, exceptionally intriguing for studies aimed at understanding our origins.

During the Big Bang at 13.78 ± 0.06 Ga, most of the hydrogen in the universe was created (Bennett et al., 2013). Hydrogen is the most abundant element in the cosmos and due to its small size, it is likely present in nearly all of Earth's phases, from the atmosphere to the core. Further, the compound H_2O is thought to be present as a gas, liquid, and/or solid in the upper lithosphere, surface, and atmosphere of all the terrestrial planets and many moons (McCubbin and Barnes, 2019). Despite the ubiquity of H on Earth and within our Solar System, it is only a minor or trace component of terrestrial planetary bodies and differentiated asteroids. Yet, H_2O is of the utmost importance to understanding the formation history and subsequent evolution of terrestrial planets and life on Earth. Furthermore, some portion of this water may be primordial, a remnant of the planet's creation. The presence of water during the early thermochemical evolution of the Earth and other terrestrial bodies could have exerted a fundamental influence on their formation, evolution, and potential for habitability. Incorporation of trace

amounts of water in Earth's upper mantle exerts a strong influence on key physical and chemical properties, including partial melting, solidus temperature, rheology, electrical conductivity, thermal conductivity, cation diffusion, phase transition boundaries, and the exchange of water between Earth's interior and exterior (see review by Peslier et al., 2017 and references therein). Interior volatile abundances, primarily H and C, may have influenced the development of Earth's oceans, atmosphere, and by inference, the emergence of life.

However, much remains unknown regarding the fundamental behaviour of water and other volatiles under the extreme conditions of early planetary interiors and magma oceans. In the bulk silicate Earth and other planetary interiors, hydrogen is one of the most elusive and poorly constrained compositional variables. Due to the large relative mass of minerals in the Earth's mantle compared to the ocean mass, trace amounts of hydrogen incorporated within nominally anhydrous minerals (NAMs) may constitute the largest reservoir of water in the planet. In these NAMs—including olivine, clinopyroxene, orthopyroxene, and garnet—hydroxide (OH^-) is the most common molecular H-bearing species, while the molecular species OH^- and H_2O are common constituents of silicate melts and glasses (Peslier et al., 2017). Indeed, what is colloquially referred to as "water" in this context more often indicates H incorporated as various species in minerals, melts, alloys, and fluids (Figure 1.1).

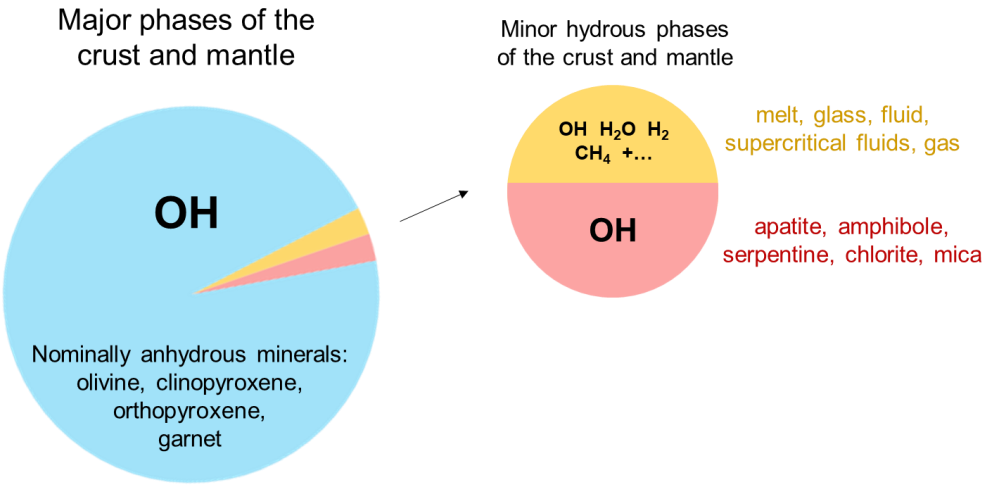

Figure 1.1. Illustration of "water" stored in the Earth's mantle and crust as different hydrous species. The relative size of the pie chart slice represents the approximate volume proportions of the phases. NAMs represent the primary reservoir for H storage, where H is incorporated via lattice defects and bonds to structural oxygen. (Figure adapted from Peslier et al., 2017.)

Carbon played a key role in the origin of life and may also have been an important volatile present during early planetary accretion events. As stated by astrophysicist Sir James Jeans (1930), "Life exists in the universe only because the carbon atom possesses certain exceptional properties." However, the carbon content of the Earth's present mantle and the behaviour of carbon during early planetary evolution remains poorly constrained. Illuminating the physics and chemistry of hydrogen and carbon in minerals and melts at the atomic or microscale is essential to understanding not only the geology of the Earth but the evolution and dynamics of other planets. While the detection of hydrogen in NAMs was pioneered in the 1970s and 80s, there have been significant recent advances in analytical capabilities that has allowed the field to explore new and exciting themes, including that of this thesis.

1.2 Oxygen fugacity

Oxygen fugacity (fO_2) plays a vital role in the complex physical and chemical aspects of planets and their building blocks. In chemical thermodynamics, fugacity is a property of a real gas defined as an effective partial pressure, which substitutes for the mechanical partial pressure in equations for an ideal gas. This in turn yields an accurate computation of the chemical equilibrium constant for the real gas. In other words, fO_2 can be defined as an equivalent of the partial pressure of oxygen in a particular environment that has been corrected for the non-ideal character of the gas. In general, the fugacity of species i may be expressed as,

$$f_i = x_i P \hat{\phi}_i = n_i P \hat{\phi}_i \sum_i n_i \tag{1.1}$$

where n_i, x_i, $\hat{\phi}_i$, f_i, and P are the number of moles, mole fraction, fugacity coefficient, fugacity of species i, and pressure respectively. For an ideal gas, $\phi = 1$ since fugacity and pressure are equal, and real gasses may approach ideality under low pressures and high-temperatures. Fugacity for a given pure gas can be calculated using a previously developed equations of state (EoS), which may be based on molecular dynamic equations, statistical mechanics calculations, and non-stoichiometric global free-energy minimization, and validated by fitting to experimental data (e.g., Holland and Powell, 1991; Sterner and Pitzer, 1994, 1995; Zhang and Duan, 2009). An example of such a calculation is shown in Figure 1.2.

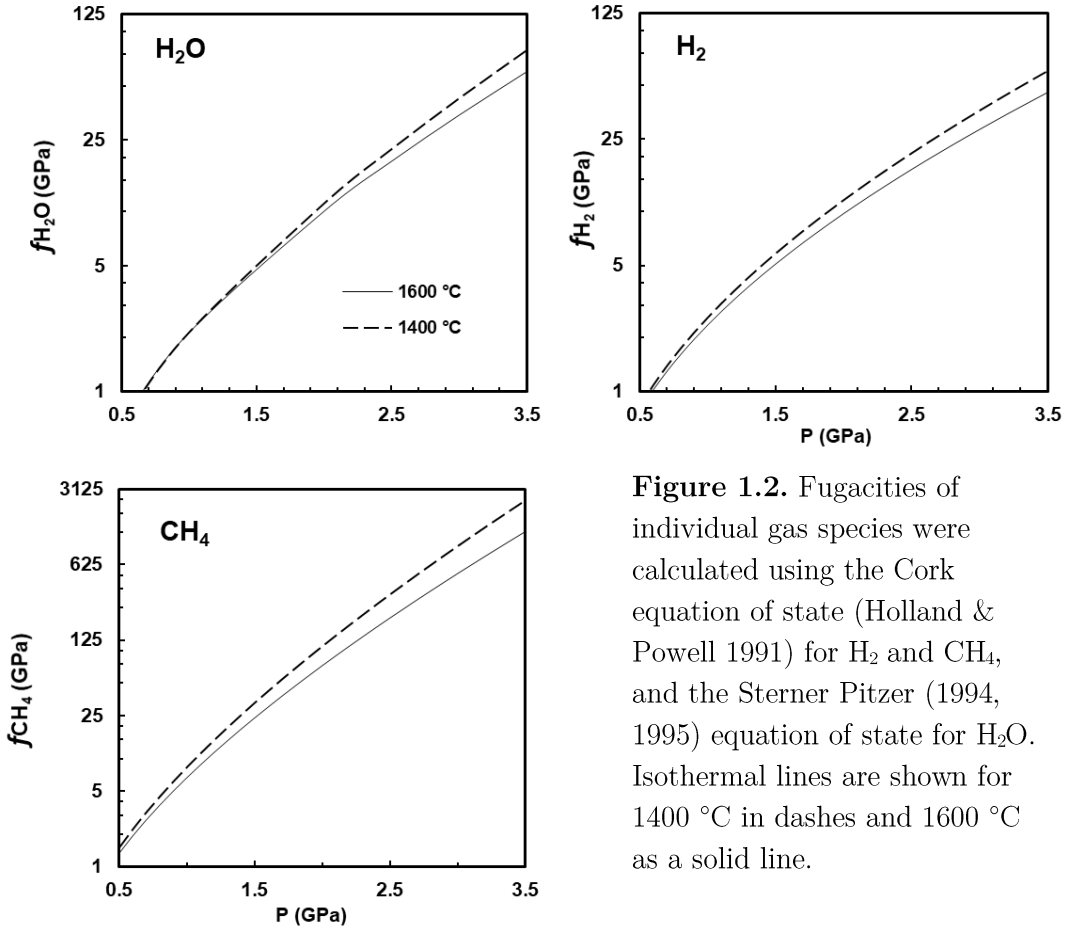

Figure 1.2. Fugacities of individual gas species were calculated using the Cork equation of state (Holland & Powell 1991) for H_2 and CH_4, and the Sterner Pitzer (1994, 1995) equation of state for H_2O. Isothermal lines are shown for 1400 °C in dashes and 1600 °C as a solid line.

In experimental petrology, fO_2 is imposed upon the system by the isothermal and isobaric invariant reaction in a mineral redox buffer (Frost, 1991, Young, 2003). The technique to impose and maintain fO_2 in piston cylinder experiments was first described by Eugster (1957) and is based on H exchange between a hydrated solid state mineral buffer and a hydrous experimental charge. For instance, the mineral buffer NNO (nickel-nickel oxide) is given by

$$\mathrm{Ni_{(s)}} + \frac{1}{2}\,\mathrm{O_{2(g)}} \rightleftharpoons \mathrm{NiO_{(s)}} \tag{1.2}$$

And the equilibrium constant can be written as (Holloway and Wood, 1988),

$$K = \frac{1}{fO_2^{1/2}} \tag{1.3}$$

Often referred to as the double-capsule technique, an inner platinum capsule (or a Ag-Pd alloy) contains the experimental starting material and the outer capsules contains a small quantity of H_2O and a mineral buffer assemblage (Frost, 1991; Young, 2003). The buffer assemblage equilibrates with H_2O and the ratio of fH_2 to fO_2 remains fixed due to the disassociation of H_2O to H_2 within the outer capsule (Young, 2003). The inner platinum capsule is permeable to diffusion; H_2 produced by the reaction can diffuse through the inner capsule to combine with available oxygen inside the inner capsule (Frost, 1991; Young, 2003). Diffused H in the inner capsule reacts to produce H_2O, buffering the oxygen fugacity in the sample so that the fO_2 of the inner capsule is fixed to that of the outside buffer (Frost, 1991). The reaction of H_2 with H_2O in the inner capsule to fix fO_2 can be described as redox couple accordingly

$$H_2 + \frac{1}{2} O_2 \rightleftharpoons H_2O \tag{1.4}$$

Thus, fO_2 will be fixed by the equation

$$fO_2 = \left(\frac{f_{H2O}}{(K)(fH_2)}\right)^2 \tag{1.5}$$

An example of the double capsule technique is shown in Figure 1.3.

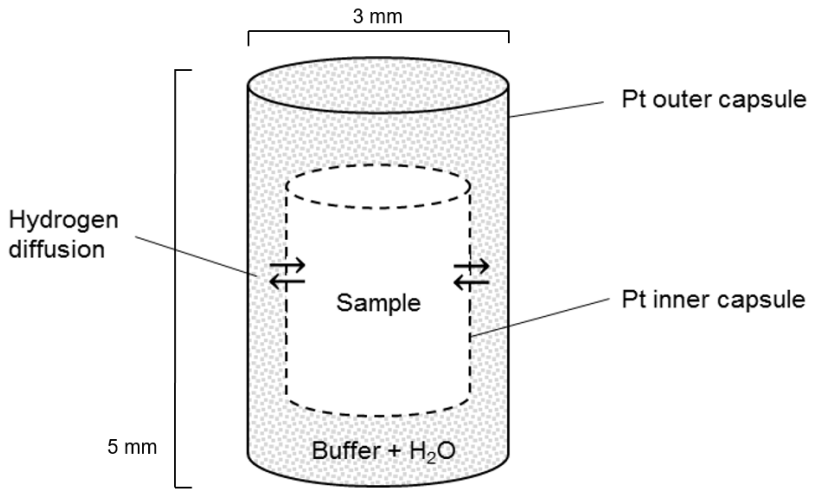

Figure 1.3. Example of the double-capsule technique. The sample is contained in the inner capsule. The inner capsule is enclosed within the outer capsule which contains the buffer and H_2O enabling hydrogen diffusion to buffer fO_2.

Equilibria for common mineral redox buffers are given in Table 1 in order of decreasing oxygen fugacity i.e., from more oxidizing to more reducing conditions in a specified temperature range. For clarity, the reactions are shown balanced with O_2, and with H_2O and H_2 respectively.

Table 1.1. Equilibria for common mineral redox buffers

Name	**Balanced with O_2**	**Balanced with H_2O and H_2**
MH, magnetite-hematite	$4Fe_3O_4 + O_2 \rightleftharpoons 6Fe_2O_3$	$2Fe_3O_4 + H_2O \rightleftharpoons 3Fe_2O_3 + H_2$
NNO, nickel-nickel oxide	$2Ni + O_2 \rightleftharpoons 2NiO$	$Ni + H_2O \rightleftharpoons NiO + H_2$
QFM, quartz- fayalite-magnetite	$3Fe_2SiO_4 + O_2 \rightleftharpoons 2Fe_3O_4 + 3SiO_2$	$3Fe_2SiO_4 + 2H_2O \rightleftharpoons 2Fe_3O_4 + 3SiO_2 + 2H_2$
IW, iron-wüstite	$2xFe + O_2 \rightleftharpoons 2\ Fe_xO$	$Fe + H_2O \rightleftharpoons FeO + H_2$
QIF, quartz-iron-fayalite	$2Fe + SiO_2 + O_2 \rightleftharpoons Fe_2SiO_4$	$2Fe + SiO_2 + 2H_2O \rightleftharpoons Fe_2SiO_4 + 2H_2$

Originally the variable controlling oxidation potential was referred to as the partial pressure of oxygen (pO_2), although the term was soon replaced with the more thermodynamically rigorous term fO_2 to better account for nonideal behaviour (Eugster and Wones, 1962; Frost, 1991). If a fluid phase is present in a rock, then pO_2 can be defined, even if it is extremely low (Frost, 1991). Yet a considerable portion of rocks contain no fluid phase at the time of formation and pO_2 loses physical meaning (Frost, 1991). In contrast, fO_2 monitors chemical potential and is suitable to describe such a condensed system. The relation between chemical potential and fugacity can be written as,

$$\mu_{i} = \mu_i^0(T) + RTln\left(\frac{f_i}{p^0}\right) \tag{1.6}$$

where μ_i^0 is chemical potential in the standard state and R is the gas constant. In Figure 1.4, the curves plotted in the fugacity-temperature diagram represent an oxidation reaction occurring in a mineral redox buffer (Frost, 1991).

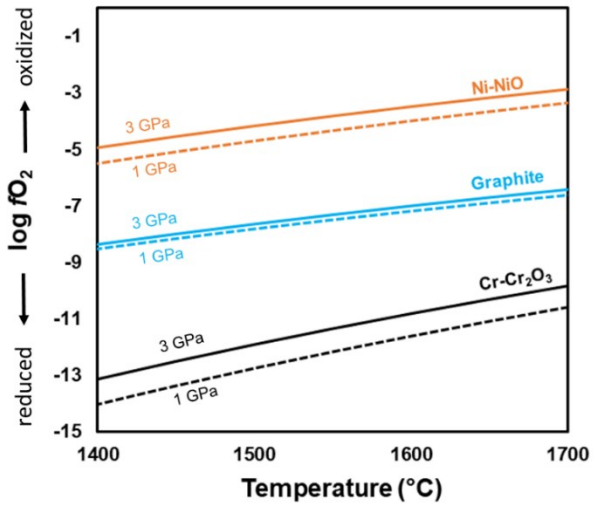

Figure 1.4. Log fO_2 versus temperature diagram of redox buffers. The dashed line represents a pressure of 1 GPA and the solid line represents 3 GPA. Note that the Cr-Cr_2O_3 buffer is considered highly reducing, while the Ni-NiO buffer is considered relatively oxidizing.

Additional practical considerations exist at water-undersaturated conditions, where the relationship between the sample redox state and that of the buffer may be described as,

$$\Delta log fO_2 = log fO_{2(sample)} - log fO_{2(buffer)} = 2log\left(\frac{fH_2O_{(\text{sample})}}{fH_2O_{(buffer)}}\right) \quad (1.7)$$

Therefore, with a lower activity of water, the fO_2 within the experiment will be reduced relative to the redox buffer in the new capsule assemblage, where aH_2O of the buffer is presumed to be near unity. In the case of a water-undersaturated buffered experiment conducted over a range of sub-liquidus temperatures, the H_2O content of the melt should increase with the crystallisation of anhydrous minerals with the aH_2O increasing progressively with decreasing temperature. In this particular case, despite not varying the buffer, the fO_2 may increase with increasing crystallisation. However, the experiments conducted in Chapter 2 are more accurately considered in terms of H_2 as the dominant H species, such that the last term instead becomes

$$\Delta log fO_2 = 2log\left(\frac{fH_{2(\text{sample})}}{fH_{2(buffer)}}\right). \quad (1.8)$$

For this purpose, it is sufficient that both the outer buffer and the inner sample enforce a high fH_2, which is further discussed in the experimental section of Chapter 2. The piston cylinder device also has an 'intrinsic' apparatus fugacity separate from the sample buffer system. Reported values of unbuffered samples run at the intrinsic fO_2 range are typically relatively oxidized and are expected to fall close to the NNO buffer for the piston cylinder devices used for this research. This intrinsic fO_2 of the press is likely determined by several components. The graphite furnace would be expected to

impose an fO_2 according to the C–CO–CO_2 (CCO) buffer, while the metal alloy of the pressure plates may also have some influence. Overcoming the intrinsic value of the piston cylinder to impose the desired fO_2 of the solid buffer is critical for achieving very reducing conditions, such as those below the IW buffer, and often proves to be particularly challenging.

1.3 Redox state of the primitive mantle

The redox state of the Earth's mantle controls and affects numerous processes, such as the behaviour of metallic elements associated with ore deposits (Jenner et al., 2010), the depth of partial melting and related mantle weakening (Sifré et al., 2014), and the speciation of magmatic gases involved with volcanic degassing (Holland, 2002; Gaillard and Scaillet, 2014). In the early Earth, the redox state of the deep interior is an important variable in defining the composition of the terrestrial atmosphere (Armstrong et al., 2019). The identification and quantification of variations in mantle redox states as well as the mechanisms that control redox state remains a broad and active debate in Earth and planetary sciences (e.g., Frost and McCammon, 2008; Gaillard et al., 2015; Hirschmann et al., 2009; Scaillet and Gaillard, 2011; Yang et al., 2014, 2016; Armstrong et al., 2019; Potts et al., 2021). Changes in the oxygen/cation ratio of the rock will modify the fO_2 of the rock. An example of such a process can be found in fluid-rock and/or melt-rock interactions as occurring in mantle metasomatism in which fluid or melt interactions with a rock generate reduction/oxidation reactions on the pervaded system by altering its oxygen/cation ratio (McCammon et al., 2001). Melting and mineralogical transitions generally alter the fO_2 of a rock (the oxygen/cation ratios of the respective phases), while degassing and crystallization can modify the fO_2 of a melt (Carmichael and Ghiorso, 1986).

During planetary accretion, the temperature was sufficiently high to produce magma oceans and the redox conditions were sufficiently reducing to produce Fe-metal saturation from molten silicate i.e., 6 fO_2 log-units below the present-day lithospheric mantle. (Wood et al., 2006). With increasing planet size, the temperature and depth of the magma ocean increases, and thus so does the pressure located at the bottom of the magma ocean (Wood et al., 2006). As shown in Figure 1.4, the Earth's current mantle possesses a range of fO_2 values near QFM±1, which is in line with mantle fO_2 values during the early Archean. This constancy indicates that the mantle may have been subjected to oxygen buffering. However, the nature of this buffer and whether one or several buffering mechanisms were present remains largely undefined. The uptake of iron(III) into garnet may have played a role (Rohrbach et al., 2011). Additionally, it is thought that carbon may have controlled the mantle redox state (Stagno et al., 2013)

Largescale geodynamics continuously reshaping the surface and deep interior of the Earth has resulted in the loss of much of the evidence of the Earth's ancient (post-accretion) composition. Other planetary objects, particularly the Moon, have remained relatively unaffected by such processes. The general assumption is that these planetary bodies were initially more reduced upon formation and then experienced a gradual or stepwise oxidation (Frost, 2008; Scaillet and Gaillard, 2011) as can be seen in Figure 1.5. The magma ocean stage, when a large portion of the planet was molten due to the energy released by accretionary processes, represents one of the primary arguments for an initially reduced planet during or soon after accretion (Scaillet and Gaillard, 2011). Approximately 30 million to 60 million years after the beginning of the Solar System, the Earth's core is thought to have formed by a massive segregation process where metals separated from silicates (Scaillet and Gaillard, 2011). The process allowed the formation of the metallic

core and a silicate-containing mantle. The coexistence of silicate and metal liquids in the magma ocean would have caused severely reduced conditions with oxygen fugacity 5 to 8 log units lower than the current upper mantle values (Scaillet and Gaillard, 2011). Once the mantle separated from the core, meteorite bombardment may have also contributed to mantle oxidation (Scaillet and Gaillard, 2011). A 'great oxidation event' occurred in the mantle causing oxygen fugacity to increase rapidly (Scaillet and Gaillard, 2011), progressing from IW-2 imposed after the core-mantle separation to QFM+0.5/-2 (IW+3/+4.5), according to the record of the oldest mantle rocks (Canil, 2002; Li and Lee, 2004).

One mechanism for the oxidation of the early Earth's mantle is self-oxidation. Self-oxidation may occur by lower mantle perovskite crystallization according to the disproportionation reaction,

$$3Fe^{II}O \rightarrow Fe^{0} + 2Fe^{III}O_{1.5} \quad (1.9)$$

In contrast to other silicate minerals stable at lower mantle pressures such as olivine and garnet, perovskite can accommodate significant portions of iron(III) (Frost et al., 2004). In a bulk composition dominated by iron(II), the crystallization of perovskite would trigger the above disproportionation reaction, and thus incorporate iron(III) in the perovskite structure with metal Fe remaining as an interstitial phase (Gaillard, 2015). The migration of metal Fe toward the forming core via diapirs would result in the oxidation of the silicate lower mantle (e.g., Rubie et al., 2003, 2011; Yoshino et al., 2003; Frost and McCammon 2008), while Fe^{3+}-rich rocks in the upper mantle may have been transferred via subsequent convective exchanges (Gaillard, 2015). It has been suggested that the great mantle oxidation event may have been triggered

by this self-oxidation process as well as have contributed to the progressive oxidation of the silicate Earth during the final stages of accretion (Scaillet and Gaillard, 2011).

Another argument is that Earth oxidized more because it was larger than the Moon and therefore able to self-oxidize, whereas smaller bodies cannot or do so to a lesser extent (Wade and Wood, 2005; Scaillet and Gaillard, 2011). The principal phase in the Earth's lower mantle is magnesium silicate perovskite which speciates iron(II) into iron(III) and metal (Wade and Wood, 2005). Crystallization of the lower mantle would force oxidized iron(III) into the upper mantle (Wade and Wood, 2005). The iron content of the magma ocean would have been raised as infalling metal was oxidized by the iron(III) into iron(II) (Wade and Wood, 2005). Because perovskite has a limited stability range in smaller planets, this process is not likely to occur (or to occur to a much lesser extent) on Mars or the Moon (Wade and Wood 2005).

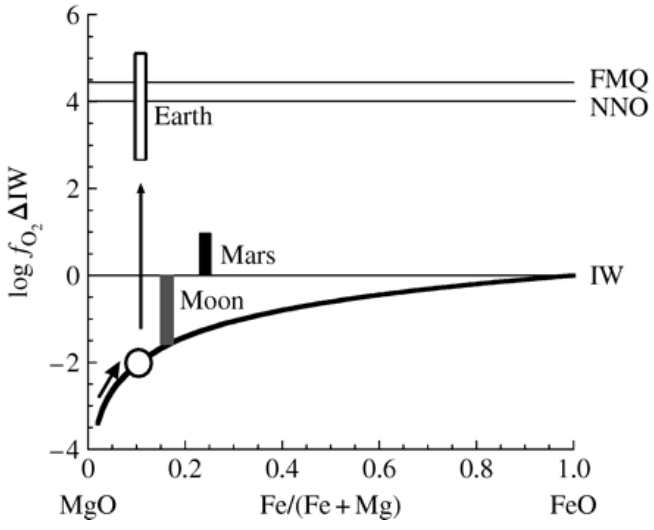

Figure 1.5. Redox evolution of Earth's mantle. The two arrows in the figure represent distinct phases of the Earth's redox evolution in the mantle. Additionally, fO_2 of the Martian mantle and for lunar basalts are also shown. The fO_2 is calculated relative to the ΔIW buffer. (Taken from Frost, 2008)

1.4 Magma oceans and terrestrial planet formation

Planetary formation is thought to predominantly involve planetary-scale collisions and melting events at extreme heats, culminating in the formation of a magma ocean. Almost all the large rocky bodies in the Solar System likely experienced at least one magma ocean phase where the planet was completely or partially molten. Following melting during largescale accretionary impacts, the crystallization of the magma ocean may lead to massive mantle overturn producing a stably stratified mantle (Elkins-Tanton, 2008, 2012; Schaefer and Elkins-Tanton, 2018). As transient stages in terrestrial planet evolution, the magma ocean stage may occur over hundreds to thousands of years followed by solidification of the silicate reservoirs (Elkins-Tanton, 2012). Melting and solidification during magma ocean events are fundamental to geodynamic development. Processes occurring during magma ocean onset and crystallization may critically affect the primordial composition, differentiation, and the planet's volatile content. In turn, these factors comprise the starting point for the production of habitable conditions through the onset of thermally driven mantle convection and plate tectonics and outgassing to form an early atmosphere (Elkins-Tanton, 2008, 2012; Schaefer and Elkins-Tanton; 2018, Deng et al., 2020). Understanding how bio-essential volatiles like H and C behaved during their initial incorporation within a magma ocean and subsequent crystallization requires consideration of the early redox state. The redox state of a magma ocean may provide the preliminary conditions that prompt different evolutionary paths of planetary bodies and have a profound effect on the subsequently forming mantle and burgeoning atmospheres (Deng et al., 2020).

1.5 Biomolecules, biosignatures, and prebiotic organic compounds

Discovering life elsewhere is one of the great scientific pursuits of our time.

A biosignature (sometimes called a molecular fossil) is any substance, such as an element, isotope, or molecule, that provides scientific evidence of past or present life. The efficacy of a biosignature depends not only on the probability that life synthesized it, but also by the improbability of abiological production. A biomolecule is a substance produced by cells and living organisms, including lipids, nucleic acids, and proteins. During the ancient Noachian period, the Martian surface possessed liquid water and may have been habitable for microorganisms. Even if Mars failed to evolve life, constraining the planet's organic table and history can provide valuable insight into prebiotic chemistry. To identify biotic organics, we must first understand the possible abiotic organic chemical reactions within the context of the geochemical environment, which would allow us to distinguish perturbations to that physiochemical system.

It is generally assumed that life emerged on Earth from geochemical conditions that allowed the synthesis of molecular building blocks, which, in turn, self-assembled to form cells. This prebiotic chemistry is necessarily an extension of the geochemical and environmental conditions. As a result of meteorite bombardment, *in situ* production, and any possible biological sources, organics are expected to exist on Mars.

Interpreting the abiotic organic chemistry in the Martian environments, such as meteoritic inputs and the preservation/diagenesis of that signal with time, is necessary to identify biotic organics. Yet organics have been under-detected on the Martian surface. Organics on Mars are unlikely to withstand the severe surface conditions for any prolonged period but may exist within a protected

organic table in the subsurface. Hence Chapter 5 of this thesis is similarly concerned with understanding H and C under elevated pressures and temperatures. At such subsurface conditions, it is necessary to discern the effects of pressure, temperature, and chemical environment, as well as other variables using high-pressure and high-temperature experiments.

1.6 End-loaded piston-cylinder apparatus

The end-loaded piston-cylinder apparatus is capable of simultaneously generating high-pressure and temperature conditions. The primary advantages of the piston-cylinder press are the relatively large volume of the sample assembly, stability over long run durations, and quick heating and quenching rates. The instrument is especially suitable for investigating the physical properties and synthesis of high-pressure and temperature materials. Experimental laboratories at the University of Edinburgh host two piston-cylinder presses that have been built and maintained within the University and are capable of achieving up to ~4 GPa and ~1700 °C. Like other high-pressure devices, such as the multi-anvil press, the pressure produced is based on the following formula,

$$P = \frac{F}{A} \tag{1.10}$$

where F is the applied force, and A refers to the area where force is applied. By converting a small load on a large piston to a comparatively large load on a small piston, pressure is greatly amplified and suitable high-pressure conditions of planetary deep interiors can be achieved. Because parts of the assembly materials allow deformation, the uniaxial pressure is distributed quasi-hydrostatically over the sample volume. The piston-cylinder apparatus is end-

loaded. Pressure is generated by pushing both ends of the sample assembly; firstly, a large end-load stabilises carbide components within the assembly stack, and then a sample load applies force directly to the sample assembly. High-temperatures are achieved through resistive heating by running a current through an internal graphite cylinder which comprises part of the sample cell. A thermocouple enables monitoring of the sample temperature throughout the experiment.

The main components of the piston-cylinder apparatus (Figure 1.6) are the pressure generating system, the pressure vessel, and the sample assembly within the vessel. The end-loaded piston-cylinder apparatus involves two hydraulic rams. The second hydraulic ram vertically loads and stabilizes the pressure vessel. Once pressurized, a controlled current is applied to the graphite furnace to produce resistive heating. After heating, the pressure conditions become essentially hydrostatic as the main components of the sample assembly (talc pressure medium and borosilicate glass) soften in response to the increased temperature. To cool the system during experiments, water circulates around the upper and lower cooling plates and the pressure plate (Figure 1.6).

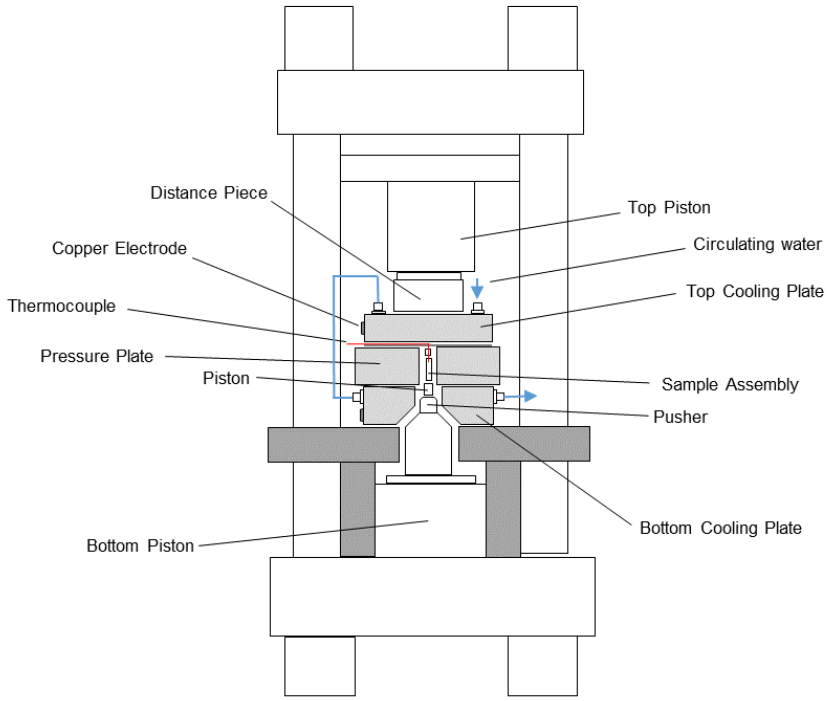

Figure 1.6. Generalized schematic of an end-loaded piston cylinder apparatus.

The sample assembly consists of a solid pressure medium, a resistance heater, and a sample capsule. This deformable sample assembly (Figure 1.7) transmits hydrostatic pressure from the compressing piston onto the sample, controls the heating of the sample, and provides a suitable oxygen fugacity environment. The outermost talc cylinder transmits pressure, reduces friction, and is constructed from electrically insulating material such as talc, but can also be composed of NaCl, $BaCO_3$, KBr, CaF_2, or borosilicate glass. Inside the talc sleeve, the electrically and thermally insulating borosilicate glass cylinder acts as an outer insulator and additional pressure transmitter, while the inner graphite cylinder functions as a "furnace." Within the graphite furnace, the crushable alumina (Al_2O_3) acts as the inner insulator and pressure transmitter, as well as ensuring that the sample is centred within the assembly.

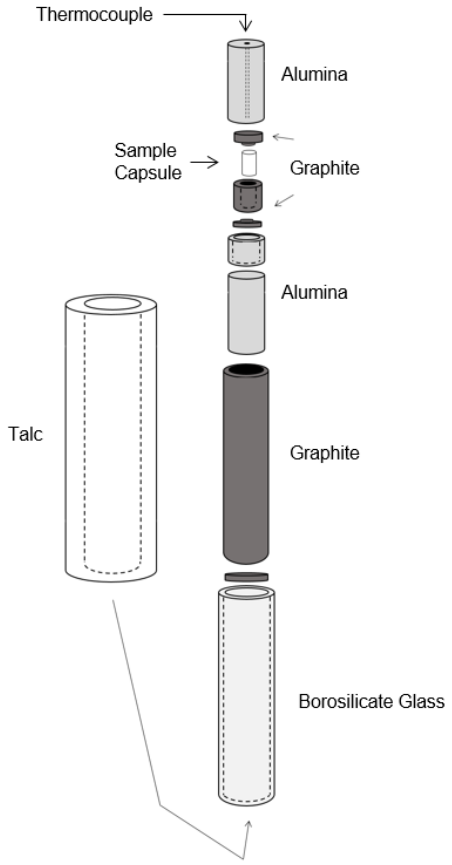

Figure 1.7. Schematic drawing of a sample assembly. Both 12.5 mm and 19 mm vertical height cells are available. Note that the graphite bucket that holds the sample capsule may be removed and the capsule instead fitted directly into the alumina sleeve depending on the required buffer assemblage.

The inner capsule contains the sample while the outer capsule contains the oxygen fugacity buffer, as previously discussed. These capsules are sufficiently deformable so as not to interfere with pressure transmission. The capsule must also not react with the sample and should prevent reactions with other materials in the sample assembly. For these purposes, the capsule is often composed high purity noble metals (e.g., Au, Pt, Ag-Pd alloys) or graphite capsules to reduce chemical contamination of the sample. A conductive steel base plug is located at the top of the sample assembly.

A thermocouple sensor measures the temperature of the sample (Figure 1.5). The thermocouple consists of two dissimilar metal wires insulated from

each other everywhere except at the sensing junction by a ceramic tube. Additional contact between the wires, or contact between the wires to other conductive objects, can modify the voltage and result in a false reading of temperature. The ceramic tube also serves as a support rod to locate the centre of the furnace. The thermocouple wires are welded at the end to form the sensing junction and this junction is placed in contact above the sample capsule. The other ends of the wires are connected to a thermocouple thermometer.

Random and systematic errors influence the accuracy of the temperature readings. Differential pressures in the assembly, temperature gradients in the assembly, contamination, and the effect of pressure on thermocouple electromotive force (EMF) can all be sources of error. In high-pressure and high-temperature experiments, the temperature is generally calculated from the EMF generated by a thermocouple with the sensing junction placed under high-pressure conditions without any pressure correction. At high-pressure, due to significant pressure effects of the thermocouple EMF this may lead to erroneous estimated temperatures (Nishihara et al., 2016). Inhomogeneous pressure distribution in the sample assembly upon pressurization is a result of the variable compressibility of the cell components (McDade et al., 2002). The result is the sample experiences a lower pressure than calculated from the applied force of the piston determined from the hydrostatic oil pressure (McDade et al., 2002). Using the hydrostatic oil pressure and the applied surface area, the nominal pressure in an experiment can be calculated. However, the characteristic yield stress of the assembly components will result in a different effective pressure. Taking into account the friction of the assembly,

$$P_{effective} = P_{nominal} + P_{correction}. \quad (1.11)$$

To determine the effective pressure, a "friction" correction is used to compensate for various sample assembly materials (McDade et al., 2002). The friction correction is determined through calibration experiments using either static or dynamic methods, which may employ known phase transitions or melting curves (McDade et al., 2002). The effective pressure for the Edinburgh piston cylinder and assemblies has been calibrated to within ±0.1 kbar using the quartz-coesite transition and albite ⇌ jadeite + quartz reaction (see Montgomery et al., 2016) and can be generally assumed to be accurate to within less than ±5% of the reported value. Thermal gradients in the piston cylinder sample assemblies also present a concern. Reduction of the temperature gradient can be achieved by using a tapered graphite furnace (McDade et al., 2002). For the following chapters, the temperature was measured using an R-type platinum-rhodium thermocouple inserted just above the sample capsule, and temperature recorded is accurate to ± 10 °C.

Chapter 2

Speciation and Partitioning of Carbon and Hydrogen During Magma Ocean Crystallization

In collaboration with

Richard Brooker (Raman analysis)

"Everything has a natural explanation. The moon is not a god but a great rock and the sun a hot rock."

Anaxagoras, fifth century BC

"Fugacity has no memory
It has no past
Only what it sees last."

Cin-Ty A. Lee
Quoted from Herd (2008)

2.1 Abstract

The original budget and speciation of major volatiles, such as hydrogen (H) and carbon (C), in the silicate material and atmospheres of rocky bodies was determined during their formation and early evolution. Nearly all the large rocky bodies in the Solar System are thought to have experienced at least one magma ocean phase as an outcome of formation processes. Highly reducing conditions well below the iron-wüstite buffer (IW) characterized by low oxygen fugacity (fO_2) are expected to be prevalent during the differentiation stages of rocky bodies. In such highly reducing conditions, the effect of volatile speciation on the mineral/melt partitioning and on H solubility in olivine is largely unknown. After three decades of interest, the influence of pressure, temperature, and composition is fairly well constrained for the storage capacity and solubility of H in olivine. However, considerably less work has been conducted on the effect of fO_2 on H solubility in olivine, especially at very low fO_2, and the few available reports on this topic show substantial inconsistency. In this chapter, we present SIMS and Raman data to determine the H content and speciation of C-O-H volatiles in olivine and silicate glasses from experiments at high-pressure (1-3.5 GPa) and temperature (1435-1750 °C). Using a Cr-Cr_2O_3 buffer and hydride-bearing starting material, the fO_2 is estimated to be ~ IW-4, which can be directly compared to more oxidized experiments run at ~ IW+4. Results demonstrate the systematic variance of C-O-H speciation, solubility, and partitioning as a function of fO_2. This variance can be further explored, but not sufficiently predicted, through C-O-H fluid models. The diminished H contents of olivine under reducing conditions indicates that future work concerning magma ocean crystallization or the reducing deep mantle of the Earth must consider the effects of low fO_2, high fH_2, and the existence of appreciable amounts of C.

Keywords: Water, Hydrogen, Carbon, Volatile Speciation, Partition Coefficient, Silicate Melt, Magma Oceans, Planet Formation

2.2 Introduction

Broad differences in the differentiation and fO_2 conditions of Earth, Mercury, Venus, and Mars may strongly influence their interior volatile budgets, the resultant outgassed atmospheres, and the volatile cycles of these planets. During early planet evolution, the redox conditions and the initial abundance and distribution of the major volatile elements may be set, both of which continue to evolve via geological cycles. The redox state of a magma ocean is dependent on the type of material accreted and the planet's growth history. During magma ocean events, the equilibration of the core and mantle results in highly reduced conditions below the iron-wüstite (IW) buffer (e.g., Rubie et al., 2011; Wade and Wood, 2005). Models suggest Earth experienced an extended growth history with several stages of alloy-silicate equilibration and progression from an initial fO_2 of IW-5.5 that gradually increased up to IW-1 during later formation stages (Wade and Wood, 2005; Rubie et al., 2011, 2015). However, smaller planets like Mars and Mercury may have undergone single-stage core-mantle differentiation events with widely different fO_2 conditions (IW-1 and IW-5.5, respectively) (Rai and Van Westrenen, 2013; Zolotov et al., 2013). The study of lunar samples indicates their formation under reducing conditions with fO_2 ranging from IW+0.2 to IW-2.5 (Wadhwa, 2008). During the earliest stages of inner Solar System evolution, H_2O was likely present in both differentiated and undifferentiated planetesimals (McCubbin and Barnes, 2019). There is a lack of quantitative constraints on the interior H_2O contents of Mercury. However, due to Mercury's low fO_2, the molecular H_2O/H_2 ratio of its mantle is estimated to be 0.034–0.0021 (McCubbin et al., 2017). Other early Solar System objects similarly display an

exceptionally broad range of redox conditions (Grossman et al., 2008), with CAIs (calcium aluminium rich inclusions) and enstatite chondrites (EC) being the most reduced objects. As the most reduced undifferentiated extra-terrestrial material, ECs may have experienced fO_2 values well below IW-3 (Larimer and Buseck, 1974; Brett and Sato, 1984) and fassaite in CAIs suggests an intrinsic fO_2 of IW-6.8 (Grossman et al., 2008). A summary of the range of redox conditions for Solar System objects is given in Figure 2.1. Consequently, the effect of fO_2 on H dissolution and partitioning between olivine and silicate melt must be determined, especially across substantial variations of fO_2.

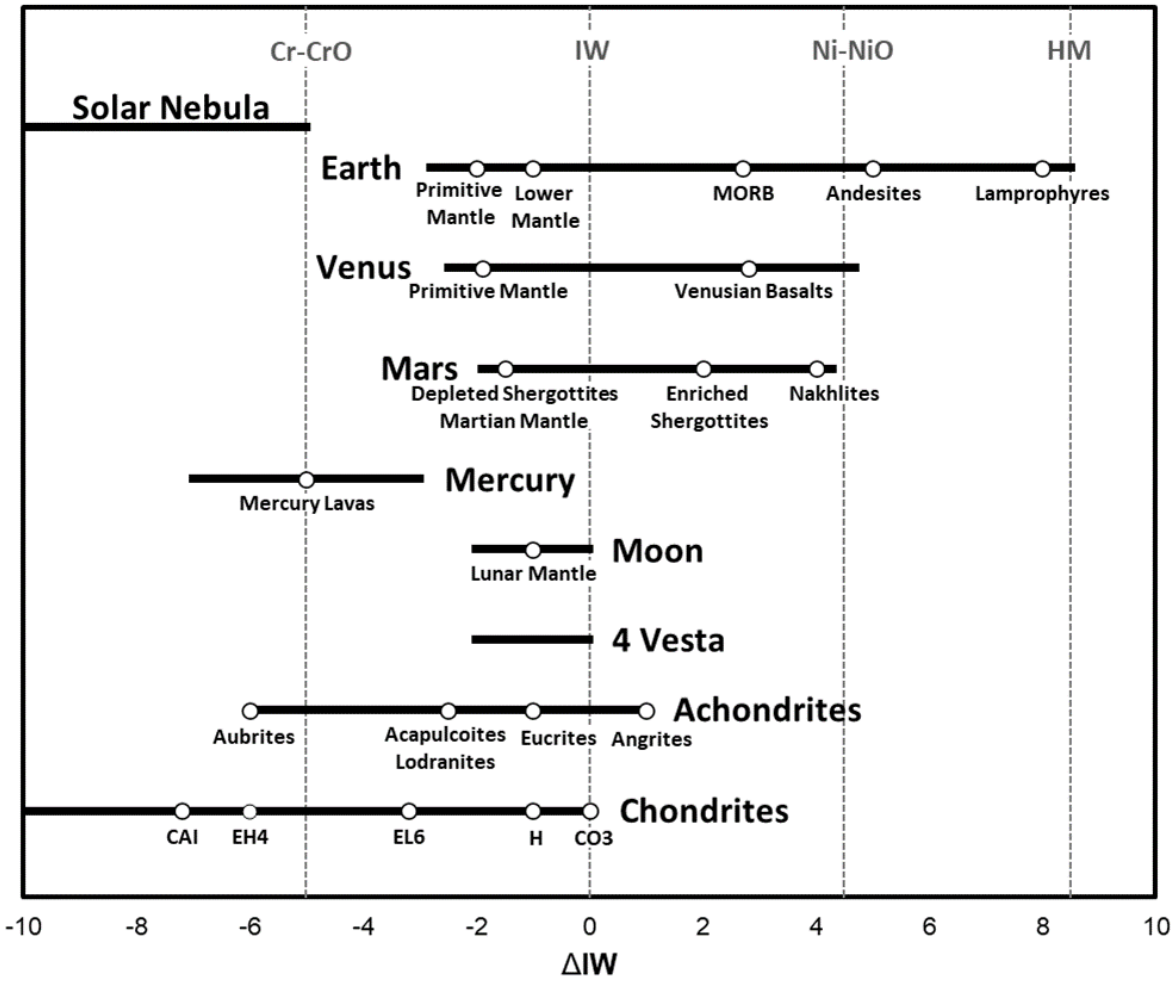

Figure 2.1. Estimated oxygen fugacities of various objects of the Solar System relative to the IW buffer equilibrium and compared with solar nebular gas. Note that chondrites are highly unequilibrated objects. Abbreviations: CAI = calcium-aluminium inclusion; CO3 chondrite = carbonaceous Ornans-type chondrite, petrologic type 3; EH4 = high-enstatite chondrite, petrologic type 4; EL6 = low-enstatite chondrite, petrologic type 6; H chondrite = high-metal chondrite; MORB = mid-ocean ridge basalt. Values and figure adapted from Cartier et al. (2014).

Previous studies on silicate melt demonstrate fO_2 controls on C-O-H speciation in the melt during and/or immediately following core-mantle differentiation. The dominant dissolved species in silicate melts under relatively oxidized conditions >IW−1 are CO_2, H_2O, OH, CO_2^{3-}, while under increasingly reducing conditions, where fO_2 is below IW−2.7, CH_4 and H_2 are expected to become prevalent (e.g., Hirschmann et al., 2012; Armstrong et al.,

2015; Dalou et al., 2017; Grewal et al., 2020). Annealing experiments on natural olivine crystals have demonstrated that fO_2 affects OH dissolution in olivine (Yang, 2015; Yang, 2016; Yang et al., 2016). However, it was not possible to directly measure olivine H_2 in these studies. The incorporation of 'water' as molecular H_2 in these studies was inferred from the re-equilibration of point defects by annealing crystals first in H_2 and then re-annealing at high fO_2, measuring the increased OH absorbance by FTIR, and then converting the absorbance into water contents to estimate presumed original H_2 concentrations (Yang et al., 2016). Previous work on H partitioning between plagioclase and silicate melt demonstrates that fO_2 has a strong influence (Lin et al., 2019).

Currently, there is no available data on the effect of fO_2 on $D_H^{ol/melt}$ under highly reducing conditions where the prevalent C-O-H species are expected to be CH_4 and H_2 based on fluid speciation models. In comparison to frequently studied state variables, such as pressure and temperature, less attention has been paid to the effect of fO_2 on olivine hydration or on partitioning of H-related species values between olivine and silicate melt. Olivine forms one of the basic silicate building blocks of the rocky planets (e.g., Schaefer and Elkins-Tanton, 2018). On Earth, olivine is the most abundant upper mantle mineral with the average volume proportion comprising ~60–70%. Consequently, olivine is of immense importance for understanding the physical properties of the Earth's upper mantle and also the mantles and dynamic evolution of other planetary interiors. Since the vast majority of published work at very reducing conditions is based solely on speciation in melts (e.g., Dalou et al., 2017; Grewal et al., 2019, 2020.), there is a critical knowledge gap that remains unfilled. Following a magma ocean phase, the effects of fO_2 have yet to be constrained in terms of H incorporation within mineral phases comprising solid planetary interiors. Post magma ocean,

the distribution of H across planetary interiors will depend on mineral-melt partitioning, and mobilization of H will depend on partitioning behaviour during subsequent magmatic processes. In such scenarios, olivine is the most important mineral phase to consider. Olivine is volumetrically dominant in silicate mantles, stable during partial melting, and commonly a liquidus phase (e.g., Schaefer and Elkins-Tanton, 2018). The speciation and partitioning of volatiles between olivine and natural silicate melts under the highly reduced conditions prevalent during rocky body formation is poorly constrained. Recent work has either focused on oxidized to only moderately reduced systems (e.g., Potts et al., 2020) or entirely on silicate melt (e.g., Hirschmann et al., 2012; Armstrong et al., 2015; Dalou et al., 2017; Grewal et al., 2019, 2020). Even in highly reduced glass experiments, evidence of the dissolution of molecular H_2 could not be detected by Raman spectra (Grewal et al., 2020), suggesting significant experimental or analytical challenges.

In this study, we present the first experimental data on partitioning of H in a highly reduced system. By combining Raman spectrographic analyses with bulk C and H concentrations of the silicate glasses, we demonstrate the influence of fO_2, with variation of P, T and NBO/T (the non-bridging oxygen to tetrahedral sites as a measure of the extent of melt polymerization) on the speciation of C-O-H volatiles in reduced silicate melts. The results may be used to predict the contents and partitioning behaviour of C-O-H volatiles in olivine and melt in a variety of magma settings applicable to assorted rocky bodies in our Solar System.

2.3 Methods

2.3.1 Starting materials

The starting materials consisted of high-purity oxides (SiO_2, Al_2O_3, MgO) and carbonates (Na_2CO_3, $CaCO_3$) with $Mg(OH)_2$ or MgH_2 acting as the H source. Atmospheric volatile contamination was minimized by storing the starting oxide and carbonate powders at 110 °C. This temperature will not induce thermal decomposition when materials are stored for short durations. An agate mortar and pestle were used to homogenize and grind the oxides and carbonates into a fine powder prior to stepwise decarbonating by heating (e.g., $CaCO_{3(s)} \rightarrow CaO_{(s)} + CO_{2(g)}$; $Na_2CO_{3(s)} \rightarrow Na_2O_{(s)} + CO_{2(g)}$) using a heating ramp from 600-1000 ℃ over at least 8 hrs. After weighing the starting mix to confirm complete decarbonation and account for transfer loss, the appropriate proportions of $Mg(OH)_2$ and MgH_2 were added. The mixture was again homogenized and stored again at 110 °C prior to capsule loading. Starting compositions are shown in Table 2.1. Three oxidized mixes were created using differing amounts of $Mg(OH)_2$ as well as three reduced starting mixes using various amounts of MgH_2.

Table 2.1. Starting compositions (weight %)

Composition	Anhydrous basis	Oxidized Mix 1	Oxidized Mix 2	Oxidized Mix 3	Reduced Mix 1	Reduced Mix 2	Reduced Mix 3
SiO_2	46.7	45.7	43.4	42.0	46.6	46.2	45.7
Al_2O_3	8.4	8.2	7.8	7.6	8.4	8.3	8.2
MgO	40.1	39.3	37.3	36.1	40.0	39.7	39.3
Na_2O	1.8	1.7	1.6	1.6	1.8	1.8	1.7
CaO	3.0	3.0	2.8	2.7	3.0	3.0	3.0
H_2O	-	2.0	7.0	10.0	-	-	-
H_2	-	-	-	-	0.2	1.1	3.2
Total	100.0	100.0	100.0	100.0	-	-	-
% H_2 in H_2O		0.2	0.8	1.1			

Before the selection of the final starting mix shown in Table 2.1, significant method development was necessary to determine a composition that was both physically meaningful as a planetary analog and conducive to experiments. The MgO-Al_2O_3-SiO_2-H_2O (MASH) system constitutes approximately 90% of the Earth's mantle (Omori and Komabayashi, 2007). Using a simplified starting composition in experimental petrology limits complicating factors associated with complex evolving crystal chemistries during crystallization experiments (Grant et al., 2006, 2007a). Other major mantle components are FeO and CaO, however including these compounds in the MASH system causes unwanted continuous reactions involving compositional changes in the solid-solution minerals (Omori and Komabayashi 2007). Experiments in FeO and/or CaO bearing systems do not produce significant differences in dehydration reactions compared with MASH pertaining to water transport in the deep mantle (Omori and Komabayashi, 2007). Therefore, the MASH system provides a reasonable approximation for investigating the mantle water system and can be used as a reference point for the investigation of more complex systems. Yet, the MASH system representing the Earth's primitive mantle is not conducive to experimentation as the solidus temperature is near or above the working limit of the piston

cylinder press. Therefore, our final composition includes CaO. Numerous papers have been published considering various bulk composition estimates for the Earth's primitive mantle, data corrections, as well as review papers with reported consensus averages (Ringwood, 1979; Anderson, 1983; Wanke et al. 1984; Palme and Nickel, 1985; Taylor and McLennan, 1985; Hart and Zindler, 1986; Wanke and Dreibus 1988; Hoffman, 1988; McDonough and Sun, 1995; Warren, 2005; Lyubetskaya and Korenaga, 2007; Palme and O'Neill, 2014). Similarly, many literature estimates exist for the Martian system (Morgan and Anders, 1979; Dreibus and Wänke, 1985; Lodders and Fegley, 1997; Bertka and Fei, 1997; Sanloup et al., 1999; Khan and Connolly, 2008; Taylor, 2013), as well as for the primitive lunar mantle (Ringwood, 1979; Buck and Toksoz, 1980; Warren, 2005; Longhi, 2006; Elardo et al., 2011). Grant et al. (2007a) utilized a synthetic composition that produced coexisting forsterite and silicate glass from a water-bearing basalt analogue in experiments conducted at 1.0, 1.5, 2.0 and 2.5 GPa. Due to the similarities in the bulk mantle compositions, especially in the simplified system, the synthetic composition used by Grant et al. (2007a) was considered a reasonable first order approximation for bulk Earth, lunar, and Martian compositions, which may also be applicable to other primitive rocky bodies. The Grant et al. (2007a) starting mix, based on 30 wt% forsterite + 70 wt% albite, provided an approximate model for a basaltic composition from which the desired run products could be produced. Using a 50:50 mix of anorthite + albite as the plagioclase endmember in the 2-phase mix (i.e., in accordance with proportions used by Grant, this would be 35 wt% albite, 35 wt% anorthite and 30 wt% forsterite), this results in a melt with an appropriate Na content (Figure 2.3). However, an additional problem with the Grant mix is the apparent inability to stabilise forsterite (fo) in equilibrium with melt and the majority of their experiments instead produce enstatite instead of the desired olivine. This is most likely due to the fact that the bulk

composition has a higher Si:Mg ratio than enstatite. At higher pressures approaching 2 GPa, the eutectic in the MgO-SiO_2 shifts to lower SiO_2 contents, and the stability field of enstatite+ liquid is enlarged (Figure 2.4). Therefore, it was necessary to further modify the starting composition to compensate by increasing the proportion of Mg. To summarize, the final synthetic composition was selected on the basis that it 1) is a composition with broad physical relevance to real world systems, 2) synthesizes olivine and silicate melt within the working parameters of the press, 3) preferentially stabilizes olivine over enstatite.

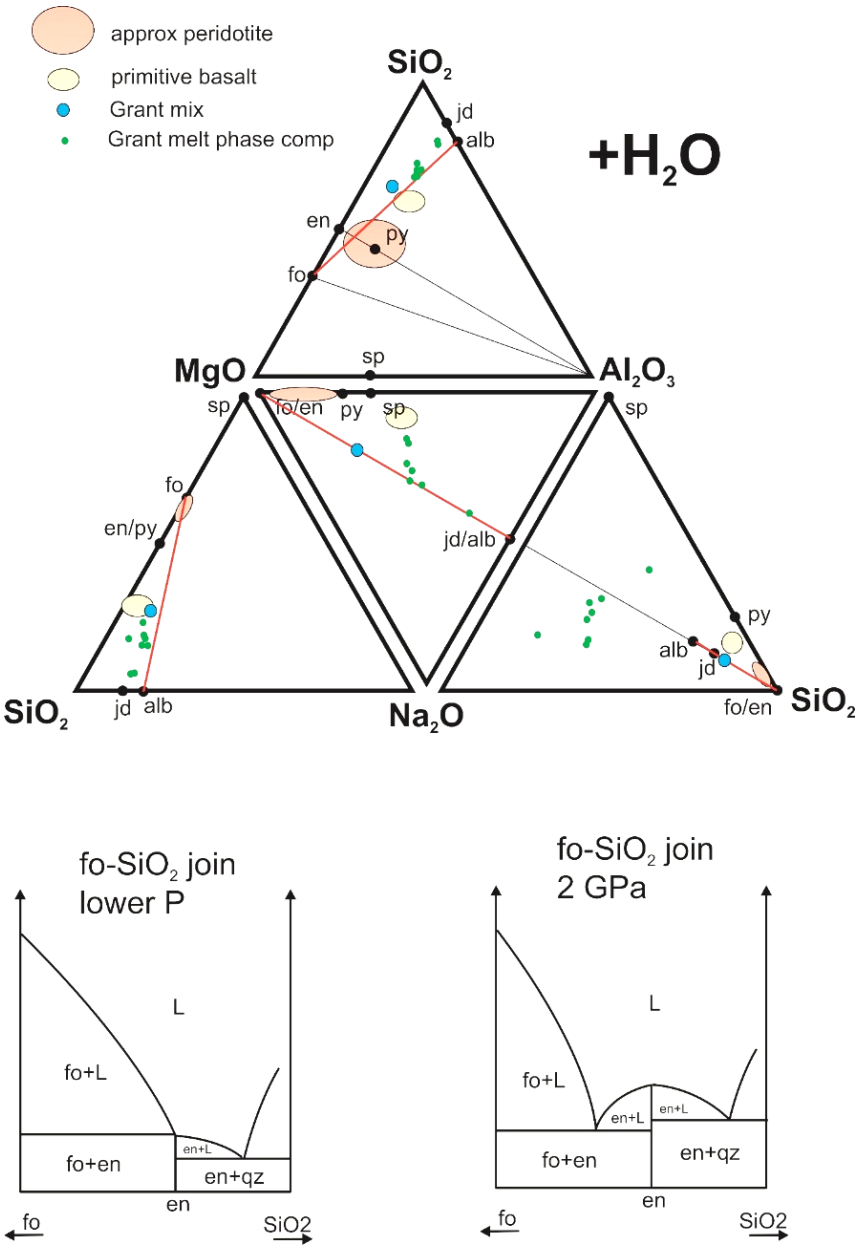

Figure 2.2. Top: Series of ternary diagrams (based on molecular proportions) showing compositions of major phases in the system MgO-SiO_2-Al_2O_3-Na_2O +H_2O (to excess). Approximate averaged compositions of peridotite and primitive basalt shown for reference. Red line denotes the fo-alb tie-line, blue circle, the bulk composition used by Grant, and green dots, melt compositions from their experiments. Most runs produced en+L rather than fo. Bottom: sections of the MgO-SiO_2 join showing phase relations as a function of increasing temperature. The bulk composition used by Grant lies towards the SiO_2-rich side of the composition of enstatite. As such, forsterite is not stable. However, in more complicated systems, the composition of enstatite is modified as it can incorporate significant Al_2O_3. This can open up the phase field fo+Al-en+L. However, at higher pressure (based on these phase diagrams and results of Grant) it still appears as if the bulk composition they used results in a mostly two-phase mix en+L, due to the effect of pressure in stabilising en+L. (Note that fo=forsterite, en=enstatite, alb=albite, L=liquid.)

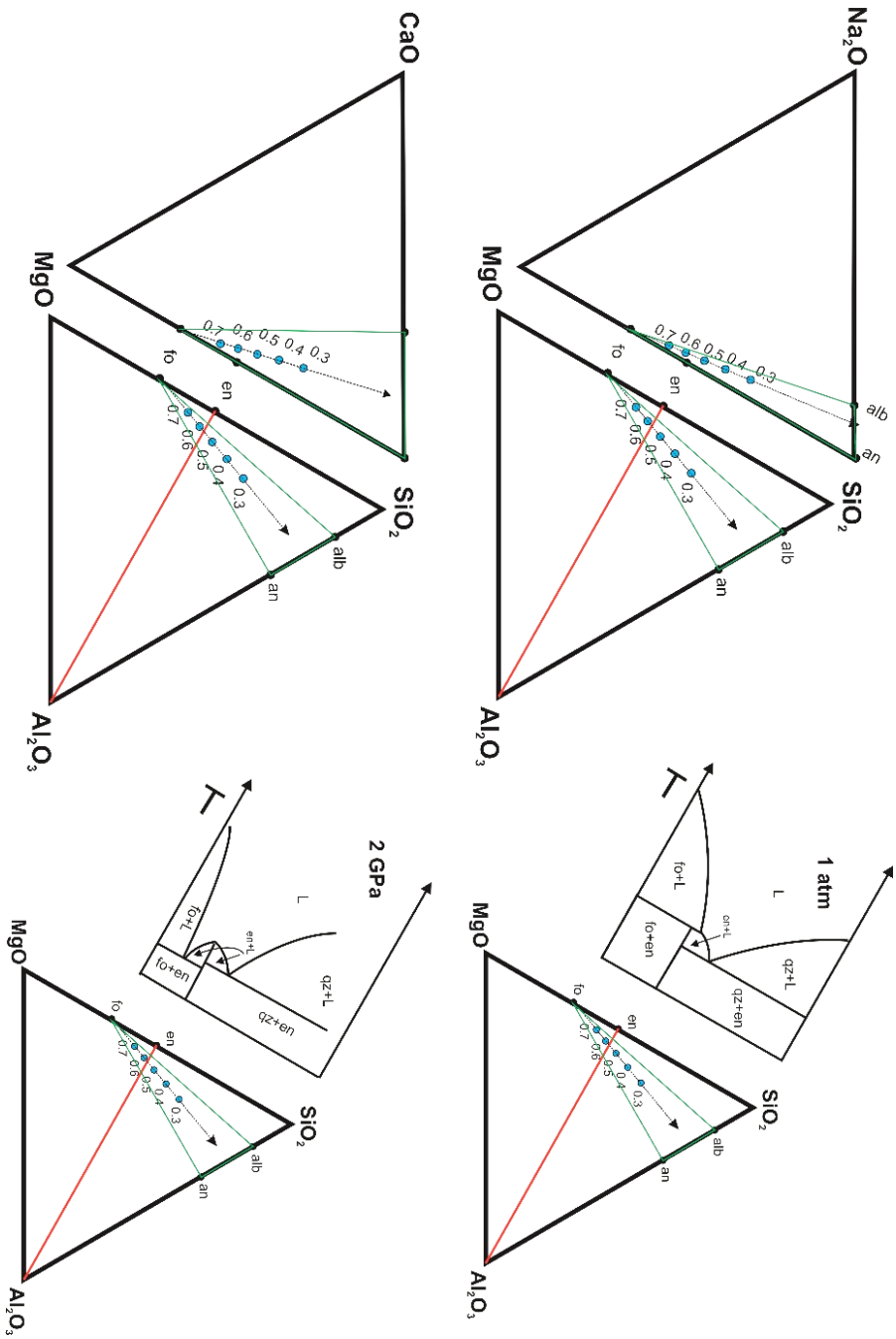

Figure 2.3. Ternary plots showing bulk compositions (listed in weight fraction forsterite, with equal proportions anorthite and albite) as blue dots. Increase in fo weight fraction also results in reduction in both CaO and Na_2O bulk contents, presumably increasing solidus temperatures. Figures to right also show high-temperature relations across the fo-SiO_2 join at 1 atm and 2 GPa. At lower pressures, 0.6 and 0.7 wt fraction fo should stabilise fo+L at high temperature. However, melting at high-pressure still causes problems, as the stability field of en+L is considerable.

2.3.2 High-pressure experiments

Experiments were performed in an end loaded piston-cylinder at the University of Edinburgh from 1-3.5 GPa and 1435-1750 °C (Table 2.2).

Table 2.2 Piston-cylinder **e**xperimental conditions

Sample	Starting mix	Carbon	P (GPa)	T (°C)	fO_2 (Bars)*	fH_2O (GPa)	ΔIW
			Oxidized				
C3	Oxidized Mix 1	-	2	1435	-4.9	10.9	3.8
C4	Oxidized Mix 1	-	2	1470	-4.7	10.8	3.8
C5	Oxidized Mix 1	-	2	1530	-4.2	10.6	3.7
C6	Oxidized Mix 1	-	2	1600	-3.7	10.4	3.6
C7	Oxidized Mix 1	-	1	1530	-4.5	2.1	3.8
C8	Oxidized Mix 1	-	3	1600	-3.5	36.6	3.6
C9	Oxidized Mix 2	-	1	1530	-4.5	2.1	3.8
C10	Oxidized Mix 3	-	2	1600	-3.7	10.4	3.6
			Reduced				
B2	Reduced Mix 1	-	2	1600	-11.1	10.4	-3.7
B5	Reduced Mix 1	-	1	1530	-12.4	2.1	-4.2
B6	Reduced Mix 1	-	3	1600	-10.8	36.6	-3.7
B7	Reduced Mix 1+ C	+	2	1600	-11.2	10.4	-3.8
B8	Oxidized Mix 1	-	1	1530	-12.4	2.1	-4.2
B12	Reduced Mix 1+ C	+	1.5	1630	-11.1	5.0	-3.8
B14	Reduced Mix 1+ C	+	2	1750	-9.7	9.9	-3.4
B18	Reduced Mix 2	-	2	1700	-10.2	10.0	-3.5
B19	Reduced Mix 2	-	2	1600	-11.1	10.4	-3.7
B21	Reduced Mix 2	-	3	1630	-10.5	35.8	-3.6
B25	Reduced Mix 2	-	1	1530	-12.4	2.1	-4.2
B26	Reduced Mix 2+ C	+	3.5	1550	-11.1	67.7	-3.8
B29	Reduced Mix 2+ C	+	3	1550	-11.3	37.9	-3.9
B30	Reduced Mix 2+ C	+	3.5	1700	-9.6	59.6	-3.4

Note: all experiment run durations were between 6-8 hours.
*fO_2 values estimated according to solid state buffer EoS as noted in Chapter 1.

For the reduced experiments, a Cr-Cr_2O_3 oxygen buffer was used to impose low fO_2 conditions. The oxygen balanced solid-state buffer reaction is given by

$$4Cr + 3O_2 \rightleftharpoons 2Cr_2O_3. \quad (2.1)$$

Since water is added to the outer capsule, the reaction may also be balanced with H_2O,

$$2Cr + 3H_2O \rightleftharpoons Cr_2O_3 + 3H_2 \tag{2.2}$$

and is expected to enforce fO_2 conditions several log-bar units below the IW for the temperature conditions of this study (Holzheid and O'Neill, 1995). For the oxidized experiments, the H source was produced from the thermal decomposition of magnesium hydroxide,

$$Mg(OH)_{2(s)} \rightarrow MgO_{(s)} + H_2O_{(g)}. \tag{2.3}$$

Unbuffered experiments represent comparatively more oxidized conditions and are assumed to be near the Ni-NiO buffer, as enforced by the end loaded piston-cylinder's intrinsic fO_2. To ensure a high fH_2, the reduced experiments utilized the thermal decomposition of magnesium hydride,

$$MgH_{2(s)} \rightarrow Mg_{(s)} + H_{2(g)} \tag{2.4}$$

and the produced magnesium is expected to react with remaining air in the capsule such that

$$2Mg_{(s)} + O_{2(g)} \rightarrow 2MgO_{(s)} \tag{2.5}$$

which will further ensure a low fO_2 by acting as a sink for $O_{2(g)}$. Both reduced and oxidized experiments were performed near the same pressure and temperature conditions to enable a clear comparison of the influence of fH_2 and

fO_2. Experimental details, including the estimated fH_2O for pure fluid under P-T conditions according to the Pitzer and Sterner (1994, 1995) EoS and fO_2 (based only on the redox buffer) are summarized in Table 2.2.

The starting mix was loaded into the inner 3 mm capsule and the capsule was sealed by arc welding under argon flow with care taken to prevent water loss due to heating. The Cr-Cr_2O_3 buffer and distilled water were loaded into the bottom of the one-end welded outer platinum capsule, which has an outer diameter of 4 mm, length ~6 mm. Using 0.5" talc-Pyrex-graphite piston-cylinder assemblies as described in Bromiley et al., (2017), experiments were pressurized to 1000 psi prior to heating at a rate of approximately 100 °C /min whilst simultaneously pressurising (hot piston in technique). Temperature was monitored throughout using a R-type thermocouple, placed 0.5 mm from the capsule. Once the desired run conditions had been reached, pressure and temperature were continually monitored and controlled. The dwell time for each run was selected to allow for equilibration between olivine and melt and to also ensure olivine crystals and areas of glass were a sufficient size for SIMS analysis via Ostwald ripening of olivine crystals. The duration for each experiment was approximately 8 hours. Samples were quenched isobarically to room temperature by switching off the power to the system. The pressure was gradually bled to avoid significant fracturing of the glass and olivine run products. Capsule integrity was checked both before and after experiments. To better ensure the efficacy of the double capsule technique, energy dispersive x-ray spectroscopy SEM-EDS was used to confirm that all components of the buffer remained following the run. The presence of reactants, products, and H_2O in the buffer assemblage following an experiment serves as an indicator that the buffer was not exhausted during an experiment (Figure 2.4). Samples that experienced catastrophic failure (such as capsule breakage or buffer leakage) were not analysed.

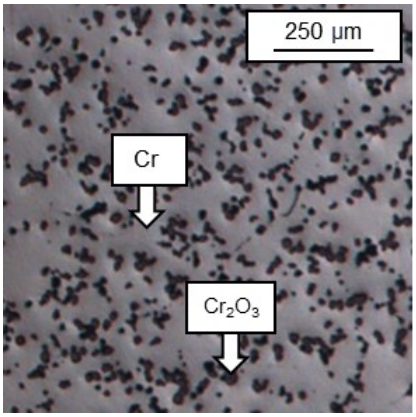

Figure 2.4 A representative image of the Cr-Cr_2O_3 buffer following an experimental run. Both Cr and Cr_2O_3 remain visible in the optical microscope image. The black areas are the Cr oxide, while the Cr appears more reflective. Visually confirming by both backscattered SEM and petrographic microscope that both parts of the oxidation-reduction buffer are present following the experiment suggests that the double capsule technique is still effectively buffering fO_2. In failed experiments where either the outer or inner capsule ruptured, the buffer components could not be distinguished.

2.3.3 Sample preparation

Each capsule was extracted from the assembly and halved using a 2 µm diamond wire saw. Both halves of the capsules were mounted in Crystalbond™ from Aremco Products and ground and double polished with diamond suspensions. Epoxy impregnation was avoided to prevent interference during Secondary Ion Mass Spectrometry (SIMS) or Raman analysis. To remove Crystalbond™ and other surface contaminants, polished samples were cleaned with multiple washes of high-purity acetone and ethanol as well as ultrasonic baths. Samples were mounted in indium, and carbon coated for analysis by SEM-EDS. Following SEM analysis, the carbon coat was removed by repolishing sample surfaces with a 0.25 µm diamond suspension and repeating the cleaning procedure. The repolished samples were gold coated in

preparation for H and C analysis by secondary ion mass spectrometry (SIMS). As discussed in the results section, many of the samples were highly fragile and only a limited number of experimental run products could be rigorously cleaned and polished as necessary.

2.3.4 SIMS analysis

Concentrations of H and C in olivine and coexisting glasses were determined by SIMS on a Cameca ims-4f at the NERC ion probe facility at the University of Edinburgh. Samples were carefully cold pressed into indium mounts, which has superior outgassing properties in comparison to more frequently used epoxy resins. To minimize H backgrounds prior to analysis, samples were stored in a vacuum desiccator at 110 °C both before and after mounting in indium (Koga et al., 2003; Hauri et al., 2006; Tenner et al., 2009). Samples were cleaned using an ultrasonic bath with isopropanol and then sputter-coated with ~35 nm gold coating to improve electrical conductivity. Available standards include ALV-519, a piece of basaltic glass containing 1700 ± 86 ppm water (Aubaud et al., 2004; Aubaud et al., 2007), orthopyroxene standards KH03-4 (216 ± 12 ppm H_2O) and 116610-10 containing (128 ± 12 ppm H_2O), clinopyroxene standards KH03-4 (427 ± 25), SC-J1 (62 ± 4), and SMC31139 (5 ± 8 ppm H_2O) (Kumamoto et al., 2017). SIMS calibration curves yield similar matrix effects for olivine and orthopyroxene identical within analytical uncertainty (Koga et al., 2003; Kovács et al., 2010; Withers et al., 2011; Mosenfelder and Rossman, 2013; Warren and Hauri, 2014) and clinopyroxene is expected to perform similarly. The in-house olivine standard DC0212 (see De Hoog et al., 2010 for sample details) as well as another in-house forsterite standard (Ol-Fo_2) were analysed to monitor for matrix effects as well as instrument performance and calibration, but this standard

was not used to quantify H or C contents. The anhydrous olivine standard 116610-2 was used to determine and subtract the H_2O background. Prior to analysing samples, calibration curves were constructed by performing background correction and then multiplying H/Si or C/Si ratios by calibration factors. The calibration curves are shown in the Appendix in Figure A.1. Prior to analyses, the sample chamber was baked for at least 24 hours to minimize volatile contamination in the vacuum and the total pressure was ~5×10^{-8} mbar during analyses. An O^- primary ion source with a beam current of 5 nA accelerated to 10 kV was used, while secondary ions were accelerated to 4500 V with a subtracted offset of 75 eV for H measurements, and 50 eV offset for C. The ion source was tuned in critical illumination mode and the beam focus was carefully examined and refocused throughout the session as necessary to produce a beam diameter of approximately 20 µm. To remove surface contaminates prior to each analysis, the spot was rastered with a 30 µm beam for 3 min. Analysis was conducted with a 10 µm small field aperture. Measurements consisted of 10 cycles, however the first 5 cycles for H measurements were discarded to lessen surface contamination. Reported errors are standard deviations on mean values for each sample based on repeat analyses. To avoid cracks and fractures, the scanning ion image was collected and archived for each measurement taken. Several measurements were purposefully taken on such features to be used as a comparison for contamination.

2.3.5 Raman analysis

Following SIMS analysis, gold coatings were removed by gentle repolishing using a 0.25 µm diamond suspension. Raman spectra were acquired using a Thermo Scientific DXRxi Raman Imaging Microscope at the University of Bristol, School of Earth Sciences. Reflected optics were used to obtain spectra on well-characterized, polished surfaces. The system was equipped with a green, 532 nm (DPSS type, frequency doubled Nd:YVO_4) laser with a spectral resolution of approximately 2 cm^{-1} and a 50× objective over the spectral range 50–4500 cm^{-1}, while targeted spectral ranges were used to confirm peaks under improved signal to noise conditions. Various acquisition times and repetitions were used to maximize the signal to noise ratio according to the sample.

2.3.6 Electron microprobe analysis (EPMA)

Carbon coated samples were analysed by electron probe microanalysis (EPMA) for the major element compositions of the minerals and melts using a Cameca EPMA at the University of Edinburgh running at 15 kV. Standards consisted of forsterite and a basaltic glass (*BCR2G*) to determine the major element compositions of olivine and silicate glass from run products, where the electron-beam conditions for glass were 2 nA and an 8 µm beam, while olivine used a 4 nA, 2µm beam. EPMA analysis was conducted after SIMS work.

2.4 Results

2.4.1 Textural description of experimental products

The analysed silicate glasses had a homogenous glass texture without evidence of bubbles, outgassing, and with only minor quench crystallization in

some samples. All experiments are expected to be at fluid-undersaturated conditions, and no experiments exhibited signs of quenching an aqueous fluid. The experiments produced clearly distinguishable olivine crystals in equilibrium with silicate melt. Many distinct and euhedral olivine crystals coexisted within the glass ranging from 10 to 200 μm across, as well as clusters of olivine crystals, and some quench crystallites as seen in B7 in Figure 2.5.

A high failure rate was evident in the highly reduced experiments with high volatile contents. At standard pressure (101.325 kPa), the melting point of platinum is 1768.3 °C. Therefore, capsule melting is not normally expected. However, the solubility of platinum in silicate melts may increase significantly in the presence of water compared to anhydrous systems. Platinum oxide is soluble at the ppb level, while hydroxide complexes are formed under fluid-excess conditions at the ppm level (Bezmen et al., 2008). An increase in platinum solubility under reducing conditions can be explained by the formation of platinum hydride complexes or platinum–fluid–silicate clusters (Bezmen et al., 2008). The formation of platinum micronuggets in melts have been reported under reducing conditions (Borisov and Palme, 1997; Ertel et al., 1999, 2006) as nonequilibrium metallic particles resulting from contamination by the starting materials used in the experiments. The platinum micronuggets seen in this study appear similar to metallic iron blobs in quenched silicate melt reported by Steenstra et al. (2017). Furthermore, hydrogen has a stronger depolymerization effect on silicate melts than water (Bezmen et al., 2005), which would promote the formation of such platinum clusters in the reduced experiments reported here. Figure 2.5 illustrates the influence of H_2 content on Pt capsule stability. At the highly reduced conditions imposed by the buffer and the hydride mixture, the Pt capsule became susceptible to capsule failure. In these experiments, metal blobs became embedded in silicate melt, causing the run products to be unsuitable

for analysis. As similarly noted by Potts et al. (2021), at low fO_2 the Pt capsule appeared more brittle and susceptible to failure as evidenced by apparent fractures cutting across the recovered capsules. Therefore, no experiments could be successfully analysed from Reduced Mix 3.

Figure 2.5. Representative capsule stability and texture of run products (B7, B18, and B1) for each reduced starting mix with the increasing amount of H_2 added as MgH_2 in the starting mixture. See text for further discussion.

2.4.2 Composition and NBO/T

Melt polymerization can be described by calculating the ratio of non-bridging oxygen to tetrahedral sites (NBO/T) using major element melt data. The NBO/T value, calculated according to Mysen et al. (1985), assumes that Si^{4+} is a network-forming cation in tetrahedral coordination. Additionally, Al^{3+} is a network-forming cation in tetrahedral coordination, since there are sufficient M^{2+} (Ca^{2+}, and Mg^{2+}) and M^{+} (Na^{+} and K^{+}) cations to form charge balanced Al^{3+} complexes (Mysen et al., 1985). Calculations used the EPMA data in Table 2.3 and 2.4.

Table 2.3. EPMA data for melt compositions

Sample	n	Na_2O	±	MgO	±	Al_2O_3	±	SiO_2	±	K_2O	±	CaO	±	Cr_2O_3	±	Total*
Oxidized																
C2	5	5.03	0.10	15.58	0.48	19.07	0.94	51.37	0.52	0.75	0.06	7.22	0.24	0.00	0.01	99.08
C3	3	5.35	1.46	13.85	2.09	19.47	1.05	49.63	0.56	0.87	0.39	8.66	1.46	0.00	0.00	97.97
C4	6	2.80	0.08	26.69	0.65	13.42	1.04	51.20	0.54	0.43	0.07	4.41	0.06	0.00	0.00	98.96
C5	5	3.31	0.18	21.83	1.17	15.21	0.46	53.05	0.45	0.51	0.05	5.44	0.48	0.00	0.01	99.40
C6	5	2.49	0.39	30.05	3.76	11.67	1.44	49.88	0.88	0.39	0.04	3.93	0.66	0.00	0.00	98.47
C7	4	2.44	0.05	30.87	0.53	11.15	0.22	50.15	0.57	0.36	0.01	3.88	0.03	0.00	0.00	98.92
C8	2	2.88	0.05	25.93	0.99	15.07	0.86	47.36	0.06	0.06	0.01	5.29	0.11	0.00	0.00	96.63
C9	2	1.64	0.08	37.93	0.41	8.38	0.08	44.12	0.48	0.02	0.01	2.79	0.01	0.00	0.00	94.92
C10	2	1.32	0.10	39.83	1.27	8.10	0.27	46.09	0.50	0.11	0.02	2.34	0.28	0.00	0.00	100.23
Reduced																
B2	4	3.09	0.09	26.78	0.22	14.36	0.11	45.59	0.56	0.04	0.01	5.97	0.15	2.82	0.02	98.66
B7	4	2.73	0.05	27.87	0.48	14.26	0.44	45.04	0.68	0.03	0.01	5.70	0.09	0.11	0.10	95.76
B8	4	0.56	0.02	30.09	0.71	17.64	0.32	45.18	0.32	0.04	0.01	1.43	0.04	4.19	0.39	99.15
B18	3	4.62	0.89	16.90	3.00	25.11	0.75	42.66	0.52	0.02	0.01	8.71	0.65	0.00	0.00	97.93
B19	4	3.36	0.14	29.10	0.80	15.34	0.46	47.20	0.56	0.00	0.01	5.40	0.24	0.45	0.03	100.82
B21	3	3.97	0.31	12.40	0.88	25.94	0.40	45.08	0.17	0.24	0.03	10.40	0.27	0.04	0.00	98.00
B25	4	4.45	0.07	21.86	0.15	17.17	0.31	49.75	0.49	0.02	0.02	6.63	0.10	0.60	0.04	100.48
B30	1	2.92	0.00	26.11	0.00	14.09	0.00	46.12	0.00	0.06	0.00	5.51	0.00	0.42	0.00	95.25

*FeO, MnO, TiO_2, P_2O_5, NiO below LoD.

Table 2.4. EPMA data for olivine compositions

Sample	n	MgO	±	SiO_2	±	Na_2O	±	Al_2O_3	±	CaO	±	Cr_2O_3	±	Total
Oxidized														
C4	4	55.82	0.35	42.79	0.26	0.02	0.00	0.16	0.01	0.10	0.00	0.00	0.01	98.91
C6	6	55.83	0.25	42.43	0.27	0.01	0.00	0.15	0.01	0.09	0.00	0.00	0.01	98.53
C7	4	55.75	0.17	42.75	0.11	0.01	0.00	0.13	0.01	0.10	0.00	0.00	0.01	98.75
C8	4	56.09	0.27	42.30	0.33	0.02	0.00	0.20	0.02	0.10	0.01	0.00	0.01	98.71
C9	6	56.78	0.27	42.44	0.14	0.00	0.00	0.10	0.00	0.06	0.00	0.00	0.00	99.39
C10	4	57.48	0.17	41.76	0.41	0.00	0.00	0.07	0.00	0.06	0.00	0.00	0.00	99.37
Reduced														
B2	4	56.61	0.19	41.61	0.23	0.02	0.00	0.23	0.03	0.16	0.01	0.49	0.26	99.13
B6	9	56.39	0.22	42.06	0.27	0.04	0.00	0.41	0.02	0.25	0.00	0.07	0.02	99.22
B7	4	56.68	0.14	41.92	0.28	0.02	0.01	0.24	0.02	0.13	0.01	0.04	0.01	99.03
B14	2	52.14	1.55	41.39	0.36	0.04	0.01	0.43	0.13	0.16	0.03	5.34	2.18	99.51
B18	4	57.39	2.91	41.94	2.74	0.02	0.00	0.42	0.04	0.20	0.00	0.01	0.01	99.97
B19	3	56.58	0.12	41.76	0.45	0.03	0.00	0.26	0.02	0.16	0.00	0.17	0.09	98.94
B21	8	57.00	0.12	41.09	0.31	0.03	0.00	0.33	0.02	0.14	0.00	0.01	0.01	98.60
B25	4	56.71	0.36	41.73	0.14	0.01	0.00	0.12	0.01	0.15	0.01	0.11	0.13	98.83
B26	10	55.73	0.32	42.54	0.27	0.02	0.01	0.18	0.03	0.07	0.01	0.25	0.22	98.79
B30	4	56.88	0.19	41.77	0.32	0.01	0.01	0.11	0.02	0.05	0.00	0.46	0.04	99.31

*FeO, MnO, TiO_2, P_2O_5, NiO below LoD.

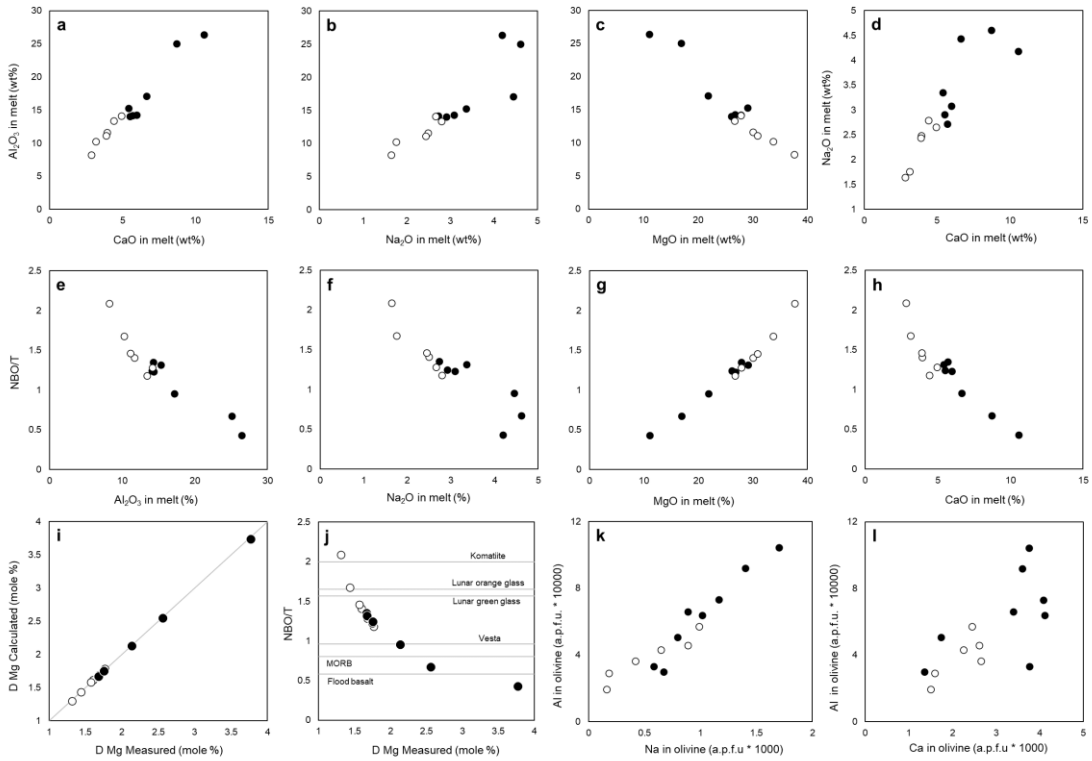

Figure 2.6. Plots from EPMA data. Open symbols represent oxidized experiments, while filled symbols represent reduced experiments. See text for further details.

A summary of variations in the major element data and NBO/T values are shown in Figure 2.6. Trends corresponding to the Al_2O_3 contents of the melt are shown in Figure 2.6a-c with the CaO vs Na_2O trend shown in Figure 2.6d. Melt variations against NBO/T are shown in Figure 2.6e-h. Despite the hydrous nature of these experiments and the variable fO_2 conditions, olivine-melt equilibrium can be assessed based on measured $D_{Mg}^{ol/L}$ values compared to values calculated with the Beattie model according to Eq. 20 in Putirka (2008),

$$D_{\mathrm{Mg}}^{ol/liq} = \frac{0.666 - \left(-0.049 X_{\mathrm{MnO}}^{liq} + 0.027 X_{\mathrm{FeO}}^{liq}\right)}{X_{\mathrm{MgO}}^{liq} + 0.259 X_{\mathrm{MnO}}^{liq} + 0.299 X_{\mathrm{FeO}}^{liq}} \tag{2.6}$$

which is derived solely from melt composition. As shown in Figure 2.6i, the resulting calculated Mg partition coefficients are in excellent agreement with the measured values. The NBO/T of the experimental melt compositions are compared against values from planetary basalts reported in Sehlke and Whittington (2016) and terrestrial basalts reported in Giordano et al. (2008) (Figure 2.6j). Plots of Na vs. Al and Ca vs Al in olivine (atoms per formula unit) are shown in Figure 2.6k and Figure 2.6l respectively, which suggests that Na and Ca may be balanced by Al. In natural mantle peridotites, Cr substitutes for Al extensively (De Hoog et al. 2010). The trace Cr in olivine and the melt in the reduced samples appears quite variable with little to no Cr in some samples, which may be evidence for Cr diffusion across the Pt capsule. However, it is also possible that the remaining buffer contaminates the surfaces of the sample during polishing for analysis.

The clear difference between the oxidized and reduced samples may be explained by the effect of H speciation and enforced fO_2, where a change in melt polymerization due to incorporated H_2 would affect phase relations and element partitioning. Under relatively oxidized conditions, it has been established that the dissolution of C–O–H volatiles in melts alters silicate melt structure, and that both the volatile concentration and carbon redox state are critical factors. Such changes in melt structure in turn alter properties such as melt viscosity, diffusion, liquidus phase relations, mineral-melt element partitioning, and redox relations of aliovalent cations (see Mysen and Richet, 2005 and Nesbitt et al., 2020 for review). Thus, it is expected that a melt structure under the influence of reduced C–O–H volatiles will exhibit different properties from its oxidized counterpart. Specifically, previous studies under oxidized conditions have reported that the speciation and bonding of water influences the degree of polymerization of melts, where H_2O_{mol} reacts with Si-O-Si bonds and H^+ and OH^- are consumed to form SiOH bonds (e.g., Le Losq et

al., 2015). The reaction of H_2O_{mol} species with the network of silicate melts is based on the self-ionization of H_2O_{mol} species (Moretti et al. 2014; Le Losq et al., 2015),

$$H_2O_{mol\ (melt)} \rightarrow H^+_{(melt)} + OH^-_{(melt)}. \quad (2.7)$$

However, in a sufficiently reduced system, the reduction of a silicate component (Si^{4+}) may form H^+ from H_2 (Mysen and Fogel, 2010),

$$Si^{4+} + H_2 \leftrightarrow Si^{2+} + 2H^+ \quad (2.8)$$

The H^+ produced from the oxidation of H_2 reacts with nonbridging oxygen in the silicate melt structure, O^-, to create Si-OH bonds (Mysen and Fogel, 2010),

$$Si{-}O{-}Si{-}O^- + H^+ \leftrightarrow Si{-}O{-}Si{-}OH. \quad (2.9)$$

Carbon also plays an important role. The dissolution of CO_3^{2-} in silicate melt results in increased melt polymerization, increases the activity coefficient of polymerized silicate species in melts, and expands the liquidus volumes of polymerized minerals (e.g., enstatite relative to forsterite) (Kushiro, 1975; Ryerson, 1985; Mysen et al., 2011). Conversely, dissolving methane in silicate melts breaks oxygen bridges where the Si_4^+ is bonded to CH_3 groups and OH groups, respectively, resulting in melt depolymerization and increasing NBO/T (Mysen et al., 2011). This solution of reduced carbon in the silicate melt decreases the activity of polymerized melt species and expands the liquidus volume of depolymerized liquidus minerals (i.e., the forsterite liquidus volume expands relative to the enstatite liquidus volume) (Eggler and Baker, 1982;

Taylor and Green et al., 1987; Mysen et al., 2011). Therefore, any discussion of melt polymerization is incomplete without considering C–O–H volatiles and redox affects.

2.4.3 Bulk C and H contents of olivine and silicate melt

The H partition coefficients and respective H content for olivine and silicate melt was determined using SIMS (Table 2.7 and 2.8).

Table 2.7. SIMS analyses of H in melt and olivine with partition coefficients.

	Melt			Olivine					
Sample	n	H (%)	±	n	H* (ppm)	±	$D_H^{ol/melt}$	±	Suspected Water Loss
					Oxidized				
C3	1	1.16	0.00	–	–	–	–	–	×
C4	4	0.40	0.04	–	–	–	–	–	×
C5	2	0.45	0.03	–	–	–	–	–	×
C6a	6	1.97	0.11	2	91	5	0.005	0.0004	×
C6b	6	1.97	0.11	2	69	7	0.004	0.0004	×
C7a	6	0.28	0.02	2	55	3	0.020	0.0014	✓
C7b	6	0.28	0.02	3	72	4	0.026	0.0018	✓
C8a	4	3.82	0.20	1	208	0	0.005	0.0003	×
C8b	4	3.82	0.20	1	162	0	0.004	0.0002	×
C9a	3	4.25	0.57	3	51	3	0.001	0.0002	×
C9b	3	4.25	0.57	2	46	1	0.001	0.0001	×
C10	3	–	–	3	57	2	–	–	–
					Reduced				
B2	2	0.01	0.00	4	47	6	0.33	0.0438	✓
B5	5	0.20	0.01	–	–	–	–	–	✓
B6a	1	0.43	0.00	4	120	6	0.03	0.0014	✓
B6b	1	0.43	0.00	2	97	6	0.02	0.0014	✓
B7a	2	0.36	0.03	3	62	6	0.02	0.0022	✓
B7b	2	0.36	0.03	4	73	4	0.02	0.0021	✓
B8	3	0.08	0.00	–	–	–	–	–	✓
B12	5	0.90	0.15	–	–	–	–	–	×
B14	–	–	–	2	7	5	–	–	–
B18	1	2.80	0.00	–	–	–	–	–	×
B19	4	1.17	0.03	4	20	3	0.002	0.0003	×
B21a	2	2.71	0.53	3	56	2	0.002	0.0004	×
B21b	2	2.71	0.53	5	65	8	0.002	0.0006	×
B25a	4	0.50	0.04	3	0	0	0.000	0.0000	×
B25b	4	0.50	0.04	1	3	0	0.001	0.0001	×
B26a	–	–	–	4	80	22	–	–	–
B26b	–	–	–	4	116	23	–	–	–
B29a	–	–	–	2	104	4	–	–	–
B29b	–	–	–	3	145	5	–	–	–
B30a	3	3.15	0.21	4	123	4	0.004	0.0003	×
B30b	3	3.15	0.21	2	135	11	0.004	0.0005	×

Errors are standard deviations on mean values for each sample based on repeat analyses.

*H calculations based on SIMS H_2O standard as detailed in text.

Table 2.8. SIMS analyses of C in melt and olivine with partition coefficients.

		Melt			Olivine				
Sample	C added	n	C (ppm)	±	n	C (ppm)	±	$D_H^{ol/melt}$	±
B2	-	2	bdl	bdl	1	bdl	bdl	bdl	
B6	-	3	232	148	2	bdl	bdl	bdl	
B7	+	4	7	8	5	bdl	bdl	bdl	
B8	-	2	bdl	bdl	1	bdl	bdl	bdl	
B18	+	1	105	4	–	–	–	–	
B19	-	4	72	36	–	–	–	–	
B21	-	–	–	–	1	8.3	0.8	–	
B25	-	4	1041	294	2	2.5	0.3	0.0024	

bdl denotes below detection limit.

There is a clear increase in olivine H contents with an increase in pressure, for both the reduced and oxidized experiments (Figure 2.7a), and the increase of $D_H^{ol/melt}$ with pressure can be seen in Figure 2.7b. While the olivine H contents and $D_H^{ol/melt}$ values are systematically lower in the reduced system, the pressure effect is similar between the reduced and oxidized experiments. For the reduced experiments, the influence of temperature on the H content of olivine is illustrated in Figure 2.7c, where increasing temperature at a given pressure decreases H content. This is most apparent in the 2 GPa experiments run at a variety of temperatures.

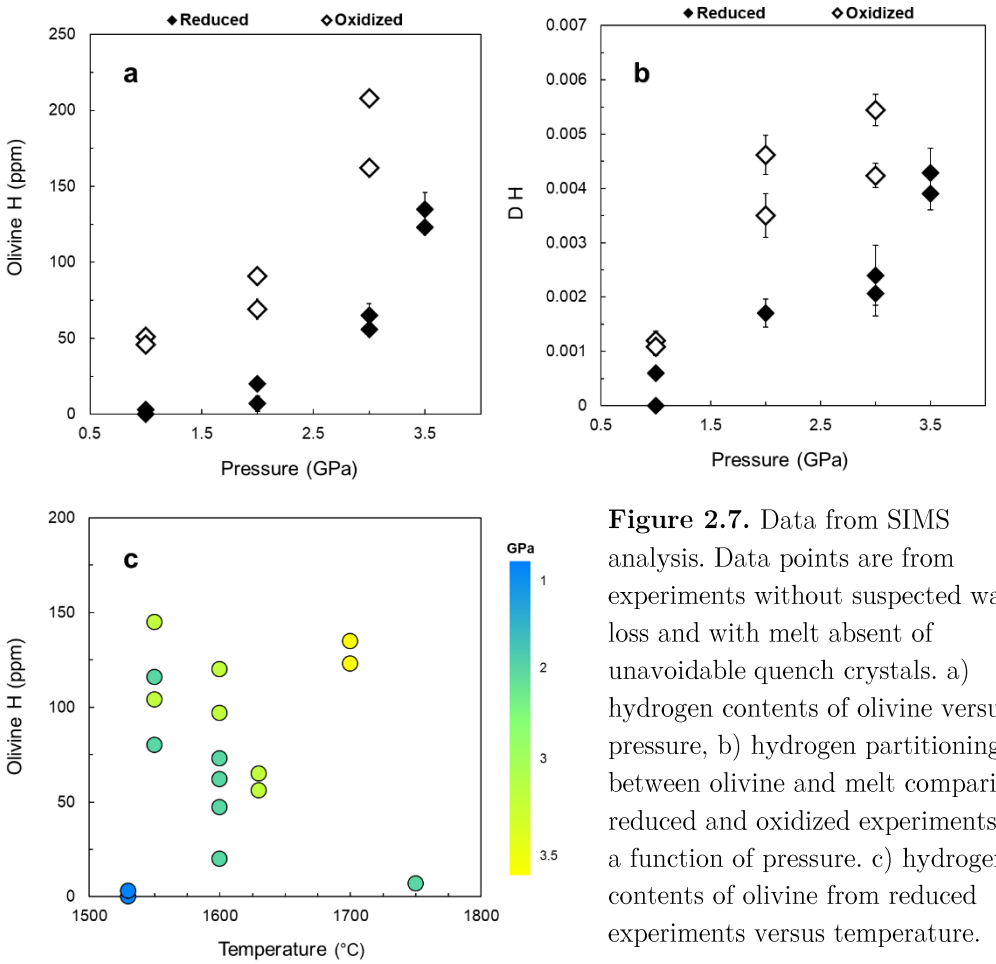

Figure 2.7. Data from SIMS analysis. Data points are from experiments without suspected water loss and with melt absent of unavoidable quench crystals. a) hydrogen contents of olivine versus pressure, b) hydrogen partitioning between olivine and melt comparing reduced and oxidized experiments as a function of pressure. c) hydrogen contents of olivine from reduced experiments versus temperature.

The effect of temperature reflects the increase in melt proportion and concurrent decrease in the activity of H in melt. The observed diminishing H content in olivine with increasing temperature can be explained due to the improved dissolution of silicate in the melt, and the decrease of fH_2O with increasing temperature as calculated using the EoS from Pitzer and Sterner, 1995. Cryoscopic behaviour is expected to lower the chemical potential of silicate melt components (e.g., Hirschmann et al., 2009), so that a greater concentration of H_2O in the melt is evident at low temperature. The SIMS water contents demonstrate rough agreement with the oxide totals of the EPMA measurements (Figure 2.8).

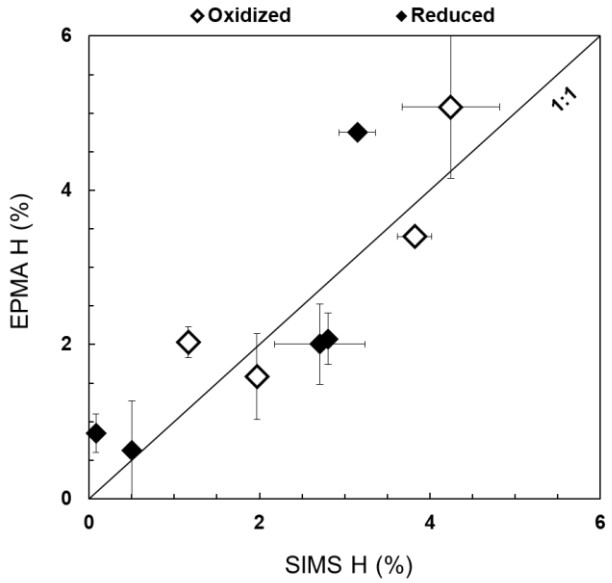

Figure 2.8. Comparison of estimation of H in glass by the EPMA difference method for glasses containing > 1 wt % H versus SIMS H.

The C contents were measured in six olivine samples and four were below the limit of detection (Table 2.8). For the seven melt pockets analysed, five had measurable C contents, while two were below the limit of detection (Table 2.8). Measurable quantities of C in olivine were 8.3 ppm and 2.5 pm for samples B21 and B25 respectively, which is still substantially greater than the <1 ppm range determined by Shcheka et al. (2006). Peridotite phases with carbon added as ^{13}C were analysed using SIMS by Keppler et al. (2003) and reanalysed by Shcheka et al. (2006), where the solubility in olivine annealed at 11 GPa was found to be 12 ppm, while at pressures comparable to this study (≤3.5 GPa) concentrations ranged primarily between 0.1 and 0.8 ppm. Rosenthal et al. (2015) reported concentrations of C in mantle minerals synthesized from a carbonated basalt enriched in ^{13}C at 0.8–3 GPa to range from 0.2 to 3.5 ppm. In studies which did not employ ^{13}C as the C source, elevated C contents for minerals have been reported. Adam et al. (2016) reported olivine CO_2 contents of 20 ± 14 ppm and 44 ± 65 ppm, while Potts

et al. (2021) reported 18 ± 5 C in the olivine sample measured. The employment of ^{13}C to improve analyte selectivity over contamination may explain the discrepancies between these studies. Both Rosenthal et al. (2015) and Adam et al. (2016) noted that SIMS analysis only occurred after samples had been previously carbon coated for SEM work, which even with careful cleaning efforts could be a source of contamination, given the prevalence of C in the environment. Potts et al. (2021) concluded that "it is likely that measured CO_2 contents here largely reflect contamination," based on spectroscopic data and lack of any partitioning between olivine and coexisting silicate melt. Even in sample B6, which had no added C, 232 ppm C was measured in the melt, which may reflect contamination during sample loading, incomplete cleaning, or C entry from the graphite furnace during the run. Brooker et al. (1998) found evidence of carbon infiltration in piston-cylinder experiments from the graphite furnace into the sample capsule, and Moore et al. (2008) interpreted CO_2 diffusion into a double-capsule assembly as migration of carbon from the graphite furnace after 24 h experiments. Furthermore, the evidence found in H_2O–CO_2 fluid inclusions suggest diffusion of C from graphite furnaces through the outer Pt-capsule capsule walls (Jakobsson, 2012). An alternate explanation for the discrepancies between studies could be the difference in mineral equilibration with silicate versus alkali carbonatite melts. There is also a significant difference in the temperature range of this study and Shcheka et al. (2006), which found no temperature influence on C solubility from 900 °C to 1100 °C at 1.5 GPa.

2.4.4 Raman analysis and C–H–O speciation

As shown in Figure 2.9, a broad asymmetrical band with a peak at 3550–3580 cm^{-1} indicating H_2O dissolved as the hydroxyl ion, OH^-, is noted in

spectra obtained from quench melt in all samples. The H_2 vibration peak at 4115–4130 cm^{-1} (Luth et al., 1987; Hirschmann et al., 2012) is apparent in the reduced samples (B14 and B18). A small CH_4 band near 2900 cm^{-1} can be observed in B18. The OH- peak is especially apparent in the oxidized samples and nearly indistinguishable in sample B14 as the H_2 peak becomes more apparent. A high fluorescence in many reduced experiments prevented assessment. While the cause of this fluorescence is unknown, it is likely due to the stabilization of a fluorescent transition metal ion at highly reduced conditions (Baert et al., 2011). Informative absorption bands could only be obtained from the melt phase as the contents in olivine were presumably below the limit of detection.

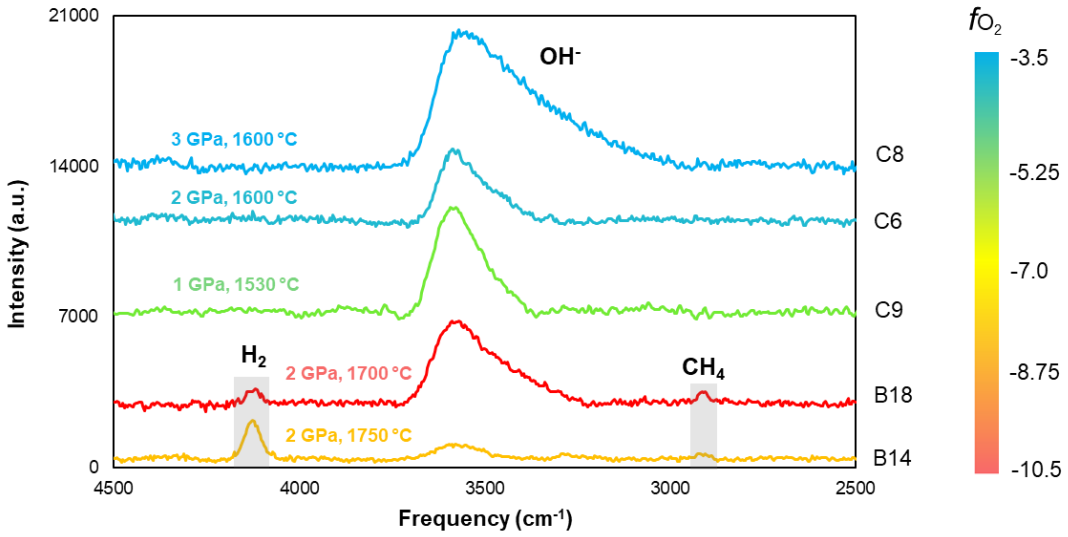

Figure 2.9. Raman spectra for representative samples C6, C8, C9, B14, and B18, where the OH^- peak at ~3550–3580 cm^{-1} is apparent in most samples, while the H_2 peak (4115–4130 cm^{-1}) and CH_4 (2900 cm^{-1}) is only evident in reduced samples. Spectra has been baseline corrected and offset vertically for clarity.

2.5. Discussion

2.5.1 Comparison to thermodynamic fluid models

Thermodynamic fluid models offer an efficient means of predicting fluid speciation at P–T conditions found in a terrestrial planet's deep interior. Most carbon bearing geological fluids at crustal and mantle conditions can be ascribed to the C–O–H system, comprised of H_2O, CO_2, CH_4, H_2, CO, O_2, C_2H_6 in various mixtures (Zhang and Duan, 2009). The observed dependence of H incorporation in olivine and $D_H^{ol/melt}$ on fO_2 (Figure 2.7 and 2.9) can be explained by several mechanisms. The first may be due to the point defects of olivine, such as the trivalent substitution mechanism (see Chapter 4 for further discussion of incorporation mechanisms). Another explanation may involve the change in the composition of fluids in experimental charges, such as the increasing proportion of H_2 and decreasing activity of water with decreasing fO_2. Based on thermodynamic fluid models, a systematic variation of fluid composition is expected to result from fO_2 at a given pressure and temperature. Figure 2.10 considers a model O-H system with calculations performed using the non-ideal mixing Van Laar model of Holland and Powell (2003) and the Sterner and Pitzer (1995) EoS for H_2O and H_2. From 1-3 GPa, pressure is expected to have a minimal effect on speciation; this figure is comparable to experiments with very low carbon activities. As shown in Figure 2.10a, fluids in our experiments are expected to contain either high or low proportions of H_2O/H_2 depending on fO_2. Figure 2.10b shows the estimated water fugacity of the fluid mixture, fH_2O^{fl}, as opposed to the fugacity of pure water, $fH_2O°$, at pressures of 1, 2 and 3 GPa and at temperatures of 1400 °C and 1600 °C to illustrate the effects of P–T. At more oxidizing conditions $XH_2O=1$ and $aH_2O=1$ and $fH_2O^{fl}= fH_2O°$, while at very reducing condition, XH_2 approaches unity and fH_2O^{fl} becomes diminishingly small.

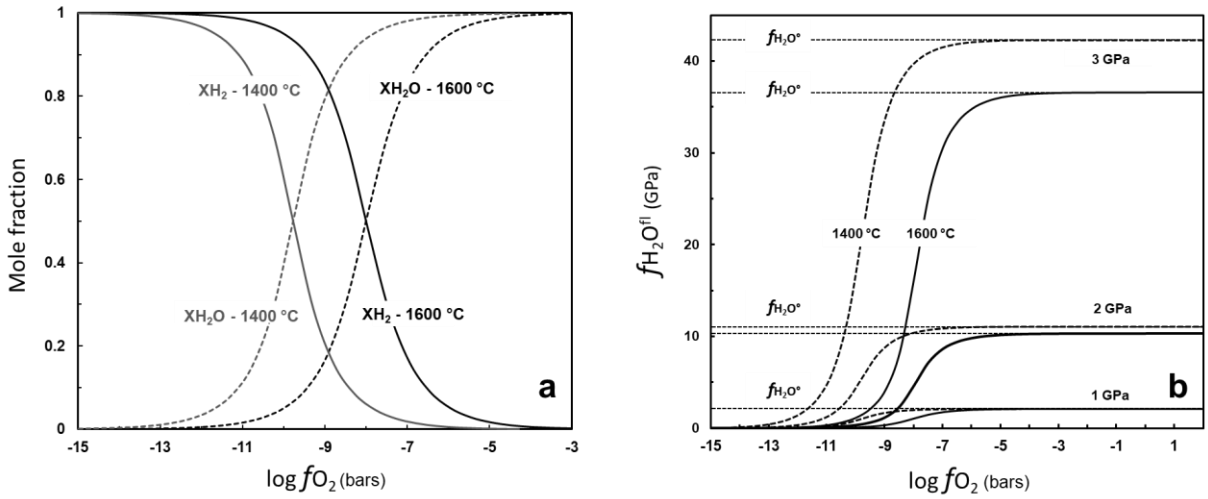

Figure 2.10. Calculated mole fractions and water fugacity in the H-O fluid system. a) Mole fractions of H_2O and H_2 and are shown with reference lines for 1400 °C and 1600 °C at 1 GPa. b) Estimated water fugacity of the fluid mixture, fH_2O^{fl}, based on the mole proportions of fluid species (XH_2O and XH_2) in the O-H system and the fugacity of pure water, $fH_2O°$. Solid lines represent 1600 °C and dashed lines represent 1400 °C. At more oxidizing conditions XH_2O=1 and aH_2O=1. Similarly, at very reducing condition, XH_2 approaches unity.

Using the non-ideal mixing Van Laar model of Holland and Powell (2003), the mole fractions of molecular species in the C-O-H system for a carbon saturated fluid can also be calculated (Figure 2.11).

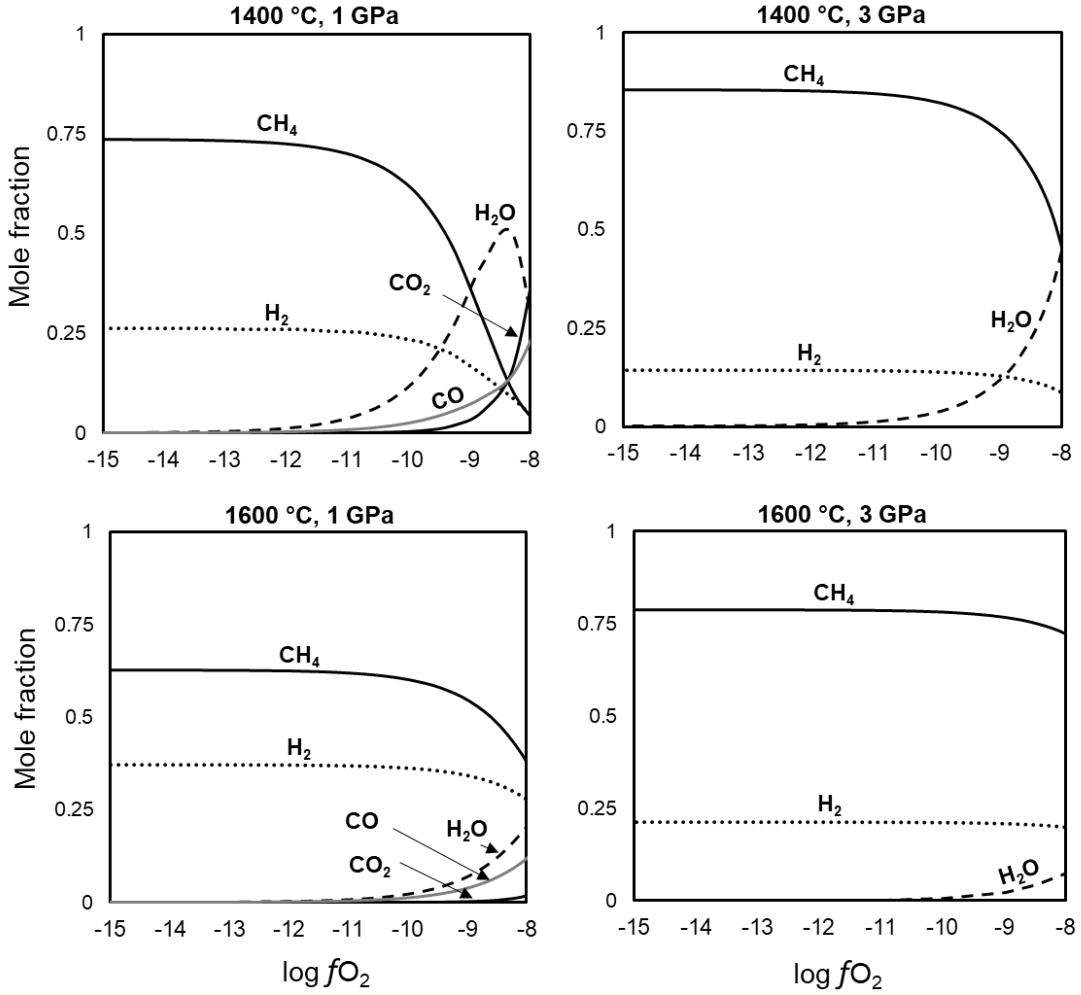

Figure 2.11. Calculated mole fractions of molecular species in the C-H-O system for a carbon saturated fluid. At reduced, carbon saturated conditions, CH_4 is expected to be the principal species, followed by H_2 and H_2O with small amounts of CO_2 and CO. Under oxidizing conditions, H_2O and CO_2 are the dominant species. Calculations were performed using the non-ideal mixing Van Laar model of Holland & Powell (2003, CMP 145.)

In such a system, under highly reduced conditions CH_4 is predicted to become the dominant species, followed by H_2 and H_2O with small amounts of CO_2 and CO. Under oxidizing conditions, H_2O and CO_2 are the dominant species. In the buffered experiments of this study, the dissociation of H_2O produces H_2 and O_2,

$$H_2 + \frac{1}{2} O_2 \rightleftharpoons H_2O \quad (2.10)$$

and

$$fO_2 = \left(\frac{f_{H2O}}{(K)(fH2)}\right)^2 \quad (2.11)$$

where if O_2 is consumed by either Mg or the buffer, then the resulting equilibrium fluids in the experimental charges are a mixture of H_2O and H_2 (neglecting C or N species). These fluid compositions at each given pressure, temperature, and fO_2 can be estimated by the above equations of state. It is expected that the molar fraction of H_2 in the oxidized runs is practically negligible so that the fluids can be reasonably regarded as H_2O only. In terms of the molar fraction of H_2O ($X(H_2O)$) and H_2 ($X(H_2)$) in the equilibrium fluid (Figure 2.11), the calculated data demonstrate clear systematic variations with fO_2 as does the water fugacity. Thus, the dependence of H incorporation in olivine and the $D_H^{ol/melt}$ values on fO_2 may be explained by the effects of diminishing water activity and systematic changes in fluid composition/water fugacity by ratio of fO_2/ fH_2. Despite not knowing the specific OH defect data for the olivine synthesized in these experiments (as it is not often feasible with these types of run products (Tollan et al., 2017)), a drastic change of the type of olivine point defects imposed by fO_2 as tied to the valence state (e.g., Fe^{3+}/Fe^{2+}, Ti^{4+}/Ti^{3+}) is not expected as the starting composition lacks these species. The analysis by Sokol et al. (2017) of the composition of reduced C–O–H fluids at pressures of 6.3 GPa and 1300–1400 °C revealed that the analysed proportions largely agree with modelling in terms of the concentrations of CH_4 increasing significantly with decreasing fO_2. However, analysis of these high-pressure fluids reveal numerous other organic species may exist within the aqueous phase with more than thirty hydrocarbon species

detected, including CH_4, C_2H_6, C_3H_8 and C_4H_{10} as well as other alkanes, alcohols, and carboxylic acids (Sokol et al., 2017). Thus, it appears that the proportion and abundance of C-O-H species in the fluid phase may not directly correspond to that of the melt phase as many of these species have never been detected in melts even under highly reducing conditions in melt only experiments (e.g., Hirschmann et al., 2012; Armstrong et al., 2015; Dalou et al. 2017; Grewal et al., 2019, 2020). Therefore, while thermodynamic fluid models may accurately predict fluid compositions, they cannot be directly applied to the volatile abundances within the melt or any coexisting mineral phase. (This result is unsurprising as water is considered the "universal solvent" and can dissolve more substances than any other liquid.) Another point of complication is that the Raman data shown in Figure 2.9 is qualitative and we cannot estimate the concentration of H_2 versus CH_4 versus H_2O in the melt. However, the key point remains that the dependency of H incorporation in olivine and the $D_H^{ol/melt}$ values on fO_2 is best explained by the fluid composition, water fugacity, and ratio of fO_2/ fH_2 as opposed to multivalency point defects.

2.5.2 Influence of pressure and temperature

To better contextualize variables for $D_H^{ol/melt}$ experiments as reported from literature, histograms for P, T, fH_2O, H in olivine, H in melt, and $D_H^{ol/melt}$ are shown in Figure 2.12.

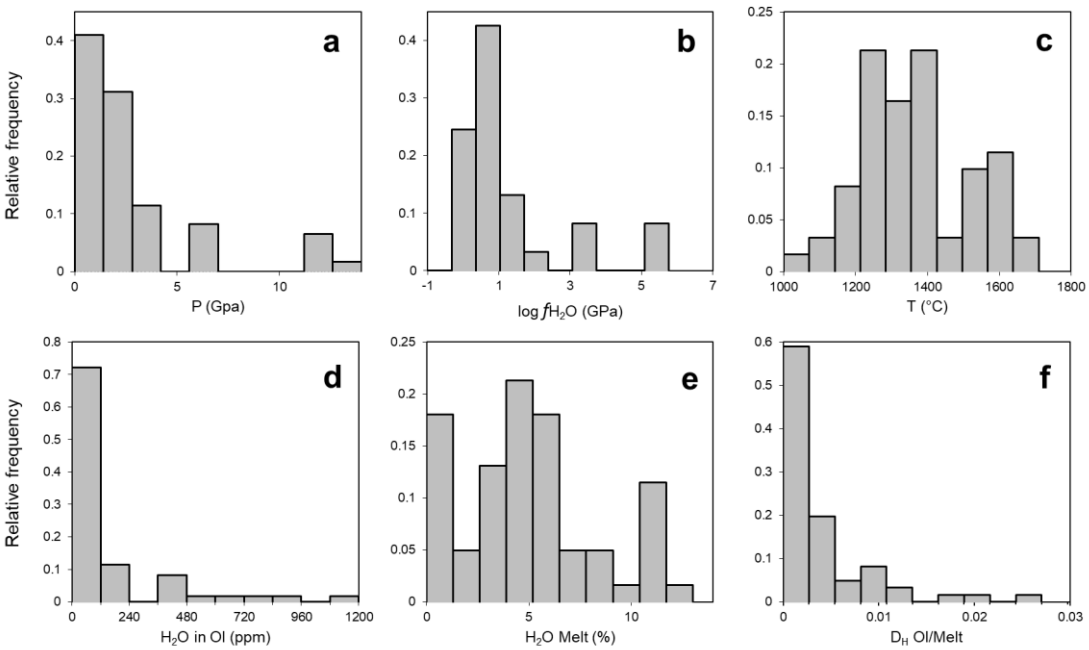

Figure 2.12. Relative frequency histograms showing the distributional features of experimental variables for partitioning experiments from Koga et al. 2003, Aubaud et al. 2004, Hauri et al 2006, Grant et al. 2007b, Tenner et al. 2008, O'Leary et al. 2012, Tenner et al. 2012, Novella et al. 2014, Rosenthal et al. 2015, Adam et al 2016, and this study. The majority of investigations have taken place at pressures below 5 GPa, with most experiments having a log fH_2O value below 3. Most experiments have been conducted between 1200-1400 °C. The majority of water contents in olivine have been recorded between 0-120 ppm, and the D_H values have ranged from 0 to 0.0027.

From 1-4 GPa, there is no strong pressure correlation (Figure 2.13a and 2.13c). In compiled literature data, a positive pressure dependence can be seen for $D_H^{ol/melt}$, however this relationship only becomes apparent at pressures exceeding 6 GPa as shown in Figure 2.13b and is further complicated by the results of this study as shown in Figure 2.13d.

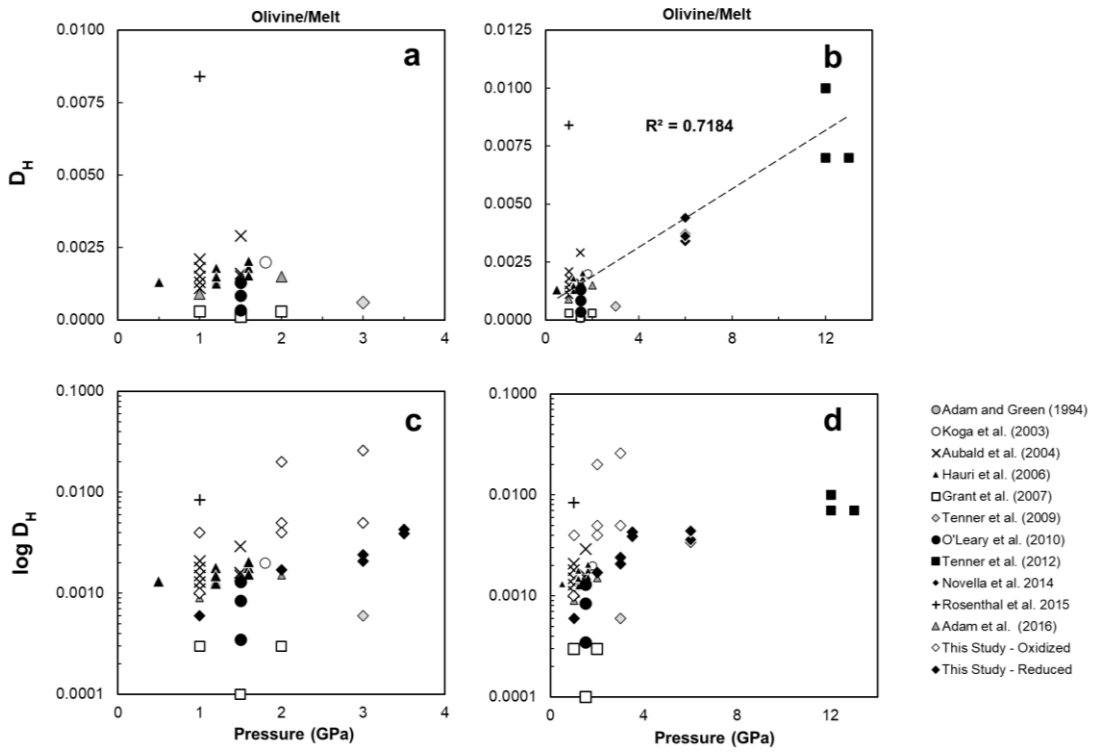

Figure 2.13. Comparison of D_H and pressure for olivine. a) D_H literature data from 1-4 GPa where no apparent pressure trend is obvious, b) literature data from 1-12 GPa where a positive trend with increasing pressure is apparent, despite the seemingly anomalous data point from Rosenthal et al. 2015, c) log(D_H) comparison of low-pressure data from this study, d) log(D_H), comparison of high-pressure data with this study.

The greater dispersion of data for low pressure experiments is explained by the greater number of experiments conducted in various chemical systems with various water activities and melt water contents. There is a lack of high-pressure data for D_H values; further studies will likely provide a more complex picture of this pressure regime. Given these observations, it is more instructive to consider trends within a given study/system as the influence of pressure or temperature alone is difficult to distinguish when combined with many other competing factors.

Within this study, the relationship between water content and pressure for olivine is illustrated in Figure 2.7 where the H contents of both the

oxidized and the reduced experiments increase with increasing pressure. For Fe-bearing olivine in melt-free experiments, OH solubility increases with pressure for experiments at 1.5-12 GPa and 1100 °C (Kohlstedt et al., 1996), and a similar effect has been observed by Mosenfelder et al. (2006), Yang (2015), and in annealing experiments on natural olivine (Yang, 2016). For olivine in hydrous melting experiments, H_2O concentrations increase with increasing pressure but decrease with increasing temperature due to a decrease in the H_2O activity in the melt (Smyth et al., 2006; Mosenfelder et al., 2006; Withers and Hirschmann, 2007; Bali et al., 2008). Similarly, in this study for the reduced experiments run at multiple temperatures for a given pressure, the water content of olivine can be seen to decrease with increasing temperature at a given pressure (Figure 2.7). This result is in agreement with previous high-pressure results from Smyth et al. (2006) and Withers et al. (2008). Withers and Hirschmann (2008) reported that at 8 GPa the H_2O storage capacity of olivine considerably decreased with increasing temperatures in the range of 1000–1600 °C. As noted by Hirschmann et al. (2005), at high-pressure the H_2O storage capacity of olivine decreases with increasing temperature due to the fluid dissolving increasing amounts of silicates and thus reducing the activity of H_2O. This dilution of the hydrous component in the melt phase corresponds to a decrease in the fugacity of H_2O in both the fluid and the coexisting olivine.

2.5.3 Influence of oxygen fugacity

Results from the few available studies on the relationship between fO_2 and the concentration of water in olivine appear to have significant inconsistencies and have led to much debate (Bai and Kohlstedt, 1992, 1993; Grant et al., 2007b; Withers and Hirschmann, 2008; Gaetani et al.,

2014; Yang, 2016; Potts et al., 2021). The experimental designs, including the P-T conditions, starting materials, experimental apparatus and assemblies, and analytical methods vary greatly between these studies, so discussions originating from these publications on the influence of fO_2 on H solubility in olivine require careful interpretation. It is possible that systematic inter-laboratory discrepancies exist between experimental and analytical setups. The experiments of Bai and Kohlstedt (1993) and Grant et al. (2007b) reveal a strong dependence of OH solubility on fO_2, while Gaetani et al. (2014) suggested a relatively modest effect. However, the experiments of Withers and Hirschmann (2008) at 8 GPa demonstrate that fO_2 has a very small to negligible effect on OH solubility, and Potts et al. (2020) similarly noted no clearly distinguishable effect of fO_2 on H partitioning, at least down to log fO_2 of approximately IW-2 and at pressures up to 2 GPa. The results from Yang (2016) show that the influence of fO_2 is modest at low pressures (1.5-3 GPa) and gradually becomes significant with increasing pressure (5-7 GPa). The observed dependence of OH solubility on fO_2 could be the result of redox sensitive point defect populations in olivine. Another possibility is that the enforced fO_2 changes the composition of the fluids in the experimental charges so that with decreasing fO_2 appreciable amounts of H_2 may exist with reduced water activity as suggested by fluid models.

At low pressures, fO_2 may influence the H_2O concentrations of olivine by controlling the point defect populations in the crystals, namely the availability of trivalent cations (abbreviated as triv) to participate in a coupled substitution mechanism. In Fe-bearing experiments, fO_2 is expected to influence OH dissolution in olivine by controlling the relative proportion of lattice Fe^{2+} and Fe^{3+} associated with OH incorporation by trivalent point defects (Berry et al., 2007, Tollan et al., 2017). Results from FTIR work suggests that the Fe^{3+} mechanism is pressure limited and therefore the

influence of oxygen fugacity is also limited at high-pressures (Berry et al., 2007; Withers and Hirschman, 2008; Yang, 2016). For experiments conducted at 2 GPa, Grant et al. (2007b) suggested the trivalent substitution involving OH- and Fe^{3+} as an explanation for the variable H_2O concentrations observed in their experiments, which is consistent with the IR peaks reported at 3,355 and 3,325 cm^{-1} in experiments buffered at NNO and Re–ReO_2. Withers and Hirschman (2008) did not observe these peaks in the FTIR spectra of experiments conducted at 8 GPa and buffered at NNO or HM. Grant et al. (2007b) conducted hydration experiments on San Carlos olivine at 2 GPa and 1100 °C with IW, NNO and Re–ReO_2 buffered conditions with talc + brucite as the water source. FTIR was used to determine the water contents and results showed that water solubility increases by a factor of 3 between IW and NNO. Gaetani et al. (2014) conducted hydration experiments on San Carlos olivine at 1–2 GPa and 1200 °C at IW, NNO and WM buffered conditions with distilled water as the water source. Water concentrations were determined by SIMS. Once the other variables are taken into account, there is no statistically significant dependence of water solubility on the Fe/Mg ratio of the olivine for forsterite contents between 88.17 and 91.41 mol% or on Ti contents in olivine (Gaetani et al., 2014). Results from Gaetani et al. (2014) suggest that that fO_2 is capable of increasing water solubility by approximately 34 % between IW and NNO.

The experiments of Withers and Hirschmann (2008) synthesized olivine in hydrous melts prepared from reagent grade oxides at 8 GPa and 1000-1600 °C at IW, NNO, and HM buffered conditions with brucite as the water source. Water contents were detected using SIMS. As with Gaetani et al. (2014), it becomes more difficult to resolve the influence of fO_2 on water solubility from that of other variables. Withers and Hirschmann (2008) found no significant effect of varying fO_2, but H_2O storage capacity increases under conditions of

low silica activity and decreases with increasing temperature. Increasing chemical complexity of a system produces a higher melt fraction at a given temperature and dilutes the hydrous component of that melt. These results further suggest that at pressures greater than 8 GPa the trivalent substitution becomes increasingly less significant.

2.5.4 Influence of olivine magnesium number

The Earth's mantle is estimated to consist of 8.1 wt% FeO (McDonough and Sun, 1995) and exhibits relatively minor variations in the composition of olivine in terms of iron content with a mean olivine Mg number of 89.5, where Mg number is defined as 100 times the molar Mg/(Mg+Fe) ratio. Estimates of FeO in the Martian mantle are substantially higher than Earth and range from 16.0–18.7 wt% (Morgan and Anders, 1979; Dreibus and Wänke, 1985; Bertka and Fei, 1997) with a Mg number of 75–77. Thus, the storage capacity of H in olivine for the Martian mantle is potentially very different from Earth. The influence of Mg number is also of relevance to the lunar magma ocean (LMO) considering the composition of the initial LMO may have been enriched in FeO relative to the bulk silicate Earth (Taylor, 1982; Jones and Delano, 1989; O'Neill, 1991; Snyder et al., 1992; Lognonné et al., 2003). The LMO crystallization model of Arai and Maruyama (2017) predicts that with increasing solidification the Mg number of olivine decreases from ~95 at 10% LMO solidification to ~75 at 85% solidification. Therefore, understanding the influence of Mg number on H solubility in olivine may be an important factor when modelling the evolution of water during LMO crystallization.

Previous high-pressure studies of olivine H storage capacity used a narrow range of olivine compositions with Mg number ranging from pure

forsterite to near mantle olivine compositions near 90. These studies found little to no effect of Mg number on H concentration (Kohlstedt et al., 1996; Mosenfelder et al., 2006; Smyth et al., 2006; Bali et al., 2008; Withers and Hirschmann, 2008). However, the experimental work of Zhao et al. (2004) at 300 MPa found an exponential increase in olivine H content with decreasing Mg number for compositions spanning pure forsterite to 83.1. In contrast, Withers et al. (2011) reported only a modest increase in H in olivine with decreasing Mg number. Specifically, the work of Withers et al. (2011) at 3 and 6 GPa found that olivine with a Mg number of 50 had a storage capacity approximately three times that of pure forsterite, which is significantly less than the factor of 50 predicted by the exponential relation reported by Zhao et al. (2004).

Using a gas-medium apparatus, Zhao et al. (2004) hydrothermally annealed single crystals of synthetic forsterite and San Carlos olivine in the presence of enstatite at 300 MPa with temperatures between 1000 °C and 1300 °C. The samples consisted of compositions between Fa0 and Fa16.9 and the fO_2 was buffered by NNO. FTIR was used to determine OH concentrations. Zhao et al. (2004) found that OH solubility increased with increasing temperature and with increasing iron content. For pure forsterite, the H concentrations appear anomalously low and Zhao et al. (2004) noted that data for forsterite are overestimated by extrapolation from the Fe-bearing olivine samples, while Hirschmann et al. (2011) suggested that kinetic impediments to hydrating gem-quality single crystals could be the reason for the inconsistency.

Withers et al. (2011) conducted olivine H_2O storage capacity experiments at 3 and 6 GPa with temperatures between 1200–1500 °C and a bulk Mg number systematically varied between 100 and 50. Assuming that all other conditions are similar, due to the compositional difference in Fe, the Martian mantle would have a storage capacity of water ~50% greater than the

Earth's upper mantle (Withers et al., 2011). While both studies suggest that Mg. no in these ranges have a significant influence on H incorporation in olivine, apart from the different pressure regimes studied, the reasons for these substantial discrepancies have not been completely identified.

2.5.5 Diffusivity of H_2 and H_2O

The diffusivity of H_2, H_2O, and O_2 can be considered in the context of the sample capsule and assembly as well as within the silicate melt and crystals. The use of a solid-state redox buffer requires H diffusion through the metal capsule to impose fO_2. This complicates maintaining a constant H concentration inherent to the starting material over the course of the experiment, particularly in undersaturated H_2 or H_2O experiments. The run duration is also expected to play a role as H_2 may be continually depleted via diffusion processes over the course of the run. As summarized by Sokol et al. (2017), "the high mobility of hydrogen and its ability to leave the samples loaded into capsules of noble metals were the major problems in experimental study of hydrocarbon stability at mantle pressures and temperatures." Previous reports suggest that H diffusion occurs, at least to some degree, when a highly permeable outer capsule is used, such as Pt, regardless of the 'intrinsic' fO_2 of the piston cylinder assembly or the nature of the assembly parts (e.g., talc/pyrophyllite, Pyrex glass, crushable alumina) or dryness of these parts (Jakobsson, 2012, 2014; Matjuschkin et al., 2015 and references therein). However, these studies focused on relatively oxidized conditions above the IW buffer where the relative proportion of H_2/H_2O would still be low.

A second consideration concerns the synthesized materials, which in this study consists of a silicate melt and olivine. The diffusivity of molecular H_2 is

different from that of H_2O, which may partially explain the differences between the oxidized and reduced experiments reported here. Under oxidized conditions, dissolved H_2O in silicate melts is frequently present as molecular H_2O_m or hydroxyl groups (–OH) (Stolper, 1982), while total H_2O content is denoted as H_2O_T. The role of H_2 diffusion relative to H_2O diffusion in silicate melts may play a significant role at very low fO_2. Under very reducing conditions where H_2/H_2O is >> 1, iron in silicate melts would be largely reduced to metallic Fe, complicating experiments. Therefore, extensive and reliable H_2 diffusion data are available only for pure silica glass and even then, as summarized by Zhang et al. (2010), "it is not clear whether the inferred molecular H_2 diffusivity data are correct." Given these experimental constraints, it appears no reliable data is available for both H_2 and H_2O_m diffusivity in any melt compositions. However, it is still instructive to consider data from separate studies. Using the diffusion model of Zhang et al. (2017) for H_2O_m in basaltic silicate melt,

$$lnD_{H_2O_m} = -4.539 - \frac{26{,}304}{T} \tag{2.12}$$

Figure 2.14 plots the diffusivity data from the above equation as well as literature estimates for diffusivity of H_2 versus H_2O_m and H_2O_T.

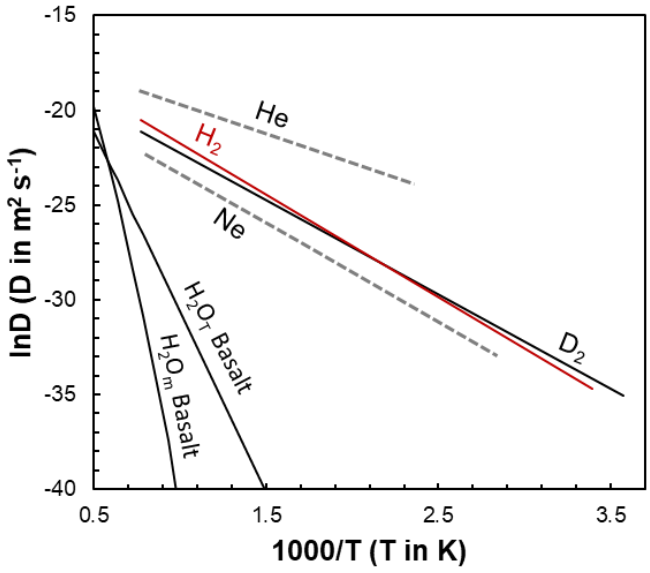

Figure 2.14. Diffusion trends plotted from data for H_2 and D_2 from literature and neutral noble gas molecules (Ne and He) in silica melt (Zhang et al., (2010) and references therein). Molecular H_2O_m diffusion in basaltic melt (Zhang et al., 2017) and basaltic melt containing 0.05% H_2O_T (Zhang et al., 2007) are also shown.

Diffusivity of H_2 falls between the diffusivities of neutral noble gas molecules of He and Ne and is substantially greater than both H_2O_m and H_2O_T for basaltic melts. Furthermore, the ratio of H_2/H_2O_m in a melt depends on fO_2 which sets the ratio of H_2/H_2O ratio in the gas or fluid phase, as well as the solubility of H_2 and H_2O in the melt. In order to relate this to diffusion, we can consider the gas phase reaction,

$$H_2O_{(g)} \rightleftharpoons H_{2(g)} + \tfrac{1}{2}\ O_{2(g)} \tag{2.13}$$

and the equilibrium constant can be written in terms of temperature dependence as follows (Robie and Hemingway, 1995),

$$K = exp\left(6.347 + \frac{29435}{T}\right) bar^{1/2} \tag{2.14}$$

where T is in K. Therefore, for any redox buffer, the ratio of fH_2/fH_2O increases with temperature. The ratio of fH_2/fH_2O as a function of temperature is shown in Figure 2.15a for multiple redox buffers.

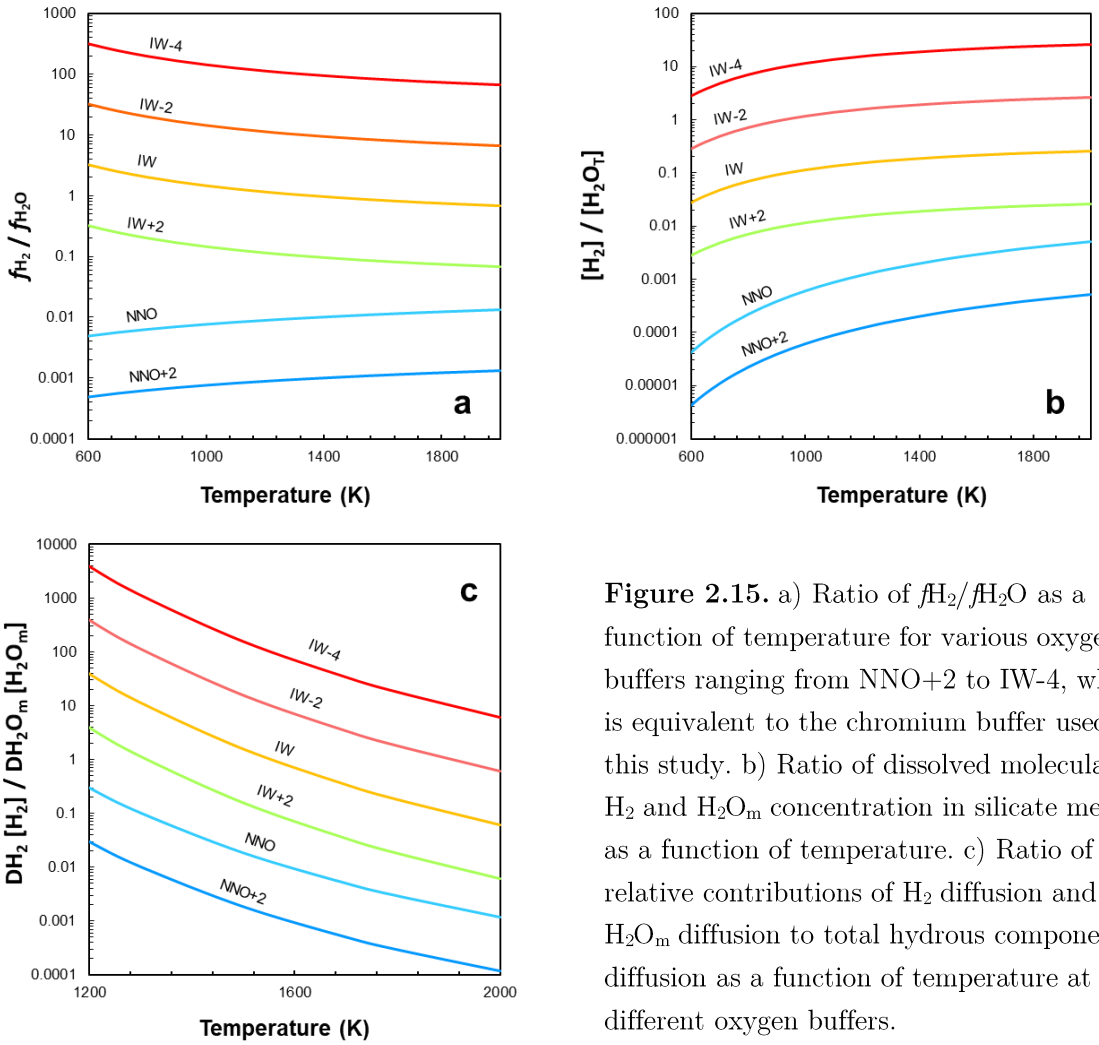

Figure 2.15. a) Ratio of fH_2/fH_2O as a function of temperature for various oxygen buffers ranging from NNO+2 to IW-4, which is equivalent to the chromium buffer used in this study. b) Ratio of dissolved molecular H_2 and H_2O_m concentration in silicate melt as a function of temperature. c) Ratio of the relative contributions of H_2 diffusion and H_2O_m diffusion to total hydrous component diffusion as a function of temperature at different oxygen buffers.

For relatively oxidizing conditions (NNO to NNO+2), the ratio of fH_2 /fH_2O is near to 10^{-4} to 0.1, while for IW it ranges from 1 to 7. At IW-2 the ratio is 7 to 68 for fH_2 /fH_2O in the gas phase in equilibrium with the melt. At the most reducing conditions considered, IW-4, which is equivalent to the chromium buffer used in this study, the ratio ranges from 67 to 681. To further consider the molar concentration ratio of dissolved H_2 to H_2O_m as influenced by fO_2, the solubility of H_2 and H_2O_m must be known. The molecular solubilities of H_2 (Shackelford et al., 1972) and H_2O_m (Zhang, 1999) in silicate melt are given by,

$$S_{H_2} = exp\left(-13.662 + \frac{1068}{T}\right) \quad (2.15)$$

$$S_{H_2O_m} = exp\left(-14.193 + \frac{3890}{T}\right) \quad (2.16)$$

where both solubilities have units of mol · m^{-3} · Pa^{-1}. For a given fO_2, the molar concentration ratio of $[H_2]/[H_2O_m]$ can be calculated from (fH_2 /fH_2O) · (SH_2 /SH_2O_m). Under relatively oxidized conditions, the ratio of $[H_2]/[H_2O_m]$ is low and the dominant hydrogen component is H_2O_m and OH. However, the ratio systematically increases with decreasing fO_2 so that the total hydrogen component is no longer the hydrous component. Extrapolating from the one-dimensional diffusion model for the total hydrogen component developed by Zhang et al. (1991, 2010), and assuming local chemical equilibrium, the contribution of the molecular H_2 diffusion can be assessed under uniform fO_2,

$$Ratio = \frac{D_{H_2}}{D_{H_2O_m}} \frac{\partial C_{H_2}}{\partial C_{H_2O_m}} = \frac{D_{H_2} C_{H_2}}{D_{H_2O_m} C_{H_2O_m}} \quad (2.17)$$

Thus, the contribution of H_2 to total H diffusion depends both on the concentration ratio and diffusivity ratio. If the ratio is less than 1, molecular H_2O diffusion dominates. If the ratio is greater than 1, then H_2 diffusion is dominate. If the ratio is equal to 1, then both species equally contribute. The molecular H_2 diffusivity in a melt can be calculated using Shang et al. (2009),

$$D_{H_2} = exp\left(-16.471 - \frac{5363}{T}\right) \quad (2.18)$$

where D is in $m^2 s^{-1}$ and T is in K. Combining the diffusivity of H_2 with the molecular H_2O_m diffusivity of Zhang et al. (2017), the ratio (DH_2

$[H_2])/(DH_2O_m[H_2O_m])$ as a function of temperature and oxygen fugacity buffer is shown in Figure 2.15c.

While these calculations involve substantial assumptions based on the availability of previous models and data, they nevertheless demonstrate some preliminary considerations for the diffusion of H under very reducing conditions. Under very reducing conditions at magmatic temperatures (≥ 1500 K), H_2 diffusion is primarily responsible for the total hydrogen flux of the system. Considering that for any given temperature, H_2 will diffuse faster than H_2O, this is an additional complication to conducting very reducing experiments using a piston cylinder device and may also have implications for transport properties during magma ocean outgassing and atmosphere formation. Previous work on silicate melts absent of crystals have also used, on average, substantially shorter run times compared to experiments synthesizing minerals in coexistence with a melt. For example, the experiments of Hirschman et al. (2012) were as short as 2 min.

2.6 Conclusion

Through SIMS and Raman analysis of experimental olivine and silicate glasses, the C-O-H contents and speciation over a range of P-T-fO_2-NBO/T conditions is shown to be strongly controlled by fO_2. Under highly reducing conditions applicable to magma oceans, molecular H_2 and CH_4 become the significant hydrous species in silicate melts as conceptualized in Figure 2.16.

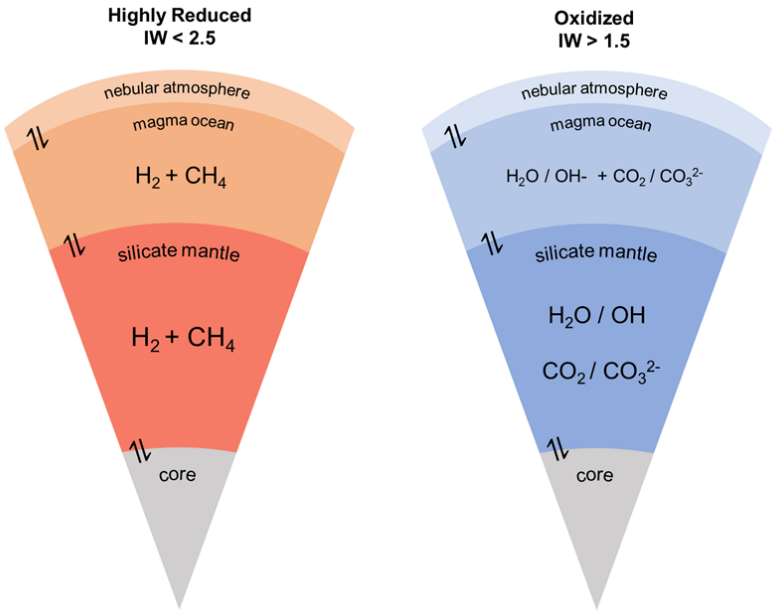

Figure 2.16. Schematic illustration (not to scale) of hydrogen storage (a) under highly reducing conditions applicable to the magma ocean stage and early evolution of terrestrial planets and (b) in a relatively oxidized mantle. Under extremely reducing conditions, such as those prevailing during the accretion and differentiation of terrestrial bodies, H_2 and perhaps CH_4 might been present in the silicate mantle. Given mantle redox stratification in modern Earth, it is also possible that H_2 exists in the deep reduced mantle, with OH groups dominating in the oxidized upper mantle.

These results are supported by thermodynamic fluid models which predict that H_2 and CH_4 should dominate under more reducing conditions in the early solar system. Systematically lower partition coefficients for $D_H^{ol/melt}$ were observed under highly reducing conditions, even in an iron-free system where the effect of the trivalent incorporation mechanism is expected to be limited. While it was not possible to detect H in olivine via Raman or IR spectra, it may be inferred from the melt data that at least some amount of H_2 and CH_4 may be incorporated in olivine. The considerably greater diffusion rates of H_2 versus H_2O are expected to add a further consideration to H_2 studies, and more work is needed on H_2 diffusion in melt systems. However, it is likely that a change in H speciation under highly reducing conditions increases H diffusivity.

2.7 Acknowledgements

Research was supported by the University of Edinburgh Research Training Support Grant (RTSG), Sigma Xi Grants in Aid of Research (GIAR), and an award of instrument time at the Edinburgh Ion Microprobe facility, IMF665/0518. We appreciate the assistance of Dr Cristina Talavera Rodriguez for SIMS analyses and Dr Chris Hayward for assistance with EPMA analyses. Deep Volatiles, a NERC funded research programme on Volatiles, Geodynamics & Solid Earth Controls on the Habitable Planet is also highly appreciated for their support and feedback throughout the project.

Chapter 3

Hydrogen and Carbon Concentrations in Synthetic Martian Basalts Under Nominally Hydrous Conditions: Implications for Water in the Martian Mantle

In collaboration with

Justin Filiberto (provided synthetic Martian samples)

Soft Landing

red planet blink, red planet wink,
I pulled you down when I was a child
on top of airports and t-v sets,

and now it seems you beat our dreams—
we came to you instead.

William Fox, *Mars, We Love You*, Pyramid (1973)

3.1 Abstract

Understanding the Martian H and C budget is critical since such dissolved volatiles reduce the Martian mantle solidus, may act as drivers for volcanism, and are vital for the development of habitable surface environments and atmospheres. Concentrations of H and C were measured by secondary ion mass spectrometry (SIMS) in experimentally produced replications of synthetic Martian systems with clinopyroxene, orthopyroxene, olivine, and coexisting silicate glass phases. Such nominally anhydrous minerals (NAMs) can contain significant amounts of H and, therefore, serve as important reservoirs for H within the silicate Earth and Mars. The determined values were used to calculate the mineral/melt partition coefficients (D values) for H and C. Experiments were previously conducted in nominally anhydrous conditions, and the H partitioning values obtained here are significantly greater than those obtained in previous studies. Comparison with literature data indicates that melt H_2O content acts as an important additional control on H mineral/melt partitioning for clinopyroxene and orthopyroxene. Experimental $D_H^{cpx/melt}$ values also differ from previous models for $D_H^{cpx/melt}$ that are based solely on clinopyroxene compositions and do not account for the activity of H_2O in the melt, especially at low activities. Combined with previous literature data on $D_H^{cpx/melt}$, a new empirically calibrated model for $D_H^{cpx/melt}$ is developed based solely on phase composition. This model is applied to Martian meteorites, such as the nakhlites, which may contain low water contents. The nakhlite suite are augite-rich and minimally shocked meteorites believed to have formed from lava flows from a single volcano, a shallow intrusion of basaltic magma, or a sill complex on Mars. Using the newly derived $D_H^{cpx/melt}$ model, the magmatic water contents of the nakhla parental melt was estimated, and subsequently used to calculate the Martian mantle source H_2O content by various equilibrium and fractional (accumulated) melting models. Both the parental

magmatic and the mantle source H_2O contents can be compared to literature estimates for the Martian mantle derived from other methods. Results suggest the H_2O contents of the source regions for the nakhlites is significantly lower than most of Earth's upper mantle, but comparable to the primitive lunar mantle and the Martian depleted and enriched sources.

Keywords: Mars, Mantle, Water, Nakhlites, Nakhla, NAMs, Clinopyroxene, Orthopyroxene

3.2 Introduction

The objective of studying hydrogen and other volatiles in experimental systems applicable to Mars is to provide estimates for the abundance of H_2O in Martian magmas, which in turn can be used to estimate the distribution of water in the Martian mantle. During the geological evolution of Mars, even trace levels of water within the planet's mantle affects both the surface environment and the interior dynamics due to the influence of H on melting, deformation, electrical and seismic properties, volcanism, and thermal properties of rocks and melts (e.g., Médard and Grove, 2007; Morschhauser et al., 2011; Pommier et al., 2012; Kiefer and Li, 2016). Constraining the amount of water and C-O-H volatiles originally in the Martian interior has further implications for the distribution of water in the Solar System, placing constraints on planetary formation models, magma oceans, and determining the origin of water in terrestrial planets (Albarède, 2009; Peslier, 2010; Alexander, 2017; Peslier et al., 2017, 2019). Furthermore, the abundance of C-O-H volatiles in the Martian interior has astrobiological consequences in terms of the generation and composition of the early Martian atmosphere, the formation of ice and liquid surface water, and the habitability and potential for

life on Mars (Elkins-Tanton, 2008; Carr and Head 2010; Cockell et al. 2012, 2016; Cottin et al., 2015). Thus, the capacity of nominally anhydrous mantle minerals, including clinopyroxene, orthopyroxene, olivine, to store C-O-H volatiles (e.g., H_2O, CH_4, CO_3^{2-}, and H_2) within the mantle has significant implications for the Martian deep volatile cycle.

The composition of the Martian mantle is expected to be inherited from magma ocean processes (e.g., Debaille et al., 2007) and the initial budget and speciation of major C-O-H volatiles in silicate reservoirs may have been similarly set during the formation and early evolution of the Earth, Mars, and other terrestrial planets. Water-poor protoplanetary bodies may be a result of terrestrial protoplanets in the inner Solar System accreting under nominally anhydrous conditions (Morbidelli et al., 2012; Alexander, 2017; Alexander et al., 2018). Several studies propose that enstatite chondrites, which may be considered representative of the inner Solar System volatile reservoir, accreted little to no water (e.g., Sarafian et al., 2017; Alexander, 2017, O'Brien et al., 2018). Consequently, if water was primarily delivered in the late stages of terrestrial accretion, magma oceans may have been nominally anhydrous to completely anhydrous (Albarède, 2009; Morbidelli et al., 2012; Dauphas and Morbidelli, 2014). Previous models of low-volatile magma oceans with water contents of 0.05 wt.% H_2O resulted in atmospheres greater than 100 bars for all magma oceans investigated on both Earth and Mars (Elkins-Tanton, 2008). Therefore, it is necessary for experimental studies to consider systems with magmatic water contents $<<$1wt%.

Key unknowns related to the evolution of the Martian crust-mantle system are the water content of the Martian magma ocean, the initial bulk mantle water content, and the water content of SNC—a group of petrologically similar achondrites with names based on the locations where the first examples of these meteorites were found, Shergotty (India), Nakhla

(Egypt), and Chassigny (France)— parental melts. As the only physically accessible samples of Mars at the present, the SNC meteorites provide an important method for investigating the Martian mantle water budget. These meteorites collectively known as SNC meteorites are categorized into three main groups: shergottites (basalts), nakhlites (clinopyroxene cumulates), and chassignites (dunites). Estimates of the water contents in the SNC parental melts range from 0.1 to 2.83 wt.% (Karlsson et al., 1992; Leshin et al., 1996; Dann et al., 2001; Boctor et al., 2003; McCubbin et al., 2010, 2013; Usui et al., 2012; Weis et al., 2017). These estimates overlap and are generally lower than magmatic water contents on Earth, which range from 0.1 to >6.0 wt.% (e.g., Danyushevsky, 2001; Wallace, 2005; Plank et al., 2013). The water content of the depleted shergottite mantle, the mafic to ultramafic suite of Martian meteorites, has been estimated to be 15-47 ppm, which is consistent with a dry mantle hypothesis (Usui et al., 2012). However, as on Earth, the Martian mantle is thought to be heterogenous. For instance, McCubbin et al. (2016) has shown that the enriched and depleted shergottite sources possess different H_2O abundances, with the enriched source containing 36-72 ppm H_2O and the depleted source containing 14-23 ppm H_2O.

Similar to H content, the C content of the Martian interior also lacks clear constraints. Current assessments differ by more than three orders of magnitude (e.g., Dasgupta et al., 2014; Filiberto et al., 2016). Constraining the abundance of C in the Martian mantle is further complicated by the expectation that magma oceans are graphite undersaturated with ultramafic silicate melts (Grewal et al., 2020), despite previous evidence that certain parts of the Martian mantle may be graphite saturated (e.g., Hirschmann and Withers, 2008; Righter et al., 2008). Furthermore, Martian meteorites contain a variety of reduced carbon in the form of graphite, polycyclic aromatic hydrocarbons (PAHs), macromolecular carbon, and aromatic organics

produced by several different abiotic synthesis mechanisms (Steele et al., 2016). Assuming a single stage core-mantle equilibration model, experiments on silicate-alloy systems suggest that carbon dissolution in reduced magma oceans was less than 500 ppm, and following core formation the magma ocean may have been entirely C-free, with the core containing ~1 wt% (Chi et al., 2014; Dasgupta et al., 2014). It is important to note that the vast majority of experimental data on C-O-H speciation in silicate glasses have been conducted under graphite saturated conditions, and further work is necessary to extend models to undersaturated conditions. It is similarly essential to determine whether previous experimental partitioning models (e.g., O'Leary et al. 2012) and values determined from abundantly hydrous systems can be extrapolated to anhydrous and nominally anhydrous magma oceans and parental magmas. The work of O'Leary et al. (2010) is based on a terrestrial system as well, and most data on C partitioning is derived from terrestrial systems. If H_2O is incompatible in mantle minerals under these conditions or has a substantially lower partition value due to a diminishingly low water activity, then the residual silicate melt would become progressively enriched in H_2O with increasing solidification.

The effect of fO_2 on C-O-H volatiles is relevant to Mars and the Moon as well as planetary accretion and differentiation processes. The Martian shallow mantle probably exhibits a range in fO_2, but is generally reduced compared to the Earth, with fO_2 values ranging from IW−1 to IW+1, while lunar basalts equilibrate to IW−1 to IW−2 (Wadhwa, 2001; Karner et al., 2006). Early in Earth's history, at least in regional zones, the Earth's shallow mantle experienced more reducing conditions (Yang et al., 2014). In the modern period, however, it is relatively oxidizing (Frost and McCammon, 2008) with fO_2 values falling between the QFM and NNO buffers. Stark differences in the fO_2 and differentiation conditions of Earth and Mars would

influence volatile budgets, the compositions of proto-atmospheres, and the resulting volatile cycles of these planets (Hirschmann et al., 2012; Dalou et al., 2017; Grewal et al., 2019). Even at modestly reduced conditions, OH and H_2O exist as hydrogen-bearing species within the melt, albeit in decreasing quantities, while molecular H_2 becomes increasingly prevalent at highly reduced conditions (Schmidt, 1998; Hirschmann et al., 2012). At extremely low fO_2 in H-rich systems, the solubility of CO_3^{2-} diminishes in proportion to fO_2 and CO_3^{2-} is replaced by more reduced entities (e.g., Hirschmann and Withers, 2008; Stanley et al., 2014). The fO_2 values for the experiments analysed in this study are generally relatively reduced and can be assessed in terms of previous C-O-H solubility models.

In this study, the H and C contents of silicate glasses were determined using SIMS analysis for experiments presented in Filiberto et al. (2008, 2010a, 2010b). Clinopyroxene, orthopyroxene, and olivine were also analysed for H and C to determine partitioning values between minerals and the coexisting silicate melts. Secondary ion mass spectrometry (SIMS) analyses were conducted at the Ion Micro-Probe Facility at The University of Edinburgh. The results make a unique contribution to the understanding of volatile behaviour in mineral/melt partitioning as these experiments represent only nominally anhydrous quantities of water, which is not represented in scientific literature but may be critical to planetary systems. The results of this study are used to assess whether C and H contents and partition values predicted by models derived from substantially more water-rich experiments also hold true for nominally anhydrous magmas as perhaps found in magma oceans and SNC parental melts.

3.3 Methods

3.3.1 Sample description

Three synthetic Martian basalts were analysed from Filiberto et al. (2008, 2010a, 2010b). The Fastball experiments consist of bulk basaltic compositions representative of the Home Plate plateau of Mars (Gusev Crater) and were conducted at near-liquidus conditions (Filiberto et al. 2010b). These samples were originally synthesized to test if the Home Plate plateau represented a primitive mantle derived melt and estimate constraints on the temperature of the ancient Martian mantle and on the lithosphere-asthenosphere boundary (Filiberto et al. 2010b). The samples designated NWA represent experiments based on the Northwest Africa (NWA) 1068 meteorite bulk composition, one of the few olivine-phyric shergottites not depleted in light rare earth elements (Filiberto et al., 2010a and references therein). The results of the original NWA study reported that the calculated parental magma was an evolved basaltic composition too ferroan to be a primitive melt directly produced from the mantle, and instead it may have ponded and crystallized near the base of the crust (Filiberto et al. 2010a). The Humphrey composition is based on one of the analysed Adirondack-class basalt compositions, the Humphrey rock, one of the least altered of the Adirondack class basalts (McSween et al., 2006; Filiberto et al., 2008). Results from Filiberto et al. (2008) suggest that the Humphrey composition may not be a direct mantle melt, but an evolved liquid composition produced by low-pressure fractionation. Regardless, the analysis of such experiments is useful to investigate the fundamental behaviour of H partitioning at relatively anhydrous conditions. SEM images of representative run products are shown in Figure 3.1 and Figure 3.2. Depending on the experiment, run products consisted of high fractions of quenched glass coexisting with crystals of olivine, orthopyroxene, and clinopyroxene.

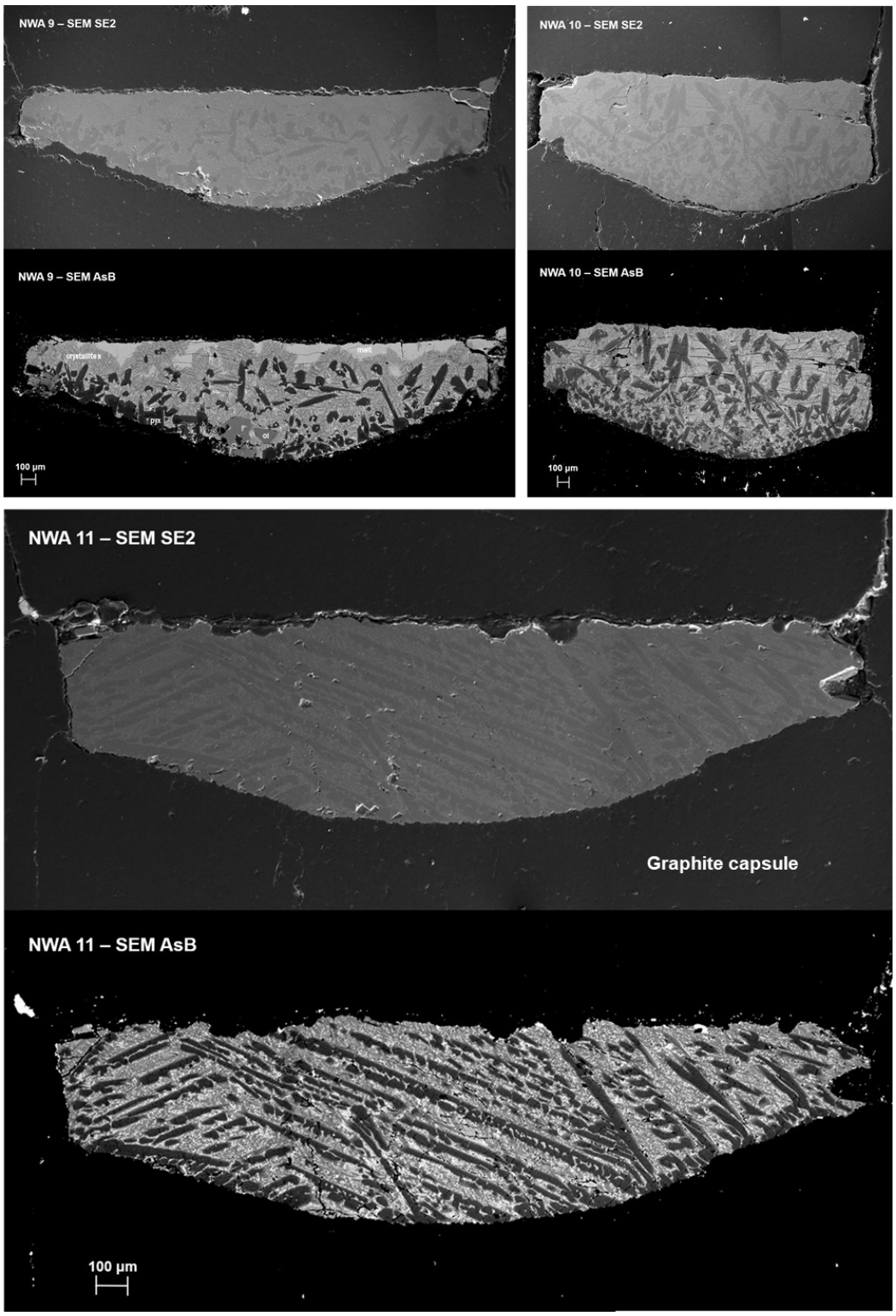

Figure 3.1. Backscattered electron images (SEM) of NWA samples 9-11 from secondary electron detector (*SE2*) and angle selective backscatter detector (*AsB*). As denoted for NWA-9, dark gray crystals are pyroxene and lighter gray crystals are olivine. Crystallites are abundant for the NWA samples.

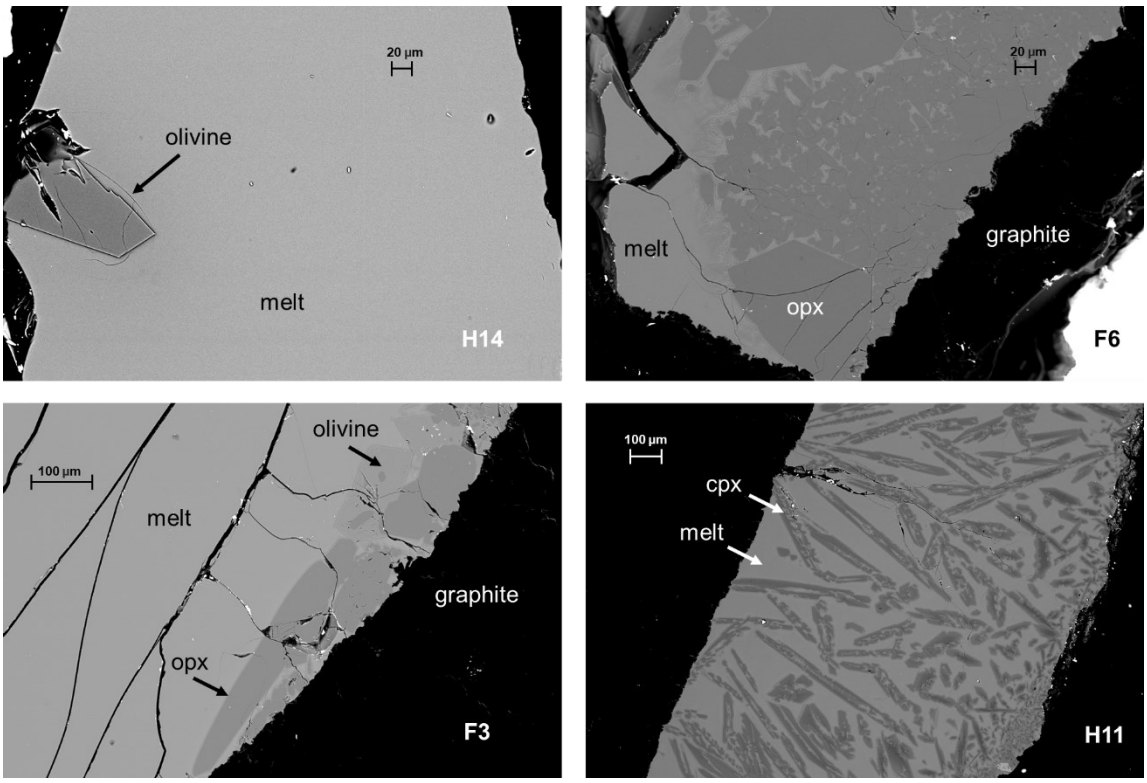

Figure 3.2. Backscattered electron images (SEM) of selected Humphrey and Fastball samples. Clear melt pockets are abundant for the Fastball and Humphrey run products.

Phase and melt relations for each series of experiments are shown in Figure 3.3. Only quench and crystallite-free melt pockets were analysed here, and care was taken to avoid grain boundaries, fractures, and uneven sample surfaces. A summary of the original experimental conditions, resultant phase assemblages, and other intensive variables is given in Table 3.1.

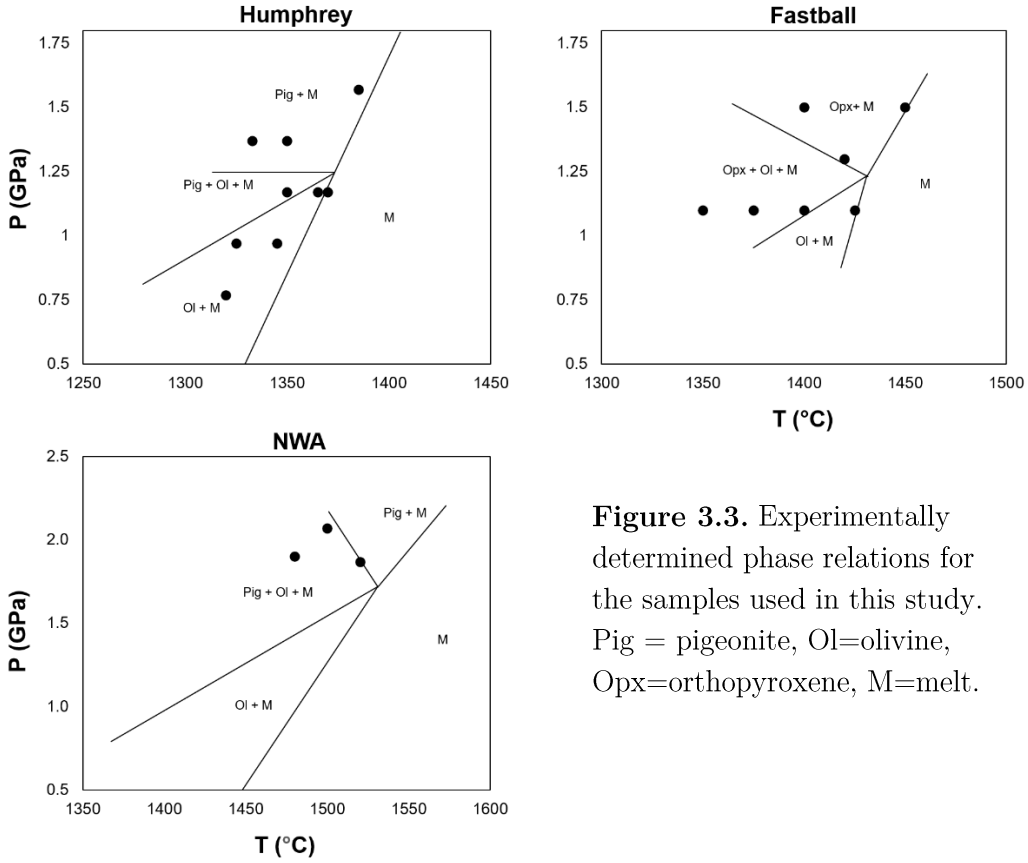

Figure 3.3. Experimentally determined phase relations for the samples used in this study. Pig = pigeonite, Ol=olivine, Opx=orthopyroxene, M=melt.

Table 3.1. Experimental conditions and intensive variables

Sample	P (GPa)	T (°C)	Phase assemblage	fO_2 (Bars)	ΔIW (Bars)	fH_2O (GPa)	H_2O (%) by iron reduction
F3	1.1	1375	gl(85)+opx(13)+ol(2)	-8.7	0.93	2.57	0.059
F4	1.1	1350	gl(81)+opx(17)+ol(2)	-8.9	0.99	2.56	0.056
F5	1.1	1400	gl(89)+opx(10)+ol(1)	-8.5	0.88	2.57	0.063
F6	1.5	1400	gl(81)+opx(19)	-8.4	0.81	5.14	0.060
F7	1.1	1425	gl(97)+ol(3)	-8.3	0.82	2.57	0.066
F8	1.5	1450	gl(97)+opx(3)	-8.1	0.71	5.11	0.066
F12	1.3	1420	gl(86)+opx(4)	-8.3	0.81	3.68	0.064
H3	0.97	1325	gl(89)+ol(11)	-9.1	1.06	1.99	0.052
H5	0.97	1345	gl(91)+ol(9)	-8.9	1.01	1.99	0.055
H6	1.17	1350	gl(89)+ol(7)+pig(4)	-8.9	0.98	2.92	0.055
H11	1.37	1333	gl(62)+pig(38)	-9.0	0.98	4.16	0.051
H12	1.17	1365	gl(97)+ol(3)	-8.7	0.94	2.92	0.056
H14	1.17	1370	gl(97)+ol(3)	-8.7	0.93	2.92	0.057
H19	1.57	1385	gl(86)+pig(14)	-8.5	0.83	5.76	0.056
H22	1.37	1350	gl(95)+pig(5)	-8.8	0.94	4.15	0.053
H27	0.77	1320	gl(96)+ol(4)	-9.2	1.07	1.30	0.052
N11	1.9	1480	gl(70)+pyx(28)+ol(2)	-7.8	0.57	9.33	0.000
N10	2.07	1500	gl(67)+pyx(23)+ol(tr)	-7.7	0.49	11.79	0.000
N9	1.87	1520	gl(78)+pyx(20)+ol(2)	-7.5	0.51	8.83	0.000

F represents Fastball, H represents Humphrey, and N represents NWA composition samples.
tr=trace

3.3.2 Oxygen fugacity

The experiments were conducted using graphite capsules, which, at elevated pressures and temperatures, constrains the fO_2 to ~1.5 to 3.5 log units below the QFM oxygen buffer (Holloway et al., 1992). While the 2 kbar experiments from Filiberto et al. (2008) were not analysed in this study, the observation of metallic iron in the 2 kbar experiments suggests the successful control of fO_2 by this method. The fO_2 of the higher-pressure experiments likely falls between the IW buffer and the quartz-iron-fayalite buffer (QIF), which is at or below the fO_2 suggested by Holloway et al. (1992). If we consider the system as hydrous, then depending on the temperature, the graphite capsule may buffer fO_2 at C-CO_2-CO to approximately IW+1 (Table 3.1).

In addition to the experimental conditions, the sample preparation must also be considered to assess sources of volatile contamination. In experiments conducted in high-pressure, high-temperature piston cylinder devices, some amount of water contamination of samples is inevitable, rendering even experiments conducted without any intentionally added H_2O only nominally anhydrous (e.g., Wasylenki et al., 2003; Médard et al., 2008; Armstrong et al., 2015). Water contents in melts may even contain approximately 0.5% H_2O and the anhydrous experiments of Wasylenki et al. (2003) measured 1.2% H_2O in one of their experiments, which is evidence of the unintended entry of H_2O into nominally anhydrous experiments. However, starting materials subjected to rigorous drying treatments can approach < 100 ppm H_2O. Despite the appropriate storage of samples, it is not uncommon for H_2O contamination to occur during capsule loading due to absorption from air. Additionally, if the sample assembly is not dehydrated beforehand, it is possible that there is water exchange with the environment during the experiment. In many previous studies conducted under 'anhydrous' conditions, the water content of the melt was not measured, but rather assumed to be zero. This unintended addition of H_2O into 'dry' experiments likely contributes some uncertainty to 'anhydrous' models as even small amounts of dissolved water can have large effects on liquidus temperatures and phases (e.g., Médard and Grove, 2007).

For the Humphrey experiments, the starting material powder was melted at 1400 °C at 1 atm to produce a homogeneous anhydrous glass in air, which was then stored in a desiccator to help ensure the material remained anhydrous (Filiberto et al., 2008). For the NWA experiments, the Fe_2O_3 content of the starting materials was previously established by placing the starting mixture in a CO/CO_2 gas mixing furnace at 1000 °C with $\log fO_2 = 4.7 \pm 0.7$ for 7 days. To ensure the NWA experiments remained volatile free, the starting mixture was loaded into a graphite capsule and the capsule was

stored at 150 °C for at least 12 h prior to each experiment. Because the starting material melts for Humphrey and Fastball compositions were produced in air and then transferred to more reducing experimental conditions as imposed by the graphite capsules, it is expected that some of the Fe_2O_3 will be reduced to FeO. The reduction of Fe^{3+} to Fe^{2+} by reaction with graphite may also increase H_2O contamination. If we assume that all iron exists as Fe_2O_3 prior to the experiment, the amount of water added to the melt by the reduction of iron during the run can be calculated using equations from Righter et al. (2013) since the FeO_T >15 wt.% to calculate Fe speciation as a function of fO_2 at P-T. The results of the calculation suggest that only very minor amounts of contamination can be expected from iron reduction (Table 3.1).

3.3.3 Analyses of H and C

The concentrations of H and C in minerals and glasses were measured by secondary ion mass spectrometry (SIMS) using a Cameca 4f instrument at the University of Edinburgh NERC Ion Microprobe Facility. Instrument settings were used as detailed in Chapter 2. The analytical methods used were similar to previous methods used for the determination of trace volatile concentrations in mantle minerals (e.g., Koga et al., 2003; Hauri et al., 2006; Adam et al., 2016; Potts et al., 2021). The number of analyses obtained for the mineral and melt phases in each experiment ranged from 1 to 9, depending upon the number of suitable spots. Data processing included background correction, filtering data for anomalies and contamination, the removal of bad data cycles, and the application of the calibration curve to determine analyte concentrations. Prior to analysing samples, calibration curves were constructed by the multiplication of H/Si or C/Si ratios by calibration factors in analytical

standards that had been independently analysed (Figure 3.4). The standard ALV-519, a piece of basaltic glass containing 1700 ± 86 ppm water (Aubaud et al., 2004; Aubaud et al., 2007), was used as a secondary standard to further account for differences in instrumental conditions. Previous studies have demonstrated that SIMS calibration curves display similar matrix effects for olivine and orthopyroxene identical within analytical uncertainty (Koga et al. 2003, Kovács et al. 2010, Withers et al. 2011, Warren and Hauri 2014). Despite availability of the standard ALV-519, the calibration curves for orthopyroxene were routinely used to determine the H contents of olivine as the H concentrations of the samples were more closely bounded by the standard curve.

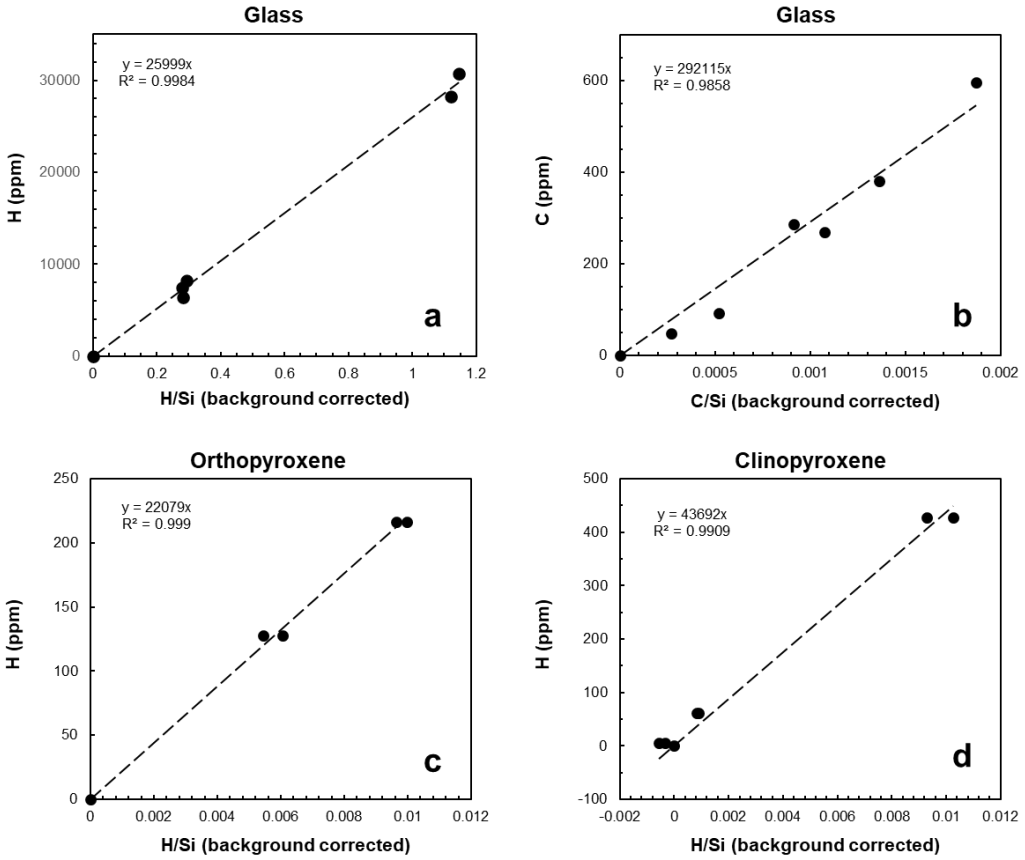

Figure 3.4. Background corrected calibration curves for SIMS analysis. The standard OL-116610 was used to measure the background for both (c) and (d) and is shown on the curve. Instrumental errors are within the markers.

3.4 Results

3.4.1 Clinopyroxene

Measured H_2O concentrations in clinopyroxenes vary from 53 to 146 ppm in the Humphrey samples with calculated D values for clinopyroxene and melt ($D_H^{cpx/melt}$) ranging from 0.070 to 0.130 (Table 3.2).

Table 3.2. SIMS results for H in orthopyroxene, clinopyroxene, and olivine

	Pyroxene H_2O					Olivine H_2O			
Sample	**n**	**ppm**	**±**	**D_H pyx/melt**	**±**	**n**	**ppm**	**±**	**D_H ol/melt**
F3	4	34	6	0.040	0.008	-	-	-	-
F4	-	-	-	-	-	-	-	-	-
F5	4	37	16	0.044	0.019	2	26	3	0.031
F6	3	52	11	0.056	0.016	-	-	-	-
F7	-	-	-	-	-	1	28	3	0.041
F8	7	21	8	0.025	0.010	-	-	-	-
F12	5	22	3	0.025	0.004	-	-	-	-
H3	-	-	-	-	-	-	-	-	-
H5	-	-	-	-	-	1	44	0.5	0.058
H6	5	53	20	0.070	0.026	4	29	15	0.038
H11	2	146	12	0.113	0.010	-	-	-	-
H12	-	-	-	-	-	2	30	5	0.040
H14	-	-	-	-	-	1	<4*	-	0.005
H19	3	91	18	0.130	0.027	-	-	-	-
H22	4	79	22	0.098	0.028	-	-	-	-
H27	-	-	-	-	-	4	28	9	0.031
N11	4	346	92	-	-	-	-	-	-
N10	2	63	6	-	-	-	-	-	-
N9	2	123	16	-	-	-	-	-	-

Note NWA samples were not used for D_H calculations due to melt texture concerns.
Errors are standard deviations on mean values for each sample based on repeat analyses.
*Estimated according to LoD.

Figure 3.5a shows the correlations of pyroxene (both clinopyroxene and orthopyroxene) H_2O contents with mineral Al_2O_3 content. The pyroxene H_2O content also correlates with the H partition coefficient (Figure 3.5b), and the H partition coefficient correlates with the Al_2O_3 content (Figure 3.5c). The H partition coefficient versus $^{IV}Al^{3+}$ content is shown in Figure 3.5d. Trendlines serve as a visual guide. Literature data for $D_H^{cpx/melt}$ were compiled from Adam and Green (1994), Dobson et al. (1995), Green et al. (2000), Hauri et al. (2006), Koga et al. (2003); Aubaud et al. (2004, 2008), Tenner et al. (2009), O'Leary et al. (2010), Kovács et al. (2012), Novella et al. (2014), and Adam et al. (2016). Following the approach for Adam et al. (2016), $D_H^{cpx/melt}$ values were estimated from the data of Kovács et al. (2012) by assuming melt H_2O solubilities of ~10 wt% per GPa. Previous studies have shown that H

partitioning between pyroxenes and melt correlates strongly with the Al_2O_3 content of pyroxenes for both orthopyroxenes and clinopyroxenes (Aubaud et al., 2004, 2008; Hauri et al., 2006; Tenner et al., 2009; O'Leary et al. 2010). More specifically, previous studies have noted $D_H^{cpx/melt}$ tends to increase with increasing $^{IV}Al^{3+}$ (e.g., Hauri et al., 2006; Tenner et al., 2009; O'Leary et al. 2010).

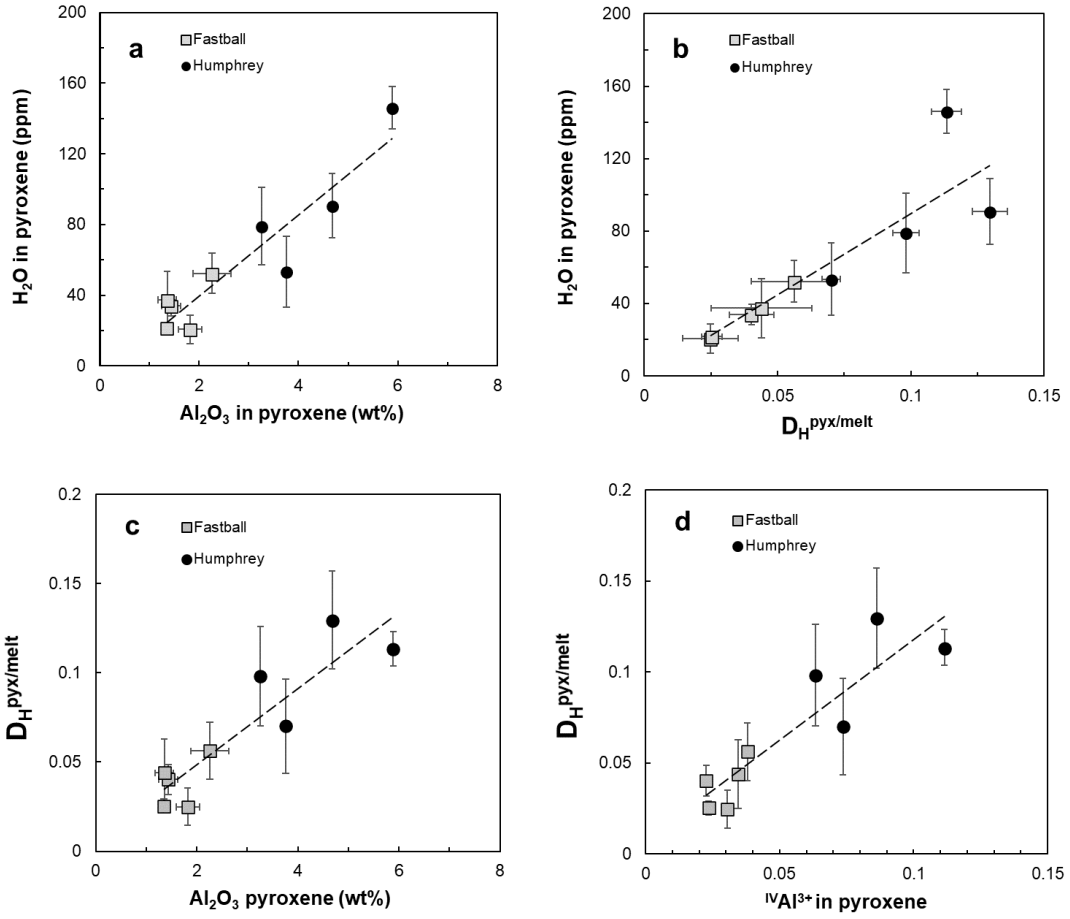

Figure 3.5. Correlations of a) pyroxene H_2O contents with mineral Al_2O_3 content, b) pyroxene H_2O contents with the H partition coefficient, c) the H partition coefficient with Al_2O_3 content, and d) the H partition coefficient with $^{IV}Al^{3+}$ content. The linear fit trendlines serve as a visual guide.

Only a small proportion of H^+ incorporated in pyroxene appears to involve the creation of metal vacancies and coupled hydroxyl defects, while the majority of H^+ is incorporated through a coupled substitution involving $^{IV}Al^{3+}$ that creates isolated hydroxyl defects (Hauri et al., 2006; O'Leary et al., 2010). When the pigeonite data from this study are plotted with the literature data (Figure 3.6a), the correlation between $D_H^{cpx/melt}$ and melt H_2O concentrations produces a distinctly curved trend. Figure 3.6b shows the remarkable divergence of the results of this study from literature data for the correlation of $D_H^{cpx/melt}$ with $^{IV}Al^{3+}$. Based on literature data, Figure 3.6c shows that any simple relationship between H_2O melt content and Al^{IV} in clinopyroxene is ambiguous.

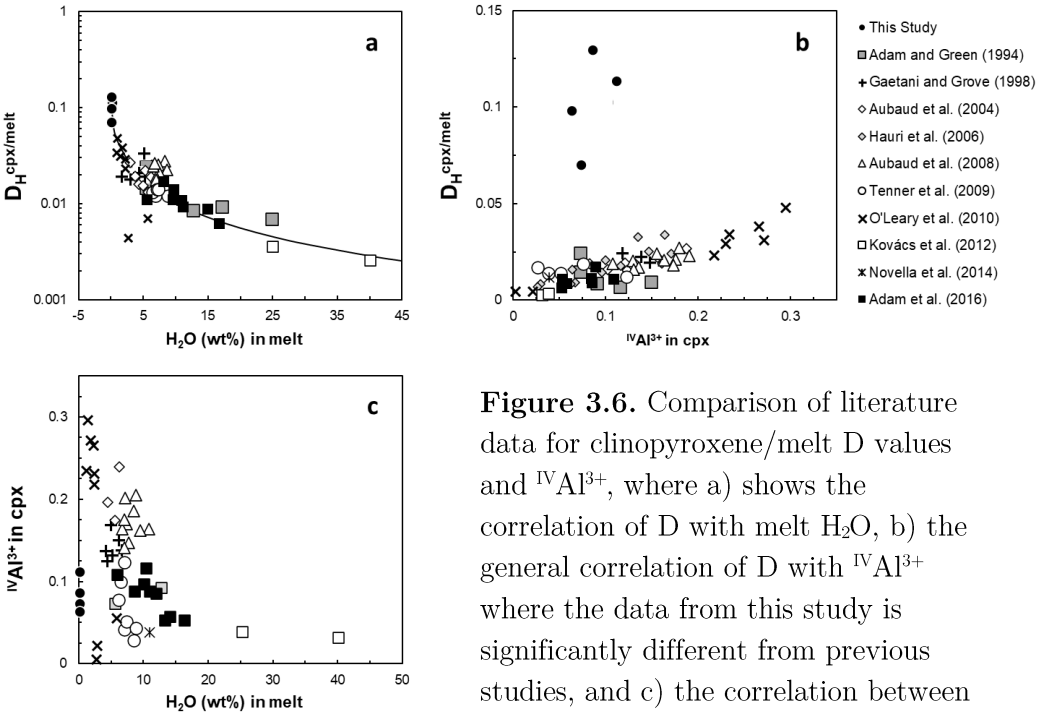

Figure 3.6. Comparison of literature data for clinopyroxene/melt D values and $^{IV}Al^{3+}$, where a) shows the correlation of D with melt H_2O, b) the general correlation of D with $^{IV}Al^{3+}$ where the data from this study is significantly different from previous studies, and c) the correlation between $^{IV}Al^{3+}$ and melt H_2O.

For Figures 3.6-7, clinopyroxene compositions were recalculated to on a 6-oxygen basis and Fe_2O_3, if not experimentally determined, was calculated according to charge balance. The overall correlation of the H partition coefficients with Al_2O_3 from this study can be seen in Figure 3.5. However, the partition coefficients reported here are significantly greater than in any previous study (Figure 3.6). This reflects the nominally anhydrous nature of these experiments with no H_2O being intentionally added to the experimental charge or starting mixture, which results in the relatively low water contents of the melt. For example, the water contents of the melts from O'Leary et al. (2010) melts ranged from 2.64 to 5.78 wt%. Furthermore, it should be noted that a decrease in tetrahedral Al with increasing pressure above 1.5 GPa is consistent with decreasing H in orthopyroxene at pressures of 2-3.5 GPa (Mierdel et al., 2007), and similar behaviour would be expected in clinopyroxenes.

3.4.2 Orthopyroxene

The concentrations of H_2O and $D_H^{pyx/melt}$ values for orthopyroxene are only slightly greater than the clinopyroxenes (Table 3.2) and similarly correlate with Al_2O_3 content of the pyroxene (Figure 3.5). The $D_H^{opx/melt}$ data from this study falls significantly off the positive correlation trend observed with ^{IV}Al in pyroxenes (Figure 3.7a). However, consistent with observations from literature data, the $D_H^{opx/melt}$ correlates negatively with H_2O concentrations in melts (Figure 3.7b).

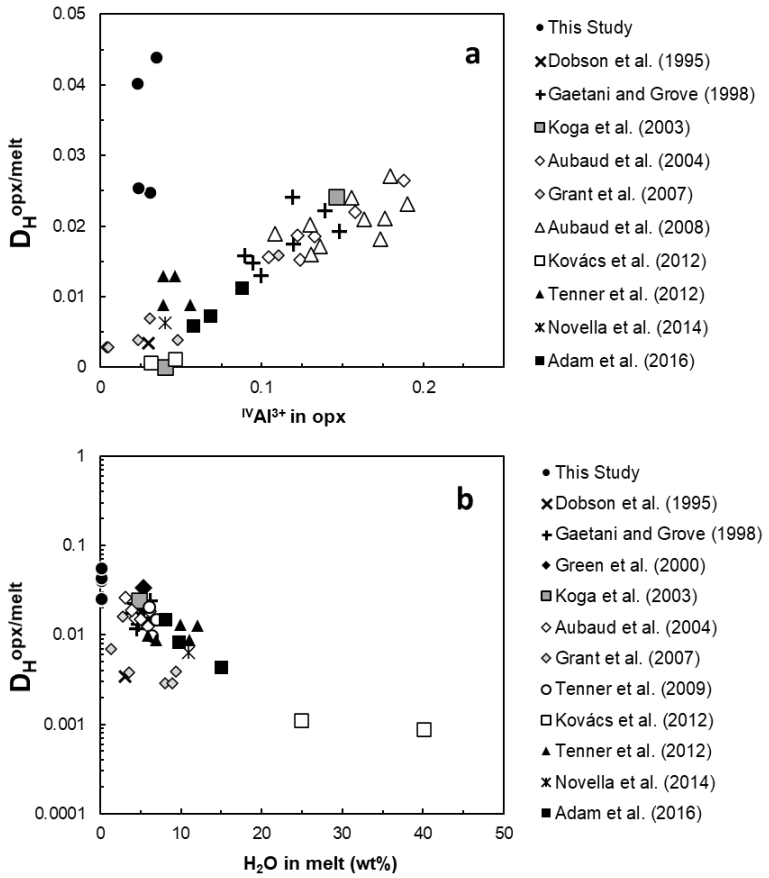

Figure 3.7. Comparison of literature data for $D_H^{opx/melt}$ values where (a) shows the variation of $D_H^{opx/melt}$ with $^{IV}Al^{3+}$ and (b) $D_H^{opx/melt}$ with H_2O contents of the melt. Data include the Humphrey samples analyses from this study, natural boninite phases from Dobson et al. (1995), and experimental basalt samples from Gaetani and Grove (1998), Green et al. (2000), Koga et al. (2003), Aubaud et al. (2004), Grant et al. (2007b), Tenner et al. (2009), and Kovács et al. (2012), Novella et al. (2014), and Adam et al. (2016). For Kovács et al. (2012), the H_2O of the melt was estimated from the data using the approach of Adam et al. (2016) assuming melt-H_2O solubilities of ~10 wt% per GPa.

3.4.3 Olivine

Results are shown in Table 3.2. Seven experiments contained olivine suitable for SIMS analysis with concentrations of H_2O (<4–44 ppm) that are at the lower end of values produced in similar experimental studies (e.g., Koga et al. 2003, Aubaud et al. 2004, Hauri et al. 2006, Grant et al. 2007, Tenner et al.

2009). As the melt contents are broadly similar across experiments used in this study, a positive correlation can be seen for H and $D_H^{ol/melt}$ (Figure 3.8a).

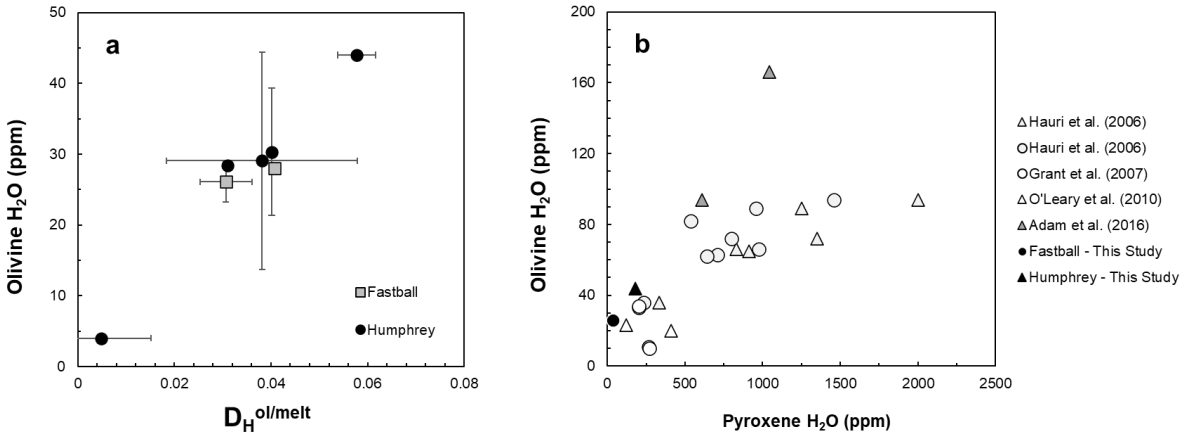

Figure 3.8. a) Correlation of olivine H_2O contents and $D_H^{ol/melt}$ b) Covariations of experimental olivine, orthopyroxene, and clinopyroxene water concentrations from this study compared to literature data synthesized under similar P-T conditions from Hauri et al (2006), Grant et al. (2007a), and O'Leary et al. (2010). Triangles represent clinopyroxenes, circles represent orthopyroxenes.

The $D_H^{ol/melt}$ are correspondingly high (<0.005–0.058) as a result of the low water contents of the melt, where in other experimental studies the water contents of the melt is largely dependent on the experiment's initial water contents and the melt fraction. The $D_H^{cpx/olivine}$ value is 1.4 ± 0.6, while the $D_H^{opx/ol}$ value is 1.8 ± 1.2, which is within error of the $D_H^{opx/olivine}$ value for iron-rich olivine at 1.1 from Withers et al. (2011). The covariation of experimental olivine and pyroxene is shown in Figure 3.8b where the results of this study are broadly consistent with previous evidence that the increased water content of pyroxenes tends to shadow increasing water content in olivine.

3.4.4 C and H contents of the silicate melt

The bulk C and H content of the silicate melts measured by SIMS are tabulated in Table 3.3.

Table 3.3. SIMS results for H and C content of the Melt.

	Melt H as H_2O			Melt Carbon as CO_2		
Sample	**n**	**ppm**	**±**	**n**	**ppm**	**±**
F3	5	841	89	5	182	44
F4	9	797	54	9	278	110
F5	3	850	24	3	404	60
F6	3	930	178	3	758	69
F7	3	688	53	4	288	51
F8	6	833	138	-	-	-
F12	6	852	56	-	-	-
H3	3	2316	33	-	629	63
H5	3	527	24	2	673	29
H6	2	762	40	2	747	40
H11	3	1287	35	3	1460	165
H12	6	755	43	6	603	88
H14	3	814	62	3	1055	27
H19	4	700	52	3	2042	310
H22	3	805	46	3	2022	534
H27	9	917	94	9	241	62
N11	-	-	-	-	-	-
N10	3	320	31	3	3454	547
N9	2	<LoD	-	2	2549	40

Note NWA samples were not used for calculations due to concerns with quench texture. LoD= limit of detection.

The H content varies from 688 to 930 ppm for the Fastball samples, 527 to 2316 ppm for the Humphrey samples, and 320 ppm H for NWA10. However, as shown in Figure 3.1, the NWA samples lack melt pockets free from fractures or crystallites and thus have a lower degree of confidence associated with SIMS results.

The results are similar to previous measurements from experimental studies conducted with no intentional H_2O added in the starting mixtures and in comparable P-T range (e.g., Li et al., 2015, 2016; Dalou et al., 2017; Grewal et al., 2020). None of the minerals analysed contained C above the limit of detection. The variation of C dissolved as CO_3^{2-} of the silicates melts is in the range of 182 to 2042 ppm. These measurements are broadly comparable to the original micro-FTIR analysis conducted by Filiberto et al. (2010b) to estimate the dissolved CO_2 contents of the experimental glasses, where Fastball samples G68-F2, G71-F4, G73-F5 were found to contain of 0.2-0.3 wt% dissolved CO_2. The SIMS measurements are consistent with values from previous studies of carbon-rich melts and fall within the parameter space of the solubility model of Eguchi and Dasgupta (2018), as shown in Figure 3.9. Using the CO_2 solubility model for silicate melts at graphite saturation by Eguchi and Dasgupta (2018), the carbon in the melt is predicted to occur only as carbonate anions, CO_3^{2-}. Generally, the C solubility decreases with decreasing log fO_2 until ~ΔIW of –2 to –1 as observed in previous studies (Dasgupta and Grewal, 2019 and references therein). At such reducing conditions, the C solubility becomes dependent on the bulk water content in the silicate melt and may increase below ~IW –2 where the contributions of C–H species such as methyl groups become more significant at high fH_2 conditions.

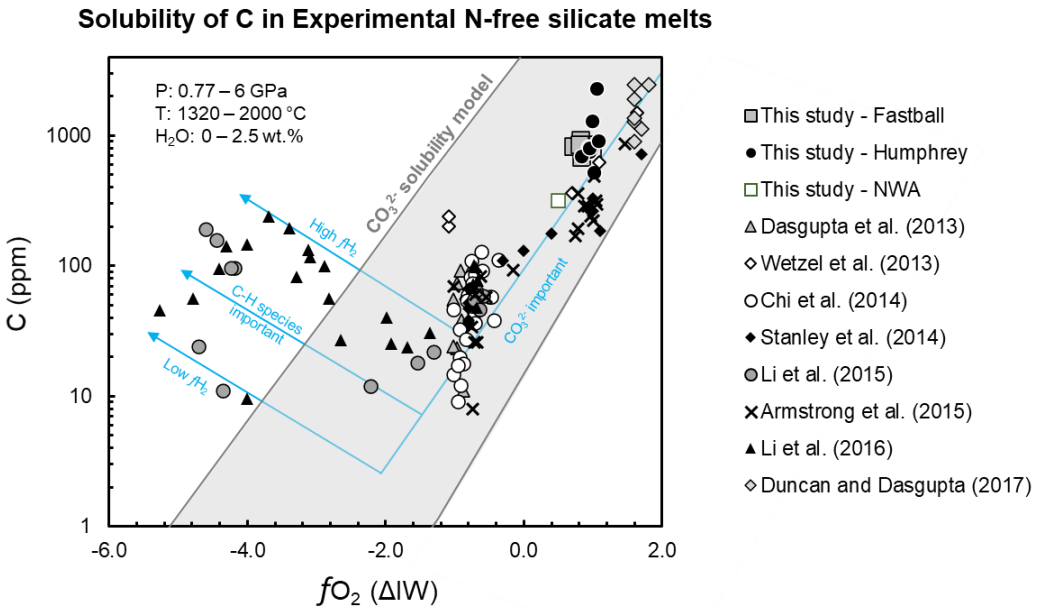

Figure 3.9. Data from this study and literature data for the solubility of C in nitrogen-free, experimentally produced silicate melts near or at graphite saturated conditions as a function of fO_2. The shaded region represents the CO_3^{2-} solubility model of Eguchi and Dasgupta (2018) for graphite saturated melts for the pressure range of the data from 0.77 to 6 GPa, the temperature ranges from 1230 to 2000 °C, and the H_2O range of the melts from 0 to 2.5 wt. %. For the model, an NBO/T value of 2.7 is used to represent peridotite-like silicate melt.

3.4.5 Possibility of C contamination

The possibility of C contamination is difficult to avoid in experiments run in graphite capsules, despite careful re-polishing efforts to remove smeared or deposited C on unlevel surfaces. Minor contamination explains the highly heterogenous measurements of C measured in crystals, which ranged from 1.7 to 47.3 ppm for olivine and may reflect that measurements took place on seven distinct spots and on four separate crystal grains (Table 3.4).

Table 3.4. SIMS results for mineral C contents

Sample	Mineral	C (ppm)	error (%)	notes
H27	olivine	5.9	11	crystal 1
	olivine	20.3	7	crystal 1
	olivine	47.3	6	crystal 2, rounded surface
	olivine	1.7	13	crystal 2, flat surface
	olivine	7.0	10	crystal 3
	olivine	38.5	6	crystal 3, slightly on edge
	olivine	12.5	8	crystal 4
N9	olivine	40.2	7	-
	pyroxene	26.8	6	-
N10	pyroxene	27.4	6	crystal 1
	pyroxene	26.5	9	crystal 2

*Note that error (%) refers to instrumental uncertainty.

The lowest value measured in this study was 1.7±0.2 ppm for olivine in Humphrey-27, which is still considerably greater than the <1 ppm range determined by Shcheka et al. (2006) for carbon-saturated peridotite phases. Other measurements for pyroxene and olivine were routinely greater than 20 ppm (Table 3.4). Similarly high concentrations of mineral C have been noted by Adam et al. (2016) as discussed in Chapter 2. Additionally, since no standards for C in olivine could be obtained to create a calibration curve, the calibration curve for glass was used. The crystals were more difficult to polish than the silicate melt as the crystals were more prone to rounding, which can interfere with SIMS analysis. The samples were polished in Crystalbond™ mounts. To remove the Crystalbond™, the samples were cleaned with multiple washes of high-purity acetone and ethanol and ultrasonicated before being mounted in indium for SIMS analysis. A higher degree of confidence can be placed in the CO_2 measurements for the melts, which falls within the range expected for moderately reduced glasses.

3.5 Discussion

3.5.1 Model of partitioning of H between clinopyroxene and silicate melt

Prior to this study, little data existed for $D_H^{cpx/melt}$ at very low bulk melt H_2O contents, leaving the influence of H_2O activity in silicate melts unclear. Previous experiments on simple systems (e.g., Stalder, 2004; O'Leary et al., 2010) demonstrated the positive influence of ^{IV}Al, on H_2O solubility in pyroxenes, and as noted by O'Leary et al. (2010), the portion of $D_H^{cpx/melt}$ attributable to the creation of metal vacancies remains relatively constant and therefore does not require specific pressure parametrization. The influence of temperature and pressure is not negligible. However, their respective effects are adequately captured by other variables, since increasing the temperature decreases melt H_2O concentrations, and many experiments reflect the positive P-T slope of the liquidus.

Although there is cross correlation between ^{IV}Al and melt H_2O concentrations, there remains significant scatter in the selected dataset (Figure 3.6c). The Bédard (2014) dataset is "a compilation of data analysed over 30 years with different methods in different laboratories" that has been filtered to account for uncertainty and bias that may typically arise from 1) older data obtained with less accurate instrumentation, 2) natural data, 3) data from phase equilibrium studies, and 4) data from experiments on melts with compositions that differ radically from those found in naturally occurring systems. Using this expansive dataset, it is possible to appreciate the significant scatter between ^{IV}Al and melt H_2O concentrations and to infer that ^{IV}Al incorporation is limited by pressure (Figure 3.10)

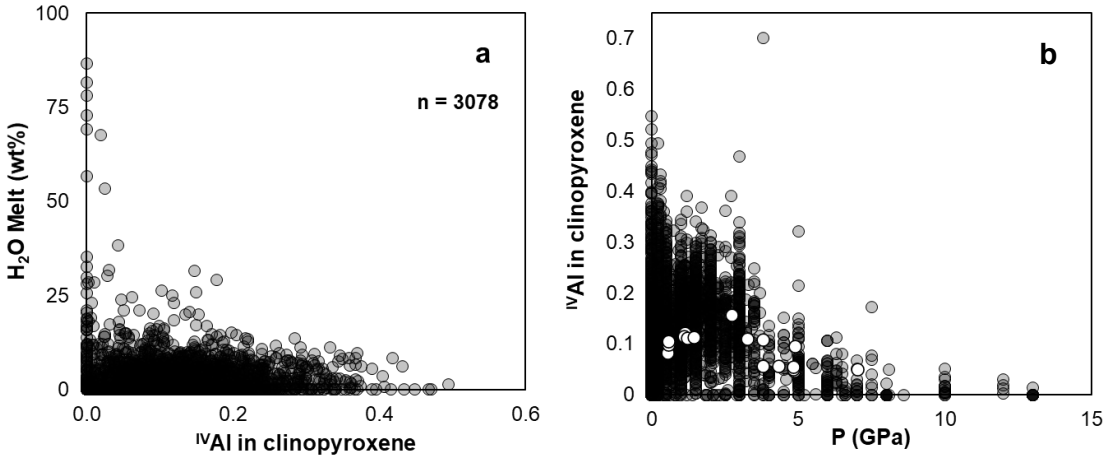

Figure 3.10. a) Variations of H_2O melt content with ^{IV}Al and b) ^{IV}Al in clinopyroxene versus pressure. White circles denote the near solidus clinopyroxene compositions from 1 to 7 GPa used by O'Leary et al. (2010) in their parameterization. Data for the filled circles is from the filtered dataset of Bédard (2014).

A combined 4th order polynomial equation can be used to empirically capture the correlation of $D_H^{cpx/melt}$, which tends to increase with increasing ^{IV}Al, as well as the negative correlation of $D_H^{cpx/melt}$ with H_2O concentrations in melts. The equation uses ln $^{IV}Al^{3+}$ and ln H in clinopyroxene (ppm) as the explanatory variables as this allows for the back calculation of the H_2O contents of the melt from which those crystals were formed. Non-linear regressions used the following generalized functional form,

$$Y = pr1 + pr2 \cdot X_1 + pr3 \cdot {X_1}^2 + pr4 \cdot {X_1}^3 + pr9 \cdot {X_1}^4 + pr5 * X_2 + pr6 \cdot {X_2}^2 + pr7 \cdot {X_2}^3 + pr8 \cdot {X_2}^4. \quad (1)$$

Where the parameters and variables are listed in Table 3.5.

Table 3.5 Parameters and explanatory variables.

Parameters	Value
pr1	123.226
pr2	-16.315
pr3	-9.382
pr4	-2.312
pr5	-97.321
pr6	24.856
pr7	-2.697
pr8	0.107
pr9	-0.191
Y	ln H in melt (wt%)
X1	ln $^{IV}Al^{3+}$
X2	ln H CPX (ppm)

The above equation was fit using a dataset of 66 experiments with pressures ranging from 0.5 to 6.0 GPa, $^{IV}Al^{3+}$ in clinopyroxene ranging from 0.002 to 0.306, and with H_2O melt contents ranging from 0.07% to 40 wt % (Aubaud et al., 2004, 2008; Hauri et al., 2006; Tenner et al., 2009; O'Leary et al., 2010; Kovács et al., 2012; Novella et al., 2014; Adam et al., 2016; and this study). Fit statistics are shown in Figure 3.11. Considering the excellent R^2 value, 96% of the variability of the dependent variable (H_2O contents of the melt) is explained by the model (Figure 3.11a). Despite the diversity of studies considered, the residuals follow an approximately normal distribution as shown by the superimposed normal density function (Figure 3.11b). The majority of data fall well within a 95% confidence interval (Figure 3.11a). In spite of not accounting for a number of other thermodynamic variables (e.g., fO_2 or compositional activities), the model performs exceedingly well given the varied

dataset, which suggests the model captures the most critical variables controlling H partitioning and is broadly applicable. Further goodness of fit statistics are provided in Table 3.6.

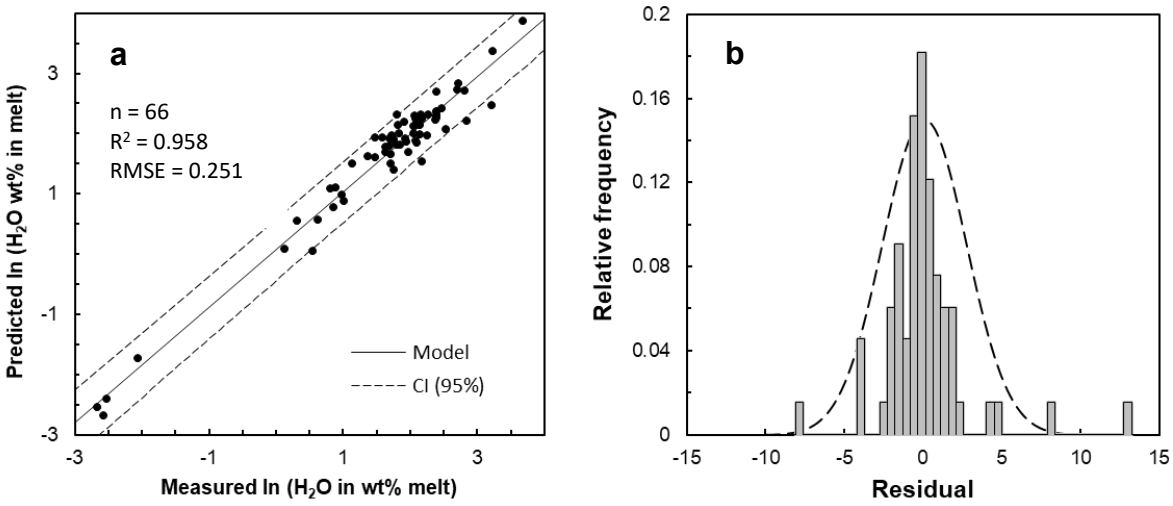

Figure 3.11 a) Comparison of experimentally determined H_2O melt values with those predicted by eqn. (3.1). The model produces good linearity ($R^2 = 0.958$) and a reasonably good fit with all but a few data points falling within the 95% confidence interval (CI) and a root mean squared error (RMSE) value of 0.251. b) illustrates an approximately normal distribution of residuals produced by the model with a superimposed normal density function.

Table 3.6 Goodness of fit statistics for Figure 3.11.

Observations	66
DF	57
R^2	0.958
SSE	4.21
MSE	0.063
RMSE	0.251
AIC	-161.645
AICC	-157.645

3.5.2 Application to the water content of the nakhlite mantle source

Nakhlites are achondrite meteorites consisting of clinopyroxenites with subcalcic augite as the most abundant mineral, which serve as an important source of data about Mars. Nakhlites are dominated by large euhedral and subhedral crystals of augite, which are commonly interpreted as cumulus grains, settled out of basaltic magma and augmented by post-cumulus overgrowths (Treiman, 2005). To date, no return missions have provided samples from Mars. This leaves only meteorites, such as the Nakhlites, which are accompanied by concerns with terrestrial contamination, shock effects, and space exposure on the measured H_2O contents. Compared to the prevalent shock effects seen in other SNC meteorites, the shock effects in the nakhlites are minor, alleviating concerns that the augite H contents may have been significantly diminished during impact processes. In terms of terrestrial interaction effects, Nakhla is the least affected of the nakhlites. Therefore, Nakhla may represent a superior candidate to decipher these various processes in order to determine Martian mantle water contents. Previous work has focused on selecting the least-degassed pyroxenes which may preserve magmatic H information (Peslier et al., 2019) or experimentally rehydrating clinopyroxenes to obtain more accurate H_2O concentrations despite dehydration and degassing effects occurring from the emplacement on or ejection from the surface of a planetary body (Weis et al., 2017). Because Martian meteorites are crustal in origin (McSween, 2015), the search for mantle signatures is greatly complicated, often resulting in poorly constrained calculations for the water content of the Martian mantle. However, H incorporated in some Nakhla augites is thought to be a mantle signature from preserved igneous water contents, as opposed to a crustal signature resulting

from Cl-bearing hydrothermal fluids being assimilated by the parent magma of nakhlites prior to pyroxene crystallization (Peslier et al. 2019).

Measuring the H_2O contents of the Nakhla augite allows for the modelling of the water content of the mantle source. If the H_2O content of the melt or the $D_H^{cpx/melt}$ value can be determined based on clinopyroxene crystal chemistry alone, then the magmatic water contents of the parental melt can be determined. The Nakhla parent melt can be estimated by utilizing eqn (1) and then compared to previous literature estimates. The mantle source H_2O content can be calculated using the H_2O content of the parent melt and the equilibrium and fractional (accumulated) melting equations (Shaw, 2005). Both the magmatic and the mantle source water contents can be compared to previous literature estimates derived by various methods.

Most nakhlite pyroxenes have experienced degassing, which explains their low water contents at <20 ppm H_2O (Peslier et al. 2019). Weis et al. (2017) quantified potential degassing effects on Nakhla clinopyroxenes by performing rehydration annealing experiments, and the rehydrated crystals were used with the $D_H^{cpx/melt}$ model from O'Leary et al. (2010) to estimate a value for the magmatic water of the Nakhla parent melt, since the core composition of the crystals are expected to represent magmatic H_2O from an early stage of crystallization. As shown in Table 3.7, the water contents of these Martian clinopyroxenes are considerably lower than those in the Earth's upper mantle, which has an estimated minimum of 191 ppm and maximum of 764 ppm (Warren and Hauri, 2014). From the calculations of Weis et al. (2017), the basaltic magma that crystallized Nakhla may have contained up to 1.42 wt.% H_2O. Peslier et al. (2019) reported that based on the O'Leary model and the average compositions of the most Mg-rich augites that have no evidence for degassing, the H_2O content of the melt in equilibrium with augite was 0.69 wt % and the modelled nakhlite mantle source water content was

approximately ~60–185 ppm H_2O (Peslier et al., 2019). However, application of the model from this study, which accounts for the effects of H_2O contents on $D_H^{cpx/melt}$ that become especially important for melts with lower water contents, predicts significantly lower water contents for the Nakhla crystallizing magma (Table 3.7).

Table 3.7 Comparison of modelled magmatic and mantle source water contents for the nakhlites

	Nakhla augite	Nakhla cpx1	Nakhla cpx2	Nakhla cpx3	Nakhlite augite, Mg-rich, least degassed
Reference for cpx	Hallis et al. (2012)	Weis et al. (2017)			Peslier et al. (2019)
Measured H_2O cpx (ppm)	97 ± 408	134 ± 26	132 ± 26	126 ± 26	61.034 ± 36.4
Melt H_2O (wt%), O'Leary Model	1.07	1.48	1.46	1.39	0.69
Melt H_2O (wt%), this study	0.25	0.47	0.45	0.41	0.18
Mantle Source, O'Leary Model (ppm)	92-287	127-396	12-391	119-372	59-185
Mantle Source, this study (ppm)	21-73	40 -131	39 - 127	35 - 116	15 - 56
Si^{4+}	1.958	1.958	1.958	1.958	1.970
$^{IV}Al^{3+}$	0.042	0.042	0.042	0.042	0.040
Ca^{2+}	0.777	0.777	0.777	0.777	0.770
$D_H^{cpx/melt}$ this study	0.040	0.021	0.021	0.024	0.055

Although it is difficult to constrain the amount of residual liquid remaining when the augites crystallized, the nakhlites' parent melt is thought to have been generated by low degrees of melting, so calculations employ a melting range of 0.5-1.5 %. Another source of uncertainty stems from the nature of the nakhlites as cumulates, since their bulk composition does not represent that of the parent melt. The Martian crust is approximately ~50 km thick (Zuber et al., 2000), and Martian magma generated from below the crust at pressures > 0.56 GPa. The parental melt of the nakhlites may have been

generated at pressures greater than or equal to 2.5 GPa from a metasomatized harzburgitic source, or a pyroxenite source at lower pressures (Longhi and Pan, 1989; Borg et al., 2003; Udry and Day, 2018). Following the approach of Peslier et al. (2019), the harzburgite is assumed to consist of 70% olivine, 24% orthopyroxene, 5% garnet and 1% clinopyroxene. The value for $D_H^{opx/olivine}$ of 1.1 is used from Withers et al. (2011), which was determined for Fe-rich olivine that more closely resembles the Martian mantle than results from Fe-low experiments. Furthermore, since the $D_H^{opx/ol}$ value (1.8 ± 1.2) from this study is within error of the $D_H^{opx/ol}$ value for Withers et al. (2011), using either number will produce the same end result. The $D_H^{garnet/melt}$ and $D^{opx/melt}$ were taken from Hirschmann et al. (2009) and a bulk partition coefficient for water between peridotite and melt is estimated. While olivine has been proposed as the mineral first on the solidus (Longhi and Pan 1989), it is more probable that augite (i.e., clinopyroxene) was first on the solidus (Sautter et al., 2012; Stockstill et al., 2005). For comparison both scenarios are modelled as shown in Figure 3.12. The degree of crystallization ranges from <1% with augite first on the solidus to 25% with olivine first on the solidus, as based on the MELTS modelling of shergottite compositions by Peslier et al. (2010). If augite crystallized first on the liquidus, the water content of the parent melt is 1779 ppmw H_2O, however if augite crystallized when 75% of the melt remained, then a fractional crystallization equation is used and the nakhlite parent melt has 1356 ± 75 ppmw H_2O (Shaw, 2005). Using a magmatic H_2O content of 1779 ppm, then if pyroxene crystallized first, the water content of the mantle source of the nakhlites becomes 26-56 ppmw H_2O for the harzburgite source and 34-42 ppmw H_2O for the pyroxenite source. Assuming a common parent melt for the nakhlites and chassignites, and that olivine crystallized first, the H_2O content is approximately 15-42 ppmw for the nakhlite source. These results are summarized in Table 3.5, and Figures 3.13-14. The effect of using

the updated clinopyroxene partition coefficient from this study can be seen by comparing against previous models; a comparison is made using the O'Leary model and all partition coefficients from Hirschmann et al. (2009). The modelled nakhlite mantle source using the model and partition coefficients of this study is significantly lower as is evident when comparing Figure 3.12a-b to Figure 3.12c-d.

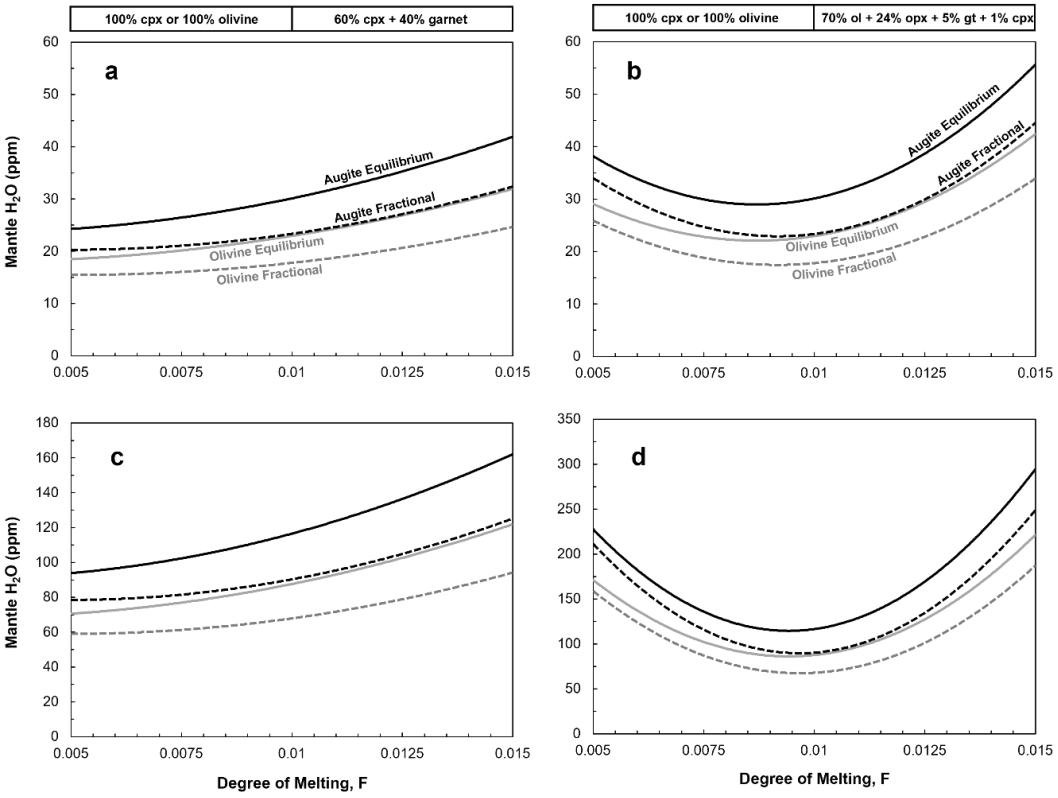

Figure 3.12. The modelled Martian Mantle H_2O abundance during solidification of the Nakhla parent melt using a magmatic H_2O content of 1779 ppm. Solid lines correspond to equilibrium melting and dashed lines correspond to fractional melting. Black lines show augite crystallizing first and gray lines assume olivine crystallizing first. a) the pyroxenite source, consisting of 60% augite (cpx) and 40% garnet (gt), b) the harzburgitic source consisting of 70% ol, 24 orthopyroxene (opx), 5% garnet (gt), and 1% clinopyroxene (cpx), c-d) comparison using the model of O'Leary et al. (2010) and all partition coefficients from Hirschmann et al. (2009), which yield systematically greater values for mantle H_2O.

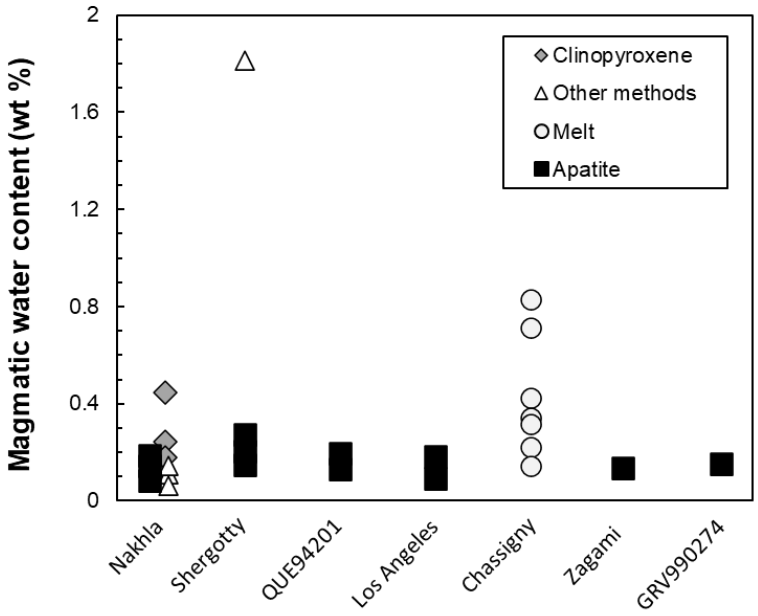

Figure 3.13. Magmatic water contents determined using Nakhla clinopyroxenes compared to Martian meteorite parental melts from available literature. Shergotty data is from Dann et al. 2001, Lentz et al. 2001, McSween et al. 2001, McCubbin et al. 2012. QUE942012, Zagami, Los Angeles, and GRV990274 are from McCubbin et al. 2012. Chassigny is from Boctor et al. 2003, McCubbin et al. 2010.

Table 3.8. Water contents of Earth's Mantle and mantle sources of the SNC meteorites.

Earth		H_2O (ppm)	Source
Upper Mantle	Continental Mantle Lithosphere Cratonc	24–100	Peslier et al. 2017 and references therein
	Continental Mantle Lithosphere off-Craton	50–100	Peslier et al. 2017 and references therein
	Oceanic Mantle Lithosphere	50–100	Peslier et al. 2017 and references therein
	Asthenosphere*	55–400 (200)	Peslier et al. 2017 and references therein
	Bulk Upper Mantle	200	Peslier et al. 2017 and references therein
		250	Keppler and Bolfan-Casanova (2006)
Subduction Zone	Mantle Wedge (Arc Basalt Source)	600–8000	Peslier et al. 2017
	Slab in Upper Mantle	300–3000	Peslier et al. 2017
	Primary melts from Supra-subduction Zones	1190–1900	Sobolev and Chaussidon (1996)
Primitive Mantle		330–1200	Peslier et al. 2017
Total mantle		382–2564 (1374)	Peslier et al. 2017
MORB		54 ± 12	Simons et al. (2002)
		142 ± 82	Saal et al. (2002)
		80–330	Sobolev and Chaussidon (1996)
		100	Hirschmann (2010)
		116	Salters and Stracke (2004)
		70–135	Workman and Hart (2005)
Mars			
Shergotty Apatite	Based on 10% partial melting of mantle source	190 ± 7	McCubbin et al. (2012)
QUE94201 Apatite		143 ± 14	McCubbin et al. (2012)
Los Angeles Apatite		129 ± 6	McCubbin et al. (2012)
Y980459 MI		26 ± 1	Usui et al. (2012)
Zagami Apatite		117 ± 17	McCubbin et al. (2012)
GRV990274 Apatite		143	McCubbin et al. (2012)
Chassigny Amphibole	Based on 3% partial melting of mantle source	191 ± 62	McCubbin et al. (2010a)
Chassigny MI		0.23 ± 0.01	Boctor et al. (2003)
Depleted Source	bulk estimate	15–23	McCubbin et al. (2016)
Enriched Source		36–72	McCubbin et al. (2016)
The Moon			
Primitive lunar mantle	alkali feldspars in lunar granitoid	10–100	Mills et al. (2017)
	olivine-hosted melt inclusions	90 - $_{30}^{+50}$	Chen et al. Ni et al.
Lunar mantle	melt inclusions	79–409	Hauri et al. (2011)

*The source of depleted MORB is ~20-250 ppm H_2O, but the deepest part of the upper mantle may have greater contents.

3.5.3 Mantle source H_2O contents for Mars, the Moon, and Earth

Calculations based on the water content in the Nakhla parental melt for different clinopyroxene samples indicate mantle water contents in the range of 15-126 ppm H_2O for Nakhla's mantle source. The values obtained in this study for the source regions for the nakhlites is significantly lower than most of Earth's upper mantle with an estimated bulk value of 200-250 ppm (Table 3.7-8). Specifically, there is significant overlap of the nakhlite source with the terrestrial mantle lithosphere, which ranges from 50-100 ppm H_2O, although it is lower than the 150-200 ppm H_2O range of the source of mid ocean ridge basalts (MORB), the Earth's upper asthenosphere H_2O (Peslier et al., 2017 and references therein). Based on apatite analyses in NWA 6234 and Shergotty, a water content similar to the MORB source-region has been suggested for the source region of the SNC meteorites (e.g., McCubbin et al., 2012; Gross et al., 2013). The modelled Nakhlite source region water content may resemble a depleted terrestrial MORB source of 100-180 ppm (Michael 1988) or 142 ± 82 ppm (Saal et al. 2002), which would also be similar to the source region for Yamato-980459 and LAR 06319, as calculated by Filiberto et al. (2016). The Nakhla's mantle source values from this study are also not dissimilar to estimates for the primitive lunar mantle. Based on lunar melt inclusions, Hauri et al. (2011) estimated that the lunar source mantle contains 79–409 ppm H_2O, while the investigation of alkali feldspars in lunar granitoid suggests the H_2O concentration in the lunar mantle is 10-100 ppm (Mills et al., 2017). Based on the study of olivine-hosted melt inclusions, the primitive lunar mantle's H_2O concentration is 90_{-30}^{+50} ppm (Chen et al., 2015; Ni et al., 2019).

The Martian mantle is comprised of multiple hydrous reservoirs and is geochemically heterogenous, which indicates incomplete mantle mixing following accretion, differentiation, and thermochemical evolution (Barnes et

al., 2020). Both at the present and at the time of Nakhlite formation 1.3 Ga ago, Mars lacked a convective mantle, making the most direct comparison to Earth a depleted upper mantle with conductive heat transfer, such as the terrestrial mantle lithosphere (Peslier et al., 2019). Therefore, sections of the Martian mantle may be slightly more hydrous (nakhlite source) or slightly less hydrous (depleted shergottite source) than the Earth's mantle lithosphere.

Based solely on Nakhla augite, the mantle water contents estimated within the constraints of this study are broadly similar to or lower than the water contents of the upper part of the Earth's mantle. While clinopyroxene should contribute significantly to the upper mantle water budget of Mars, other important minerals include olivine and possibly garnet. If olivine is considered, particularly for relatively Fe-rich olivine compositions (Withers et al., 2011) most applicable to Mars, the bulk water contents might be >200 ppm H_2O compared to the presently modelled nakhlite source. However, in the NWA 998, Nakhla, MIL 03346, and NWA 6148 olivine grains analysed by Peslier et al. (2019), no water could be detected, perhaps due to degassing effects, leaving the H contents of Martian olivine ambiguous. Similar issues have been noted in terrestrial samples. For instance, the pre-eruptive H_2O contents for terrestrial arc lavas calculated on the basis of H in clinopyroxene phenocrysts are systematically higher than those inferred from olivine-hosted melt inclusions, suggesting that clinopyroxenes provide a record that is closer to primary (undegassed) values (O'Leary et al., 2010). Additionally, a number of studies on natural olivine and pyroxenes from xenoliths have noted that natural pyroxenes appear to retain their mantle water contents, whereas olivine has lost its water (Warren and Hauri, 2014 and references therein). Therefore, using direct measurements from pyroxene, as opposed to olivine, is highly preferable when modelling mantle source H_2O content and magmatic

water. The original mantle water content of olivine can be determined from pyroxene mantle water concentrations using $D_H^{pyx/ol}$.

Based on an amphibole in a melt inclusion in Chassigny, the water content for the source of chassignites ranges from 130-250 ppm H_2O (McCubbin et al. 2010) and is greater than that of the nakhlites. However, the modelled Nakhla mantle water content range overlaps with the Chassigny and nakhlite source region based on H_2O/Cl measurements from amphibole and apatite in chassignites and apatite in nakhlites, which has a combined value of 68 ± 113 ppm H_2O in the source region (Filiberto et al., 2016). Based on Y980459 melt inclusion data, the water contents of the depleted shergottite source ranges from 15–47 ppm H_2O (Usui et al., 2012), while calculations based on apatite suggest 36–73 ppm H_2O for the enriched shergottite source (McCubbin et al., 2016), both of which are in the modelled range of the Nakhla source. McCubbin et al. (2016), estimated the abundance of H_2O in the Martian mantle through the combination of data from studies on apatite (McCubbin et al., 2012; Gross et al., 2013), amphibole (McCubbin et al. 2010; Giesting et al., 2015;), and glasses inside olivine-hosted melt inclusions (Usui et al. 2012; Filiberto et al., 2016). The Martian mantle consists of at least two distinct geochemical reservoirs, including a geochemically depleted source and a geochemically enriched source. For the geochemically depleted source regions, the mantle source region abundances were estimated to be 15–23 ppm H_2O, while the geochemically enriched source regions contained 36–72 ppm H_2O (McCubbin et al., 2016). Based on the Nakhla source H_2O determined in this study, there is considerable overlap with both the enriched and depleted source H_2O. Comparing the values calculated here to literature data for the SNC meteorites allows for an estimate of the Martian H_2O range and provides a comprehensive overview for the water contents of the Martian mantle (Figure 3.14).

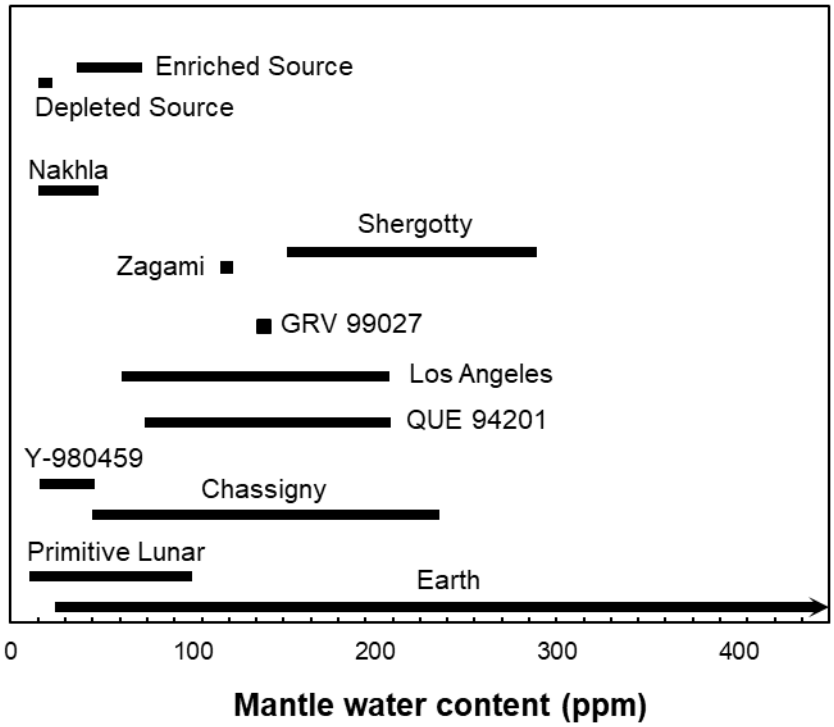

Figure 3.14. Mantle water concentrations determined for Martian meteorites in comparison to the enriched and depleted sources, the primitive moon, and Earth. Data is from this study and literature refences compiled in Table 3.6.

3.6 Conclusion

This study provides new measurements of H and C concentrations in nominally anhydrous minerals in experimentally produced Martian basalts. The analysis of synthetic Martian basalts provides insight into the effect of activity-composition relations for H_2O melt contents on the partitioning of H between clinopyroxene and silicate melt, and form the basis for new models that build on previous parameterizations based primarily on $^{IV}Al^{3+}$ in clinopyroxene. Since the $D_H^{min/melt}$ for mineral phases is significantly influenced by the H_2O content in silicate melts, the addition of the nominally anhydrous data from this study bridges a significant gap in the literature and allows for systems with low magmatic water contents (<1%) to be freshly considered.

Applying this model to either experimentally rehydrated crystals or nakhlite clinopyroxenes with evidence of preserved magmatic H content enables improved constraints on the accuracy of Martian parental magmas, which may have diminishingly low water contents. The Martian mantle may not be as hydrous as indicated by previous estimates based on previous clinopyroxene models that did not extend to nominally anhydrous conditions. Results suggest that the water content of the source of the Nakhla parental melts overlaps the depleted and enriched Martian mantle reservoirs and contains water contents similar to or lower than water contents of the upper part of the Earth's mantle.

3.7 Acknowledgements

Research was supported by Sigma Xi Grants in Aid of Research (GIAR), the University of Edinburgh Research Training Support Grant (RTSG), and award of instrument time at the Edinburgh Ion Microprobe facility, IMF665/0518. We especially appreciate Dr Filiberto for generously providing the synthetic Martian samples. We appreciate the assistance of Dr Cristina Talavera Rodriguez for SIMS analyses. Deep Volatiles, a NERC funded research programme on Volatiles, Geodynamics & Solid Earth Controls on the Habitable Planet (NE/M000346/1) is also highly appreciated for their support and feedback throughout the project.

Chapter 4

Semi-empirical Thermodynamic Models for H Solubility in Olivine

"If a law has many adjustable parameters then it will be significantly preferred to the simpler law only if its predictions are considerably more accurate."

Jefferys and Berger (1992)

4.1 Abstract

The incorporation of H into olivine is influenced by a considerable number of thermodynamic variables (T, P, fO_2, fH_2O, etc.). Due to the importance of olivine H contents within the scope of Earth and planetary sciences, the development of a model to calculate the H contents in olivine over a range of conditions found in the Earth's upper mantle as well as in shallow magma oceans would represent a vitally useful tool for the field. This Chapter presents modelling and statistical results based on data from Chapters 2 and 3 as well as datasets available in the literature. Both synthetic experiments that create new minerals and point defects as well as hydration experiments that hydroxylate the pre-existing point defect structure of natural olivine are considered. The sensitivity and potential for olivine solubility to be parameterized as function of T-P-fO_2-fH_2O and chemical composition is assessed for existing literature data. While it is unlikely that a single set of parameters can provide a universal and physically meaningful solubility law based on the currently available dataset, various useful models are presented which represent the amalgamated contributions of each different defect within the context of the specific environment. First, a case-by-case examination of previous studies is conducted using semi-empirical models derived from a thermodynamic starting point, which demonstrates the internal consistency of the study in question and validates the efficacy of the modelling approach. However, the resultant models naturally lack widespread applicability. Second, two additional models were created that consider the entire dataset with the intention of working toward a universal law within existing parameters.

Keywords: Thermodynamics, Empirical Models, Point Defects, Water Fugacity, Oxygen Fugacity

4.2 Introduction

Despite a number of experimental investigations over the last 30 years, the influence of thermodynamic variables on H solubility in olivine remains uncertain (e.g., Bai and Kohlstedt, 1992, 1993; Kohlstedt et al., 1996; Matveev et al., 2001; Lemaire et al., 2004; Berry et al., 2005, 2007; Grant et al., 2006, 2007; Mosenfelder et al. 2006; Bali et al., 2008; Férot and Bolfan-Casanova 2012; Tenner et al., 2009, 2012; O'Leary et al., 2010; Novella et al., 2014; Rosenthal et al. 2015; Adam, 2016, Tollan et al., 2017). These experiments fall into two categories: 1) annealing experiments where a pre-existing olivine crystal is equilibrated in a hydrous environment 2) crystallization experiments where olivine is synthesized from a hydrous silicate melt. For synthesis experiments, such as presented in Chapters 2 and 3, the objective is to grow olivine from a silicate melt and achieve complete equilibrium with the surrounding melt, which creates both intrinsic and extrinsic protonated defects reflective of that specific thermodynamic environment. These olivine crystals are expected to reflect the imposed conditions in terms of stoichiometry, trace-elements, and point-defect structure (e.g., Bai and Kohlstedt, 1992; Matveev et al., 2001; Berry et al., 2005; Grant et al., 2007; Withers and Hirschmann, 2008; Withers et al., 2011; Férot and Bolfan-Casanova, 2012; Padrón-Navarta et al., 2014). In contrast, annealing experiments often use well-characterized, large crystals of natural mantle olivine that have the advantage of having easily identifiable crystallographic axes for Fourier transform infrared (FTIR) spectroscopy analysis. Annealing experiments seek to decorate pre-existing point defects with H, which may reflect the last equilibration environment in regard to T, P, fO_2, and $a(SiO_2)$, however, it is unclear the extent to which the olivine point-defect structure will be altered by the T, P, fO_2 and $a(SiO_2)$ of the hydroxylation. It is likely that most annealing experiments are situated between these two dichotomies. Additionally, two-stage experiments also exist

where olivine is first annealed at known T, P, fO_2 and $a(SiO_2)$, and then subsequently hydroxylated to decorate the previously created point-defect structure.

A fundamental question in both annealing and synthesis experiments is the substitution mechanism for H incorporation and the structure of these point defects. There is a general consensus that in olivine H substitutes into vacant tetrahedral or octahedral sites to charge balance neighbour O sites to form hydroxyl groups (Matveev et al., 2001; Lemaire et al., 2004; Smyth et al., 2006), however interstitial H may also contribute to the overall H budget (Balan et al., 2014). This may be especially important for H_2, a considerably smaller molecule than H_2O that is expected to exhibit more ideal behaviour. FTIR can be effective in elucidating the relative proportions of these point defects, since hydroxyl groups are infrared active and the O–H stretching frequency depends on the local bonding environment. However, FTIR data obtained from synthetic systems inadequately replicate bands obtained from natural system (Berry et al., 2005). Experimental studies of Smyth et al., (2006), Withers and Hirschmann (2008), Férot and Bolfan-Casanova (2012), and Gaetani et al., (2014) could not find evidence that trace element-related defects play a significant role in water incorporation in olivine. For instance, Gaetani et al., (2014) writes that "our data argue strongly against a Ti-clinohumite-like defect being the most important mechanism for incorporation of H into Ol in the shallow upper mantle." Similarly, Demouchy and Bolfan-Casanova (2016) concluded that there is a lack of evidence for significant coupled substitution of H with Ti for typical naturally occurring mantle olivine compositions in existing literature data. However, correlations of H derived from SIMS data offer little information specific to incorporation mechanisms, considering the complexity of H substitution mechanisms in multicomponent olivine (e.g., Tollan 2017, 2018). While FTIR offers fingerprinting of the

substitution mechanism, it is rarely feasible to conduct on small, melt embedded crystals produced from synthesis experiments, such as those in Chapter 2 and 3, and is better suited to large gem-quality crystals that allow polarized transmitted light infrared spectra to be collected along identified crystallographic axes. For annealing, metastable equilibrium experiments, the resultant H incorporated depends on how the experiment is conducted, including the initial state of the starting material. Therefore, H incorporation at a given T, P, fO_2, and fH_2O for these experiments does not necessarily mean that the same amount of H incorporated or the substitution mechanisms identified can be recreated in global equilibrium experiments. A quantitative comparison between studies is therefore greatly problematized due to such "hidden moderators," the unmeasured and unquantified differences between experiments resulting in differences in the underlying effects, and thus in the observed experimental results. As stated by Tollan et al., (2018), "it is fallacious to suppose that a constitutive equation exists to quantify H contents in such circumstances," further implying that previous modelling approaches of compiling data sets to deduce thermodynamic constants cannot be applied. This, however, does not negate the discussion regarding the effect of fO_2 on H solubility or partitioning and the possible implications, because, whatever the thermodynamic modelling means regarding the H substitution mechanism, what is important is that it does describe correctly the measured data. In this Chapter, I provide empirical parameterizations based on underlying thermodynamics for previous experimental studies and discuss the implications of these relationships for predicting the H contents of mantle olivine in various environments.

4.3 Background

4.3.1 Substitution mechanisms for H in olivine

The four main substitution mechanisms identified for olivine are [Si], [Mg], [Ti] and [triv] (Tollan et al., 2017, 2018 and references therein) and are expected to be additive such that,

$$C_{H_2O}^{Total} = C_{H_2O}^{[Si]} + C_{H_2O}^{[Mg]} + C_{H_2O}^{[Ti]} + \sum_{R^{(3+)}} C_{[H_2O]}^{[triv]} \quad (4.1)$$

while in natural olivine only three trivalent cations (Al, Fe, and Cr) are expected to exist in sufficient concentrations to account for the observed [triv] absorbance (De Hoog et al., 2010; Tollan et al., 2017). A thermodynamically meaningful equation for the calculation of H in olivine as a function of these four substitution mechanisms requires the sequential parameterization of each term on the right-hand side of the above equation as a function of their related variables. Previous empirical models follow the successful approach applied to orthopyroxenes (e.g., Lu and Keppler, 1997) and is given by the equation,

$$C_{OH}^{olivine} = A f_{H_2O}^{n} \, exp\left(-\frac{\Delta V^{solid} P + \Delta H}{RT}\right)$$

where A is an empirically derived constant related to entropy, f_{H_2O} is the fugacity of H_2O, n is dependent on the nature of the crystal defect and charge neutrality condition, and ΔV^{solid} is the volume change associated with the hydration of the mineral, ΔH is enthalpy. Using nonlinear regression, it is supposedly possible to resolve the influences of individual variables by fitting data. The exponent n is related to a single or dominant incorporation mechanism of H in olivine. While it is tempting to attempt to develop a single

additive equation for convenient application, it is also not possible to obtain thermodynamically meaningful answers from fitting to the above equation. As succinctly stated by Ingrin et al., (2013), the convenience of such empirical fits to solve for thermodynamic variables "should be balanced against the guarantee that it would produce the wrong answers." Instead, it is essential to individually fit each separate incorporation mechanism as evidenced by their FTIR bands. Clearly, this approach is not possible in many crystal synthesis type experiments! Despite this conundrum, previous work, such as Zhao et al., (2004) and Gaetani et al., (2014), have modelled the concentration of the oxidized water species (OH) in olivine with terms added to account for fO_2 and as well as other mole fractions. Adapting this approach, we may use an equation of the form,

$$C_{OH}^{olivine}(T,P,fH_2O,fO_2,\alpha[triv]) = Af_{H_2O}^{n}\, exp\left(-\frac{\Delta V^{solid}P+\Delta H}{RT}\right)\exp\left(\frac{fO_2}{RT}\right)\exp\left(\frac{\alpha[triv]}{RT}\right) \quad (4.2)$$

where fO_2 is the oxygen fugacity term and $\alpha[triv]$ represents the concentration of trivalent cations participating in the [triv] substitution mechanism. The exponent n is related to the incorporation mechanism of H in olivine:

1) $n = 0.5$ for isolated OH groups where the substitution can occur with a H^+ and a trivalent cation for a tetravalent cation ($Fe^{3+,}$ $H^+ + Fe^{3+} = Si^{4+}$), or by the substitution of a H^+ for a univalent cation (Li+, H+ = Li+),
2) $n = 1$ for pairs of OH groups where the substitution consists of two H+ for a divalent cation such as Mg^{2+}, $2H^+ = Mg^{2+}$,

3) $n = 2$ represents the "hydrogarnet-type" of OH groups facilitated by the substitution of four H+ for a tetravalent cation such as Si^{4+} (see review by Keppler and Smyth, (2006) for further information).

In consideration of these multiple substitution mechanisms with simultaneously isolated, pairs of, and clusters of OH groups, n could be a value other than 0.5, 1 or 2. Since a general consensus has not been reached regarding the dominant substitution mechanism, it is unsurprising that a value for n also remains elusive. Considering the myriad complexity of H substitution mechanisms in olivine, it is also unsurprising that adequate fits to the data can be obtained by using different n and ΔV couples, such as reported by Yang (2016) for the data of their study and through Yang's analysis of the data for Kohlstedt et al. (1996) and Mosenfelder et al. (2006). As noted by Férot and Bolfan-Casanova (2012), the choice of $n = 1$ and the resultant 10 cm^3/mole as well as the choice of $n = 2$ and 23 cm^3/mole both equally fit the data, restricting any conclusions about dominant mechanisms. The OH annealing experiments of Yang (2016) reach the same conclusion. Yang (2016) found that all couples of n and ΔV fit the data, where ΔV values of 4.55, 11.58, and 25.63 cm^3/mol were obtained for n = 0.5, 1, and 2, respectively. Indeed, as stated by Ingrin et al. (2013), "the main problem in determining the n exponent from experiments at high-pressure is that data can be fitted by an infinite number of (n, ΔV^{solid}) couples." As noted by Mosenfelder et al. (2006), "the mechanism of hydrogen incorporation in olivine in the low-pressure experiments may be fundamentally different from that in high-pressure experiments," which can be seen in the data from Kohlstedt et al. (1996) where the OH infrared spectra for olivine incorporation at 0.3 GPa is notably different compared to the one above 2.5 GPa. If the incorporation mechanism varies with pressure, then the variables solved for at low pressure, particularly

the value of n, should not be extrapolated to higher pressures near 2.5 GPa. Since there is a strong correlation between pressure and gas fugacity, it is difficult to distinguish one influence from another.

These previous efforts do at least suggest that not all OH defects in olivine are due to Si vacancies ($4H^{+} = Si^{4+}$) or any other single mechanism. Until new research resolves this issue, it is possible to obtain equally good fits by either iteratively fitting n or arbitrarily selecting a value given sufficient other variables for tunability. Clearly, in the second approach, these other variables sacrifice physical meaning to accommodate the mathematical fit.

Unfortunately, there does not exist a sufficiently comprehensive dataset to strategically solve for each variable before solving for the next and again it is difficult to establish a value that has physical meaning. A further issue is that these experiments do not isolate incorporation mechanisms, but instead reflect the chemical activities of the system surrounding olivine. Indeed, competing effects that would otherwise on their own increase olivine solubility may be coupled. For example, it appears water solubility in iron-rich olivine is greater than that in pure forsterite due to the enhancing effect of iron (Zhao et al., 2004; Withers et al., 2011); yet in more chemically complex systems, the solidus will be depressed leading to a decrease in water activity in the surrounding melt. It is also highly unlikely that these separate incorporation mechanisms would have the same activation volume or enthalpy.

Despite the difficulty discerning the specific or multiple incorporation mechanisms of H in olivine, this information is not strictly necessary to effectively model solubility within existing studies. Although the correct choice of thermodynamic parameters remains ambiguous, it is still possible to develop empirical equations that adequately describe experimental observations and prove useful for prediction.

4.4 Model Results

4.4.1 Summary statistics and importance of silicate melt

The performance of a model depends strongly on the appropriate selection of data. It is first instructive to characterize the dataset by correlation testing. Summary statistics were collected from eleven previous literature studies and are shown in Table 4.1. A correlation scatter plot of selected variables from Table 4.1 with frequency histograms is given in Figure 4.1 and the matrices illustrated in Figure 4.2.

Table 4.1. Summary statistics for selected variables from previous experimental studies.

Variables	Total observations (n)	Minimum	Maximum
P (GPa)	63	0.5	13
T (°C)		1025	1700
D_H		0	0.026
H_2O Melt (%)		0.075	12
log fH_2O (GPa)		-0.235	5.673
H_2O in Ol (ppm)		0	1140

Data is from Koga et al., (2003), Aubaud et al., (2004, 2008), Grant et al., (2007), Hauri et al., (2006), Tenner et al., (2009, 2012), O'Leary et al., (2010), Novella et al., (2014), Rosenthal et al. (2015), and Adam, (2016).

As previously discussed in Chapter 2, several relationships become evident in Figure 4.1, such as the positive correlation of H_2O in olivine and pressure. There is also the expected positive correlation of H_2O in olivine with the theoretical pure water fugacity based on the Pitzer and Sterner EoS for water (Pitzer and Sterner, 1994, 1995). Interestingly, we see two diverging trends for the D_H values. As previously discussed in Chapter 3, these trends can be understood in terms of melt H contents, which will be explored further.

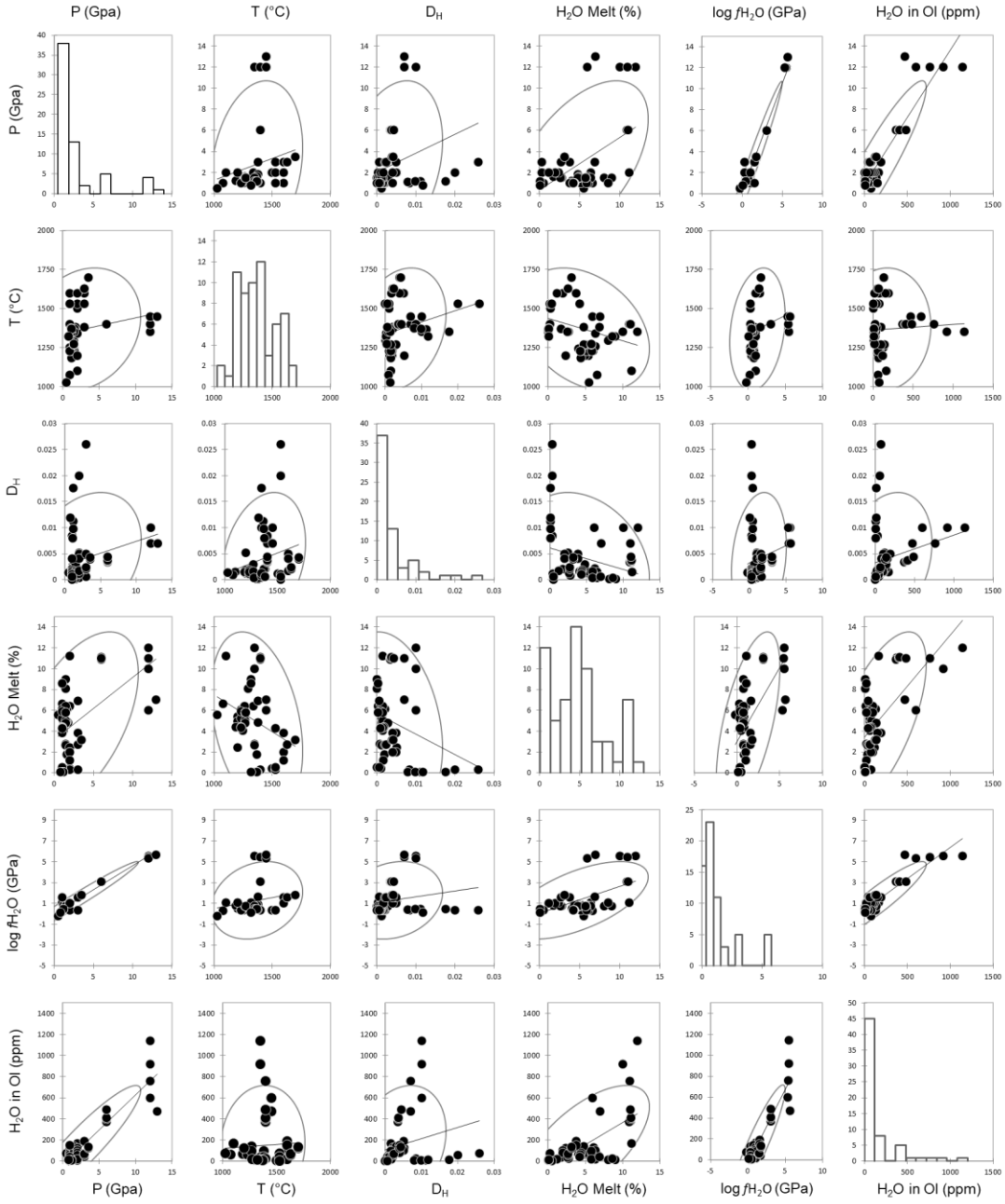

Figure 4.1. Correlation scatter plot of selected variables from Table 4.1 with frequency histograms. Additional statistics are reported in Tables A.1-4.

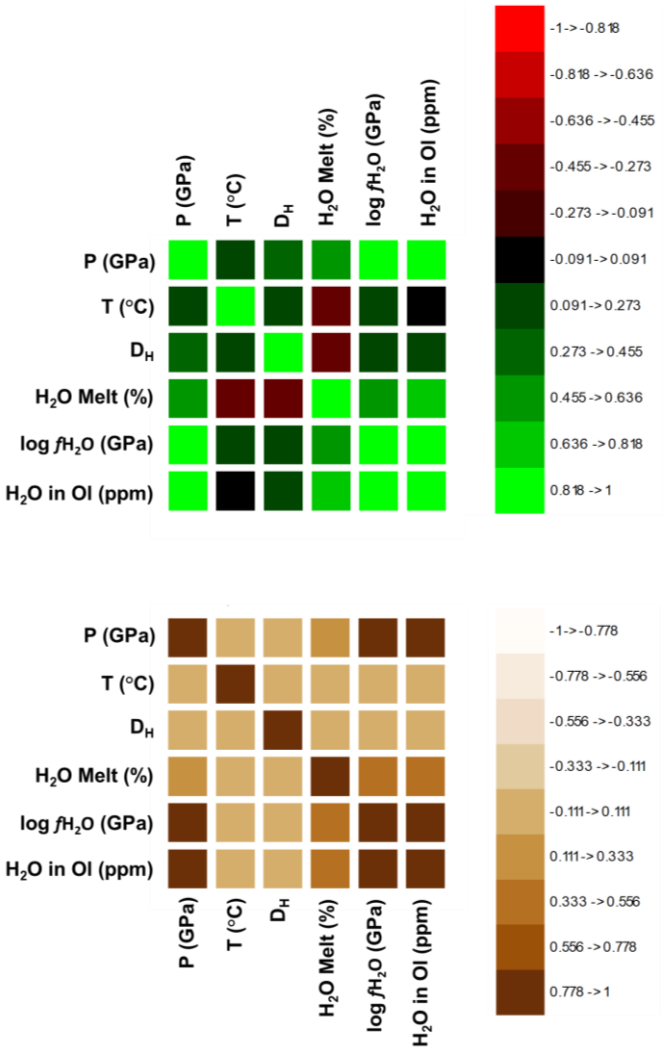

Figure 4.2. Top: image of the correlation matrix. Note that -1 indicates a negative, correlation between two variables, 0 indicates no linear correlation between two variables, and 1 indicates a perfectly positive linear correlation between two variables. For example, a strong correlation is readily apparent between H_2O in olivine and pressure, while a negative correlation is evident between temperature and H_2O in the melt

Bottom image: image of the matrix of coefficients of determination.

Further data is given in the appendix in Tables 1-4.

Similar to the analysis conducted in Chapter 3, we may consider the H_2O content of the melt against the partitioning value, and in terms of the initial bulk water content added to the experiment (Figure 4.3). As shown in Figure 4.3a, it is interesting to note that several experiments fall in line with the previously established D_H trend (Figure 4.3c) of the Martian samples from Chapter 3, including the single data point from Rosenthal et al. (2015) and several of the oxidized experiments from Chapter 2. A positive correlation between the olivine H_2O content and the D_H value becomes apparent when the initial water content is also considered (Figure 4.3d).

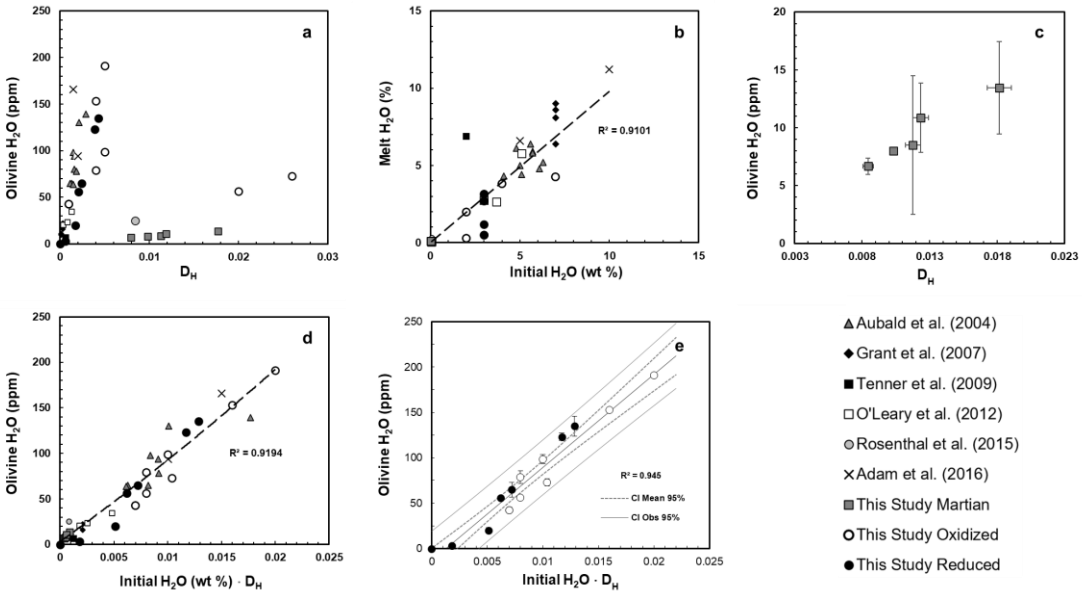

Figure 4.3. a) Olivine vs D_H, b) melt H_2O vs initial H_2O added to the experiment, c) correlation of olivine H_2O contents and D_H values for Martian experiments, d) trend for olivine vs initial H contents multiplied by D_H values for all experiments, e) olivine H contents vs D_H values for experiments conducted in Chapter 2. Note that B6 and B7 were excluded from the reduced data due to the large standard deviations in olivine H_2O concentration and lack of melt data.

In Figure 4.3e, given the R^2, 94% of the variability of the dependent variable (olivine H contents) can explained by the explanatory variable (initial H_2O contents of the experiment multiplied by the D_H value for olivine and melt). In addition to the R^2 value, further goodness of fit statistics are reported in Table A.5 of the appendix. The predicted olivine contents as shown in Figure 4.3e, as well as an example of the calculated and plotted confidence intervals on both the mean and the observations are provided in appendix Table A.6. Clearly, the information provided in the explanatory variable produces a significantly better model than what a basic mean (specifically, 74.012 H ppm with a standard deviation of 53.855 H ppm) would bring. The residuals also do not suggest a systematic bias in favour of the oxidized or reduced experiments. In Figure 4.4a, a regression is performed on the larger dataset following the

approach of Figure 4.3e and the 95% confidence interval is shown for both the observed data and the mean. Figure 4.4b plots the measured versus predicted values from the regression, which are in remarkably good agreement considering the nature of the data. For Figure 4.4, studies with insufficient data were excluded, while Tenner et al. (2012) was excluded due to the anomalously small melt fraction ranging from 0.04 to 0.1. (Indeed, the next step to this line of thought would be to include the melt fraction in the analysis. However, melt fractions are often unreported in papers. Estimating the melt fraction from published sample images is also impractical as it is often the case that only representative sample images are made available for select run products, which confines the dataset to very small number of points.) As evidenced by Figure 4.4, 93% of the variability of the H contents measured in olivine can be explained by considering the initial H_2O content multiplied by the D_H. These findings suggest that the D_H value is strongly influenced by the initial water content added to the experiment, which in turn strongly influences the resultant melt content.

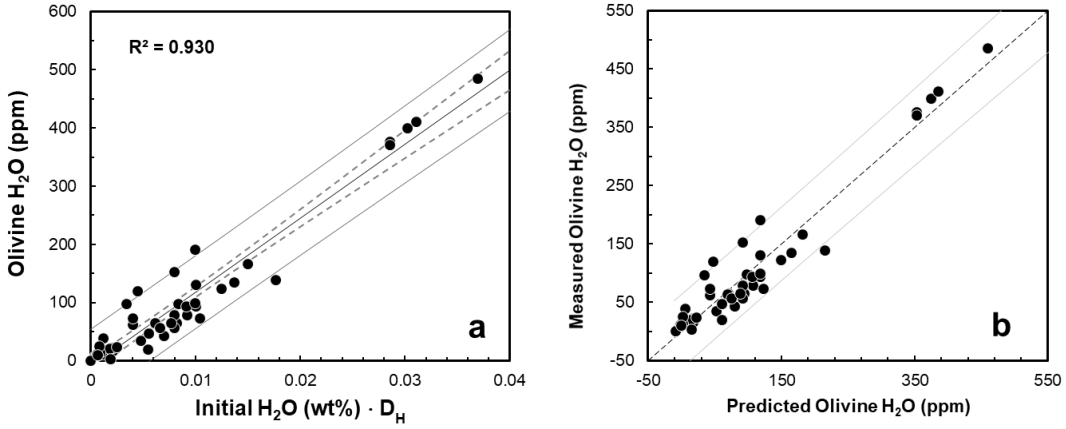

Figure 4.4. a) Regression of expanded data set ($n = 50$) following the approach of Figure 4.4e, b) comparison of measured versus predicted values.

4.4.2 Models of olivine solubility

The positive correlation of H in olivine with increasing Al has been observed by SIMS data from Hauri et al. (2006) and Férot and Bolfan-Casanova (2012), indicating that a reaction may take place according to Kröger–Vink notation,

$$H^{fluid} + Al^{fluid} + Si_T^X + O_O^X = Si^{fluid} + \{OH_O - Al'_T\} \quad (4.3)$$

where Si_T^X and Al'_T represent Si^{4+} and Al^{3+}, which occupy tetrahedral lattice sites, and O_O^X and OH_O are O^{2-} and $OH-$, respectively, occupying oxygen sites in olivine, and curly brackets indicate associated point defects (Kröger and Vink, 1956). However, SIMS work by Gaetani et al. (2014) observed a negative correlation ($R^2 = 0.348$) between Al and H contents for olivine in the raw data when all variables except Al were held constant. Gaetani et al. (2014) suggested that such an apparent negative correlation may reflect $a SiO_2$ overshadowing the [Al^{3+}] mechanism so that it became unresolvable. However, as noted by Tollan et al. (2018), "the Al concentrations in the olivines of these experiments are within the range of typical San Carlos crystals from the Cr-diopside suite, giving no reason to suppose that they were not the original concentrations, and not a reflection of $a SiO_2$." Varying $a SiO_2$ has multiple effects on the substitution mechanisms. An increase in $a SiO_2$ increases Mg vacancies but decreases Si vacancies, and further an increase in $a SiO_2$ is expected to promote the [triv] substitution and decrease [Ti] (Tollan et al., 2018). If $a SiO_2$ is controlled through buffering by magnesiowüstite or pyroxene, then it will also be variable with P and T. Similarly, fO_2 may have multiple effects. In highly reducing conditions the proportion of Cr^{2+}/Cr^{3+} and Fe^{2+}/Fe^{3+} will be drastically increased so that predominantly Al will be available for the [triv] mechanism.

Functional equations derived from thermodynamic descriptions have formed the basis of widely applied thermometers and barometers for volcanic systems (e.g., Putirka 2008). Indeed, as stated by Putirka, "the differentiation of 'empirical' and 'theoretical' is not always clear," and in fact the original enquiries in thermodynamics itself are founded on fundamentally empirical expressions. Therefore, the eqn. (4.1) may be restated as

$$C_{OH}^{olivine} = (T, P, fH_2O, fO_2, []) = Af_{H_2O}^{n}\, exp\left(-\frac{B}{T}\right) \exp\left(C\frac{fO_2}{T}\right) \exp\left(D\frac{[\,]}{T}\right)\ldots \quad (4.4)$$

where [] suggests any other variable influence that may be considered, such as $a\mathrm{SiO_2}$. The empirical form of the equation is highly preferred for the purposes of this Chapter as it prioritizes improved data fitting without erroneously assigning values that lack physical significance. Another consideration is the elegance and ease of implementation of the final equation. Jefferys and Berger (1992) simply state that "if a law has many adjustable parameters then it will be significantly preferred to the simpler law only if its predictions are considerably more accurate." A solubility model that requires many extensive (internal energy, entropy, volume, or number of particles) or intensive (pressure, temperature, chemical potential) parameters is also undesirable. Therefore, this study attempts to use the minimum number of necessary variables to adequately describe olivine solubility. To this end, data (in order of presentation) from Yang (2016), Gaetani et al. (2014), Withers and Hirschmann (2008), Grant et al. (2007a), Withers et al. (2011), Zhao et al. (2004), Kohlstedt et al. (1996), Aubaud et al. (2004), Hauri et al. (2006), Grant et al. (2006), Withers and Hirschmann (2008), Bali et al. (2008), Tenner et al. (2012), Férot and Bolfan-Casanova (2012), and Ardia et al. (2012) were all fit to eqn. (4.1) and then to eqn. (4.4) with necessary variables added till an acceptable fit could be achieved. Results are shown in Figures 4.5-11. For

Figures 4.5-11, if reported, error bars for the measured values are taken from the original publications.

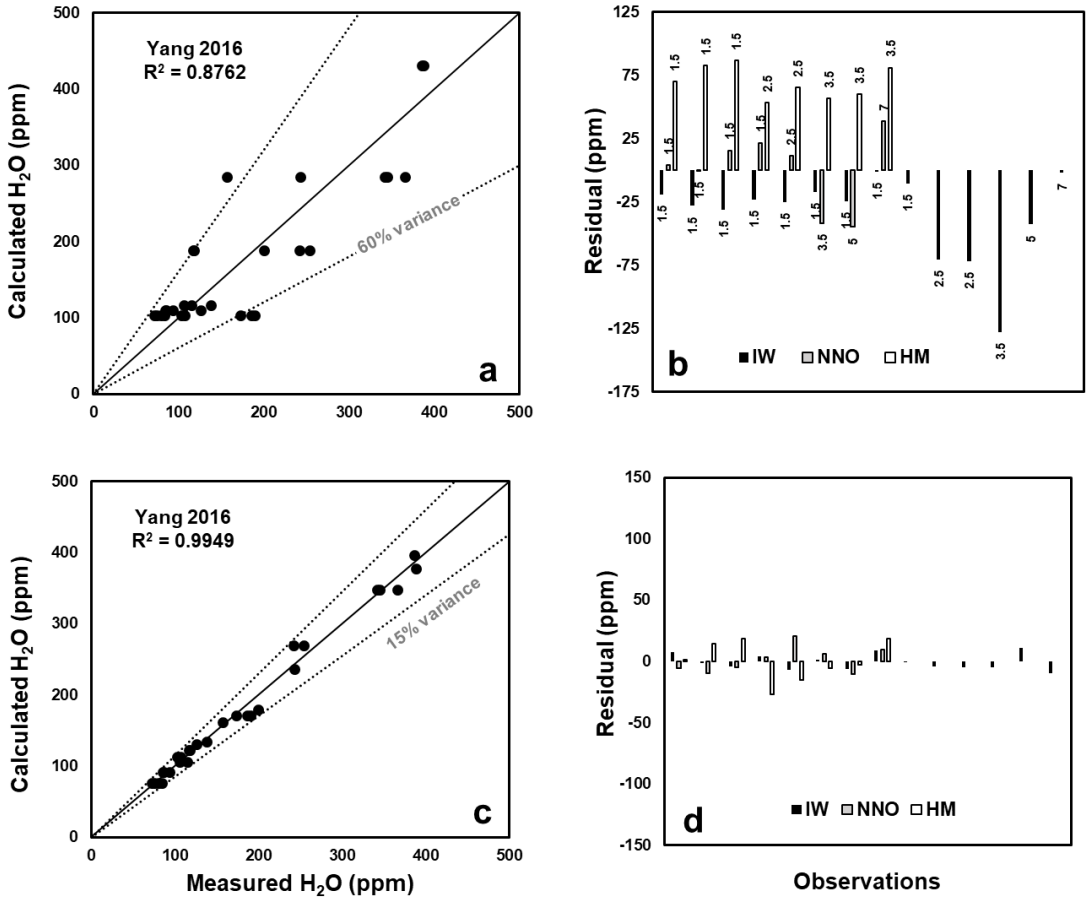

Figure 4.5. Comparison of measured water solubilities in olivine (ppm) and water solubilities predicted by thermodynamic calculation for Yang (2016). a) the solubility calculated without considering fO_2 with b) showing the systematic underestimation and overestimation according to redox buffer (IW, NNO, and HM) with pressure noted. Both c) and d) show a significantly improved model when accounting for fO_2.

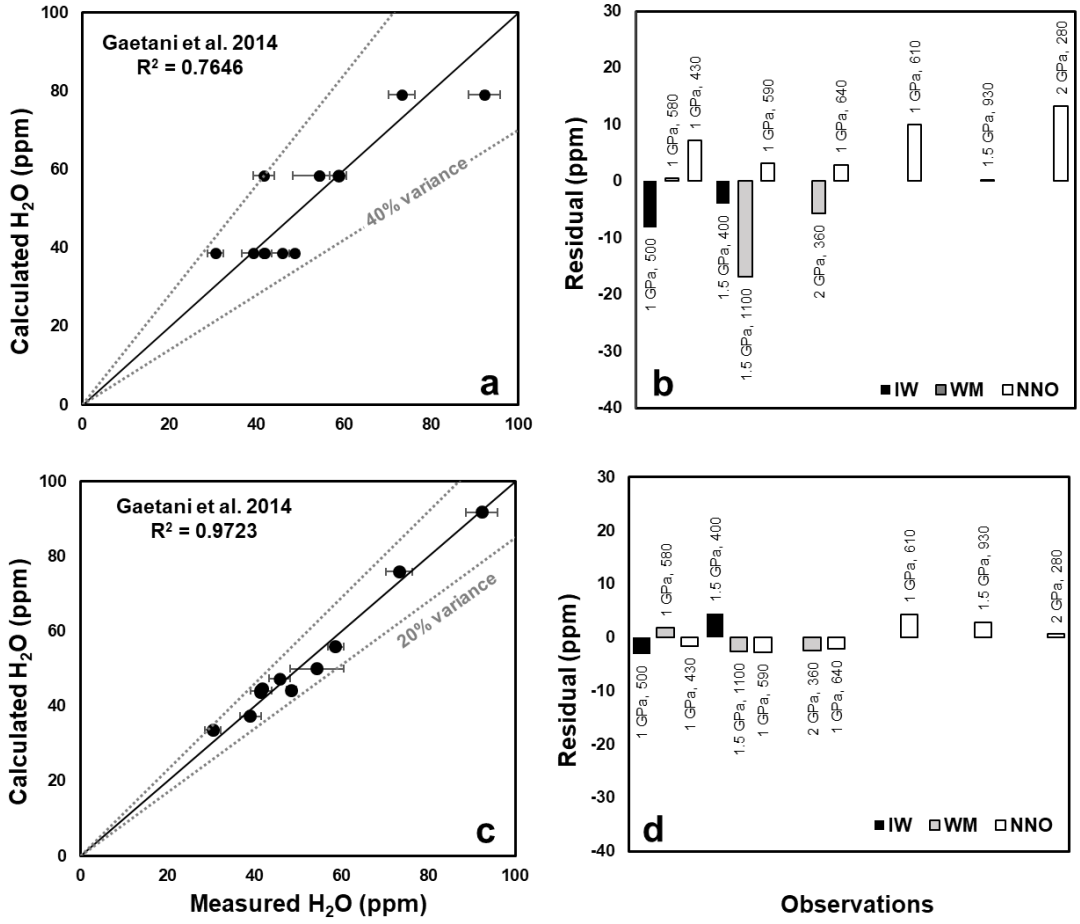

Figure 4.6. Comparison of measured water solubilities in olivine (ppm) and water solubilities predicted by thermodynamic calculations for (Gaetani et al. 2014). a) the solubility calculated without considering fO_2 and olivine Al (10^6 Si) content with b) showing the systematic underestimation and overestimation according to the buffer redox (IW, WM, NNO) as well as the run pressure and olivine Al (10^6 Si) contents. Both c) and d) show a significantly improved model when accounting for fO_2 and olivine Al (10^6 Si) content.

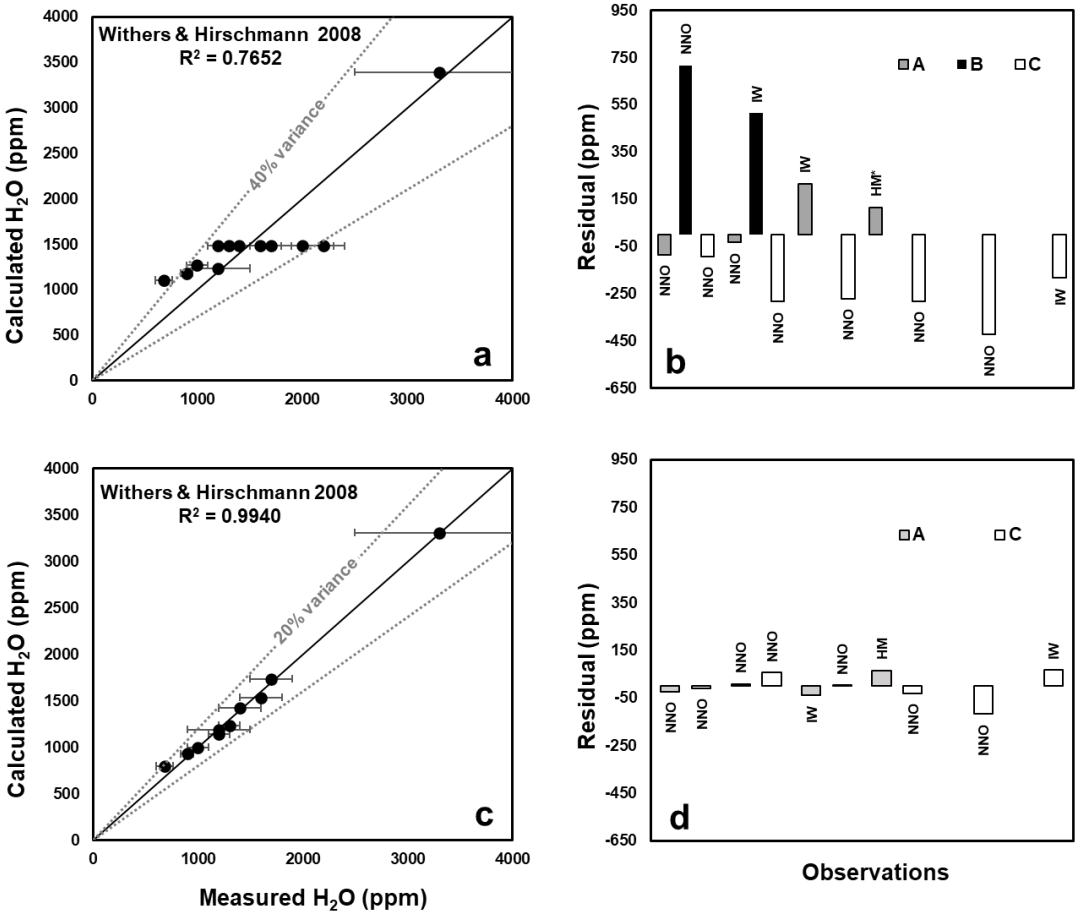

Figure 4.7. Comparison of measured water solubilities in olivine (ppm) and water solubilities predicted by thermodynamic calculations for Withers and Hirschmann (2008). Note that A, B, and C represent different starting compositions. a) the solubility calculated without considering fO_2 and olivine Al_2O_3 content with b) showing the systematic underestimation and overestimation according to the starting composition as well the redox buffer (NNO, HM, IW). Both c) and d) show a significantly improved model for the runs with olivine and pyroxene when accounting for fO_2 and the composition of the buffering pyroxene. Note that for M287 pure Fe_2O_3 oxidant was added to experiment and fO_2 was estimated to be near the HM buffer.

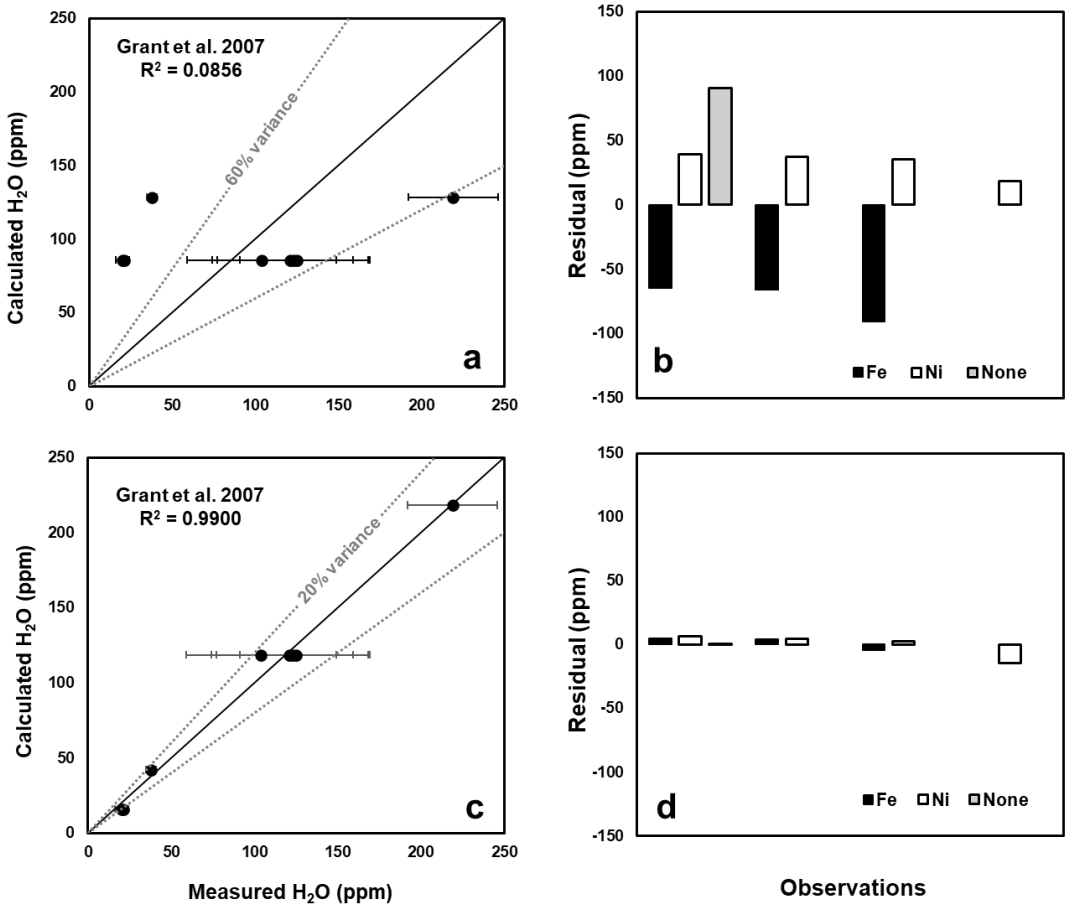

Figure 4.8. Comparison of measured water solubilities in olivine (ppm by weight) and water solubilities predicted by thermodynamic calculations for Grant et al. (2007b). a) the solubility calculated without considering fO_2 with b) showing the systematic underestimation and overestimation according to the metal foil used to buffer redox (Fe, Ni, or none used). Both c) and d) show a significantly improved model when accounting for fO_2.

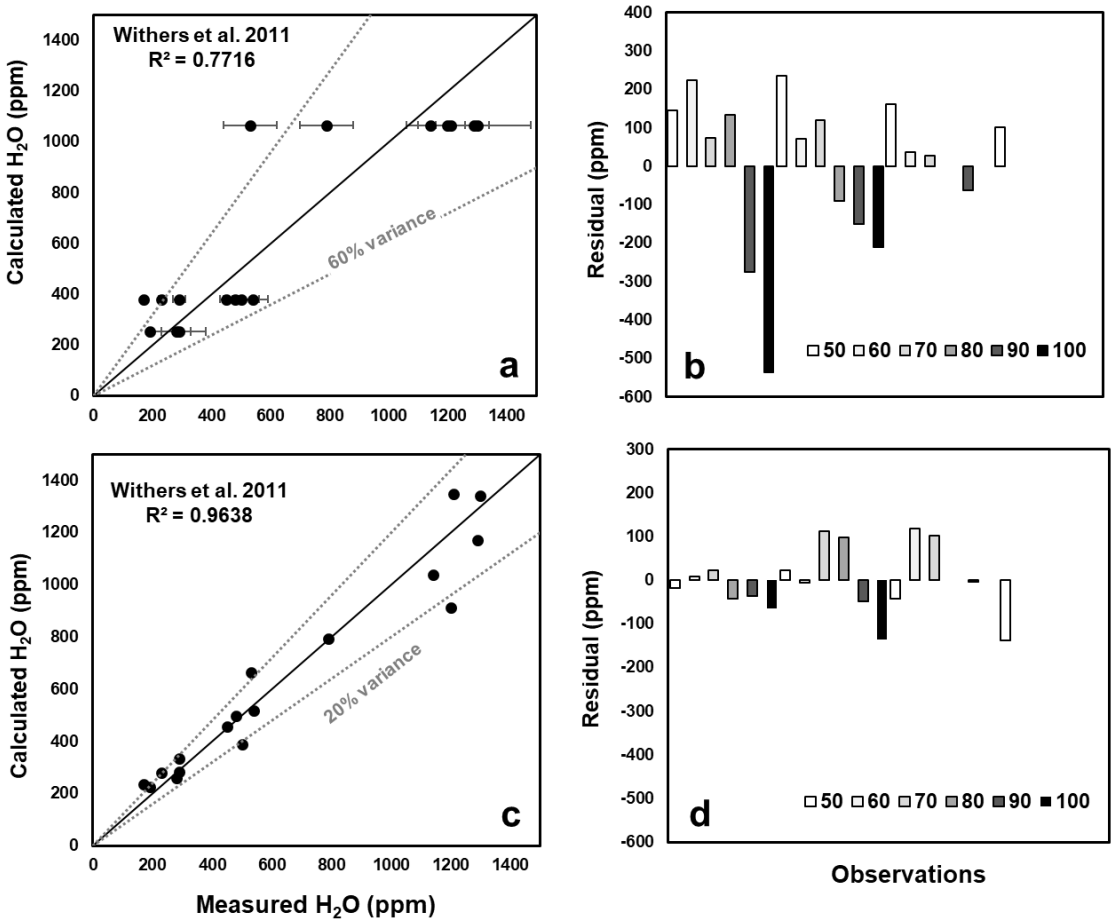

Figure 4.9. Comparison of measured water solubilities in olivine (ppm by weight) and water solubilities predicted by thermodynamic calculations for Wither et al. (2011). a) the solubility calculated without Mg number with b) showing the systematic underestimation and overestimation. Both c) and d) show a significantly improved model when accounting for the Mg number. Note that run B220 was not included due to the large difference in water contents measured at the top and bottom of the experiment. Note that runs in this study with supposedly the same conditions produced statistically significant different results, which suggests either an unaccounted for variable or large experimental or analytical uncertainty.

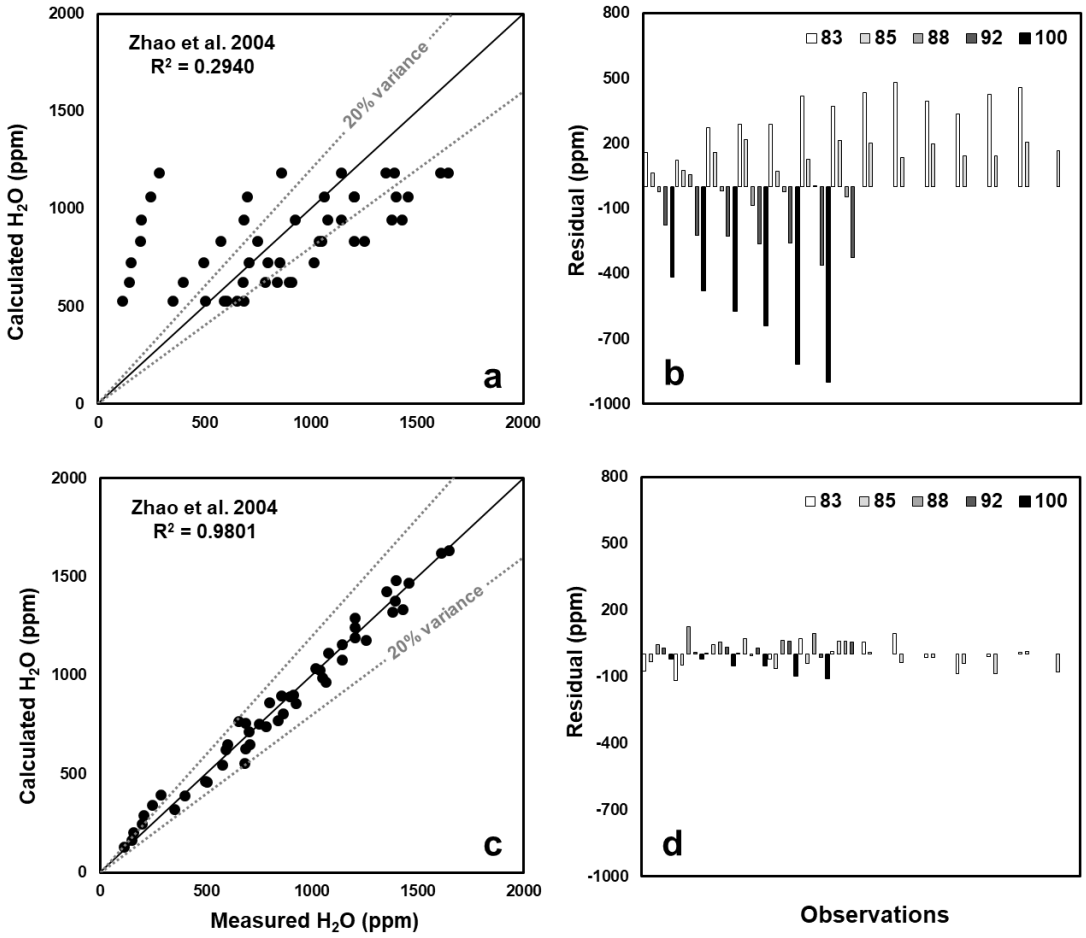

Figure 4.10. Comparison of measured water solubilities in olivine (ppm by weight) and water solubilities predicted by thermodynamic calculations for Zhao et al. (2004). a) the solubility calculated without Mg# with b) showing the systematic underestimation and overestimation. Both c) and d) show a significantly improved model when accounting for Mg number, however, Mg100 is still systematically underestimated.

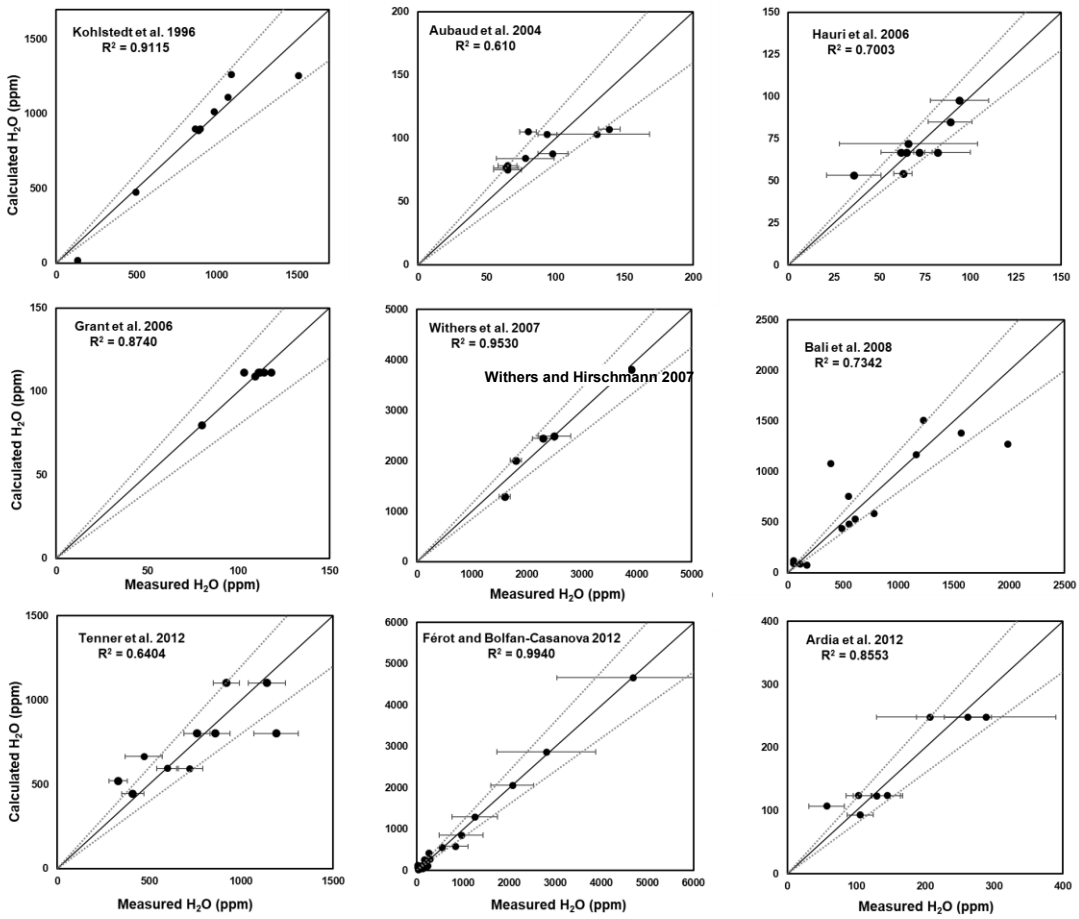

Figure 4.11. Comparison of measured water solubilities in olivine and predicted water solubilities for previous literature studies, including Kohlstedt et al. (1996), Aubaud et al. (2004), Hauri et al. (2006), Grant et al. (2006), Withers and Hirschmann (2007), Bali et al. (2008), Tenner et al. (2012), Férot and Bolfan-Casanova (2012), Ardia et al. (2012).

4.5 Discussion and conclusion

As shown in Figures 4.5-4.11, with perhaps the exception of Bali et al. (2008), all previous studies can be adequately parameterized with semi-empirical equations given the reported experimental variables. Therefore, the solubility of H is decipherable within the context of these experiments and their respective analytical procedures.

However, one encounters severe difficulty when attempting to develop an equation that behaves appropriately for the entire published dataset, which is likely due to interlaboratory discrepancies, and hidden and unaccounted for variables between and within experiments. In the scope of data science, the available studies on H in olivine comprise a relatively limited dataset that presents many unique challenges. How can one be sure which data are genuinely erroneous, since outliers could simply reflect the effects on solubility marked by unrecorded changes in experimental design, such as changes in chemical activity, volatile activity, bulk composition, or crystal chemistry? Furthermore, many of the high-pressure/high-temperature devices used in these experiments are custom built and non-standardized. As previously discussed, this dataset is comprised of both synthesis, annealing, and hybrid experiments that have had H contents appraised by different methods (FTIR versus SIMS) at different laboratories. Rigorous statistical methods are infrequently applied in experimental petrology. Due to the nature of experimental petrology, it is rarely feasible to adhere to standards set in other quantitative laboratory fields. For instance, it is often not cost-effective or standard practice to run experiments in triplicate under the same conditions, or subject results to outlier tests. Without rigorous error reporting (e.g., both variance of experimental results and analytical uncertainty of measurements), it is difficult to apply meaningful weights to the dataset. While the data within studies appears internally consistent, the extent to which the entire dataset

can be considered consistent is dubious at best. In light of these considerations, it is unlikely that the entire dataset can be explained by a single, imaginary, theoretically defined model. Indeed, if the data were made to exhibit such a fit, it would raise questions about overfitting and physical relevance, given the quality of the data and dispersion. Supposing a model were made to fit this dataset, systematically separating the data into training and testing datasets represents another challenge due to a lack of consistency across the data; whatever data happens to be arbitrarily selected in training or testing will severely bias the model. To summarize, due to inherent issues with data quality and standardization, there is essentially no method to construct a model that provides a conventionally good fit without overfitting. Rather the objective of analysing the complete dataset should be, as described by Bédard (2014), "to generate an equation that passes a line through the main data cloud," and provide a starting point for further inquiry. It is also worth questioning the utility of an equation which fits numerous variables that may not even be known in the context of planetary modelling, especially when there is apparently a strong parameterization based on fH_2O or pressure alone, particularly when the melt H contents are considered. As shown in Figure 4.12, 77% of the variability of H in olivine (ppm) is explained by log fH_2O, which is significantly better than what a basic mean would achieve. The majority of datapoints fall within the 95% confidence interval except for three datapoints.

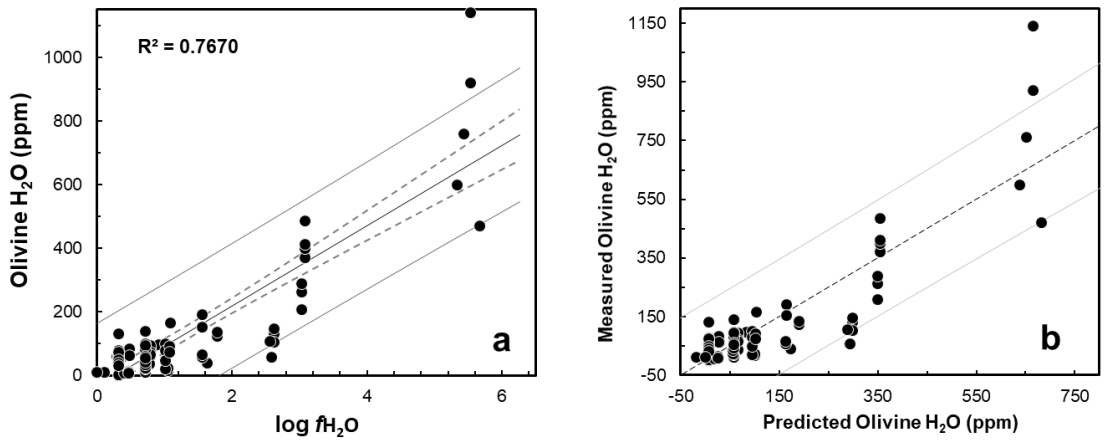

Figure 4.12. a) Regression of expanded dataset ($n = 81$). b) Comparison of measured versus predicted values. The data is from Koga et al., (2003), Aubaud et al., (2004), Grant et al., (2007), Hauri et al., (2006); Tenner et al., (2009, 2012); O'Leary et al., (2010); Ardia et al. (2012), Novella et al., (2014), Gaetani et al. (2014), Rosenthal et al. (2015), and Adam, (2016).

This suggests using a parameterization based on log fH_2O as a useful first approximation,

$$H\ in\ Ol\ (ppm) = 126.026 \cdot log\ (f_{H_2O}) - 32.882. \quad (4.5)$$

where additional statistics are reported in Table A.7. However, it should be noted that fH_2O is an inferred quantity based on P-T rather than directly measured; it is not controlled as an independent variable. No study included here attempted to systematically evaluate the effect of varying fH_2O independent of the total pressure or attempt to estimate the actual fugacity (as opposed to this calculated theoretical pure fugacity) of the gas/fluid mixture within the experiment. It may well be the case that such an adjusted true fH_2O more accurately describes the H solubility within olivine.

A second approach involves applying the nonlinear regression method using eqn. (4.4), which yields the parameterization,

$$H\ in\ Ol\ (ppm)\ =\ 0.169 \cdot f_{H_2O}\ \cdot\ exp\left(-1 \cdot \left(\frac{8.89E(-03)*P-81511.360}{RT}\right)\right)\ exp\left(\frac{1536.865*fo2}{RT}\right) exp\left(\frac{-76.79*Mg\#}{RT}\right). \quad (4.6)$$

While the nonlinear fit method does more accurately capture the behaviour of the data, it also requires two additional variables regarding the thermodynamic environment surrounding the olivine (fO_2 and magnesium number in addition to P, T), while the simple correlation requires only P and T to calculate fH_2O according to the EoS. Figure 4.13 shows the results using eqn. (4.6) and additional statistics are reported in Table A.8. It should also be noted that the nonlinear model offers superior performance at very low H concentrations where an estimation using eqn. (4.5) may predict negative concentrations. Regardless, both models would significantly benefit from an expanded fH_2O data set as well as more data at both high H contents and very low contents. It is apparent that modelling based on the current dataset is subject to limitations due to the difficulty in separating the effect of fH_2O from the intrinsic pressure-volume term. Future studies should seek to control fH_2O as an independent variable at constant pressure and temperature, which will allow for greater insight into microscopic incorporation mechanisms and provide the basis for more robust empirical models.

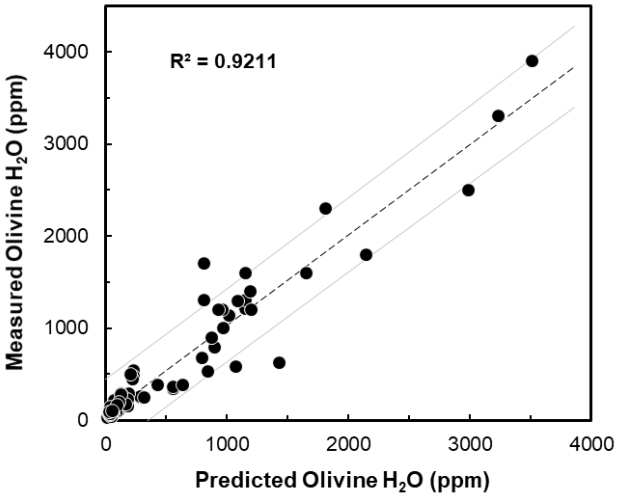

Figure 4.13. Results from nonlinear fit of expanded dataset ($n = 108$) with data from Koga et al., (2003), Aubaud et al., (2004), Grant et al., (2007b), Withers and Hirschmann (2007), Withers et al. (2008, 2011), Hauri et al., (2006); Tenner et al., (2009, 2012); O'Leary et al., (2010);

Chapter 5

Preservation of Organic Compounds Under Simulated Sub-Surface Conditions: Implications for Early Life and Mars

In collaboration with

Claire Cousins (providing samples)

Wren Montgomery (conducting py-GC-MS analysis)

"Who cares about germs or viruses or bare organic remnants halfway to life but never making it?

Astronomers and biologists do!"

Isaac Asimov
Mars, We Love You, Pyramid (1973)

5.1 Abstract

Due to the largely inhospitable surface environment of Mars, if biotic evidence does exist it likely resides hidden in the subsurface. Martian subsurface conditions provide sufficient protection from harmful radiation and the geothermal gradient may even accommodate liquid water. In order to effectively search for evidence of life on Mars, and accurately interpret data from future missions, it is vital to understand the effect of subsurface conditions on the preservation of biosignatures and other organic compounds. Detailed organic chemical analysis is necessary to determine the preservation potential of biosignatures in the Martian subsurface/geosphere. Experimental studies of the interactions between bio-organics and minerals under conditions simulating the harsh Martian environment provide key insights into possible prebiotic processes and the search for life. Despite protection from UV and oxidative degradation, buried biosignatures may undergo diagenetic processes that decrease the concentration of organic matter as well as other degradation mechanisms resulting from elevated temperatures, pressures, and mineral-organic interactions. The aim of this study is to experimentally determine whether biosignatures can survive burial, metamorphism, and diagenetic events at various Martian metamorphic facies. A drill is planned in the forthcoming ExoMars rover mission to access such subsurface environments. Minerals may have played a crucial role in the hypothetical origin and evolution of microbial life on Mars as well as its potential preservation. The survival of molecular biosignatures likely depends on a precarious balance between a number of preservation and degradation mechanisms. These mechanisms are governed by multiple variables (e.g., radiation exposure, chemical environment, reaction kinetics, and temperature), but may be regulated by mineral matrices. Experimental studies of the interactions between bio-organics and minerals under conditions simulating the harsh

Martian environment provide key insights into possible prebiotic processes and biosignature preservation. The aim of this study is to experimentally determine whether organic compounds and biosignatures of life can survive burial, metamorphism, and diagenetic events at various Martian metamorphic facies. Results will inform future *in situ* searches for life on Mars as well as the interpretation of organic analyses from past missions.

Keywords: Mars, Organics, Biosignatures, Subsurface, Gas-chromatography Mass Spectrometry, Carbonates, Endoliths, Microbes, Cyanobacteria

5.2 Introduction

Carbonates have been detected on Mars in ancient terrains by orbital remote sensing (Ehlmann et al., 2008; Wray et al., 2016) in high latitude sediments near the Phoenix landing site (Boynton et al., 2009), in carbonate-bearing deposits in the Jezero crater and in the Jezero delta (Goudge et al., 2015; Horgan et al., 2019), and identified in outcrops by the Mars Exploration Rover Spirit (Morris et al., 2010). Further carbonates may also exist in environments unexplored by rovers (Ehlmann et al., 2008; Michalski and Niles, 2010). Carbonates on Mars represent a high priority target for future rover exploration missions to search for signs of extinct and extant life and cache samples for eventual return. The ancient lacustrine environment at Jezero Crater has been selected as a site for investigation for the Mars 2020 *Perseverance* rover. The goals of Mars 2020 include assessing past habitability and biosignature preservation potential, searching for potential biosignatures, and assembling a cache of samples that may one day be returned to Earth by a future mission (Grant et al., 2018). Mg-carbonate deposits represent high priority targets due to their high potential for

preservation of biosignatures and because their isotopic composition could serve as a record of atmospheric loss on Mars (Hu et al., 2015). Developing strategies to search for and identify biosignatures in carbonates has implications for maximizing the scientific return of future missions to Mars, including Mars 2020 and the 2022 ExoMars Rover.

If molecular biotic evidence does exist on Mars, then it is likely preserved within or below the crust where it would be protected from surface radiation and photolytic decomposition (Cockell, 2016; Rostel et al., 2020). For extant biotic evidence to be detectable today, it may need to survive in some form on the timescale of billions of years without degrading or evolving to an organic profile indistinguishable from abiotic organic sources. A schematic of the preservation potential for various classes of organic compounds is shown in Figure 5.1. The combined effects of UV radiation and oxidative stresses on such timescales would likely have destroyed or degraded biosignatures beyond recognition as such (Dartnell, 2011; Hassler et al., 2014). A drill is planned in the forthcoming ExoMars 2022 rover mission to access such subsurface environments (Vago et al., 2017). Recently exposed surfaces may still contain previously protected organic material, such as relatively fresh impact ejection sites (Montgomery et al., 2016).

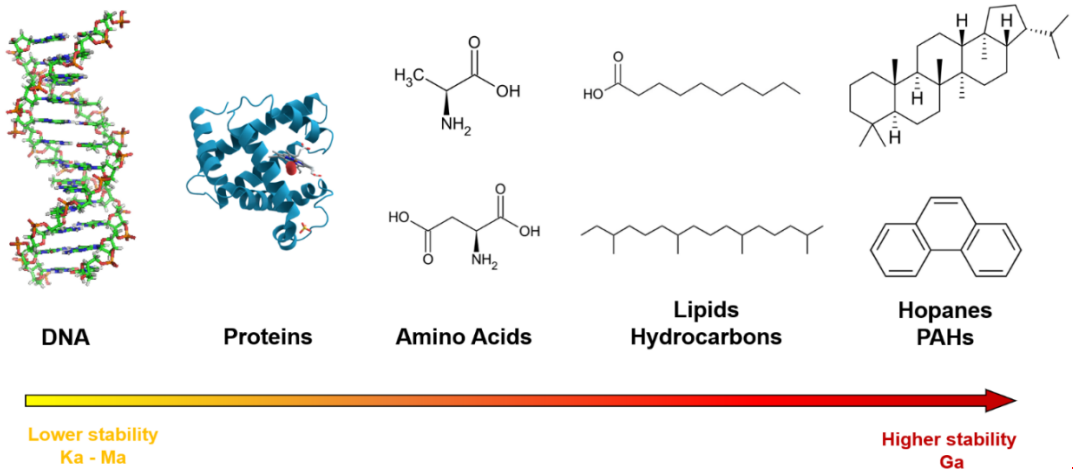

Figure 5.1. Illustration of preservation potential of several potential biomarkers in Ka (thousand years) to Ga (billion years).

Another barrier to biomarker preservation is oxidative degradation. The highly oxidized layer at the surface of Mars originates from interactions between the regolith, the atmosphere, and UV radiation (Yen et al., 2000; Zent et al., 2008). Constraining the extent of oxidation-driven reactions on the surface is an ongoing research topic. A highly oxidizing layer is expected to exist as a result of UV radiation penetrating the Martian regolith to a depth of 0.5-1 mm, with a mildly oxidizing layer existing from 1.5-200 m (Lasne, 2016). Diffusion models of oxidative conditions on Mars suggest that an unoxidized layer may exist past a depth of 200 m (Zent, 1998; Lasne, 2016). Therefore, if biosignatures do exist at subsurface conditions, they are likely less impacted by oxidative degradation. As previously noted, ExoMars will employ a core drill intended to recover oxidant-free samples down to a depth of 2 m.

Despite being shielded from UV and oxidative degradation, buried organics may undergo diagenetic processes that could decrease the concentration of intracrystalline organic matter as a result of the partial destruction and alteration of the mineral matrix (Benner et al., 2000) and may experience other degradation mechanisms as a result of elevated temperatures, pressures, and mineral-organic interactions. In aqueous environments,

carbonate precipitation has been recognized as an efficient mechanism for morphological biosignature preservation (Farmer and Des Marais, 1999). While micromorphology may potentially be used to distinguish biotic from abiotic carbonates (D'Elia et al., 2017), carbonates experience significant loss of primary microfabric and destruction of fossil evidence due to pervasive recrystallization during diagnosis (Farmer and Des Marais, 1999). Therefore, molecular biosignatures may become increasingly important indicators of life under such sub-surface conditions.

Models of meteoritic influx to Mars suggest that significant amounts of carbonaceous meteoritic materials should be present in the Martian regolith (Bland and Smith, 2000). Secondary carbonate minerals formed in an aqueous environment and polycyclic aromatic hydrocarbons are preserved in the 4.1-billion-year-old meteorite Allan Hills 84001 (ALH84001), which is the oldest known sample of the Martian crust (McKay et al. 2009; Thomas-Keprta et al. 2009; Halevy et al. 2011). Theoretical studies on mineral matrices suggest that a carbonate matrix may offer superior protection to embedded prebiotic matter from thermal stresses when compared to silicates or limestone (Bisceglia et al., 2017). Therefore, mineral-organic matrix interactions are critical to understanding the preservation of biosignatures. Evidence that organic compounds, including hydrocarbons, exist at high-temperatures and pressures in natural geological matrices is confirmed by the extraction of organic compounds from metamorphic and intrusive rocks by various studies (e.g., Shock et al., 2019).

In general, organic matter analysed from a geologic environment can fall into three categories: abiotic compounds that are not associated with biological organisms, biogenic compounds produced by biological organisms, and thermogenic compounds derived from the thermal decomposition of biologically generated compounds undergoing diagenetic processes (McCollom and Seewald,

2007). A general outline of such biotic and abiotic classes is illustrated in Table 5.1 with Group 1 representing compounds most useful to assess recent life processes, Group 2 showing compounds useful to assess biosynthesis in prior geological times, and Group 3 listing abiogenic/abiotic organic compounds that are expected to be ubiquitous regardless of origin. The report of the Mars 2020 Science Definition Team (Mustard et al., 2013) states that "the scientific significance of any potential sign of past life comes not only from the probability of life having produced it, but also from the improbability of non-biological processes producing it." Therefore, it is critical that biosignatures used to evidence past or present life on Mars are not only biogenic or thermogenic, but discernible from abiotic compounds despite significant diagenetic or fluid alteration processes.

Table 5.1. Summary of biotic and abiotic groups for various compounds

Compound class	Common biotic source
Group 1: Compounds to assess recent life processes	
Nucleotides, bases, etc.	All life
L-Amino acids/peptides	All life
Proteins	All life
Biopolymers	All life
Sugars/polysaccharides	Flora (some fauna)
Group 2: Compounds to assess biosynthesis in prior geological times	
Aliphatic hydrocarbons	Ubiquitous/not specific
Aliphatic acids, alcohols	Ubiquitous/some specific
Lipids	Ubiquitous/some specific
Isoprenoids	Biogenic
Steroids	Flora/fauna
Triterpenoids	Flora/microbes
Diterpenoids	Flora/microbes
Pigments	Flora/microbes
Biopolymers	Flora/microbes
Hopanoids	Biogenic
Group 3: Abiogenic organic compounds	
D/L-Amino acids	Abiotic
Aliphatic alcohols, acids, hydrocarbons	Abiotic
PAHs	Abiotic

Another complication for identifying biosignatures in Martian samples is the potential organic contribution from abiotic sources. For example, meteorites and asteroids may host a rich diversity of organic compounds (Chyba and Sagan, 1992) and *in situ* processes may produce lipids via Fischer–Tropsch type synthesis (e.g., McCollom and Seewald, 2007). In such complex environments, careful contextual evaluation of biologically and abiotically derived organic matter is essential to identify true biosignatures. Characterization of organic compound types, particularly the identification of which functional groups dominate under various mineral facies, is currently extremely limited (e.g., Orcutt et al. 2019), especially in the context of differing geological matrices. It has been established that organic molecules degrade via various chemical and physical processes, including thermal degradation, mineral-mediated oxidation, and photolysis (Bada et al., 1995; Bada and Lazcano, 2002; ten Kate et al., 2005; Marshall-Bowman et al., 2010). Ancient organic compounds preserved in geological material, especially in Archean rocks, are influenced by various variables over geological time, such as changing temperature and pressure conditions, which may lead to a loss of important source information (Brocks and Summons, 2003). There have been several studies simulating surface conditions. For instance, under simulated Martian surface conditions calcite provides improved protection to biomolecules purine, pyrimidine, and uracil against UV photolysis when compared to organic compounds subjected directly to photodegradation (Ertem et al., 2017). Assessing the evolution of organic molecules in subsurface environments has significant implications for evaluating plausible scenarios for the origins of life and improved targeting of biomarkers and organic compounds during missions.

In this study, I seek to constrain the preservation potential of various molecular biosignatures and organic species in natural endolithic carbonate

under subsurface conditions. A secondary sample of cyanobacteria necromass was also studied for comparison and to better generalize results. Experimental simulation to replicate key features of the Martian subsurface is required to better understand potential mineral-organic reaction pathways. Pyrolysis gas chromatography-mass spectrometry (Py-GC-MS) and solvent/liquid extracted GC-MS data was obtained for the untreated and treated samples. Pyrolysis accesses both the soluble and insoluble organic matter contained within the whole rock and is suitable for more thermally matured organic materials. However, pyrolysis may alter or degrade molecular structures. For whole rock samples the mineral surfaces may act as catalysts to rearrange or increase other alteration products. Liquid injection GC-MS offers the advantage of greater sensitivity via sample reduction and the retention of highly volatile or thermally fragile compounds. Therefore, both sample introduction methods were employed in this study. Comparisons of the material before and following the experiments reveal how the overall organic profile and specific biosignatures respond to temperature, pressure, and experimental duration. Experiments were performed under various pressure and temperature conditions up to 1.5 GPa and 600 °C.

5.3. Experimental and analytical methods

5.3.1 Starting materials

A microbial-rich natural Mg-calcite (calcium carbonate with minor amounts of clay and silica) deposited from a CO_2-rich hot spring acted as the starting material. Samples were provided by Claire Cousins and are similar to those collected from Spitzbergen, Svalbard, during the Arctic Mars Analog Svalbard Expeditions from 2006-2011 (Starke et al., 2013). Visible green and orange endoliths embedded within the sample ensured that the material is

sufficiently bioorganic. The use of such natural samples allows for a more realistic view of natural processes and the chemical evolution within the matrix as opposed to spiking minerals with chemical standards. The total organic carbon (TOC) and nitrogen (N) contents of the samples were assessed for both the regions with evident endoliths (microbe-rich) and regions without (microbe-poor) as shown in Figure 5.2. The whole rock samples were carefully cored using a 6 mm diamond core drill. All samples were approximately 0.5-0.8 g. A second starting material containing dried cyanobacterial necromass of anabaena cylindrica embedded within a solid sodium silicate matrix was prepared. To dry the sample, the mixture was dehydrated in an oven at 200 °C overnight.

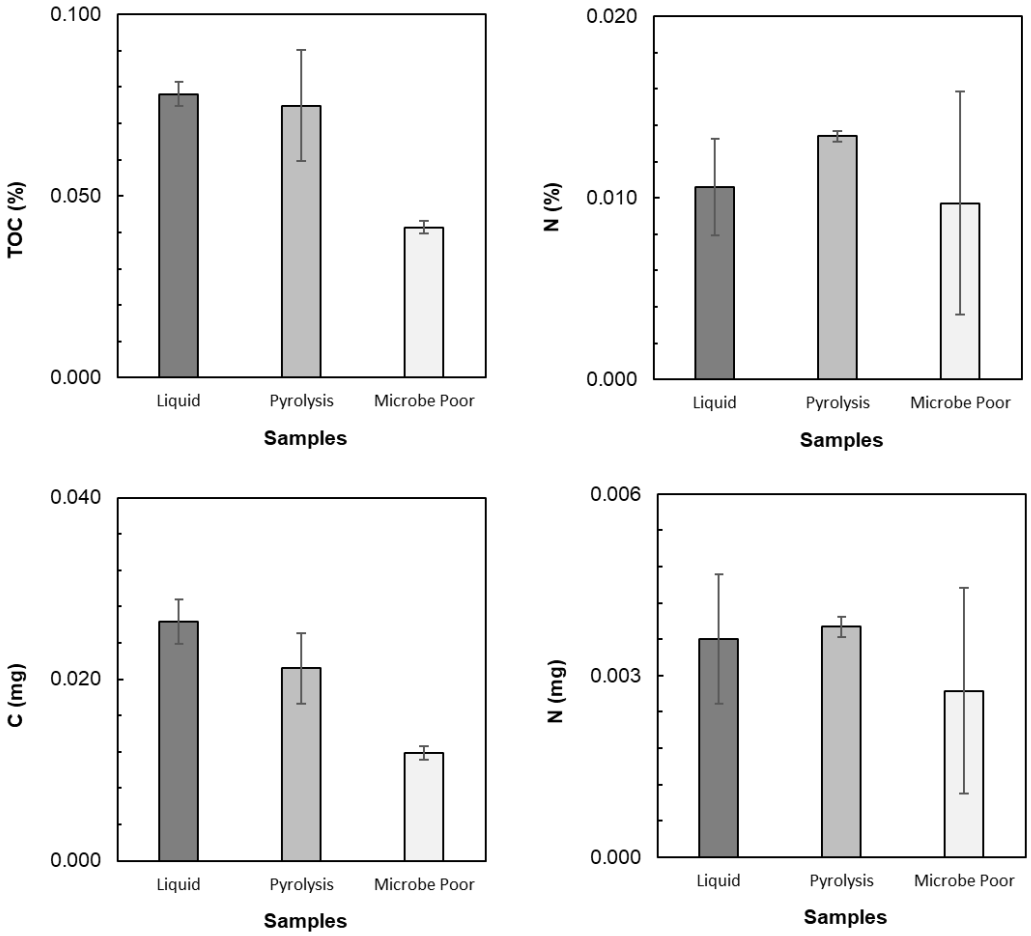

Figure 5.2. Total organic carbon (TOC) in % and mg and nitrogen in % and mg for sample batches analysed by liquid injection GC-MS and pyrolysis GC-MS as well as the microbe poor control samples. The TOC (non-carbonate) indicates the total amount of organic matter present, where a TOC below 0.5% is relatively carbon poor as found in these samples. Similarly, the samples have a very low nitrogen content (<0.5%). A carbon and nitrogen poor scenario is relevant to the search for biosignatures which may exist in trace amounts.

5.3.2 XRD characterization

The carbonate starting material was ground to a fine powder and analysed with X-ray diffraction (XRD) at The University of Edinburgh using the Bruker D8 Advance with Sol-X Energy Dispersive detector. Results were analysed using the Bruker Diffrac.EVA software in combination with the International Centre for Diffraction Data (ICDD) database. As shown in Figure 5.3, the carbonate starting material is primarily calcite with minor

amounts of clay and quartz. In order to monitor mineral degradation, the material was re-analysed by XRD. The decomposition of calcite initiates at a slow rate and then rapidly decomposes above 750 °C (Karunadasa et al., 2019). The mineral matrix, consisting predominantly of calcite, is expected to be stable at the temperatures of this study and under the stabilizing effect of high-pressure conditions. Degradation was monitored by XRD since the matrix is a complex natural system with low amounts of both organic and inorganic impurities. No significant degradation took place at any temperature (110-550 °C) in the furnace experiments with the sample only decomposing at 600 °C after two hours in ambient conditions.

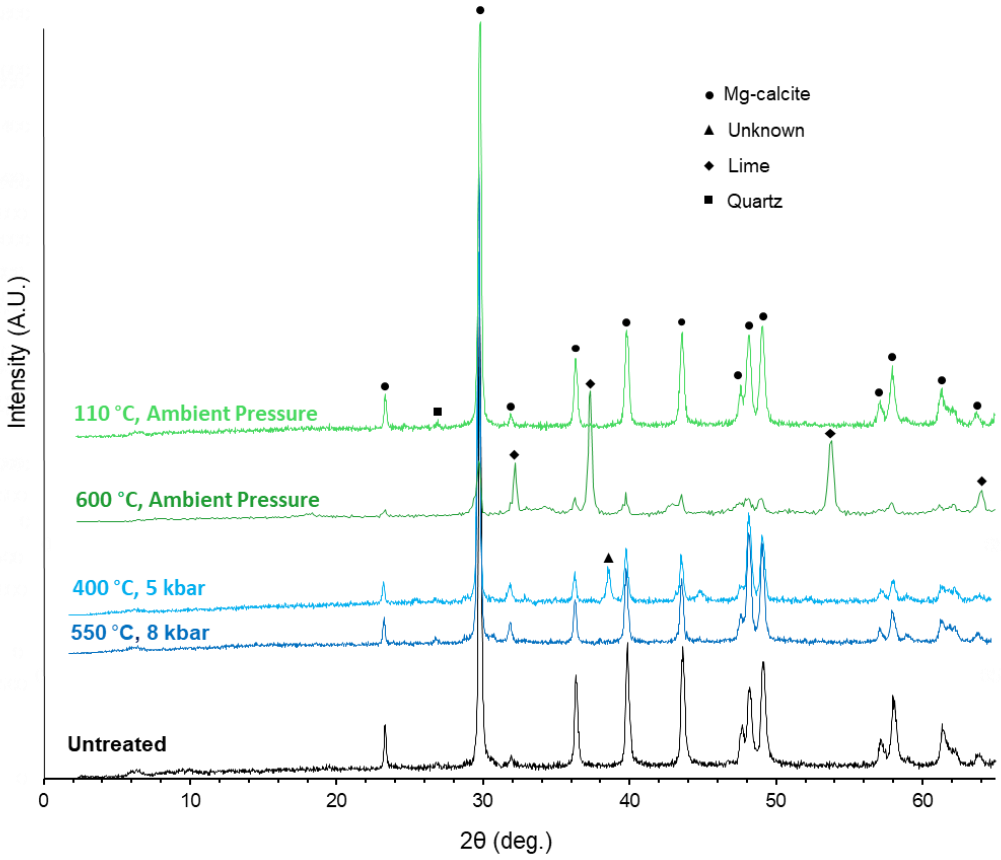

Figure 5.3. XRD (Bruker D8 Advance with Sol-X Energy Dispersive detector) data for samples run at various pressure and temperature conditions.

5.3.3 High-pressure and high-temperature experiments

Small quantities of each whole rock sample were cut into cores to fit within the 75% silver 30% pallidum capsules with dimensions of 6 mm outer diameter, 0.3 mm wall thickness, ~8 mm length. An example of a post run capsule is shown in Figure 5.4. Prior to sample loading, capsules were cleaned with dichloromethane (DCM) and annealed to prevent contamination. Capsules were welded shut under argon flow, and care was taken to prevent unwanted heating and degradation of the sample during welding.

Figure 5.4. Example of a halved post run sample enclosed in 70% silver, 30% pallidum capsule. The previously visible green and orange endoliths embedded within the sample are no longer visible.

Capsules were loaded into salt-Pyrex assemblies with internal graphite furnaces and then run in an end-loaded piston-cylinder apparatus at the conditions given in Figure 5.5 and listed in Table 5.2. The pressure was previously calibrated to ensure accuracy within the range ±0.1 kbars as detailed in Montgomery et al. (2016). An R-type thermocouple was positioned above the capsule within the assembly to monitor the temperature throughout the run time and temperature accuracy is approximately ±10 °C. To return the experiments to room temperature in less than 10 seconds, the power to the heating circuit was turned off. Once the sample had cooled to room temperature, the sample pressure was slowly bled to prevent sample or capsule

cracking. Care was taken to prevent sample contamination during the removal of the sample material from the capsule.

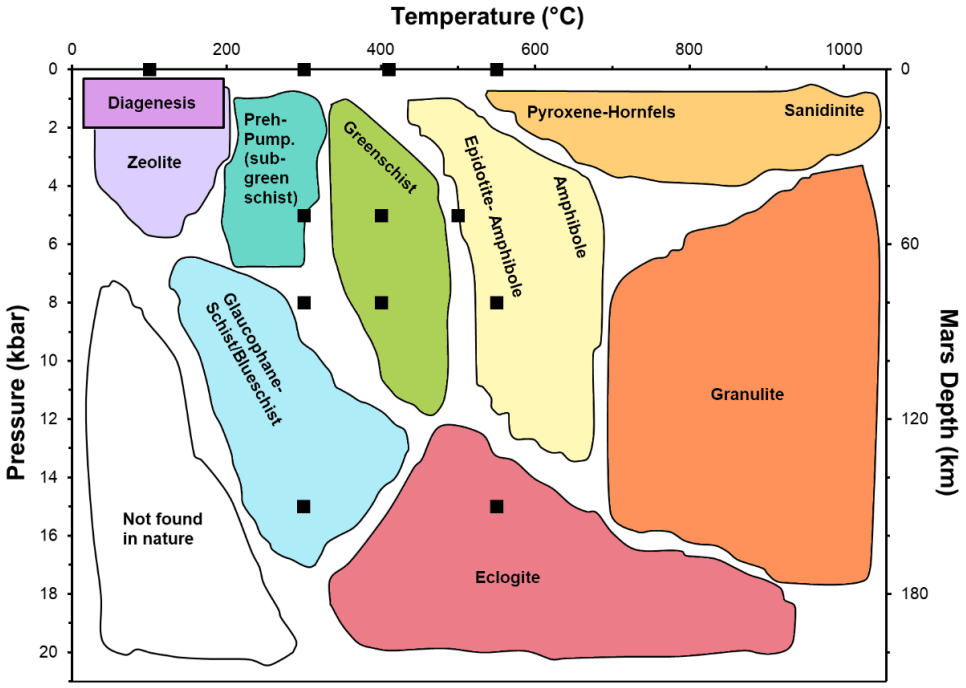

Figure 5.5. Experimental conditions superimposed on a pressure-temperature metamorphic facies diagram (Ehlmann et al. 2011). Experimental conditions are shown in black squares with several experiments being run under multiple experimental durations. Such expansive experimental conditions allow for the elucidation of temperature and pressure effects which may not otherwise be apparent in the narrow range where carbonates naturally occur. Preh.= Prehnite, Pump.= pumpellyite.

Table 5.2. Summary of piston-cylinder and furnace experimental conditions

Run #	P (GPa)	T (°C)	Duration (hours)	Analysis
Metamorphic Facies				
HS_01	0.8	550	120	py
HS_02	0.5	300	336	py
HS_03	0.8	(300-600) 410*	120	py
HS_04	0.5	500	192	py
HS_05	0.8	300	192	py
HS_07	0.5	410*	240	py
Necromass	0.8	400	6	liq
Time Duration / Kinetics				
HS11	0.8	550	2	liq
HS12	0.8	550	48	liq
HS13	1.5	300	2	liq
HS14	1.5	550	48	liq
High-pressure Thermal Degradation				
HP13	1.5	300	96	liq
HP14	1.5	410	96	liq
HP15	1.5	550	96	liq
Ambient Pressure / Furnace				
MR2	ambient	110	2	liq
MR3	ambient	410	2	liq
MR4	ambient	300	2	liq
MR5	ambient	550	2	liq

*Thermocouple failure during run, temperature estimated.

5.3.4 Pyrolysis gas chromatography mass spectrometry analysis

For GC-MS pyrolysis, the whole core samples were placed in quartz sample tubes and loaded into a CDS Analytical Model 5200 pyrolysis unit. Samples were flash heated at 650 °C at a heating rate of 20 °C ms^{-1}. The pyrolysis products were introduced to an Agilent 6890 gas chromatograph equipped with a 30 m J&W Scientific DB-5MS Ultra Inert column. Samples were run in split mode with helium as the carrier gas at an initial flow rate of 1.1 mL/min, a split ratio of 10:1, a split flow of 10.9 mL/min, and a total front inlet flow of 15.1 mL/min and an inlet temperature of 270 °C. The oven temperature program began at a start temperature of 40 °C held for 2 minutes,

followed by a ramp of 7.50 °C min^{-1} to hold at 310 °C for a total run time was 48 minutes. Following column separation, spectral compound analysis used an Agilent 5973 inert mass selective detector set to collect data over a scan range of m/z = 50 to 550. Compound identifications were made by considering the elution time and order against literature data and the mass spectra against the NIST08 library.

5.3.5 Biosignature extraction

The recovered sample (approximately 0.85 g of each sample) was extracted with a chloroform/methanol mixture (10 ml; 2:1 v/v). Following ultrasonication for 20 minutes, samples were allowed to settle and extract over 72 hours. The clear supernatant layer was transferred into a clean glass vial/test tube, and the extract was centrifuged at high speeds to remove any residual solid material and the supernatant recovered. Extracts were treated with activated copper to remove elemental sulfur that could interfere with GC-MS analysis. Prior to use, the copper wire was treated with 12 M hydrochloric acid. The acid was decanted, and the copper was rinsed with a copious amount of nanopure water until pH neutral, then rinsed with methanol (seven times), followed by a final rinse with chloroform (seven times). The cleaned copper was added to each of the extract vials and left for 8 hours. Afterwards the copper had blackened, indicating a reaction with elemental sulfur. Samples were reduced to 0.250 uL for free organic analysis under gentle nitrogen flow. A procedural blank was also carried through the procedure with only the extraction solvents to ensure no systematic contamination (Figure 5.6). The optimal 0.250 uL volume was determined based on the abundance of sample and the analyte response for the GC-MS as shown in Figure 5.7 with a comparison of injected solvent concentrations from 10 mL, 1.5 mL, to 250 uL.

Two further solvent extractions were performed each lasting 72 h, which confirmed that the initial extract recovered the total free extractable portion (Figure 5.8).

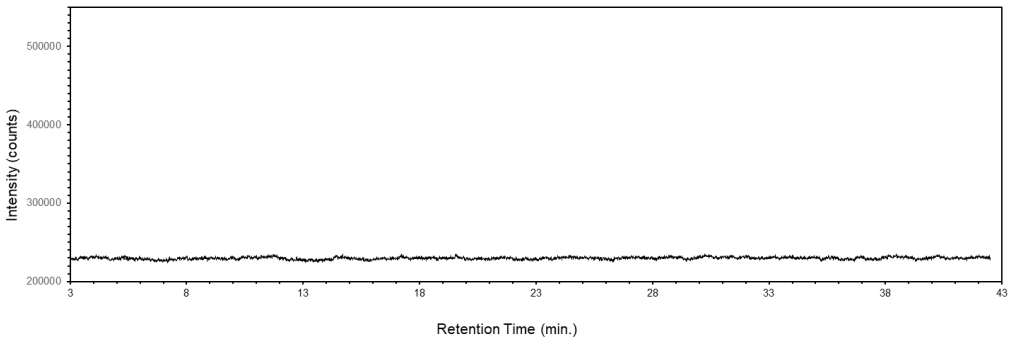

Figure 5.6. Example of a procedure blank ensuring the GC-MS system is free of contamination and peak identification is uncomplicated. Note the flat baseline. The y-axis is set to the same scale as the standard shown in Figure 5.10 to allow for straightforward comparison.

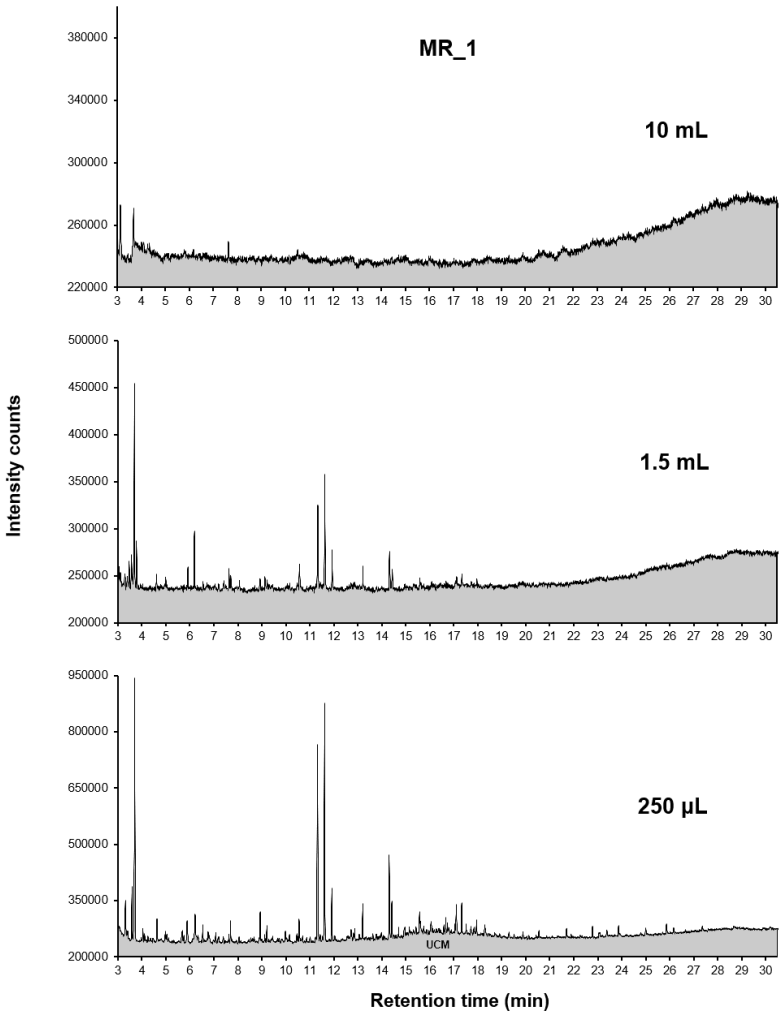

Figure 5.7. Starting material characterization (MR1) by liq-GC-MS with comparison of injected solvent concentrations from 10 mL, 1.5 mL, to 250 uL using a vial micro-insert, where the more concentrated sample provided ideal analyte concentrations. The UCM (unresolved complex mixture) becomes apparent only in the most reduced sample.

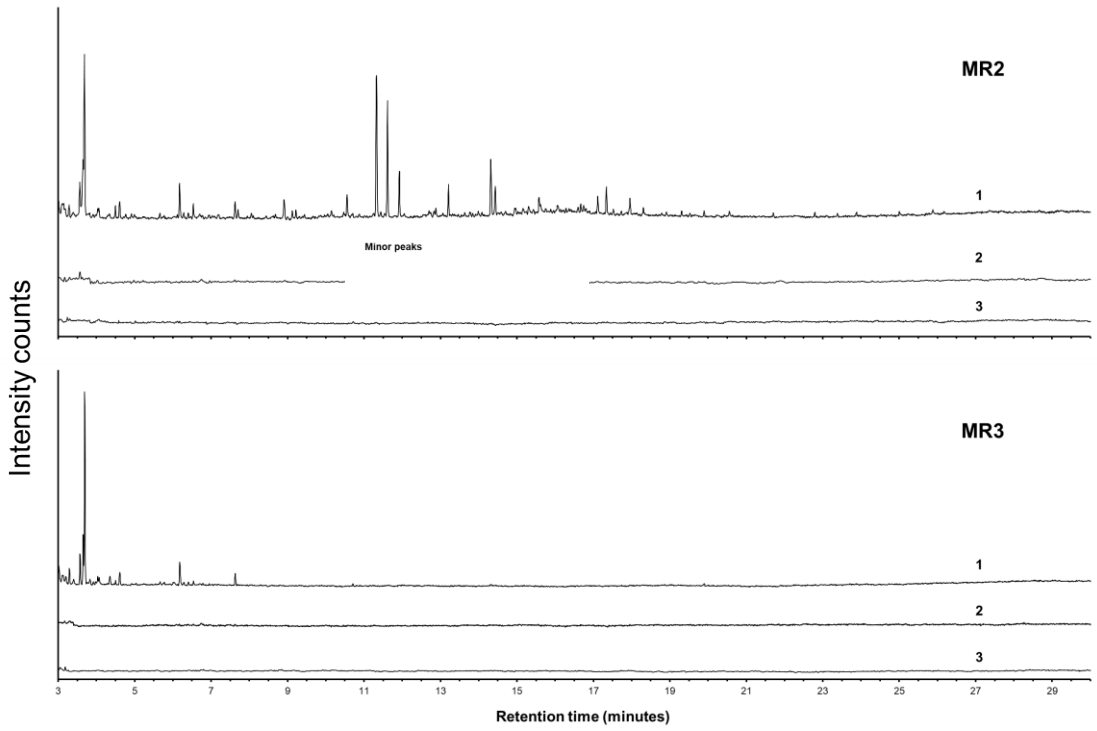

Figure 5.8. Comparison of first, second, and third solvent extracts on MR2 and MR3. In the second extract of MR2, minor peaks are visible, while in extract three no peaks are visible suggesting a full extraction of the free organics. In MR3, both the second and third extraction show a flat baseline. Therefore, all free organics were extracted. Intensity counts on the y-axis have been set to the same scale for all chromatograms.

5.3.6 Gas chromatography mass spectrometry analysis

Analysis by GC-MS was performed on a Shimadzu model GCMS-QP 2010 ultra-gas chromatograph at Millsaps College located in Jackson, Mississippi, USA. The instrument was operating in electron ionization (EI) mode at 70 eV with an ion source temperature of 200 °C and was equipped with a Rtx-5MS crossbond 5% diphenyl – 95% dimethyl polysiloxane capillary column (30 m length, 0.25 mm I.D., 0.25 µm film thickness). Ultra-high purity helium acted as the carrier gas with a total flow of 4.8 mL/min and a purge flow of 1.0 mL/min. The GC-MS was equipped with an auto-injector that injected 1.0 µL of the sample solution in split mode with a split ratio of 5:1. To eliminate carryover contamination, the auto-sampler syringe was rinsed

with methanol and hexane from two separate wash vials for a combined total of ten pre- and post-washes for each sample. The injector and interface temperatures were both set at 250 °C. The ion source temperature was set at 200 °C. The initial column oven temperature was set at 50 °C and ramped at a rate of 10 °C per minute until reaching 275 °C then ramped to 300 °C at a rate of 5°C per minute with a final hold time of 15 minutes at 300 °C. The total GC run time was 42.5 minutes. The mass range of scan spectra was 35–350 m/z with a scan speed of 1000. For the scan mode data, potential background contaminants were excluded after background adjustment by subtracting the procedural blank from the sample. Total ion chromatograms (TIC) as well as SIM (selected ion monitoring) mode were both utilized. The SIM mode considerably increased sensitivity and reduced noise as shown in Figure 5.9. For liq-GC-MS, analysis no organics were detected above the noise level in the procedural blank and solvent blanks were run before and after each sample to ensure that no carryover contamination occurred. Similarly, the pyrolysis blank appeared free of significant contamination. A 10 ppm fatty acid methyl ester (FAME) standard was used to regularly monitor system performance and sensitivity.

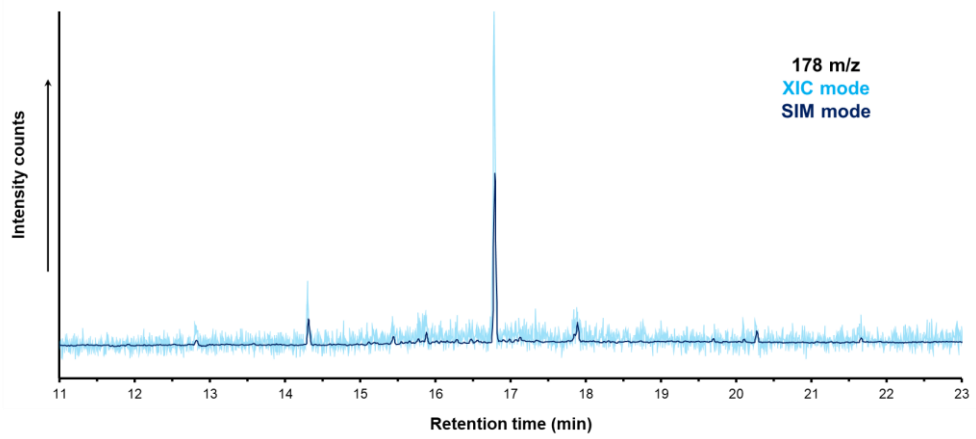

Figure 5.9. Liq-GC-MS chromatogram of the starting material, MR1 comparing the SIM and XIC chromatograms for the detection of phenanthrene's characteristic mass fragment 178 m/z.

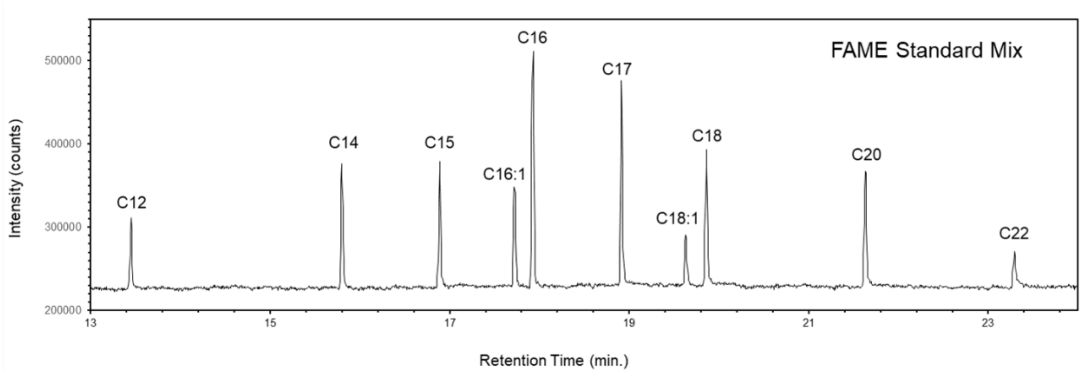

Figure 5.10. Liq-GC-MS chromatogram of the 10 ppm FAME standard containing a methylated fatty acid mixture. The carbon chain length is denoted. For example, C12 refers to dodecanoic acid and C16:1 refers to palmitoleic acid.

5.4 Results

5.4.1 Thermal degradation

Artificial thermal maturation experiments conducted at ambient pressure and atmosphere conditions demonstrate a strong influence on organic compound degradation. Minimal differences appear between the untreated sample and the sample heated for 2 hours at 110 °C (MR2), while the experiments at 300, 410, and 550 °C (MR4, MR3, and MR5) reveal severe degradation of the organic profile (Figure 5.10). For the sample treated at 410 °C (MR3), the combined alkanes + alkenes + aromatic portion drastically increase at early retention times, while the compounds in this fraction found at greater retention times decreased dramatically (Figure 5.11). In this early elution fraction, the abundance inversely follows the temperature with 300 °C having the highest abundance followed by 410 °C then 500 °C. This implies that such early eluting compounds are volatile degradation products, which are expected to be unsuitable as biosignatures as Group 3 compounds. NIST peak identifications are shown in Table 5.3 for compounds that could be identified with relatively high certainty. Even the relatively stable polycyclic aromatic

hydrocarbon (PAH) phenanthrene, which exhibits π-bonding interactions, i.e., aromaticity, has thermally degraded at metamorphic temperatures. The results of these experiments on biogenic organic material indigenous to carbonates bears similarities to results from immature kerogens. A previous study on shale kerogens experimentally maturated at 300 °C demonstrated a prominent increased in the abundance of n-alkanes as a function of experimental durations at 24, 240 and 2400 h, respectively (Mißbach, 2018). Furthermore, a number of kerogen studies have noted that source-specific features of individual n-alkane chain lengths gradually disappear with increasing sample maturity (Tissot et al., 1978; Price, 1993; Peters et al., 2005, Mißbach, 2018). A further consideration for near surface biosignatures is that the radiolysis rate of large molecules is considerably faster than for smaller ones (Pavlov et al., 2012). The isolation of temperature as a variable is necessary to inform high-pressure experiments also conducted at high-temperatures and identify thermal degradation products distinct from pressure alteration.

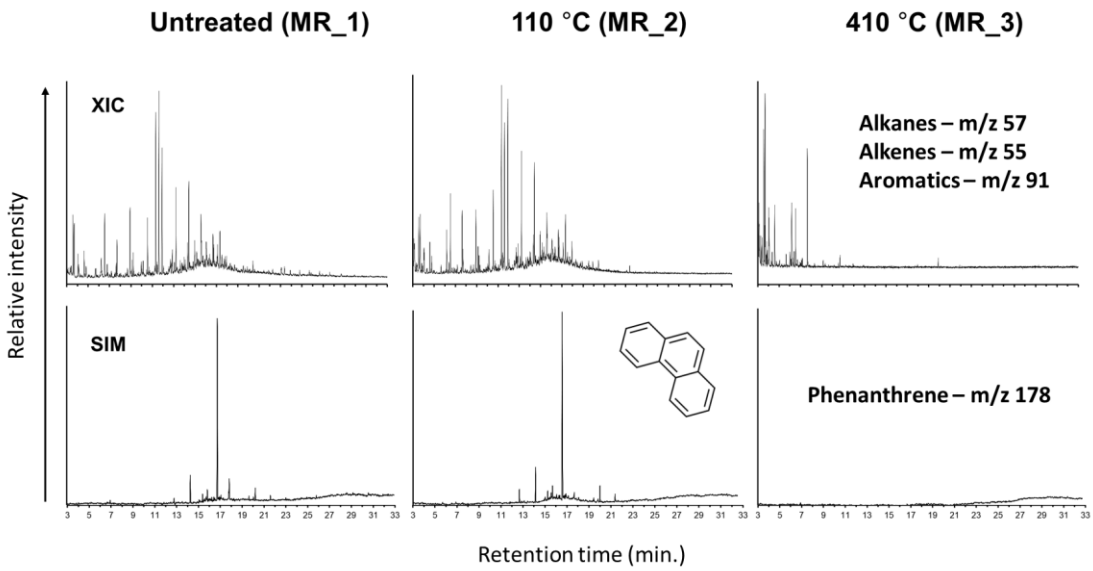

Figure 5.11. Liq-GC-MS XIC data from samples run at 110 °C and 410 °C compared to the untreated sample. The SIM for the PAH phenanthrene is also shown, which may be a compound indicative of biotic activity.

Table 5.3. NIST identifications for thermal degradation samples based on TIC

Retention time (min.)	Compound name	Match index
MR1 (Starting Material / Untreated)		
5.7	Hexanoic Acid	93
5.7	2H-Pyran, 2-(3-butynloxy)tetrahydro	80
5.9	Pentachloroethane	88
6.2	4-Chloro-3-methylbut-2-en-1-ol	91
6.5	2-Ethyl-1-Hexanol	94
6.8	S-Propyl propane-1-sulfonothioate	77
7.1	(2-[2-(Carboxymethoxy)ethoxy]ethoxy)acetic acid	81
7.6	3-Octanol, 3,7-dimethyl	83
7.7	Nonanal	95
8.9	Butoxyethoxyethanol	96
9.1	Dodecane	90
9.2	Decanal	94
10.6	Tridecane	96
11.3	Propanoic acid, 2-methyl-, 3-hydroxy-2,2,4-trimethylpentyl ester	86
11.6	Propanoic acid, 2-methyl-, 3-hydroxy-2,2,4-trimethylpentyl ester	96
11.9	Tetradecane	97
13.2	Pentadecane	97
14.3	2,2,4-Trimethyl-1,3-pentanediol diisobutyrate	91
14.4	Hexadecane	96
14.9	Dodecane, 2,6,10-trimethyl	80
15.6	2-Methyltetracosane	91

16.1	2-Methyltetracosane	90
17.1	(9E)-8-Methyl-9-tetradecenyl acetate	79
17.3	Phthalic acid, isobutyl octadecyl ester	90
17.5	Undec-10-ynoic acid, tetradecyl ester	87
17.7	7-Hexadecenal, (Z)	84
17.8	Dodecane, 1,2-dibromo	76
18.0	Cyclopentanetridecanoic acid, methyl ester	89
18.3	Dibutyl phthalate	90
19.5	Bromoacetic acid, octadecyl ester	87
19.9	Heptadecanoic acid, 10-methyl-, methyl ester	84
23.1	Hexadecanoic acid, 2-bromo	71
23.4	Bis(tridecyl) phthalate	66
25.9	1, 6, 10, 14, 18, 22-Tetracoshexaen-3-ol, 2,6,10,15,19,23-hexamethyl	73
	MR2 (110 °C)	
6.2	4-Chloro-3-methylbut-2-en-1-ol	90
6.3	3-Pentanol, 2,4-dimethyl	78
6.4	Octane, 4-chloro	81
6.5	1-Hexanol, 2-ethyl	93
7.6	Undecane	93
7.7	Nonanal	93
8.9	Butoxyethoxyethanol	95
9.1	2-Methyldecane	90
9.2	Decanal	92
10.6	Tridecane	97
11.3	2,2,4-Trimethyl-1, 3-pentanediol diisobutyrate	86
11.6	Propanoic acid, 2-methyl-, 3-hydroxy-2,2,4-trimethylpentyl ester	95
11.9	Tetradecane	97
13.2	Pentadecane	97
14.3	Pentanoic acid, 2,2,3-trimethyl-3-carboxyisopropyl, isobutyl ester	89
14.4	Hexadecane	96
15.6	Hexadecane	92
17.1	Cyclooctaneacetic acid, 2-oxo	79
17.3	Phthalic acid, isobutyl octadecyl ester	89
18.0	Tetradecanoic acid, 12-methyl-, methyl ester	91
18.3	Dibutyl phthalate	91
19.9	Tetradecanoic acid, 12-methyl-, methyl ester	85
	MR3 (410 °C)	
6.2	4-Chloro-3-methylbut-2-en-1-ol	90
6.3	3-Hexanol, 3,5-dimethyl	80
6.4	2-Octenal, (E)-	80
6.5	1-Hexanol, 2-ethyl	90
7.6	Undecane	96
	MR4 (300 °C)	
5.0	Acetylene tetrachloride	85
6.2	4-Chloro-3-methylbut-2-en-1-ol	91
6.4	4-Chlorooctane	81
6.5	1-Hexanol, 2-ethyl	89
7.6	Undecane	95
7.7	Nonanal	85

10.7	Heptane, 3-ethyl-5-methylene	76
	MR5 (500 °C)	
4.9	Butanoic acid, 2-propenyl ester	80
5.0	S-Tetrachloroethane	92
5.0	1-(2,2-Dimethyl[1,3]dioxan-4-yl)ethanol	78
6.2	4-Chloro-3-methylbut-2-en-1-ol	90
6.4	4-Chlorooctane	79
6.5	1-Hexanol, 2-ethyl	86
7.6	Undecane	93

*Note that phthalates represent contamination not indigenous to the sample. Repeating compounds indicate insufficient information for NIST identification by m/z.

5.4.2 Time duration and kinetic studies at high-pressure and temperatures

The extrapolation of laboratory results to natural geological timescales remains a significant challenge as experimental replication is largely impossible. However, identifying when stable and metastable compounds first form under experimental conditions can elucidate steady state behaviour and constrain necessary experimental durations. For example, in the time durations experiments (HS-11, HS-12, HS-13, and HS-14), the similarity between the overall organic profile of HS-11 and HS-12 demonstrates that 2-hour experiments produce comparable products as 48 hours, which suggests that the degradation products are formed relatively quickly and persist throughout the duration of longer experiments (Figure 5.12 and Table 5.4). The HS-13 and HS-14 experiments, however, demonstrate more disparity between products, suggesting time duration and kinetic considerations may become more important at lower pressures and that competing reactions may occur due to other factors (Figure 5.12). The SIM scans for biosignature mass fragments follow the same overall pattern as the TIC chromatograms; the longer experiment duration has more of an impact on samples run at higher tempatures and pressures found at more extreme metamorphic gradients. Regardless, the organic profiles are largely comparable between different time

frames as suggested by the relatively quick forming volatile mixtures in the ambient pressure thermal degradation experiments. In addition to the early eluting thermal degradation profile, straight, long-chain saturated fatty acids were found to be particularly apparent in these experiments, appearing in all samples. Such lipids have been proposed as a biosignature for distinguishing different domains of life and potentially forming a significant reservoir of fossil carbon on Mars (Tan et al., 2018).

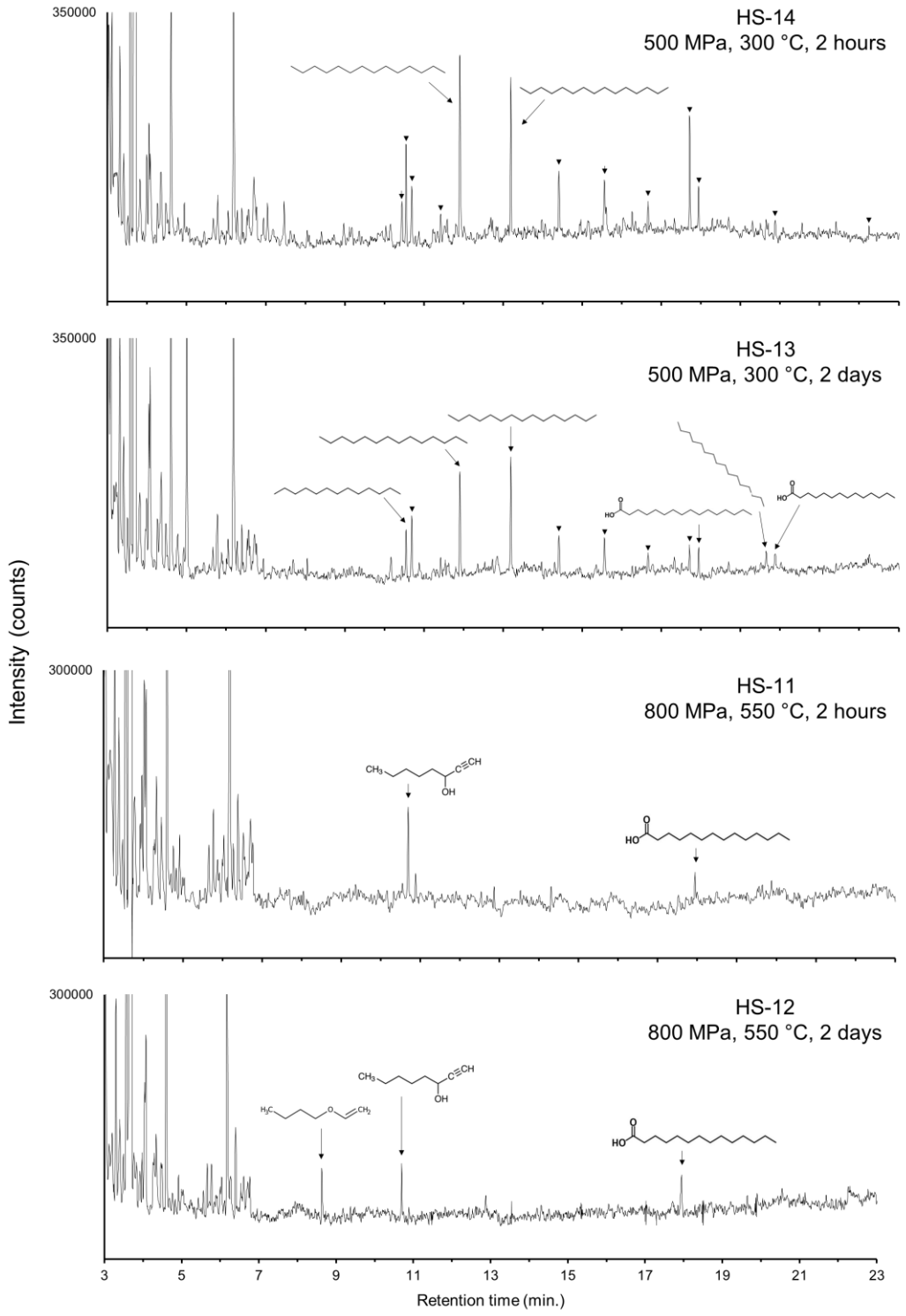

Figure 5.12. Total ion current chromatograms (TIC) for time durations experiments (HS-11, HS-12, HS-13, and HS-14) The similarity between the overall organic profile of HS-11 and HS-12 demonstrate that 2 hour experiments produce comparable products as 48 hours, which suggests that the degradation products are formed relatively quickly and persist throughout the duration of longer experiments. The HS-13 and HS-14 experiments, however, demonstrate more disparity between products, suggesting time duration and kinetic considerations may become more important at lower pressures.

Table 5.4. NIST identifications for kinetic / time duration experiments

Retention time (min.)	Compound name	Match index
	HS-11	
17.95	tetradecanoic acid	82
10.695	1-octyn-3-ol	77
	HS-12	
17.95	decanoic acid	88
12.875	1-chloroundecane	80
10.695	5-isopropyl-6-methyl-hepta 3,5-dien-2-ol	77
8.635	1-butylvinyl methyl ether	84
	HS-13	
19.87	tetradecanoic acid	67
19.645	hexadecane	78
17.945	hexadecanoic acid	88
17.705	oxirane	81
16.66	2-methyltetracosane	83
15.565	eicosane, 10-methyl-	93
14.415	hexadecane	91
13.195	pentadecane	96
11.905	tetradecane	96
10.69	5-isopropyl-6-methyl-hepta 3,5-dien-2-ol	75
10.545	tridecane	93
	HS-14	
23.07	dotriacontyl isopropyl ether	77
22.25	2-methyltetracosane	78
19.88	tetradecanoic acid	75
17.94	hexadecanoic acid	89
17.72	2-nonadecanone	92
16.66	2-methyltetracosane	88
15.57	octasane	91
14.41	hexadecane	94
13.19	pentadecane	96
11.91	tetradecane	87
11.42	decane, 2,3,5,8-tetramethyl-	83
10.69	5-isopropyl-6-methyl-hepta 3,5-dien-2-ol	78
10.55	tridecane	96
10.44	2-ethnyl-1,3,3-trimethyl-cyclohexane	80

5.4.3 High-pressure thermal degradation

For the experiments analysed by liquid injection GC-MS, all experiments were rich in early eluting degradation products as shown by the high abundance of peaks between 3-7 minutes (Figure 5.13 and Table 5.5). Identified peaks are marked and reported in Table 5.5. While HP-13 and HP-14 are comparable to the ambient pressure experiments, HP-15 contains significant organics, including aromatics and branched aliphatics.

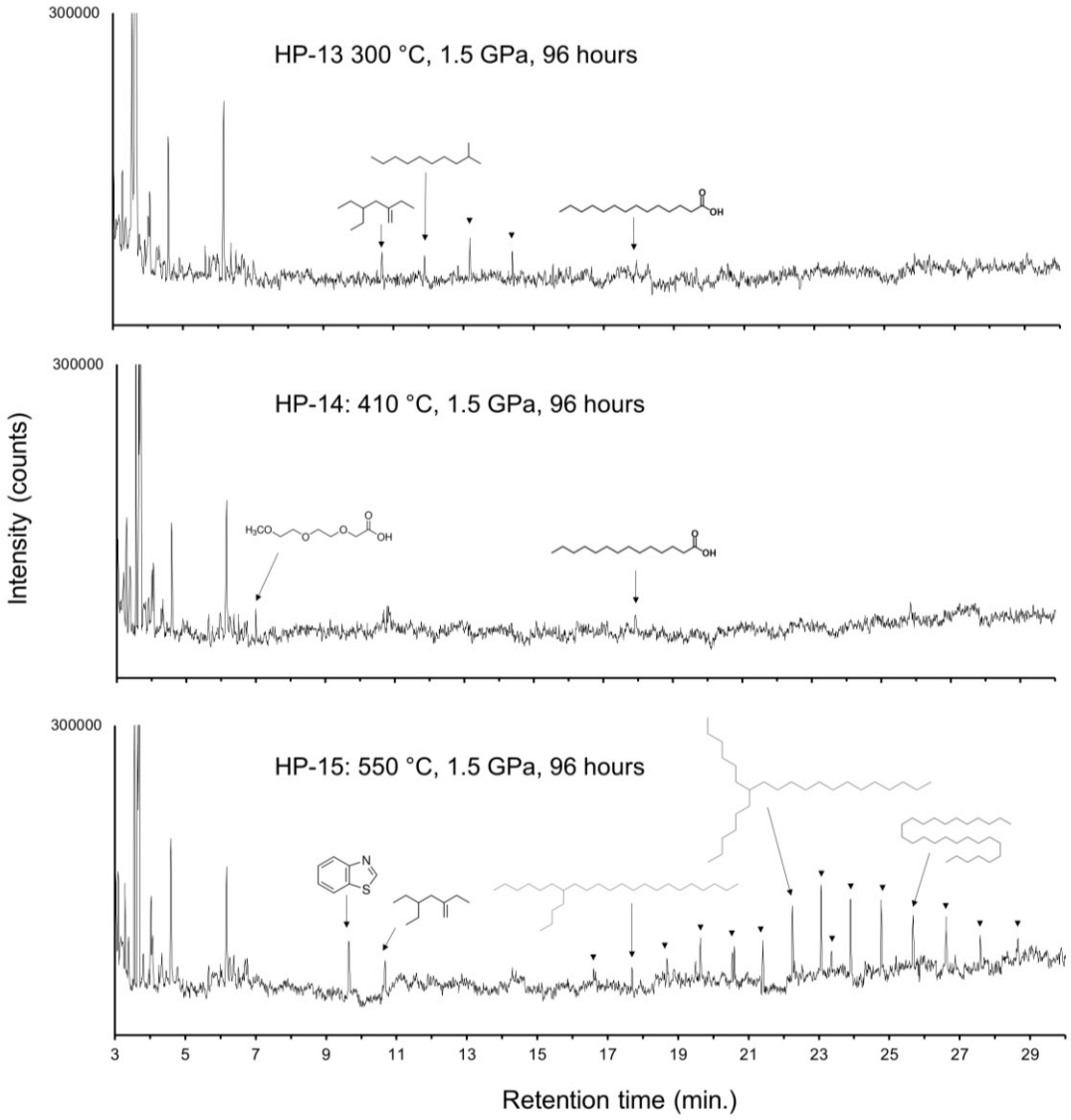

Figure 5.13. Total ion current chromatograms (TIC) from liq-GC-MS for varied temperature experiments at 1.5 GPa and after 96 hours (HP-13, HP-14, HP-15).

Table 5.5. NIST identifications for Samples

Retention time (min.)	Compound name	Match index
	HP-13	
3.28	3-Penten-2-ol	89
3.55	3-Hexen-1-ol	89
3.68	2-Pentanol, 4-methyl	93
4.06	Oxane-2-carboxylic acid	73
4.59	1-Hexene, 3-Chloro	80
5.64	2H-Pyran,2(3-butynyloxy)tetrahydro	74
5.75	Propanoic acid, 2-hydroxy-2-methyl-	70
5.98	2-Methoxy-2-methylbut-3-ene	71
6.16	4-Chloro-3-methylbut-2-en-1-ol	89
6.38	Octane, 4-Chloro	78
6.51	1-Pentanol,2-ethyl-4-methyl	82
10.68	3-Ethyl-5-methylheptane	73
11.89	2-methyl decane	83
13.18	Pentadecane	86
14.40	Hexadecane	81
15.55	Decane, 2,3,5,8-tetramethyl	82
15.55	Decane, 2,3,5,8-tetramethyl	82
16.65	Decane, 2,3,5,8-tetramethyl	70
17.93	Tetradecanoic acid	72
	HP-14	
10.79	Pthalic anhydride	88
10.67	3-trifluoroacetooxydodecane	69
7.01	2-(2-(2-(2-Methoxyethoxy)ethoxy)ethoxy)acetic	74
6.51	1-Hexanol, 2-ethyl	84
6.37	Oxetane, 2-methyl-4-propyl	77
6.16	4-Chloro-3-methylbut-2-en-1-ol	88
5.98	cis-2,3-Epoxyoctane	75
5.65	2H-Pyran, 2-(3-butynloxy)tetrahydro-	73
4.58	1-Hexene, 3-Chloro	80
4.34	2-Propenoix acid, 2-methyl-, 2-aminoethyl ester	76
4.07	Oxane-2-carboxylic acid	82
4.02	3-Pentanol, 2-Chloro-4-methyl	80
3.91	cyclobutanemethanol, alpha, methyl	75
3.68	2-Pentanol, 4-Methyl	93
3.65	4-Chloro-2-methylbutan-2-ol	91
3.55	2-Hexen-1-ol	92
3.29	3- Penten-2-ol	90
3.39	2-Pentenal	82
3.38	2-Methyl-3-vinyl-oxirane	81
3.20	Pentan-2-ol, 4-allyloxy-2-methyl	82
3.03	Tetrahydro-4Hpyran-4-ol	84
	HP-15	

28.66	Di-n-decylsulfone	28.655
27.59	Di-n-decylsulfone	27.585
25.85	Squalene	25.845
25.68	Heptacosane	25.675
24.77	Heptacosane	24.77
23.90	Heptacosane	23.9
23.37	1-Bromo-4-Bromomethyldecane	23.365
23.06	Eicosane, 7-hexyl-	23.06
22.25	2-Methyltetrcosane	22.25
21.41	Heptadecane, 9-octyl-	21.405
20.60	Heptadecyl acetate	20.595
20.55	Heptadecane, 9-octyl-	20.545
19.64	2-Methyltetracosane	19.635
19.50	n-Nondecanol	19.495
18.69	Pentadecane, 8-hexyl-	18.685
17.69	Docosane, 7-butyl-	17.69
16.65	Methoxyacetic acid, 4-tridecyl ester	16.65
10.68	Heptane, 3-ethyl-5methylene	10.68
9.65	Benzothiazole	9.65
6.76	2-Buten-1-ol, 3-methyl, acetate	6.755
6.70	Acetoacetic acid, 1,3-dithio-, S-isopropyl ester	6.695
6.51	1-pentanol, 2-ethyl-4-methyl	6.51
6.38	3-Trifluroacteoxydodecane	6.38
6.26	1-(Methoxymethoxy)-3-methyl-3hydroxybutane	6.26
6.17	4-Chloro-3-methylbut-2-en-1-ol	6.165
6.00	2H-pyran,2(4-chlorocutoxy)tetrahydro-	5.995
4.59	1-Hexene, 3-chloro	4.59
4.33	2-Butanone, 4-hydroxy-3-methyl	4.33
4.03	3-Pentanol, 2-Chloro-4-methyl	4.025
3.69	2-Pentanol, 4-methyl	3.685
3.65	4-Chloro-2-methylbutan-2-ol	3.645
3.56	3-hexen-1-ol	3.555
3.40	2-Pentanal	3.395
3.29	3-Penten-2-ol	3.29
3.09	Carbamic acid, methyl ester	3.09

Pyrolysis GC-MS has a greater probability of detecting both the soluble and the insoluble organic fractions compared to liq-GC-MS. Similar to liq-GC-MS analysis, the extracted ion chromatograms (XIC) were used to monitor categories of organic molecules relating to biological activity that will be targeted by ExoMars and MOMA (Goesmann et al. 2017; Vago et al., 2017) as

well as molecules potentially resulting from abiotic synthesis (Rushdi and Simoneit, 2001; Mißbach et al., 2018). These compounds include alkanes (m/z = 55) and alkenes (m/z = 57), furfural (m/z = 96) and aldehydes (m/ z = 105) which may be indicators of carbohydrates, alkanols (m/z = 103), and alkanoic acids (m/z = 117). Types of organic compounds known to have been delivered to Mars via meteorites were also prioritized, specifically alkylbenzenes (m/z = 91), naphthalene (m/z = 128), 1-methylnaphthalene (m/z = 142), acenaphthalene (m/z = 154), and higher polycyclic aromatic hydrocarbons such as phenanthracene. The chromatograms analysed by pyrolysis notably lack the early eluting, low molecular weight fraction in comparison to the liq-injection GC-MS chromatograms. This indicates that these organic compounds have either prematurely volatilized during analysis or have been otherwise transformed to be unresponsive to online pyrolysis. Analysis of organic matter following pressure-temperature treatment produces considerably fewer peaks available for identification. The pyrolysis chromatograms were largely unamenable to identification via NIST database search as the match percent index seldom returned sufficiently high values.

For the 5 kbar experiments severe degradation is evident in the TIC and in all XIC chromatograms (Figure 5.14-15). Both the experiments run at 300 °C and 500 °C show similar degradation patterns with the overall organic profile of both dominated by early eluting alkanes and alkenes, while only select other compounds can be distinguished in lower abundance, such as those shown in the aromatic m/z and napthalenes (Figure 5.14). Furfural can only be detected in the experiment run at 300 °C, and phenanthrene is below the LoD in both high-temperature experiments. Both the naphthalene, 1-methylnaphthalene, acenaphthalene, and phenanthracene increased in proportion at 300 °C, while all other monitored XIC show a decrease in monitored groups (Figure 5.15). PAHs are a component of the interstellar

medium and have been identified in numerous meteorites, including the soluble and insoluble matter of carbonaceous chondrites (Sephton et al., 2002; Steele et al., 2016; Giese et al., 2019). Furthermore, naphthalene has been detected by the Mars Science Laboratory, which may indicate a that complex macromolecular organic material exists in the Martian sediments (Eigenbrode et al., 2018).

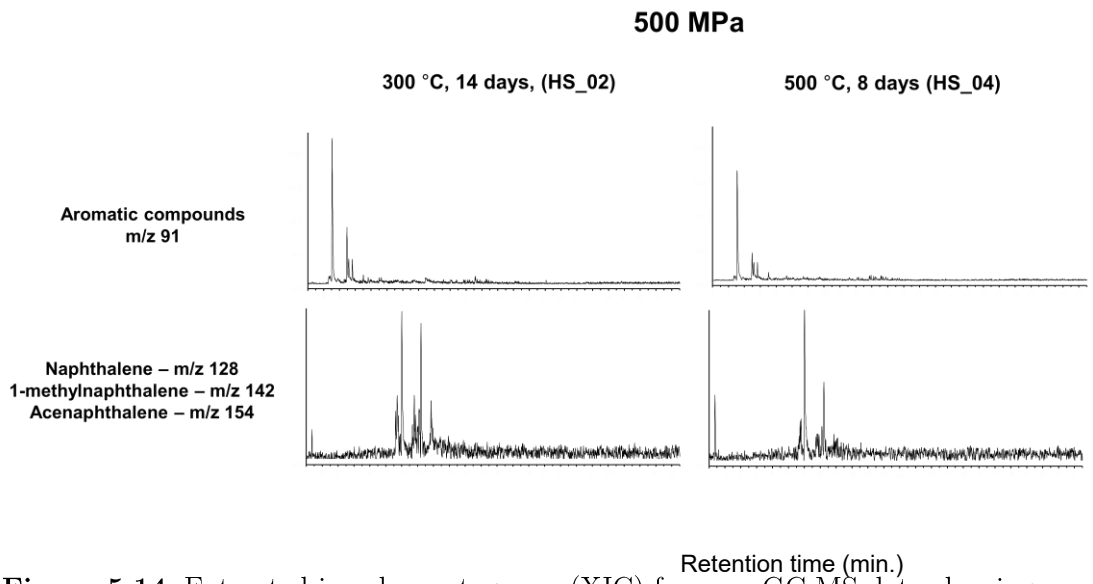

Figure 5.14. Extracted ion chromatograms (XIC) from py-GC-MS data showing aromatic compounds (m/z 91) and mass fragments associated with selected PAHs (m/z 128, m/z 142, and m/z 154). These compounds show remarkable preservation potential even under diagenetic subsurface conditions.

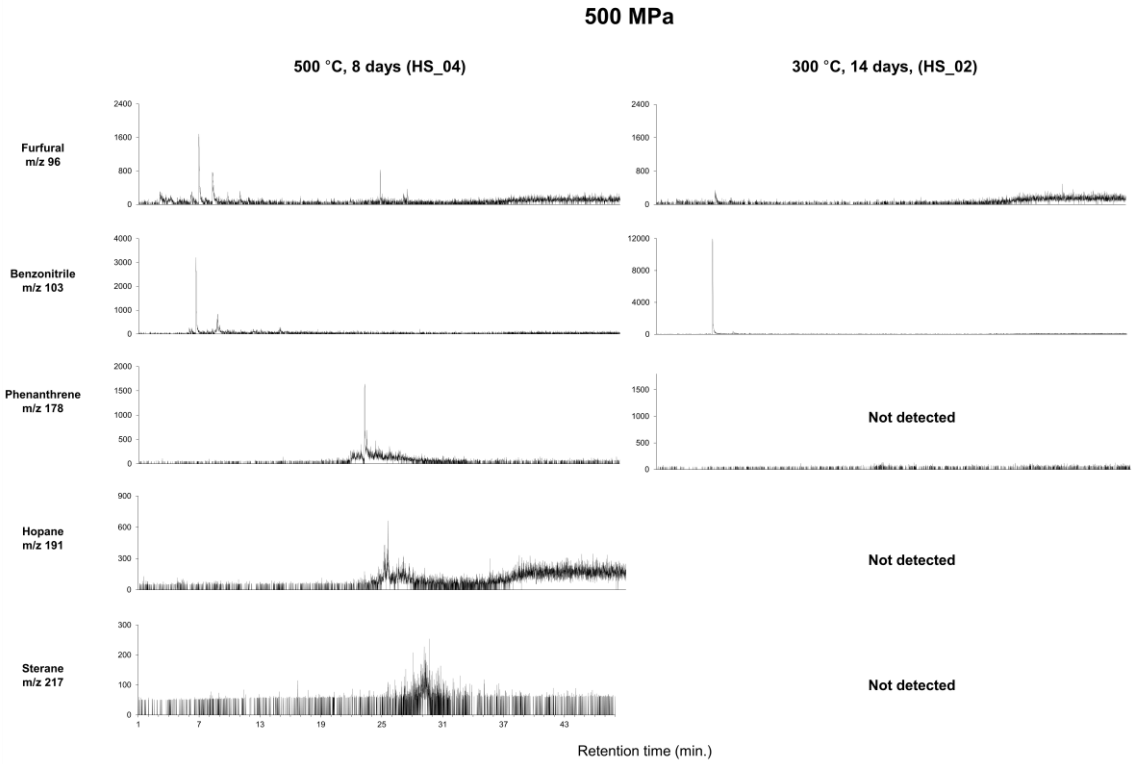

Figure 5.15. Extracted ion chromatograms (XIC) from py-GC-MS data showing several classes of compounds. Note the progressive destruction of all compounds from 300 °C to 500 °C. The noisy baseline and relatively low intensity counts indicate that the m/z are in very low abundance rendering detection of these compounds via NIST improbable. Intensity counts on the y-axis are scaled for each chromatogram to optimally show present peaks.

For the experiments conducted at 8 kbar, the 300 °C experiments remain considerably better preserved than the experiments run at 550 °C, despite the 300 °C experiment being run for a longer duration. As shown in Figure 5.16-17, the abundance of most compounds decreases dramatically from 300-550 °C, with little high-pressure products produced. The aromatic compounds XIC, which includes benzonitrile, appears only subtly affected by temperature. Interestingly, the abundance of naphthalene, 1-methylnaphthalene, acenaphthalene, and phenanthrene increase from the untreated sample to the 300 °C sample. The UCM (unresolved complex

mixture) apparent in the untreated TIC chromatogram has also been resolved in the matured samples.

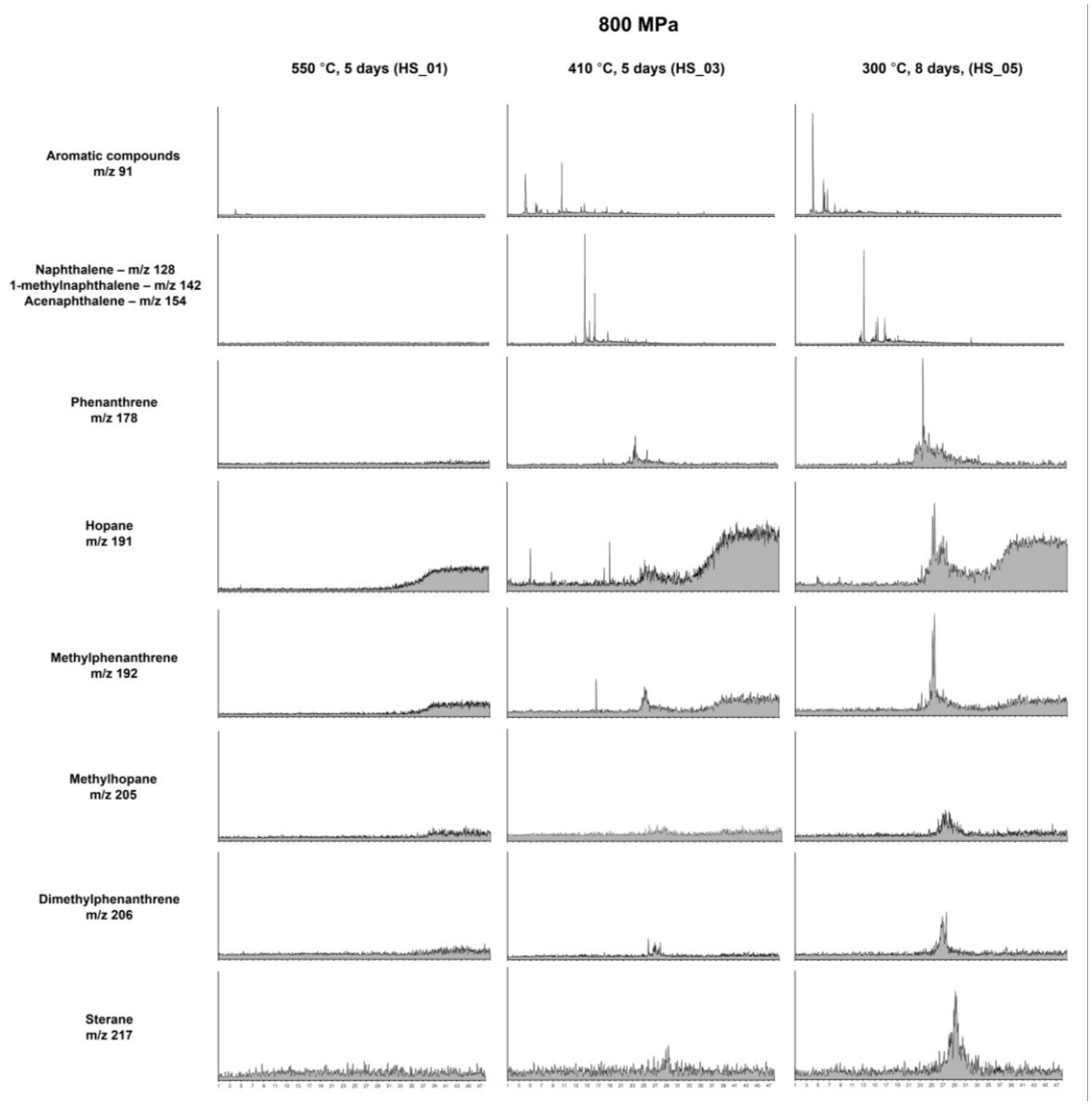

Figure 5.16. Extracted ion chromatograms (XIC) from py-GC-MS data showing several classes of compounds. Note the progressive destruction of all compounds from 300 °C to 410 °C to 550 °C.

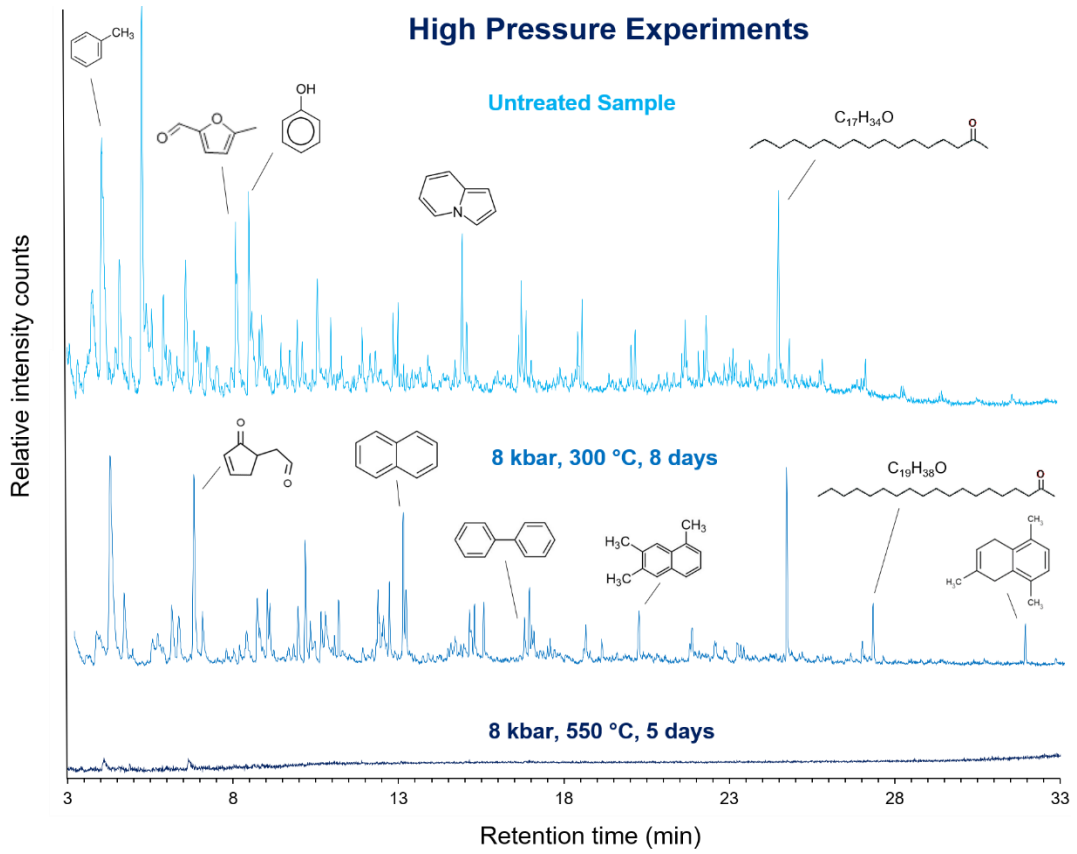

Figure 5.17. Excerpt of Py-GC-MS TIC data for the untreated sample and 8 kbar runs at 300 °C, 500 °C respectively. Despite the low match index given by NIST rending identification unfeasible, some tentative structures are shown for illustrative purposes. The small peaks remaining in the bottom chromatogram represent degradation products rather than potential biosignatures.

Previous studies on pressurized organic matter found that aromatic and polar polymers appear more likely than aliphatic hydrocarbons to remain accessible by online pyrolysis when subjected to pressure (Montgomery et al., 2016). However, these experiments were run for far greater lengths, while these 2-hour experiments capture the initial, metastable thermal degradation products that are expected to initially occur but are unlikely to be stable over geological lengths. Despite differences in the sample nature and experimental and analytical techniques, our data shows trends consistent with literature data for thermal maturity in kerogen and bitumen systems via semi-open pyrolysis. For increasing maturity, both kerogen and bitumen increase in

aromatic character, and kerogen follows the previously observed trend with aliphatic carbon chains that became shorter and/or more branched as kerogen is consumed during artificial maturation. Bitumen is principally generated from kerogen and aliphatic carbon chains may undergo lengthening within the same artificial maturity range (Craddock et al., 2015). In both kerogen and bitumen, aliphatic carbons may be lost from aromatic centres leading to protonation of the residual aromatic rings (Craddock et al., 2015).

5.4.4 Necromass

The mass fragments 57, 71, and 85 indicate the presence of aliphatic alkane hydrocarbons, which are abundantly present in the untreated necromass but show rapid depletion in the treated sample, with the exception of the early eluting fraction (Figure 5.18). The marked decrease of the slower eluting compound in the treated vs untreated sample demonstrates the vulnerability of straight chain hydrocarbons to destruction at high-temperatures and pressures, which is perhaps not immediately evident from the TIC comparison (Figure 5.19). NIST peak assignments are provided in Table 5.6.

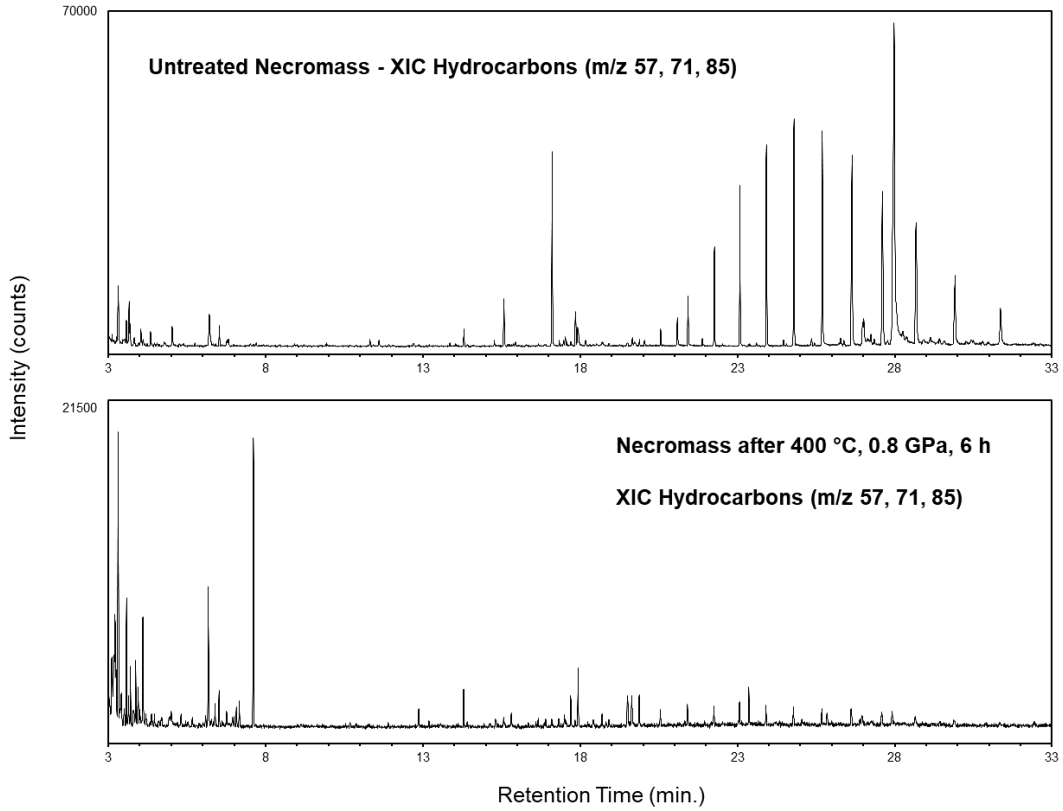

Figure 5.18. Extracted ion chromatograms (XIC) of mass fragments m/z 57, 71, and 85 of the necromass material before (initial) and after (final) pressure treatment.

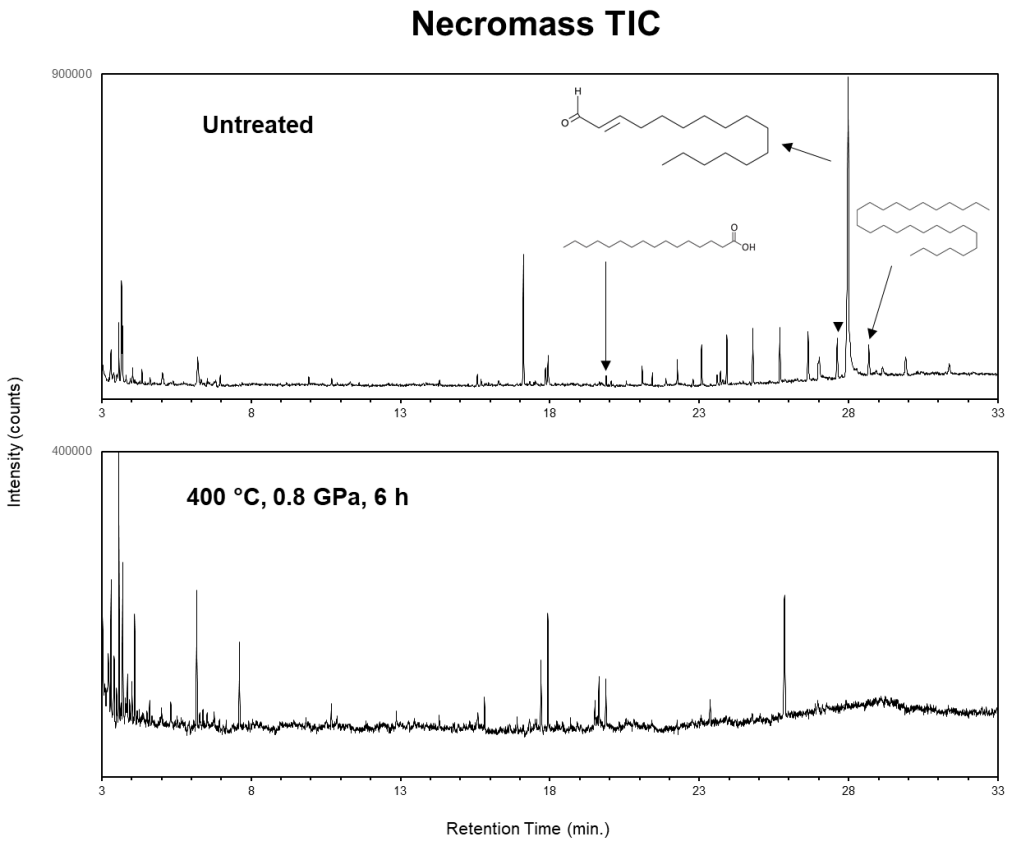

Figure 5.19. TIC comparison of the necromass material before (initial) and after (final) pressure treatment. Note the scaled y-axis for each chromatogram.

Table 5.6. Necromass NIST peak identification.

Retention time (min.)	Compound name	Match index
	Necromass Untreated	
5.0	3-Penten-2-ol	71
6.2	4-Chloro-3-methylbut-2-en-1-ol	90
6.3	2-(2-Methoxy-1-methyloxy)	78
6.5	1-Hexanol, 2-ethyl	89
6.8	2-Buten-1-ol, 3-methyl-, acetate	80
7.0	Arsenous acid, tris(trimethlsiyl) ester	81
9.9	2-Butenoic acid, 1-methylethyl ester	79
10.7	5-Isopropyl-6-methyl-hepta-3,5-dien-2-ol	77
10.9	3-Pentanol, 1-chloro-3-methyl	64
11.3	Butanoic acid, heptyl ester	75
11.6	Propanoic acid, 2-methyl, butyl ester	75
14.3	Pentanoic acid, 2,2,4-trimethyl3-carboxyisopropyl	82
15.3	Dichloroacetic acid, 2-pentadecyl ester	78
15.6	Tetradecane	94
15.7	5-Methyl-isoxazolidin-3-one	77
16.3	3(2H)-Furanone, dihydro-2,2-dimethyl-5-phenyl	82
17.1	2-Pentadecanone, 6,10,14-trimethyl	91
17.3	Propane, 1-(dodecyloxy)-2,3-epoxy	73
17.5	Tridecenal	80
17.5	2-Decen-1-ol, (E)-	81
17.9	2-Pentadecanone, 6,10,14-trimethyl	89
17.9	Palmitic acid, methyl ester	95
19.7	Undecanal	82
19.9	Methyl stearate	90
20.1	Bromoacetic acid, 2-pentadecyl ester	80
20.6	Octadecane, 2-methyl	86
21.1	Phytol	87
21.4	Hexacosane	93
21.9	Octadecanoic acid, 5-hydroxy	83
22.3	Octacosane	96
22.8	(2,3-Diphenylcyclopropyl)methyl phenyl sulfoxide, trans-	75
23.1	Octacosane	97
23.6	(2,3-Diphenylcyclopropyl)methyl phenyl sulfoxide, trans-	77
23.7	(2,3-Diphenylcyclopropyl)methyl phenyl sulfoxide, trans-	82
23.8	Thiocarbamic acid, N,N-dimethyl, S-1,3-diphenyl-2-butenyl-ester	75
23.9	Octacosane	96
24.8	Octacosane	96
25.7	Octacosane	96
26.6	Octacosane	96
27.0	2,25-Hexacosanedione	79
27.6	Heptacosane	93
28.0	2-Hexadecenal, (2E)	82
28.7	Heptacosane	89

29.9	Heptacosane	81
31.4	Di-n-decylsulfone	69
33.1	1,4-Bis(trimethylsilyl)benzene	71
	Necromass Treated	
3.02	Propanoic Acid	94
3.22	2-Nitrohexane	88
3.31	3-Penten-2-ol	92
3.41	Dicyclopropyl carbinol	85
3.50	Butanamide	84
3.58	3-Hexen-1-ol	92
3.71	2-Pentanol, 4-Methyl	92
3.86	(2,3-Dimethyloxiranyl)Methanol	87
3.94	(2,3-Dimethyloxiranyl)Methanol	84
4.01	Hydroperoxide	82
4.10	Hydroperoxide	85
4.61	1-Hexane, 3-chloro	76
5.01	5,6-Dihydro-4-methoxy-2H-pyran	75
5.31	2-Heptanol, 4-Methyl	83
6.18	4-Chloro-3-methylbut-2-en-1-ol	90
7.61	Undecane	94
10.69	5-isopropyl-6-methyl-hepta-3,5-dien-2-ol	78
10.88	1,2-Decadiene-7,9-dione	65
12.86	3-Chloropropionic acid, hexadecyl ester	81
14.30	Pentanoic acid	81
15.59	6-Octadecenoic acid, methyl ester	81
15.81	Tridecanoic acid	93
16.90	Tridecanoic acid	86
17.32	6-Octadecenoic acid, methyl ester	78
17.71	6-Octadecenoic acid, methyl ester	93
17.94	Hexadecanoic acid, methyl ester	95
19.51	1-Eicosanol	92
19.58	Cyclopropaneoctanoic acid	82
19.64	6-Octadecenoic acid, methyl ester	91
19.87	Methyl stearate	93
23.36	Di-n-octyl phthalate	85

5.4.5 Principal component analysis (PCA)

Principal component analysis (PCA) was conducted on the py-GC-MS TIC data based on peak areas and retention times. Following peak detection and integration, 161 peaks could be identified in the TIC for the starting material in sample HS_00, which the PCA plots are based on in Figure 20. PCA showed several distinct groups. The highly degraded samples and the starting material are separate clusters. HS_05, run at 800 °C and 8 kbar, appears most similar of all samples to the starting material, suggesting a higher retention of the original organic profile, similarly the next closest sample is HS_02, which was run at 300 °C and 5 kbar. The most dissimilar sample from the starting material is HS_04, which was run at the highest temperature 550 °C. The PCA analysis of both the pyrolysis and the extracted solvent appear similar, where there are two distinct clusters of the starting and degradation signatures, respectively. For the solvent extracted samples, several sub-clusters can be distinguished within the degraded cluster, where the ambient pressure experiments are more closely grouped than the 15 kbar experiments. As expected, the time series experiments HS_11 to HS_14 show the most variation with HS_14 being run at the least extreme conditions and more closely resembling the starting signature profile and HS_12, being run for 2 days at 550 °C, showing a degradation profile more similar to ambient and 15 kbar experiments. Based on the comparison of the ambient pressure experiment to the high-pressure experiments, it appears that the effect of pressure can be minimized as after longer durations experiments appear more comparable to ambient pressure experiments.

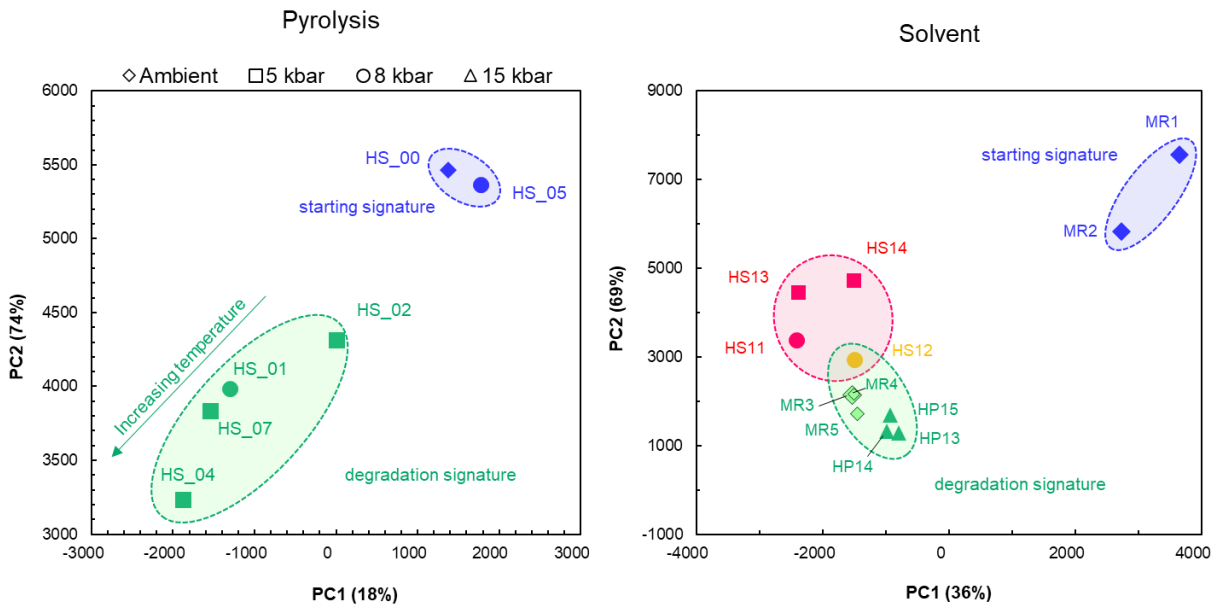

Figure 5.20. PCA analysis of the GC-MS data from high-pressure experiments demonstrates clear degradation signatures at high-pressures. For pyrolysis data, a clear degradation signature can be seen with increasing temperature. For GC-MS solvent injection, a similar trend may be discerned, which is further complicated by time series data, although there is substantial overlap.

5.5. Discussion

Experiments performed on a MOMA flight analog system coupled to a commercial GC-MS reported that such a pyrolysis analysis is not ideally suited to identifying functional compounds and is better reserved for more complex macromolecular materials (Mißbach et al., 2019). Therefore, pyrolysis is appropriate to detect ancient or mature organics synthesized at subsurface conditions. The free portion of organics were obtained by conventional liquid extraction aided by ultrasonication, while the bound and free portion was released by pyrolysis. It should be noted that the intracrystalline portion is likely to be exceptionally small in comparison to the free portion. For organics in petroleum systems, pressure may induce a retardation effect (Price and Wenger, 1992) on the breakdown of organic matter (Blanc and Connan, 1992). A similar increase in preservation potential was noted in this study.

For certain analytes liquid extraction greatly out-performs pyrolysis as an extraction technique, especially at low concentrations and trace levels. Therefore, for this study, where the majority of organics have been lost via diagenetic processes, the two extraction methods are highly complementary for obtaining a fuller conceptual model of the degradation processes. Pyrolysis of *n*-alkanols and *n*-alkanoic acids may yield *n*-alkenes, *n*-alkanals, *n*-alkanones as thermal decomposition products (e.g, Mißbach et al., 2019.) Higher pyrolysis temperatures can produce a variety of byproduct aromatic compounds (Mißbach 2019 et al., 2019), resulting in the aromatic fraction containing not only those derived from kerogen but also aromatics produced by thermal decomposition and aromatization of aliphatic parent organics. A comparison with the liq-GC-MS data indicates a similar relative abundance of *n*-alkanols and *n*-alkanoic acids, suggesting that the parent molecules are accurately represented. Similarly, the proportions of benzene, toluene, naphthalene did not differ greatly between techniques, suggesting that for our samples significant thermal by-products were not produced.

While biomarkers undergo major structural changes during catagenesis (corresponding to temperatures of 50–150°C; Tissot and Welte 1984; Brocks & Summons 2003), they are almost entirely decomposed during metagenesis and metamorphism (corresponding to temperatures of 150–200°C and >200°C, respectively; Tissot and Welte 1984). Sedimentary rocks which have experienced burial metamorphism (i.e., > 200 °C e.g., Price, 1993; Brocks and Summons, 2003, and references therein) may still contain hydrocarbons with >C15. The preservation of biomarkers in natural systems is also influenced by the mineral matrix, including mineral chemistry, lithology (grain size), presence of water, and presence of water and fluid pressures (Price, 1993). The extrapolation of laboratory results to the natural world remains a challenge as

geological timescales are not reproducible within the laboratory (Li et al., 2014).

5.5.1 Generalized pressure-temperature model

In a high-temperature environment, thermal decomposition, cracking, and pyrolysis processes may convert large hydrocarbons to carbocations, which then undergo numerous rearrangements. As shown in the simplified schematic diagram (figure 17), long, straight-chain alkanes may produce shorter chain alkanes as well as branched-chain alkanes (aliphatics), branched alkenes (olefins) and cycloalkanes (naphthenes). A proportion of the smaller products may continue to decompose into gas products, such as ethylene, propylene, butylenes, and isobutylenes. Cycloalkanes may undergo further aromatization to form, for example, benzene, toluene, and xylenes and various branched products. Under moderate elevated pressure and temperature conditions, multiple predominant chemical families are expected to form from cyclic alkanes including normal alkanes (methane, ethane, propane and n-butane), bicyclics, hydroaromatics, and diaramatics (e.g., naphthalene and 1-methylnaphthalene) (e.g., Rakotoalimanana et al., 2017). With increasing pressure, product distributions indicate aromatization reactions and breaking of alkyl side chains becomes more dominant (e.g., Rakotoalimanana et al., 2016, 2017).

It is observed that the percentage of aromatic carbons that increases with pyrolysis temperature is always higher at high-pressure. Furthermore, low pressures favour the concentration of protonated aromatic carbons (Michels et al., 1994) while high-pressure favours the preservation of alkyl-substituted aromatic carbons. Static and shock pressure experiments on phenol and similar compounds demonstrate this class of molecules may be stable at high-pressure

(Allan et al., 2002). Pressure-induced polymerization has been investigated for benzene (Wen et al., 2011, Shinozaki et al., 2014; Fitzgibbons, T. C. et al. 2015), propene (Mugnai et al., 2004a), butadiene (Mugnai et al., 2004b), glycine (Sugahara et al., 2014; Otake et al., 2011) and alanine (Otake et al., 2011; Ohara et al. 2007), and limited temperature stability was defined for PAHs at 1.5–8.0 GPa (Chanyshev et al., 2015, 2017).The oligomerization of the PAHs naphthalene, anthracene, pyrene, and coronene have been studied at ambient pressure and 3.5 GPa with high-temperatures (Chanyshev et al., 2017), with the most intensive oligomerization at both 1 bar and 3.5 GPa occurring at 740–823 K (Chanyshev et al. 2017).

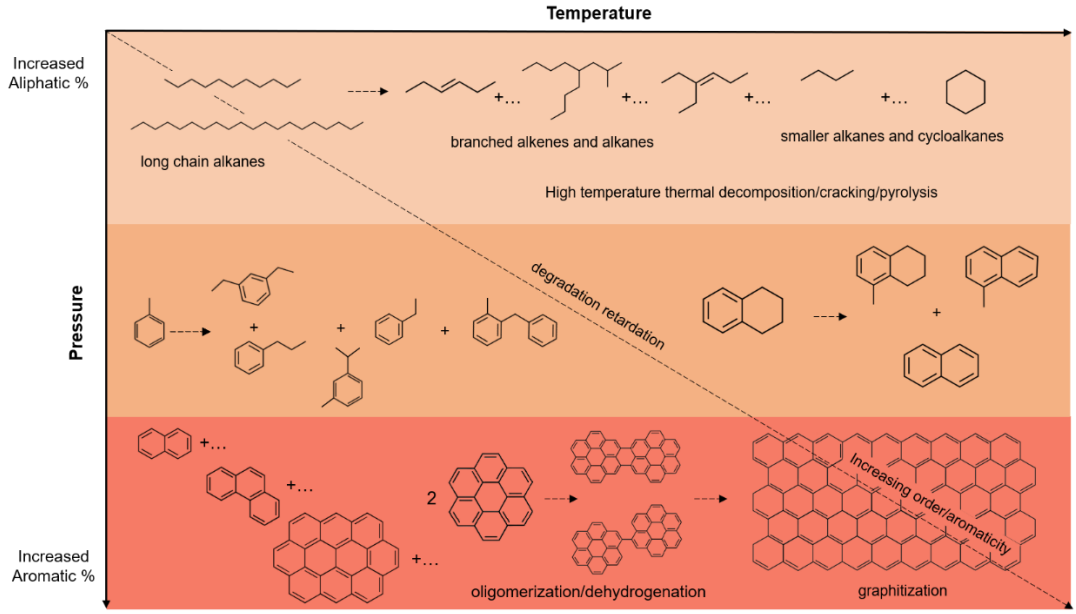

Figure 5.21. Schematic model showing the process of progressive molecular degradation and increased aromaticity under high-pressure conditions. Thermal degradation (pyrolysis, thermolysis, cracking) reactions are shown for high-temperature/low-pressure.

During initial burial, compounds with low preservation potentials, such as nucleic acids and proteins, will degrade into an aliphatic and hydrocarbon-

rich residual mixture. Organic matter may also gradually aromatize under the influence of post burial maturation. Impact events may offer a similar preservation bias, depleting smaller molecules and the aliphatic fraction via volatilization or macromolecule transformation, while stabilized aromatic and polar molecules may persist in the material in a more pristine state. These degradation products may have undergone such extensive transformations that the original composition of the material cannot be deconvoluted. The detection of organic remnants of microbes via degradation products is not straightforward. In the context of searching for biosignatures on Mars, the potential for multiple inputs of biotic and abiotic organic material suggests that highly aromatic meteorite macromolecules, such as PAHs, may coexist with degraded and potentially unrecognizable fossil organic matter. Chemical analysis, particularly by rovers, may therefore superficially imply a Martian organic budget prevailing in either newly formed degradation fragments or aromatized macromolecules not indicative of the original chemical compositions.

5.6 Conclusion

The present experimental study provides insights on the molecular degradation of endolithic biosignatures under burial-induced processes at various pressures and temperatures. Due to surface oxidation and radiation, the Martian subsurface environment is more likely to preserve organic matter and biosignatures than the surface. However, the pressure and temperature associated with meteoric impacts and burial events are expected to alter the original material with many small, volatile molecules strongly affected. The results of this study confirm that different biomarkers follow significantly different degradation pathways during advanced diagenesis and catagenesis.

The influence of pressure can be clearly identified in our experiments, which reveal that it has a stabilizing and preservative influence on organic and biomarker preservation. This likely occurs for multiple reasons, i.e., stabilization of the mineral matrix and stabilization of the organic molecules. Organics analysed from drilling on the Martian surface or excavated from impact events are likely influenced by such preservation biases where thermally metamorphosed or degraded organic matter is preferentially preserved. The effects of thermal degradation and burial pressures on the preservation of biosignatures and other organic compounds must be considered during future life detection missions and in evaluating the overall Martian organic budget.

5.7 Acknowledgments

Thank you to Dr. Nic Odling for technical assistance with XRD analysis, and Dr. Jon Watson for additional sample analysis on py-GC-MS. Thank you to Sean McMahon for providing the necromass starting material. Thank you to Gavin Sim for providing the TOC analysis. Thank you to the W.M. Keck Center and Dr. Timothy Ward for use of the liquid injection GC-MS instrument and undergraduate research students, Christine Rose Ward and Gavisha Mugon for assisting with sample extractions and analysis.

Chapter 6

Future Work

"Science is an ongoing process. It never ends. There is no single ultimate truth to be achieved, after which all the scientists can retire."

Carl Sagan
Cosmos (1980)

The results described in Chapters 2, 3, 4, and 5 have highlighted several potential new research directions open for future investigations. Some future work is discussed below.

- As highlighted in Chapters 2-3 and discussed in more detail in Chapter 4, future investigations of H solubility in NAMs should consider water fugacity as an independent variable decoupled from total pressure. Otsuka and Karato (2011) proposed an experimental setup using a water buffer that could produce the desired control.

- To reduce difficulty deciphering contamination from analyte, future work on C solubility in NAMs should utilize the ^{13}C isotope as the carbon analyte. Similarly, deuterium could be used for H whenever deciphering contamination is a concern.

- In a highly reducing (<IW−3), anhydrous, carbon-rich magma ocean, the dissolved C could potentially take the form C^{4-} as opposed to the hydrous form CH_4. However, no current experiment study has attempted to create this species.

- As highlighted in 2.5.5 Diffusivity of H_2 and H_2O, there is the need for considerably more experimental work on the diffusion of hydrous species in silicate melts under highly reducing conditions in various compositions and under differing P-T conditions.

- In general, experimental petrology investigations into volatiles within NAMs would benefit from extending the pressure range to >5 GPa and ideally to far greater pressures, which would substantially expand the

field of application. Not only would such a pressure regime be applicable to greater mantle pressures for planets within our Solar System, but it would also begin to extend investigations into exo-planetary Super Earths.

- Near the end of the Martian Noachian period between 4.1 and about 3.7 billion years ago, salt-saturated solutions became prevalent in groundwater environments and the surface hydrological environment subsisted. During this transition, brine solutions may have presented a barrier to habitability as well as biosignature preservation. Future work is needed to understand how molecular biosignatures are preserved, degraded, and transformed in such fluid-rich environments. Future research on biosignatures should expand the research in Chapter 5 to investigate the influence of cold, lower-pressure regimes (Figure 6.1). Environments of interest include a dynamic fluid/brine environment, salty glasses, and microfluidic channels. A fundamental investigation into habitability and preservation in such an environment would not only be applicable to Mars, but perhaps even to glassy particles within Enceladus' plumes.

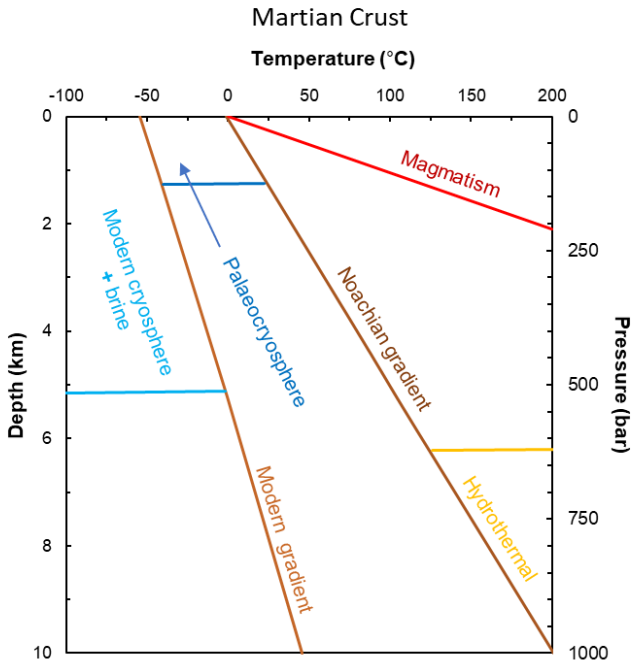

Figure 6.1 Schematic showing pressure-temperature regimes in the modern and ancient Martian crust (Michalski et al., 2013). The Noachian gradient is of particular interest as higher temperatures increase thermal degradation products.

Bibliography

Adam J, Green TH (1994). The effects of pressure and temperature on the partitioning of Ti, Sr and REE between amphibole, clinopyroxene and basanitic melts. *Chem. Geol.* 117, 219–233,

Adam J, Turner M, Hauri EH, Turner S (2016). Crystal/melt partitioning of water and other volatiles during the near–solidus melting of mantle peridotite: comparisons with non–volatile incompatible elements and implications for the generation of intraplate magmatism. *Am. Mineral.* 101, 876–888.

Albarède F (2009). Volatile accretion history of the terrestrial planets and dynamic implications. *Nature* 461, 1227-1233.

Alexander CMO'D (2017). The origin of inner Solar System water. *Philos. Trans. Royal Soc. A*, 375, 20150384.

Alexander CMO'D, McKeegan KD, Altwegg K (2018). Water reservoirs in small planetary bodies: meteorites, asteroids, and comets. *Space Sci. Rev.* 214.

Allan DR, Clark SJ, Dawson A, McGregor PA, Parsons S (2002). Pressure-induced polymorphism in phenol. *Acta Crystallographica B* **58**, 1018–1024.

Anderson DL (1983). Chemical composition of the mantle. *Proceedings, 14th Lunar and Planetary Science Conference* B41–B52.

Arai T, Maruyama S (2017). Formation of anorthosite on the Moon through magma ocean fractional crystallization. Geoscience Frontiers, 8(2), 299-308.

Ardia P, Hirschmann MM, Withers AC, Tenner, TJ (2012). H_2O storage capacity of olivine at 5–8 GPa and consequences for dehydration partial melting of the upper mantle. *Earth. Planet. Sci. Lett.* 348, 104–116.

Armstrong LS, Hirschmann MM, Stanley BD, Falksen EG, and Jacobsen SD (2015). Speciation and solubility of reduced C-O-H-N volatiles in mafic melt: Implications for volcanism, atmospheric evolution, and deep volatile cycles in the terrestrial planets. *Geochim. Cosmochim. Acta* 171, 283-302.

Armstrong K, Frost DJ, McCammon CA, Rubie DC, Boffa Ballaran T (2019). Deep magma ocean formation set the oxidation state of Earth's mantle. *Science* 365, 903-906.

Aubaud C, Hauri EH, Hirschmann MM (2004). Hydrogen partition coefficients between nominally anhydrous minerals and basaltic melts. *Geophys. Res. Lett.* 31.

Aubaud C, Withers AC, Hirschmann MM, Guan Y, Leshin LA, Mackwell SJ, Bell DR (2007). Intercalibration of FTIR and SIMS for hydrogen measurements in glasses and nominally anhydrous minerals. *Am. Min.* 92, 811–828.

Aubaud C, Hirschmann MM, Withers AC, and Hervig, RL (2008). Hydrogen partitioning between melt, clinopyroxene, and garnet at 3 GPa in a hydrous MORB with 6 wt% H_2O. *Contrib. Miner. Petrol.* 156, 607–625.

Bada JL, Miller SL, Zhao M (1995). The stability of amino acids at submarine hydrothermal vent conditions. *Origins Life Evol. Biosph.* 25, 111–118.

Bada JL, Lazcano A (2002). Some like it hot, but not the first biomolecules. *Science* 296, 1982–1983.

Baert K, Meulebroeck W, Wouters H, Cosyns P, Nys K, Thienpont H, and Terryn H. (2011). Using Raman spectroscopy as a tool for the detection of iron in glass. *J Raman Spectrosc* 42, 1789–1795.

Bai Q, Kohlstedt DL (1992). Substantial hydrogen solubility in olivine and implications for water storage in the mantle. *Nature* 357(6380), 672–674.

Bai Q, Kohlstedt DL (1993). Effects of chemical environment on the solubility and incorporation mechanism for hydrogen in olivine. *Phys. Chem. Min.* 19, 460–471.

Balan E, Blanchard E, Lazzeri M, Ingrin J (2014). Contribution of interstitial OH groups to the incorporation of water in forsterite. *Phys. Chem. Min.* 41, 105–114.

Bali E, Bolfan–Casanova N, Koga KT (2008). Pressure and temperature dependence of H solubility in forsterite: an implication to water activity in the Earth interior. *Earth. Planet. Sci. Lett.* 268, 354–363.

Balta JB, Asimow PD, Mosenfelder J L (2011). Hydrous, low-carbon melting of garnet peridotite. *J. Petrol.* 52, 2079-2105.

Barnes JJ, McCubbin FM, Santos AR, Day JMD, Boyce JW, Schwenzer SP, Ott U, Franchi IA, Messenger S, Anand M, Agee CB (2020). Multiple early-formed water reservoirs in the interior of Mars. *Nat. Geosci.* **1**3, 260–264 .

Bédard JH (2014). Parameterizations of calcic clinopyroxene—Melt trace element partition coefficients. *Geochem. Geophys. Geosyst.* 15, 303– 336.

Benner SA, Devine KG, Matveeva LN, Powell DH (2000). The Missing organic molecules on Mars. *Proc. Natl. Acad. Sci. U.S.A.* 97(6), 2425-2430.

Bennett CL, Larson D, Weiland JL, Jarosik N, Hinshaw G, Odegard N, Smith KM, Hill RS, Gold B, Halpern M, Komatsu E, Nolta MR, Page L, Spergel DN, Wollack E, Dunkley J, Kogut A, Limon M, Meyer, SS, Tucker GS, Wright EL (2013). Nine-year Wilkinson Microwave Anisotropy Probe (WMAP) observations: final maps and results. *Astrophys. J. Suppl. Ser.* 208, 54.

Berry AJ, Hermann J, O'Neill HSC, Foran GJ (2005). Fingerprinting the water site in mantle olivine. *Geology* 33, 869–872.

Berry AJ, O'Neill HSC, Hermann J, Scott DR (2007). The infrared signature of water associated with trivalent cations in olivine. *Earth. Planet. Sci. Lett.* 261, 134–142.

Bertka CM and Fei Y (1997). Mineralogy of the martian interior up to core-mantle boundary pressures. *J Geophys Research* 102, 5251–5264.

Bezmen NI, Gorbachev PN, Shalynin AI, Asif M, Naldrett AJ (2008). Solubility of Platinum and Palladium in Silicate Melts under High Water Pressure as a Function of Redox Conditions. *Petrology* 16, 2, 161–176.

Bezmen NI, Zharikov VA, Zavelsky VO, and Kalinichev AG (2005). Melting of Alkali Aluminosilicate Systems under Hydrogen–Water Fluid Pressure, Platinum at = 2 kbar. *Petrologiya* 13, 451–472.

Bisceglia E, Micca G, Longo S (2017). Thermal decomposition rate of MgCO3 as an inorganic astrobiological matrix in meteorites. *Int. J. Astrobiology* 16(2), 130136.

Blanc P, Connan J (1992). Origin and occurrence of 25-norhopanes: a statistical study. *Org. Geochem.* 18, 813-828

Bland PA, Smith TB (2000). Meteorite Accumulations on Mars. *Icarus*, 144(1), 21-26.

Boctor NZ, Alexander CMO'D, Wang J, Hauri E (2003). The sources of water in Martian meteorites: clues from hydrogen isotopes. *Geochim. Cosmochim. Acta,* 67, 3971- 3989.

Borg LE, Nyquist LE, Wiesmann H, Shih CY, Reese Y (2003). The age of Dar al Gani 476 and the differentiation history of the martian meteorites inferred from their radiogenic isotopic systematics. *Geochim. Cosmochim. Acta*, 67, 3519-3536

Borisov A and Palme H (1995). The Solubility of Iridium in Silicate Melts: New Data from Experiments with Ir10Platinum 90 Alloys. *Geochim. Cosmochim. Acta* 59, 481–485.

Borisov A and Palme H (1997) Experimental determination of the solubility of Pt in silicate melts. *Geochim. Cosmochin Acta* 61, 4349–4357.

Borisov A, Pack A, Kropf A, Palme H (2008). Partitioning of Na between olivine and melt: an experimental study with application to the formation of meteoritic Na2O-rich chondrule glass and refractory forsterite grains.
Geochim. Cosmochin Acta, 72, 5558-5573.

Boynton WV, Ming DW, Kounaves SP, Young SM, Arvidson RE, Hecht MH, Hoffman J, Niles PB, Hamara DK, Quinn RC, Smith PH, Sutter B, Catling DC, Morris RV. (2009). Evidence for Calcium Carbonate at the Mars Phoenix Landing Site. *Science* 325(5936):61–64.

Brett R and Sato M (1984) Intrinsic oxygen fugacity measurements on seven chondrites, a pallasite and a tektite and the redox state of meteorite parent bodies.
Geochim. Cosmochin 48, 111-120.

Brocks, J. J. and Summons, R. E. (2003). Biomarkers for Early Life. In W. H. Schlesinger (ed.), Biogeochemistry. Elsevier, Oxford, 63–115.

Bromiley GD, Brooke J, and Kohn SC (2017). Hydrogen and deuterium diffusion in nonstoichiometric spinel. *High Press. Res.* 37, 360–376.

Brooker R, Holloway JR, and Hervig R (1998). Reduction in piston-cylinder experiments: The detection of carbon infiltration into platinum capsules. *Am Min*, 83, 985–994.

Buck WR, Toksöz MN (1980). The bulk composition of the Moon based on geophysical constraints. *Proceedings of Lunar and Planetary Science Conference* 11th, 2043.

Canil D (2002). Vanadium in peridotites, mantle redox and tectonic environments: Archean to present. *Earth Planet. Sci. Lett.* 195, 75–90.

Carmichael ISE, Ghiorso MS (1986). Oxidation–reduction relations in basic magma: a case for homogeneous equilibria. *Earth Planet. Sci. Lett.* 78, 200–210.

Carr MH, Head JW (2010). Geologic history of Mars. *Earth Planet Sci Lett* 294, 185–203.

Cartier C, Hammouda T, Doucelance R, Boyet M, Devidal J, Moine B (2014). Experimental study oftrace element partitioning between enstatite and melt in enstatite chondrites at low oxygen fugacities and 5 GPa. *Geochim. Cosmochim. Acta*, 130, 167–187.

Chanyshev AD, Litasov KD, Shatskiy AF, Ohtani E (2015). In situ X-ray diffraction study of polycyclic aromatic hydrocarbons at pressures of 7-15 GPa: Implication to deep-seated fluids in the Earth and planetary environments. *Chem. Geol.* 405, 39–47.

Chanyshev AD, Litasov KD, Shatskiy AF, Sharygin IS, Higo Y, Ohtani E (2017). Transition from melting to carbonization of naphthalene, anthracene, pyrene and coronene at high-pressure. *Phys. Earth Planet. Inter.* 270, 29–39. doi:10.1016/j.pepi.2017.06.011.

Chen Y, Zhang YX, Liu Y, Guan YB, Eiler J, Stolper EM (2015). Water, fluorine, and sulfur concentrations in the lunar mantle. *Earth Planet. Sci. Lett.*, 427, 37-46.

Chi H, Dasgupta R, Duncan MS, Shimizu N (2014). Partitioning of carbon between Fe-rich alloy melt and silicate melt in a magma ocean – implications for the abundance and origin of volatiles in Earth, Mars, and the Moon. *Geochim. Cosmochim. Acta* 139, 447–471.

Chyba C, Sagan C (1992). Endogenous production, exogenous delivery and impact-shock synthesis of organic molecules: an inventory for the origins of life. *Nature.* 355. 125–132.

Cockell CS, Balme M, Bridges JC, Davila A, Schwenzer SP (2012). Uninhabited habitats on Mars. *Icarus* 217, 184–193.

Cockell CS, Bush T, Bryce C, Direito S, Fox-Powell M, Harrison JP, Lammer H, Landenmark H, Martin Torres J, Nicholson N, Noack L, O'Malley-James J, Payler SJ, Rushby A, Samuels T, Schwendner P, Wadsworth J, Zorzano MP (2016). Habitability: a review. *Astrobio.* 16, 89–117.

Cottin H, Kotler JM, Bartik K, Cleaves HJ, Cockell CS, de Vera JPP., Ehrenfreund P, Leuko S, Ten Kate IL, Martins Z, Pascal R, Quinn R, Rettberg P, and Westall, F (2015). Astrobiology and the possibility of life on earth and elsewhere. *Space. Sci. Rev.* doi:10.1007/s11214-015- 0196-1.

Craddock PR, Le Doan TV, Bake KD, Polyakov M, Charsky AM, Pomerantz AE (2015). Evolution of kerogen and bitumen during thermal maturation by semi-open pyrolysis investigated by infrared spectroscopy. *Energy Fuel,* 29, 2197-2210,

D'Elia M, Blanco A, Galiano A, Orofino V, Fonti S, Mancarella F, Guido A, Russo F, Mastandrea A (2017). SEM morphological studies of carbonates and the search for ancient life on Mars *Int. J. Astrobiol.* 16 (2) (2017), 137142.

Dalou C, Hirschmann MM, von der Handt A, Mosenfelder J, Armstrong LS (2017). Nitrogen and carbon fractionation during core–mantle differentiation at shallow depth. *Earth Planet Sci Lett* 458(15), 141-151.

Dann JC, Holzheid AH, Grove TL, McSween HY (2001). Phase equilibria of the Shergotty meteorite: constraints on pre-eruptive water contents of Martian magmas and fractional crystallization under hydrous conditions. *Meteorit. Planet. Sci.,* 36, 793-806

Danyushevsky LV (2001). The effect of small amounts of H_2O on crystallisation of mid-ocean ridge and backarc basin magmas. *J. Volcanol. Geotherm. Res.,* 110, 265-280.

Dartnell LR (2011). Ionizing radiation and life. *Astrobio.* 11, 551–582.

Dasgupta R, Nelson JD, Chi H, Ding S, Li Y, Duncan MS, Tsuno K (2014). Carbon in the Martian interior: Core-mantle fractionation and extraction by mantle melting at oxidized conditions (abstract #1012) Workshop on Volatiles in the Martian Interior, 3-4 November, Houston, Texas. LPI Contribution No. 1819.

Dauphas N and Morbidelli A (2014). Geochemical and planetary dynamical views on the origin of Earth's atmosphere and oceans. *Treatise on geochemistry*, 2nd ed, 6 (eds HD Holland, KK Turekian), Oxford, UK: Elsevier, 1–35.

De Hoog CM, Gall L, Cornell DH (2010). Trace–element geochemistry of mantle olivine and application to mantle petrogenesis and geothermobarometry. *Chem. Geol.* 270, 196–215.

Debaille V, Brandon AD, Yin QZ, Jacobsen B (2007). Coupled ^{142}Nd-^{143}Nd evidence for a protracted magma ocean in Mars. *Nature* 450, 525-528.

Demouchy S, Bolfan–Casanova N (2016). Distribution and transport of hydrogen in the lithospheric mantle: a review. *Lithos* 240, 402–425.

Deng J, Du Z, Karki B, Ghosh D, Lee K (2020). A magma ocean origin to divergent redox evolutions of rocky planetary bodies and early atmospheres. *Nat Commun* 11.

Dobson P, Skogby H, Rossman GR (1995). Water in boninite glass and coexisting orthopyroxene: concentration and partitioning. *Contrib. Miner. Petrol.* 118, 414–419.

Dreibus G, Wanke H (1985). Mars, a volatile rich planet. *Meteoritics* 20, 367-381.

Eggler DH and Baker DR (1982) Reduced volatiles in the system C–O–H: implications to mantle melting,fluid formation, and diamond genesis. *High Press. Res. Geophys.* 237-250.

Ehlmann BL, Mustard JF, Clark RN, Swayze GA, Murchie SL (2011). Evidence for Low Grade Metamorphism, Hydrothermal Alteration, and Diagensis on Mars from Phyllosilicate Mineral Assemblages. *Clays Clay Miner.* 59(4), 359-377.

Eigenbrode JL, Summons RE, Steele A, Freissinet C, Millan M, Navarro-González R, Sutter B et al., (2018). Organic matter preserved in 3-billion-year-old mudstones at Gale crater, Mars. *Science* 360(6393), 1096–1101.

Elardo SM, Draper DS, Shearer CK (2011). Lunar Magma Ocean crystallization revisited: Bulk composition, early cumulate mineralogy, and the source regions of the highlands Mg-suite. *Geochim. Cosmochim. Acta* . 75(11), 3024–3045.

Elkins-Tanton, LT (2008). Linked magma ocean solidification and atmospheric growth for Earth and Mars. *Earth Planet Sci Lett* 271, 181–191.

Elkins-Tanton, LT (2012). (2012). Magma Oceans in the Inner Solar System. *Annu. Rev. Earth Planet. Sci.* 40(1), 113-139.

Ertel W, O'Neill HStC, Sylvester PJ, and Dingwell DB (1999). Solubilities of Platinum and Rh in a Haplobasaltic Silicate Melt at 1300 °C. *Geochim. Cosmochim. Acta* 63, 2439–2449.

Ertel WM, Walter J, Drake MJ, and Sylvester PJ (2006). Experimental Study of Platinum Solubility in Silicate Melt to 14 GPa and 2273 K: Implications for Accretion and Core Formation in the Earth. *Geochim. Cosmochim. Acta* 70, 2591–2602.

Ertem G, Ertem M, McKay C, Hazen R (2017). Shielding biomolecules from effects of radiation by Mars analogue minerals and soils. *Int. J. Astrobiology* 16(3), 280-285.

Eugster HP (1957). Heterogeneous Reactions Involving Oxidation and Reduction at High pressures and Temperatures. *J. Chem. Phys.* 26(6), 1760–1761.

Eugster HP, Wones DR (1962). Stability Relations of the Ferruginous Biotite, Annite. *J. Petrol.* 3(1), 82–125.

Farmer JD, Des Marais DJ (1999). Exploring for a record of ancient Martian life. *J. Geophys. Res. Planets* 104 (E11), 26977-26995.

Fegley B. (2012) Practical Chemical Thermodynamics for Geoscientists. Elsevier Science.

Férot A, Bolfan–Casanova N (2012). Water storage capacity in olivine and pyroxene to 14GPa: implications for the water content of the Earth's upper mantle and nature of seismic discontinuities. *Earth. Planet. Sci. Lett.* 349–350:218–230.

Filiberto J (2008). Experimental constraints on the parental liquid of the Chassigny meteorite: A possible link between the Chassigny meteorite and a Martian Gusev basalt. *Geochim. Cosmochim. Acta* 72, 690–701.

Filiberto J, Musselwhite DS, Gross J, Burgess K, Le L, Treiman AH (2010a). Experimental petrology, crystallization history, and parental magma characteristics of olivine-phyric shergottite NWA 1068: implications for the petrogenesis of "enriched" olivine-phyric shergottites. *Meteorit. Planet. Sci.* 45, 1258-1270.

Filiberto J, Dasgupta R, Kiefer WS, Treiman AH (2010b). High-pressure, near-liquidus phase equilibria of the Home Plate basalt Fastball and melting in the Martian mantle. *Geophys. Res. Lett.* 37, L13201.

Filiberto J, Baratoux JD, Beaty D, Breuer D, Farcy B, Grott M, Jones J, Keifer W, McCubbin F, and Schwenzer S (2016). A review of volatiles in the Martian interior. *Meteoritics Planet. Sci.,* doi:10.1111/maps.12680.

Fitzgibbons TC, Guthrie M, Xu ES, Crespi VH, Davidowski SK, Cody GD, Alem N, Badding JV (2015). Benzene-derived carbon nanothreads. *Nat. Mat.* 14, 43–47 (2015).

Frost BR (1991). An introduction to oxygen fugacity and its petrologic importance. *Mineralogical Society of America, Reviews in Mineralogy* 25, 1-9.

Frost DJ, Liebske C, Langenhorst F, McCammon CA, Trønnes RG, Rubie DC (2004). Experimental evidence for the existence of iron-rich metal in the Earth's lower mantle. *Nature* 248**,** 409–412

Frost DJ, McCammon CA (2008). The Redox State of Earth's Mantle. *Annu. Rev. Earth Planet. Sci.* 36(1), 389–420.

Gaetani GA, Grove TL (1998). The influence of water on melting of mantle peridotite. *Contrib. Miner. Petrol.* 131, 323–346.

Gaetani GA, O'Leary JA, Koga KT, Hauri EH, Rose-Koga EF, Monteleone BD (2014). Hydration of mantle olivine under variable water and oxygen fugacity conditions. *Contrib. Miner. Petrol.* 167, 965.

Gaillard F, Scaillet B (2014). A theoretical framework for volcanic degassing chemistry in a planetology perspective and implications for planetary atmospheres. *Earth Planet. Sci. Lett.* 403, 307–316.

Gaillard F, Scaillet B, Pichavant M, Iacono-Marziano G (2015). The redox geodynamics linking basalts and their mantle sources through space and time. *Chem. Geol.* 418, 217–233

Giese CC, Ten Kate IL, Plümper O, King HE, Lenting C, Liu Y, Tielens AGGM (2019). The evolution of polycyclic aromatic hydrocarbons under simulated inner asteroid conditions. *Meteorit Planet Sci* 54, 1930-1950.

Giesting PA, Schwenzer SP, Filiberto J, Starkey NA, Franchi IA, Treiman AH, Tindle AG, Grady MM (2015). Igneous and shock processes affecting chassignite amphibole evaluated using chlorine/water partitioning and hydrogen isotopes. *Meteor. Planet. Sci.*, 50, 433-460

Giordano D, Russell JK, Dingwell DB (2008) Viscosity of magmatic liquids: a model. *Earth Planet. Sci. Lett.* 271 (1–4) (2008), 123-134.

Goesmann F, Brinckerhoff WB, Raulin F, Goetz W, Danell RM, Getty SA, Siljeström S, Mißbach H, Steininger H, Arevalo RD Jr, Buch A, Freissinet C, Grubisic A, Meierhenrich UJ, Pinnick VT, Stalport F, Szopa C, Vago JL, Lindner R, Schulte MD, Brucato JR, Glavin DP, Grand N, Li X, van Amerom FHW. (2017) The Mars Organic Molecule Analyser (MOMA) instrument: characterization of organic material in martian sediments. Astrobiology 17:655–685.

Goudge TA, Mustard JF, Head JW, Fassett CI, Wiseman SM. (2015). Assessing the mineralogy of the watershed and fan deposits of the Jezero crater paleolake system, Mars. *J. Geophys. Res.* 120, 775-808.

Grant KJ, Kohn SC, Brooker RA (2006). Solubility and partitioning of water in synthetic forsterite and enstatite in the system MgO–SiO2–H2O ± Al2O3. *Contrib. Miner. Petrol.* 151, 651–664.

Grant KJ, Kohn SC, Brooker RA (2007a). The partitioning of water between olivine, orthopyroxene and melt synthesised in the system albite-forsterite-H2O. *Earth Planet. Sci. Lett.* 260 (12), 227-241.

Grant KJ, Brooker RA, Kohn SC, Wood BJ (2007b). The effect of oxygen fugacity on hydroxyl concentrations and speciation in olivine: implications for water solubility in the upper mantle. *Earth. Planet. Sci. Lett.* 261, 217–229.

Grant JA, Golombek MP, Wilson SA, Farley KA, Williford KH, Chen A (2018). The science process for selecting the landing site for the 2020 Mars rover. *Planet. Space Sci.*, doi: 10.1016/j.pss.2018.07.001.

Green TH, Blundy JD, Adam J, Yaxley GM (2000). SIMS determination of trace elements partition coefficients between garnet, clinopyroxene and hydrous basaltic liquids at 2-7.5 GPa and 1080-1200 °C. *Lithos*, 53, 165–187.

Grewal DS, Dasgupta R, Holmes AK, Costin G, Li Y, Tsuno K (2019). The fate of nitrogen during core mantle separation on Earth. *Geochim. Cosmochim. Acta* 251, 87–115.

Grewal DS, Dasgupta R, Farnell A (2020). The speciation of carbon, nitrogen, and water in magma oceans and its effect on volatile partitioning between major reservoirs of the Solar System rocky bodies. *Geochim. Cosmochim. Acta*, 280, 281-301.

Gross J, Filiberto J, Bell AS (2013). Water in the martian interior: evidence for terrestrial MORB mantle like volatile contents from hydroxyl-rich apatite in olivine–phyric shergottite NWA-6234. *Earth Planet. Sci. Lett.* 369–370, 120-128

Grossman L, Beckett JR, Fedkin AV, Simon SB, Ciesla FJ (2008). Redox conditions in the solar nebula: Observational, experimental, and theoretical constraints. In Oxygen in the solar system, edited by MacPherson GJ, Mittlefehldt DW, Jones JH, Simon SB. *Reviews in Mineralogy and Geochemistry 68,* 93-140.

Halevy I, Fischer WW, Eiler JM (2011). Carbonates in the Martian meteorite Allan Hills 84001 formed at 18 ± 4 ◦ C in a near-surface aqueous environment. *Proc. Natl. Acad. Sci. U.S.A.* 108, 16895–99.

Hallis LJ, Taylor GJ, Nagashima K, Huss GR (2012). Magmatic water in the martian meteorite Nakhla. *Earth. Planet. Sci. Lett.* 359–360, 84-92.

Hart SR, Zindler A (1986). In search of a bulk-earth composition. *Chem. Geol.* 57, 247- 267.

Hassler DM, Zeitlin C, Wimmer-Schweingruber RF, Ehresmann B, Rafkin S, Eigenbrode JL, Brinza DE, Weigle G, Böttcher S, Böhm E, Burmeister S, Guo J, Köhler J, Martin C, Reitz G, Cucinotta FA, Kim MH, Grinspoon D, Bullock MA, Posner A, Gómez-Elvira J, Vasavada A, Grotzinger JP; MSL Science Team. Mars' surface radiation environment measured with the Mars Science Laboratory's Curiosity rover. (2014) Mars' surface radiation environment measured with the Mars Science Laboratory's Curiosity Rover. *Science* 343 10.1126/science.1244797.

Hauri EH, Gaetani GA, Green TH (2006). Partitioning of water during melting of the Earth's upper mantle at H2O–undersaturated conditions. *Earth. Planet. Sci. Lett.* 248, 715–734.

Hauri EH, Weinreich T, Saal AE, Rutherford MC, Van Orman JA (2011). High pre-eruptive water contents preserved in lunar melt inclusions. *Science,* 333, 213-215

Herd CDK (2008). Basalts as Probes of Planetary Interior Redox State. (2008). *Rev. Mineral. Geochem.* 68(1), 527–553.

Hirschmann MM, Aubaud C, Withers AC (2005). Storage capacity of H2O in nominally anhydrous minerals in the upper mantle. *Earth Planet. Sci. Lett.* 236(1), 167-181.

Hirschmann MM and Withers AC (2008). Ventilation of CO2 from a reduced mantle and consequences forthe early Martian greenhouse. *Earth Planet. Sci. Lett.,* 270, 147-155.

Hirschmann MM, Tenner T, Aubaud C, Withers AC (2009). Dehydration melting of nominally anhydrous mantle: the primacy of partitioning. *Phys. Earth Planet. Inter.* 176, 54-68.

Hirschmann MM, Withers AC, Ardia, P, Foley NT (2012). Solubility of molecular hydrogen in silicate melts and consequences for volatile evolution of terrestrial planets. *Earth Planet. Sci. Lett.* 345, 348, 38-48.

Hofmann AW (1988). Chemical differentiation of the Earth: The relationship between mantle, continental crust, and oceanic crust. *Earth Planet. Sci. Lett.* 90, 297–314.

Holland T, Powell R (1991). Compensated-Redlich-Kwong (CORK) equation for volumes and fugacities of CO2 and H2O in the range 1 bar to 50 kbar and 100–1600°C. *Contr. Mineral. and Petrol.*, 109, 265–273.

Holland HD (2002). Volcanic gases, black smokers, and the great oxidation event. *Geochim. Cosmochim. Acta* 66, 3811–3826.

Holland T, Powell R (2003). Activity-composition relations for phases in petrological calculations: an asymmetric multicomponent formulation. *Contrib. Mineral. Petrol.* 145(4), 492–501.

Holloway JR, Pan V, Gudmundsson G (1992). High-pressure fluid-absent melting experiments in the presence of graphite: oxygen fugacity, ferric/ferrous ratio and dissolved CO2. *Eur. J. Mineral.* 4, 105-114

Holloway JR, Wood BJ (1988). *Simulating the Earth: Experimental Geochemistry.* Boston, MA: Unwin Hyman, 72–73.

Holzheid, A and O'Neill HSC (1995). The Cr-Cr2O3 oxygen buffer and the free energy of formation 517 of Cr2O3 from high-temperature electrochemical measurements. *Geochim. Cosmochim. Acta,* 59(3), 475-479.

Horgan BHN, Anderson RB, Dromart G, Amador ES, Rice MS (2020). The mineral diversity of Jezero crater: Evidence for possible lacustrine carbonates on Mars. *Icarus* 339, 113526.

Hu R, Kass DM, Ehlmann BL, Yung YL (2015). Tracing the fate of carbon and the atmospheric evolution of Mars. *Nat. Commun.* 6, 10003.

Jakobsson S (2012). Oxygen fugacity control in piston-cylinder experiments. *Contrib. Mineral. Petrol.*164(3), 397–406.

Jakobsson S, Blundy J, and Moore G (2014). Oxygen fugacity control in piston-cylinder experiments: a revaluation. *Contrib. Mineral. Petrol.* 167(6), 1007.

Jean J (1930). The Mysterious Universe (1930), Pelican Books.

Jefferys WH, and Berger JO (1992). Ockham's razor and Bayesian analysis. *Am. Sci.* 80, 64–72.

Jenner FE, O'Neill HSC, Arculus RJ, Mavrogenes JA (2010). The magnetite crisis in the evolution of arc related magmas and the initial concentration of Au, Ag and Cu. *J. Petrol.* 51, 2445–2464

Jones JH, Delano JW (1989) A three component model for the bulk composition of the Moon. *Geochim. Cosmochim. Acta*, 53, 513–527.

Ingrin J, Liu J, Depecker C, Kohn SC, Balan E, Grant KJ (2013) Low–temperature evolution of OH bands in synthetic forsterite, implication for the nature of H defects at high pressure. *Phys. Chem. Miner.* 40(6), 499–510.

Karlsson HR, Clayton RN, Gibson EK, Mayeda, TK (1992). Water in SNC meteorites: evidence for a Martian hydrosphere. *Science,* 255, 1409-1411.

Karner JM, Sutton SR, Papike JJ, Shearer CK, Jones JH, Newville M (2006). Application of a new vanadium valence oxybarometer to basaltic glasses from the Earth, Moon, and Mars. *Am. Min.,* 91, 270–277.

Karunadasa KSP, Manoratne CH, Pitawala HMTGA, Rajapakse RMG (2017). Thermal decomposition of calcium carbonate (calcite polymorph) as examined by in-situ high temperature X-ray powder diffraction. *J. Phys. Chem. Solids* 134, 21-28,

Keppler H, Wiedenbeck M, Shcheka SS (2003). Carbon solubility in olivine and the mode of carbon storage in the Earth's mantle. *Nature*, 424, 414-416.

Keppler, H. and Smyth, J.R., Eds. (2006). Water in Nominally Anhydrous Minerals, vol. 62. Reviews of Mineralogy and Geochemistry, Mineralogical Society of America, Chantilly, Virginia.

Khan A, Connolly JAD (2008). Constraining the composition and thermal state of Mars from inversion of geophysical data. *J. Geophys. Res.* 113, E07003.

Koga K, Hauri EH, Hirschmann M, Bell DR (2003). Hydrogen concentration analyses using SIMS and FTIR: comparison and calibration for nominally anhydrous minerals. *Geochem Geophys Geosys* 4.

Kohlstedt DL, Keppler H, Rubie DC (1996). Solubility of water in the α, β and γ phases of (Mg, Fe)2SiO4. *Contrib. Miner. Petrol.* 123, 345–357.

Kovács I, O'Neill HStC, Hermann J, and Hauri EH (2010). Site-specific infrared O-H absorption coefficients for water substitution into olivine. *Am. Min.* 95, 292–299.

Kovács, I, Green DH, Rosenthal A, Hermann J, O'Neill H, Hibberson WO, Udvardi B (2012). An experimental study of water in nominally anhydrous minerals in the upper mantle near thewater saturated solidus. *J. Petrol.,* 53, 2067–2093.

Kröger FA, Vink HH (1956). Relations between the concentrations of imperfections in crystalline solids. Seitz F, Turnbull D (eds) Solid state physics. Academic Press, New York.

Kumamoto KM, Warren JM, and Hauri EH (2017). New SIMS reference materials for measuring waterin upper mantle minerals. *Am. Min.* 102(3): 537-547.

Kushiro I (1975). On the nature of silicate melt and its significance in magma genesis: regularities in the shift of liquidus boundaries involving olivine, orthopyroxene and silica minerals. *Am. J. Sci.* 275, 411-431.

Larimer JW and Buseck PR (1974). Equilibration temperatures in enstatite chondrites. *Geochim. Cosmochim. Acta*, 38 (1974), 471-477.

Lasne, J. Noblet A, Szopa C, Navarro-González R, Cabane M, Poch O, et al. (2016). Oxidants at the surface of Mars: a review in light of recent exploration results. *Astrobiology* 16, 977–996.

Le Losq C, Mysen BO, Cody GD (2015). Water and magmas: insights about the water solution mechanisms in alkali silicate melts from infrared, Raman, and 29Si solid-state NMR spectroscopies. *Prog. Earth Planet. Sci.* 2, 22

Lemaire C, Kohn SC, Brooker RA (2004). The effect of silica activity on the incorporation mechanisms of water in synthetic forsterite: a polarised infrared spectroscopic study. *Contrib. Miner. Petrol.* 147, 48–57.

Lentz RFC, McSween JY, Ryan J, Riciputi LR (2001). Water in Martian magmas: clues from light lithophile elements in shergottite and nakhlite pyroxenes. *Geochim. Cosmochim. Acta*, 65, 4551 4565

Leshin LA, Epstein S, Stolper, EM (1996). Hydrogen isotope geochemistry of SNC meteorites *Geochim. Cosmochim. Acta*, 60, 2635-2650.

Li ZXA, Lee CTA (2004) The constancy of upper mantle fO2 through time inferred from V/Sc ratios inbasalts. *Earth Planet. Sci. Lett.* 228, 483–493.

Li J, Bernard S, Benzerara K, Beyssac O, Allard T, Cosmidis J, Moussou J (2014). Impact of biomineralization on the preservation of microorganisms during fossilization: An experimental perspective. *Earth Planet. Sci. Lett.* 400, 113-122,

Li Y, Dasgupta R, Tsuno K (2015). The effects of sulfur, silicon, water, and oxygen fugacity on carbon solubility and partitioning in Fe-rich alloy and silicate melt systems at 3 GPa and 1600 °C: implications for core-mantle differentiation and degassing of magma oceans and reduced planet. *Earth Planet. Sci. Lett.* 415, 54-66.

Li Y, Dasgupta R, Tsuno K, Monteleone B, Shimizu N (2016). Carbon and sulfur budget of the silicate Earth explained by accretion of differentiated planetary embryos. *Nat. Geosci.* 781-785.

Lin Y, Hui H, Li Y, Xu Y, van Westrenen W (2019). A lunar hygrometer based on plagioclase-melt partitioning of water. *Geochem. Perspect. Lett.,* 10, 14-19.

Lodders K, Fegley B (1997). An oxygen isotope model for the composition of Mars. *Icarus* 126, 373–394.

Lognonné P, Gagnepain-Beyneix J, Chenet H (2003). A new seismic model of the Moon: implications for structure, thermal evolution and formation of the Moon. *Earth Planet. Sci. Lett.* 211, 27-44.

Longhi J, Pan V (1989). The parent magmas of the SNC meteorites. 19th Lunar and Planetary Conference Houston, TX, 451-464.

Longhi J. (2006) Petrogenesis of picritic mare magmas: Constraints on the extent of early lunar differentiation. *Geochim. Cosmochim. Acta* 70, 5919–5934.

Lu R, and Keppler H. (1997). Water solubility in pyrope to 100 kbar. *Contrib. Miner. Petrol.* 129: 35–42.

Luth RW, Mysen BO, and Virgo D (1987). Raman spectroscopic study of the solubility behavior of H2 in the system Na2O—Al2O3—SiO2—H2. *Am. Min.* 72, 481-486.

Lyubetskaya T, Korenaga J (2007). Chemical composition of Earth's primitive mantle and its variance: 1. Method and results. *J. Geophys. Res.* 112(B3), B03211.

Marshall-Bowman K, Ohara S, Sverjensky DA, Hazen RM, Cleaves HJII (2010). Catalytic peptide hydrolysis by mineral surface: implications for prebiotic chemistry. *Geochim. Cosmochim. Acta* 74, 5852–5861.

Matjuschkin V, Brooker RA, Tattitch B, Blundy JD, and Stamper CC (2015). Control and monitoring of oxygen fugacity in piston cylinder experiments. *Contrib. Miner. Petrol.* 169(1), 9.

Matveev S, O'Neill HSTC, Ballhaus C, Taylor WR, Green DH (2001). Effect of silica activity on OH– IR spectra of olivine: implications for low–aSiO2 mantle metasomatism. *J. Petrol.* 42, 721–729.

McCammon, CA, Griffin WL, Shee SR, O'Neill HSC (2001). Oxidation during metasomatism in ultramafic xenoliths from the Wesselton kimberlite, South Africa: implications for the survival of diamond. *Contrib. Mineral. Petrol.* 141, 287–296.

McCollom TM, Seewald JS (2007). Abiotic synthesis of organic compounds in deep-sea hydrothermal environments. *Chem Rev.* 107(2), 382-401.

McCubbin FM, Smirnov A, Nekvasil H, Wang J, Hauri E, Lindsley DH (2010). Hydrous magmatism on Mars: a source of water for the surface and subsurface during the Amazonian. *Earth Planet. Sci. Lett.,* 292, 132-138.

McCubbin FM, Hauri EH, Elardo SM, Vander Kaaden KE, Wang J, Shearer CK (2012). Hydrousmelting of the martian mantle produced both depleted and enriched shergottites. *Geology,* 40, 683-686.

McCubbin FM, Elardo SM, Shearer CK, Smirnov A, Hauri EH, Draper DS (2013). A petrogenetic model for the comagmatic origin of chassignites and nakhlites: inferences from chlorine-rich minerals, petrology, and geochemistry. *Meteorit. Planet. Sci.,* 48, 819-853.

McCubbin FM, Boyce JW, Srinivasan P, Santos AR, Elardo SM, Filiberto J, Steele A, Shearer CK (2016). Heterogeneous distribution of H2O in the Martian interior: Implications for the abundance of H2O in depleted and enriched mantle sources. *Meteorit. Planet. Sci.,* doi:10.1111/maps.12639

McCubbin FM, Vander Kaaden KE, Peplowski PN, Bell AS, Nittler LR, Boyce JW, Evans LG, Keller LP, Elardo SM, McCoy, TJ (2017). A low O/Si ratio on the surface of Mercury: evidence for silicon smelting? *J. Geophys. Res., Planets*, 122, 2053-2076

McCubbin FM, Barnes JJ (2019). Origin and abundances of H2O in the terrestrial planets, Moon, and asteroids. *Earth Planet. Sci. Lett.* 526, 115771.

McDade P, Wood BJ, van Westrenen W, Brooker R, Gudmundsson G, Soulard H, Najorka J, Blundy J (2002). Pressure corrections for a selection of piston-cylinder cell assemblies. *Min. Mag.* 66(6), 102–1028.

McDonough WF and Sun SS (1995). Composition of the Earth. *Chem. Geol.* 120: 223-253.

McKay DS, Thomas-Keprta KL, Clemett SJ, Gibson EK, Spencer L, Wentworth SJ (2009) Life on Mars: new evidence from martian meteorites. *Proc SPIE* 7441, doi:10.1117/12.832317.

McSween HY, Grove TL, Lentz RCF, Dann JC, Holzheid AH, Riciputi LR, Ryan JG (2001). Geochemical evidence for magmatic water within Mars from pyroxenes in the Shergotty meteorite. *Nature* 409, 487-490.

McSween HY, Ruff SW, Morris RV, Bell JF, Herkenhoff K, Gellert R, Stockstill KR, Tornabene LL, Squyres SW, Crisp JA, Christensen PR, McCoy TJ, Mittlefehldt DW, Schmidt M (2006). Alkaline volcanic rocks from the Columbia Hills, Gusev crater, Mars. *J. Geophys. Res.* 111, 9.

McSween HY (2015). Petrology on Mars. *Am. Mineral.* 100, 2380-2395

Médard E, Grove T (2007). The effect of H2O on the olivine liquidus of basaltic melts: experiments and thermodynamic models. *Contrib. to Mineral. Petrol.* 155, 417–432.

Médard E, McCammon CA, Barr JA, Grove TL (2008). Oxygen fugacity, temperature reproducibility, and H_2O content for nominally dry piston-cylinder experiments using graphite capsules. Am. Min. 93: 1838-1844.

Mißbach H, Schmidt BC, Duda JP, Lünsdorf NK, Goetz W, Thiel V (2018). Assessing the diversity of lipids formed via Fischer-Tropsch-type reactions. *Org. Geochem.* 119, 110–121.

Mißbach H (2018). Formation and preservation of abiotic organic signatures vs. lipid biomarkers experimental studies in preparation for the ExoMars 2020 mission. Dissertation. The University of Göttingen.

Mißbach H, Steininger H, Thiel V, Goetz W (2019). Investigating the Effect of Perchlorate on Flight-like Gas Chromatography–Mass Spectrometry as Performed by MOMA on board the ExoMars 2020 Rover. *Astrobiology.* 19, 1339-1352.

Michalski JR, Niles PB (2010). Deep crustal carbonate rocks exposed by meteor impact on Mars. *Nat. Geosci.* 3, 751–755.

Michalski JR, Onstott TC, Mojzsis SJ, Mustard J, Chan QHS, Niles PB, Johnson SS (2013). The Martian subsurface as a potential window into the origin of life. *Nat. Geosci.* 6, 133–138.

Michels R, Landais P, Philp RP, Torkelson BE (1994). Effects of Pressure on Organic Matter Maturation during Confined Pyrolysis of Woodford Kerogen. *Energy Fuels* 1994, 8, 3, 741–754

Mierdel K, Keppler H, Smyth J R, et al. (2007). Water solubility in aluminous orthopyroxene and the origin of Earth's asthenosphere. *Science,* 315: 364–368.

Mills RD, Simon JI, Alexander CMOD, Wang J, Hauri EH (2017). Water in alkali feldspar:the effect of rhyolite generation on the lunar hydrogen budget. *Geochem. Perspectives Lett.* 2017, *3*, 115-123.

Montgomery W, Bromiley G, Sephton M (2016). The nature of organic records in impact excavated rocks on Mars. *Sci Rep* 6**,** 30947.

Moore G, Roggensack K, Klonowski S (2008). A low-pressure – high-temperature technique for the piston cylinder. *Am Min.* 93,48-52

Morbidelli A, Marchi S, Bottke WF, Kring DA (2012). A sawtooth-like timeline for the first billion years of lunar bombardment. *Earth Planet. Sci. Lett.* 355, 144-151.

Moretti R, Le Losq C, Neuville DR (2014). The amphoteric behavior of water in silicate melts from the point of view of their ionic-polymeric constitution. *Chem. Geol.* 367, 23–33.

Morgan JW and Anders E (1979.) Chemical composition of Mars. *Geochim. Cosmochim. Acta* 43, 1601–1610.

Morris RV, Ruff SW, Gellert R, Ming DW, Arvidson RE, Clark BC, Golden DC, Siebach K, Klingelhöfer G, Schröder C (2010). Identification of carbonate-rich outcrops on Mars by the Spirit rover. *Science*, 329, 421-424.

Mosenfelder JL, Deligne NI, Asmiow PAD, Rossman GR (2006). Hydrogen incorporation in olivine from 2 to 12 GPa. *Am. Miner.* 91, 285–294.

Mosenfelder JL, and Rossman GR (2013). Analysis of hydrogen and fluorine in pyroxenes: I. Orthopyroxene. *Am. Miner.* 98, 1026–1041.

Mugnai M, Cardini G, Schettino V (2004a). High-pressure reactivity of propene by first principles molecular dynamics calculations. *J. Chem Phys.* 120, 5327–5333.

Mugnai M, Cardini G, Schettino V (2004b). Charge separation and polymerization of hydrocarbons at an ultra high-pressure. *Phys. Rev. B* 70, 020101.

Mustard JF, Adler M, Allwood A, Bass DS, Beaty DW, Bell III JF, Brinckerhoff WB, Carr M, Des Marais DJ, Drake B, Edgett KS, Eigenbrode J, Elkins-Tanton LT, Grant JA, Milkovich SM, Ming D, Moore C, Murchie S, Onstott TC, Ruff SW, Sephton MA, Steele A, Treiman A (2013). Appendix to the Report of the Mars 2020 Science

Definition Team. Mars Exploration Program Analysis Group (MEPAG), 51. http://mepag.jpl.nasa.gov/reports/MEP/Mars_2020_SDT_Report_Appendix.pdf.

Mysen BO, Virgo D, and Seifert FA (1985). Relationships between properties and structure of aluminosilicate melts. *Am. Min.* 70, 88–105.

Mysen BO and Richet P. (2005). *Silicate Glasses and Melts: Properties and Structure (Developments in Geochemistry).* Elsevier, Amsterdam (2005).

Mysen BO and Fogel ML. (2010) Nitrogen and hydrogen isotope compositions and solubility in silicate melts in equilibrium with reduced (N+H)-bearing fluids at high-pressure and temperature: Effects of melt structure. *Am. Min,* 95 (7): 987–999.

Mysen BO, Kumamoto K, Cody GD, Fogel ML (2011). Solubility and solution mechanisms of C–O–H volatiles in silicate melt with variable redox conditions and melt composition at upper mantle temperatures and pressures. *Geochim. Cosmochim. Acta*, 75, 6183-6199

Nesbitt HW, Bancroft GM, Henderson GS (2020). Polymerization during melting of ortho- and meta silicates: Effects on Q species stability, heats of fusion, and redox state of mid ocean range basalts (MORBs). *Am. Min.* 105, 716–726.

Ni P, Zhang Y, Chen S, Gagnon J (2019). A melt inclusion study on volatile abundances in the lunar mantle. *Geochim. Cosmochim. Acta,* 249, 17-41.

Nishihara Y, Fuke K, Tange Y, Higo Y (2016). Determination of pressure effect on thermocouple electromotive force using multi-anvil apparatus. *High Press. Res.* 36(2), 121–139.

Novella D, Frost DJ, Hauri EH, Bureau H, Raepsaet C, and Roberge M (2014). The distribution of H2O between silicate melt and nominally anhydrous peridotite and the onset of hydrous melting in the deep upper mantle. *Earth. Planet. Sci. Lett.* 400, 1–13.

O'Brien DP, Izidoro A, Jacobson SA, Raymond SN, Rubie DC (2018). The delivery of water during terrestrial planet formation. *Space Sci. Rev.* 214.

O'Leary JA, Gaetani GA, and Hauri EH (2010). The effect of tetrahedral Al3+ on the partitioning of water between clinopyroxene and silicate melt. *Earth. Planet. Sci. Lett.* 297, 111–120.

O'Neill HStC (1991). The origin of the Moon and the early history of the Earth — A chemical model, Part 1: The Moon. *Geochim. Cosmochim. Acta*, 55, 1135–1157.

Ohara S, Kakegawa T, Nakazawa H (2007). Pressure effects on the abiotic polymerization of glycine. *Orig. Life Evol. Biosph.* 37, 215–223.

Omori S, Komabayashi T (2007). Superplumes: Beyond Plate Tectonics, 113-138. Springer Netherlands.

Otake T, Taniguchi T, Furukawa Y, Kawamura F, Nakazawa H, Kakegawa T (2011). Stability of amino acids and their oligomerization under high-pressure conditions: implications for prebiotic chemistry. *Astrobiology* 11, 799–813 (2011).

Otsuka K, Karato S (2011). Control of the water fugacity at high-pressures and temperatures: Applications to the incorporation mechanisms of water in olivine. *Phys. Earth Planet. Inter.* 189, 27–33.

Padrón–Navarta JA, Hermann J, O'Neill HStC (2014). Site–specific hydrogen diffusion rates in forsterite. *Earth. Planet. Sci. Lett.* 392, 100–112.

Palme H, Nickel KG (1985). Ca/Al ratio and composition of the Earth's upper mantle. *Geochim. Cosmochim. Acta* 49, 2123-2132.

Palme H, O'Neill HSC (2014). Cosmochemical Estimates of Mantle Composition. *Treatise on Geochemistry 2nd Edition.*

Pavlov AA, Vasilyev G, Ostryakov VM, Pavlov AK, Mahaffy P (2012). Degradation of the organic molecules in the shallow subsurface of Mars due to irradiation by cosmic rays. *Geophys. Res. Lett.* 39, L13202.

Peslier A, Schönbächler M, Busemann H, Karato SI (2017). Water in the Earth's interior: distribution and origin. *Space Sci. Rev.* 212 (1–2), 743-810

Peslier A, Hervig R, Yang S, Humayun M, Barnes J, Irving A, Brandon A. (2019). Determination of the water content and D/H ratio of the martian mantle by unraveling degassing and crystallization effects in nakhlites. *Geochim. Cosmochim. Acta 266*, 382–415.

Peters KE, Walters CC, Moldowan JM (2005). The Biomarker Guide - Part I – Biomarkers and Isotopes in the Environment and Human History. Cambridge University Press, New York.

Pitzer KS, Sterner SM (1994). Equations of state valid continuously from zero to extreme pressures for H2O and CO2. *J. Chem. Phys.* 101, 3111–3116.

Pitzer KS, Sterner SM (1995). Equations of state valid continuously from zero to extreme pressures with H2O and CO2 as examples. *Int. J. Thermophys.* 16(2), 511–518.

Plank T, Kelley KA, Zimmer MM, Hauri EH, Wallace PJ (2013). Why do mafic arc magmas contain ~4 wt% water on average? *Earth Planet Sci. Lett.* 364, 168-179.

Potts NJ, GD Bromiley, RA Brooker (2021). An experimental investigation of F, Cl and H2O mineral melt partitioning in a reduced, model lunar system. *Geochim. Cosmochim. Acta*, 294, 232-254.

Price LC, Wenger LM (1992). The influence of pressure on petroleum generation and maturation as suggested by aqueous pyrolysis. *Org. Geochem.* 19, 141–159.

Price LC (1993). Thermal stability of hydrocarbons in nature: Limits, evidence, characteristics, and possible controls. *Geochim. Cosmochim. Acta*, 57, 3261–3280.

Putirka KD (2008). Thermometers and barometers for volcanic systems, Minerals, Inclusions and Volcanic Processes. *Rev in Min and Geochem.* 69, 61–120.

Rai N, van Westrenen W (2013). Core-mantle differentiation in Mars. *J. Geophys. Res. Planets*, 118, 1195–1203.

Rakotoalimanana DA, Behar F, Bounaceur R, Burklé-Vitzthum V, Marquaire P (2016). Thermal cracking of n-butylcyclohexane at high-pressure (100 bar)—Part 1: Experimental study. *J Anal. Appl. Pyrolysis* 117, 1-16.

Rakotoalimanana DA, Bounaceur R, Sirjean B, Behar F, Burklé-Vitzthum V, Marquaire P (2017). Thermal cracking of 1-n-butyldecalin at high-pressure (100 bar). *J Anal. Appl. Pyrolysis, 123*, 204-215.

Righter K, Yang H, Costin G, Downs RT (2008). Oxygen fugacity in the Martian mantle controlled by carbon: new constraints from the nakhlite MIL03346. *Meteorit. Planet. Sci.,* 43, 1709-1723.

Ringwood AE (1979). Origin of the Earth and Moon. New York: Springer-Verlag. 295.

Robie RA and Hemingway BS (1995). Thermodynamic properties of minerals and related substances at 298.15 K and 1 bar (105 Pascals) pressure and at higher temperatures. *U.S. Geological Survey Bulletin* 2131, 461.

Rohrbach A, Ballhaus C, Ulmer P, Golla-Schindler U, Schoenbohm D (2011). Experimental evidence for a reduced metal-saturated upper mantle. *J. Petrol.* 52, 717–731.

Rosenthal, A., Hauri, E.H., and Hirschmann, M.M. (2015). Experimental determination of C, F, and H partitioning between mantle minerals and carbonated basalt, CO2/Ba and CO2/Nb systematics of partial melting, and the CO2 contents of basaltic source regions. *Earth. Planet. Sci. Lett.* 412, 77–87.

Rostel L, Guo J, Banjac S, Wimmer-Schweingruber RF, Heber B (2020). Subsurface radiation environment of Mars and its implication for shielding protection of future habitats. *J. Geophys. Res. Planets* 125, e2019JE006246.

Rubie DC, Melosh HJ, Reid JE, Liebske C, Righter K (2003). Mechanisms of metal– silicate equilibration in the terrestrial magma ocean. *Earth Planet. Sci. Lett.* 205, 239–255.

Rubie DC, Frost DJ, Mann U, Asahara Y, Nimmo F, Tsuno K, Kegler P, Holzheid A, Palme H (2011).Heterogeneous accretion, composition and core–mantle differentiation of the Earth. *Earth. Planet. Sci. Lett.* 301(1), 31–42.

Rubie DC, Jacobson SA, Morbidelli A, O'Brien DP, Young ED, de Vries J, Nimmo F, Palme H, Frost DJ (2015). Accretion and differentiation of the terrestrial planets with implications for the compositions of early-formed Solar System bodies and accretion of water. *Icarus* 248, 89-108.

Rushdi AI, Simoneit BRT (2001). Lipid formation by aqueous Fischer–Tropsch type synthesis over a temperature range of 100 to 400 °C. *Orig Life Evol Biosph.* 31, 103–118

Ryerson FJ (1985). Oxide solution mechanisms in silicate melts: Systematic variations in the activity coefficient of SiO2. *Geochim. Cosmochim. Acta*, 49, 637–649.

Sanloup C, Jambon A, Gillet P (1999). A simple chondritic model of Mars. *Phys. Earth Planet. Int.* 112, 43–54.

Sarafian AR, Hauri EH, McCubbin FM, Lapen TJ, Berger EL, Nielsen SG, Marschall HR, Gaetani GA, Righter K, Sarafian E (2017). Early accretion of water and volatile elements to the inner Solar System: evidence from angrites. *Philos. Trans. R. Soc., Math. Phys. Eng. Sci.,* 375.

Sautter V, Toplis MJ, Lorand JP, Macri M (2012). Melt inclusions in augite from the nakhlite meteorites: A reassessment of nakhlite parental melt and implications for petrogenesis. *Meteor. Planet. Sci.* 47, 330-344.

Scaillet B, Gaillard F (2011). Redox state of early magmas. *Nature*, 480, 48-49.

Schaefer L, Elkins-Tanton LT (2018). Magma oceans as a critical stage in the tectonic development of rocky planets. *Phil. Trans. R. Soc. A*, 376, 2132.

Schmidt BC (1998). Incorporation of H_2 in vitreous silica, qualitative and quantitative determination from Raman and infrared spectroscopy. *J. Non-crystall. Solids,* 240, 91-103.

Sephton MA (2002). Organic compounds in carbonaceous meteorites. *Nat. Prod. Rep.* **19**, 292–311.

Sehlke and Whittington (2016). The viscosity of planetary tholeiitic melts: A configurational entropy model. *Geochim Cosmochim Acta*, 191, 277-299.

Shackelford JF, Studt PL, Fulrath RM (1972). Solubility of gases in glass, lI, He, Ne, and H2 in fused silica. *J. Appl. Phys.,* 43, 1619-1626.

Shang LB, Chou IM, Lu WJ, Burruss RC, Zhang Y (2009). Determination of diffusion coefficients of hydrogen in fused silica between 296 and 523 K by Raman spectroscopy and application of fused silica capilaries in studying redox reactions. *Geochim Cosmochim Acta* 73, 5435-5443.

Shaw DM (2005). Trace elements in magmas: a theoretical treatment. Cambridge University Press.

Shcheka S, Wiedenbeck M, Frost D, Keppler H (2006). Carbon solubility in mantle minerals. *Earth Planet. Sci. Lett.* 245, 730– 742.

Shinozaki A, Mimura K, Kagi H, Komatu K, Noguchi N, Gotou H (2014). Pressure induced oligomerization of benzene at room temperature as a precursory reaction of amorphization. *J. Chem. Phys.* 41, 084306.

Shock E, Bockisch C, Estrada C, Fecteau K, Gould IR, Hartnett H, Johnson K, Robinson K, Shipp J,Williams L (2019). Deep Carbon: Past to Present: Earth as Organic Chemist. (ed) Orcutt B, Daniel I, Dasgupta R. Cambridge University Press, 415-446.

Sifré D, Gardés E, Massuyeau M, Hashim L, Hier-Majumder S, Gaillard F (2014). Electrical conductivity during incipient melting in the oceanic low-velocity zone. *Nature* 509, 81–85.

Smyth JR, Frost DJ, Nestola F, Holl CM, Bromiley G (2006). Olivine hydration in the deep upper mantle: effects of temperature and silica activity. *Geophys. Res. Lett.* 33, L15301.

Snyder GA, Taylor LA, Neal CR (1992). A chemical model for generating the sources of mare basalts: combined equilibrium and fractional crystallization of the lunar magmasphere. *Geochim. Cosmochim. Acta*, 56, 3809-3823.

Sokol AG, Tomilenko AA, Bul'bak TA et al. (2017). Carbon and Nitrogen Speciation in N poor C-O-H-N Fluids at 6.3 GPa and 1100–1400 °C. *Sci. Rep.* 7, 706.

Stagno V, Ojwang DO, McCammon CA, Frost DJ (2013). The oxidation state of the mantle and the extraction of carbon from Earth's interior. *Nature* 493, 84–87.

Stalder R (2004). Influence of Fe, Cr and Al on hydrogen incorporation in orthopyroxene. *Eur. J. Mineral.* 16(5), 703–711.

Stanley BD, Hirschmann MM, Withers AC (2014). Solubility of COH volatiles in graphite saturated martian basalts. *Geochim. Cosmochim. Acta,* 129, 54-76.

Starke V, Kirshtein J, Fogel ML, Steele A (2013). Microbial community composition and endolithcolonization at an Arctic thermal spring are driven by calcite precipitation. *Environ. Microbiol. Rep.* 5, 648-59.

Steele A, McCubbin FM, Fries, MD (2016). The provenance, formation, and implications of reduced carbon phases in Martian meteorites. *Meteorit. Planet. Sci.* 51, 2203-2225.

Steenstra ES, Sitabi AB, Lin YH, Rai N, Knibbe JS, Berndt J, Matveev S, van Westrenen W (2017). The effect of melt composition on metal-silicate partitioning of siderophile elements and constraints on core formation in the angrite parent body. *Geochim. Cosmochim. Acta* 212(1), 62-83.

Steenstra ES, Lin Y, Dankers D. et al. (2017). The lunar core can be a major reservoir for volatile elements S, Se, Te and Sb. *Sci. Rep.* 7, 14552 (2017).

Stockstill KR, McSween HY, Bodnar RJ (2005). Melt inclusions in augite of the Nakhla martian meteorite: Evidence for basaltic parental melt. *Meteor. Planet. Sci.* 40, 377-396.

Stolper E. (1982). The speciation of water in silicate melts. *Geochim. Cosmochim. Acta* 46, 2609-2620.

Sugahara H, Mimura K (2014). Glycine oligomerization up to triglycine by shock experiments simulating comet impacts. *Geochem. J.* 48, 51–62.

Tan J, Lewis JMT, Sephton MA (2018). The fate of lipid biosignatures in a mars-analogue sulfur stream. *Sci. Rep.* 8, 7586.

Taylor SR (1982). Planetary Science: A Lunar Perspective. LPI, Houston, TX.

Taylor WR, Green DH (1987). The petrogenetic role of methane: effect on liquidus phase relations and the solubility mechanism of reduced C-H volatiles. Mysen, BO (ed.) *Magmatic Processes: Physicochemical Principles. Washington, DC: Geochemical Society*, 121-138.

Taylor SR, McLennan SM (1985). The continental crust: Its composition and evolution. *Oxford: Blackwell Scientific*, 312.

Taylor GJ (2013). The bulk composition of Mars. (2013) *Chemie der Erde* 73, 401–420.

Ten Kate IL, Gerry JRC, Peters Z, Quinn R, Foing B, Ehrenfreund P (2005). Amino acid photostability on the Martian surface. *Meteoritics Planet. Sci.* 40 1185–1193.

Tenner TJ, Hirschmann MM, Withers AC, Hervig RL (2009). Hydrogen partitioning between nominally anhydrous upper mantle minerals and melt between 3 and 5 GPa and applications to hydrous peridotite partial melting. *Chem Geol.* 262, 42–56.

Tenner TJ, Hirschmann MM, Withers AC, Ardia P (2012). H2O storage capacity of olivine and low–Ca pyroxene from 10 to 13 GPa: Consequences for dehydration melting above the transition zone. *Contrib. Mineral. Petrol.* 163, 297–316.

Thomas-Keprta KL, Clemett SJ, McKay DS, Gibson EK, Wentworth SJ (2009). Origins of magnetite nanocrystals in martian meteorite ALH84001. *Geochim. Cosmochim. Acta* 73, 6631–6677.

Tissot BP, Deroo G, Hood A (1978). Geochemical study of the Uinta Basin: formation of petroleum from the Green River formation. *Geochim. Cosmochim. Acta* 42, 1469–1485.

Tissot BP, and Welte DH. (1984). Petroleum Formation and Occurrence. 2. edition, Springer, Berlin, Heidelberg.

Tollan PME, Smith R, O'Neill HS, Hermann J (2017) The responses of the four main substitution mechanisms of H in olivine to H2O activity at 1050∘C and 3 GPa. *Prog. Earth Planet. Sci.* 4, 14.

Tollan PME, O'Neill HSC, Hermann J (2018). The role of trace elements in controlling H incorporation in San Carlos olivine. *Contrib. Mineral. Petrol.* 173(11), 89.

Udry A, Day JMD (2018). 1.34 billion-year-old magmatism on Mars evaluated from the co genetic nakhliteand chassignite meteorites. *Geochim. Cosmochim. Acta,* 238, 292-315.

Usui T, Alexander CMO'D, Wang J, Simon JI, Jones JH (2012). Origin of water and mantle crust interactions on Mars inferred from hydrogen isotopes and volatile abundances of olivine-hosted melt inclusions of primitive shergottites. *Earth Planet. Sci. Lett.,* 357–358, 119-129.

Vago, JL, Westall F, Coates AJ, Jaumann R, Korablev O, Ciarletti V et al. (2017) Habitability on early Mars and the search for biosignatures with the ExoMars rover. *Astrobio.* 17, 471–510.

Wade J, Wood BJ (2005). Core formation and the oxidation state of the Earth. *Earth Planet. Sci. Lett.*, 236, 78-95.

Wadhwa, M. (2008). Redox Conditions on Small Bodies, the Moon and Mars. *Rev. Mineral. Geochem.* 68(1), 493–510.

Wallace PJ (2005). Volatiles in subduction zone magmas: concentrations and fluxes based on melt inclusion and volcanic gas data. *J. Volcanol. Geotherm. Res.,* 140, 217-240.

Wänke H, Dreibus G, Jagoutz E (1984). Mantle chemistry and accretion history of the Earth, in Archean Geochemistry. 1-24, Springer-Verlag, Berlin.

Wänke H, Dreibus G (1988). Chemical composition and accretion history of the terrestrial planets. *Philos. Trans. Royal Soc. A* 325, 545–557.

Warren PH (2005). "New" lunar meteorites: Implications for composition of the global lunar surface, lunar crust, and the bulk Moon. *Meteorit. Planet. Sci.* 40, 477–506.

Warren JM and Hauri EH (2014). Pyroxenes as tracers of mantle water variations. *J. Geophys. Res. Solid Earth* 119, 1851–1881.

Wasylenki LE, Baker MB, Kent AJR, Stolper EM (2003). Near-solidus melting of the shallow upper mantle: Partial melting experiments on depleted peridotite. *J. of Petrol.* 44, 1163–1191.

Weis FA, Bellucci JJ, Skogby H, Stadler R, Nemchin AA, Whitehouse MJ (2017). Water content in the Martian mantle: a Nahkla perspective. *Geochim. Cosmochim. Acta*, 212, 84-98.

Wen XD, Hofmann R, Ashcrof N (2011). Benzene under high-pressure: a story of molecular crystals transforming to saturated networks, with a possible intermediate metallic phase. *J. Am. Chem. Soc.* 133, 9023–9035.

Withers AC and Hirschmann MM (2007). H2O storage capacity of MgSiO3 clinoenstatite at 8–13 GPa, 1100–1400 degrees C. *Contrib. Mineral. Petrol.* 154, 663-674

Withers AC, Hirschmann MM (2008). Influence of temperature, composition, silica activity and oxygen fugacity on the H2O storage capacity of olivine at 8 GPa. *Contrib. Mineral. Petrol.* 165, 595–605.

Withers AC, Hirschmann MM, and Tenner TJ (2011). The effect of Fe on olivine H2O storage capacity: consequences for H2O in the martian mantle. *Am. Miner.* 96, 1039–1053.

Wood BJ, Walter MJ, Wade J (2006). Accretion of the Earth and segregation of its core. *Nature* 441, 825–833

Wray JJ, Murchie SL, Bishop JL, Ehlmann BL, Milliken RE, Wilhelm MB, Seelos KD, Chojnacki M (2016). Orbital evidence for more widespread carbonate-bearing rocks on Mars. *J. Geophys. Res. Planets* 121, 652–677.

Yang X, Gaillard F, Scaillet B (2014). A relatively reduced Hadean continental crust and implications for the early atmosphere and crustal rheology. *Earth. Planet. Sci. Lett.*, 393, 210–219.

Yang X (2015) OH solubility in olivine in the peridotite–COH system under reducing conditions and implications for water storage and hydrous melting in the reducing upper mantle. *Earth Planet. Sci. Lett.* 432, 199-209

Yang X, Keppler H, Li Y (2016). Molecular hydrogen in mantle minerals. *Geochem. Perspect. Lett.* 2, 160-168

Yang X (2016). Effect of oxygen fugacity on OH dissolution in olivine under peridotite saturated conditions: an experimental study at 1.5–7 GPa and 1100–1300 °C. *Geochim. Cosmochin. Acta* 173, 319–336.

Yen AS, Kim SS, Hecht MH, Frant MS, Murray B (2000). Evidence that the reactivity of the Martian soil is due to superoxide ions. *Science* 289, 1909-1912.

Yoshino T, Walter MJ, Katsura T (2003). Core formation in planetesimals triggered by permeable flow. *Nature* 422, 154–157.

Young DA (2003) Mind over Magma: The Story of Igneous Petrology. Princeton University Press.

Zent AP (1998). On the thickness of the oxidized layer of the martian regolith. *J. Geophys. Res.* 103, 31491–31498.

Zent AP, Ichimura AS, Quinn RC, Harding HK (2008). The formation and stability of the superoxide radical (O2-) on rock-forming minerals: band gaps, hydroxylation state, and implications for Mars oxidant chemistry. *J. Geophys. Res.* 113, doi:10.1029/2007JE003001.

Zhang C, Duan Z (2009). A model for C–O–H fluid in the Earth's mantle. *Geochim Cosmochim Acta* 73, 2089–2102.

Zhang Y. and Ni H. (2010) Diffusion of H, C, and O components in silicate melts. Reviews in Mineralogy and Geochemistry 72, 171-225.

Zhang Y (1999). H2O in rhyolitic glasses and melts: measurement, speciation solubility, and diffusion. *Rev. Geophys.* 37, 493-516

Zhang Y, Stolper EM, Wasserburg GJ (1991). Diffusion of water in rhyolitic glasses. *Geochim. Cosmochim. Acta,* 55, 441-456

Zhang L, Guo X, Wang Q, Ding J, Ni H (2017). Diffusion of hydrous species in model basaltic melt. *Geochim. Cosmochim. Acta*, 215, 377-386.

Zhao Y–H, Ginsberg SB, Kohlstedt DL (2004). Solubility of hydrogen in olivine: dependence on temperature and iron content. *Contrib. Mineral. Petrol.* 147, 155–161.

Zolotov M Y, Sprague AL, Hauck SA, Nittler LR, Solomon SC, Weider SZ (2013), The redox state, FeO content, and origin of sulfur-rich magmas on Mercury. *J. Geophys. Res.* 118, 138–146.

Zuber MT, Solomon SC, Phillips RJ, Smith DE, Tyler GL, Aharonson O, Balmino G, Banerdt WB, Head JW, Johnson CL, Lemoine FG, McGovern PJ, Neumann GA, Rowlands DD, Zhong S (2000). Internal structure and early thermal evolution of Mars from Mars Global Surveyor topography and gravity, *Science*, 287, 1788–1793.

Appendix

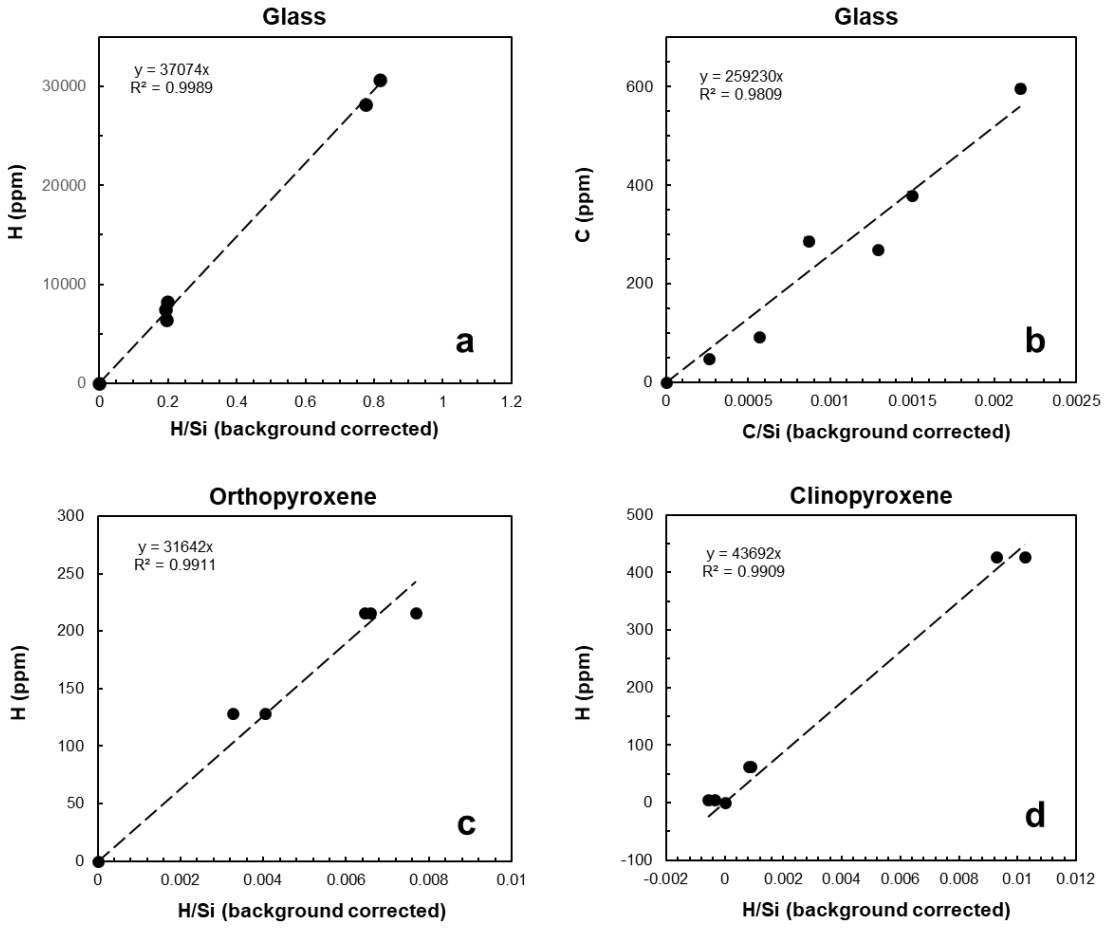

Figure A.1. Background corrected calibration curves for SIMS analysis. The standard OL-116610 was used to measure the background for both (c) and (d) and is shown on the curve. Instrumental errors are within the markers.

Table A.1. Pearson correlation matrix for Figure 4.1 and Figure 4.2.

Variables	P (GPa)	T (°C)	D_H	H_2O Melt (%)	log fH_2O (GPa)	H_2O in Ol (ppm)
P (GPa)	**1**	0.205	**0.287**	**0.543**	**0.981**	**0.917**
T (°C)	0.205	**1**	0.248	**-0.322**	0.220	0.053
D_H	**0.287**	0.248	**1**	**-0.284**	0.193	0.241
H_2O Melt (%)	**0.543**	**-0.322**	**-0.284**	**1**	**0.604**	**0.646**
log fH_2O (GPa)	**0.981**	0.220	0.193	**0.604**	**1**	**0.919**
H_2O in Ol (ppm)	**0.917**	0.053	0.241	**0.646**	**0.919**	**1**

Values in bold are different from 0 with a significance level alpha=0.05.

Table A.2. Confidence intervals (95%) for Figure 4.1 and Figure 4.2.

Variables	P (GPa)	T (°C)	D_H	H_2O Melt (%)	log fH_2O (GPa)	H_2O in Ol (ppm)
P (GPa)	**1**	[-0.045 , 0.431]	[0.042 , 0.499]	[0.341 , 0.697]	[0.969 , 0.988]	[0.866 , 0.949]
T (°C)	[-0.045 , 0.431]	**1**	[0.000 , 0.467]	[-0.527 , -0.080]	[-0.029 , 0.444]	[-0.197 , 0.297]
D_H	[0.042 , 0.499]	[0.000 , 0.467]	**1**	[-0.497 , -0.039]	[-0.057 , 0.421]	[-0.008 , 0.461]
H_2O Melt (%)	[0.341 , 0.697]	[-0.527 , -0.080]	[-0.497 , -0.039]	**1**	[0.419 , 0.741]	[0.474 , 0.770]
log fH_2O (GPa)	[0.969 , 0.988]	[-0.029 , 0.444]	[-0.057 , 0.421]	[0.419 , 0.741]	**1**	[0.869 , 0.950]
H_2O in Ol (ppm)	0.866 , 0.949]	[-0.197 , 0.297]	[-0.008 , 0.461]	[0.474 , 0.770]	[0.869 , 0.950]	**1**

Table A.3. Pearson p-values **for** Figure 4.1 and Figure 4.2.

Variables	P (GPa)	T (°C)	D_H	H_2O Melt (%)	log fH_2O (GPa)	H_2O in Ol (ppm)
P (GPa)	**0**	0.108	**0.023**	**<0.0001**	**<0.0001**	**<0.0001**
T (°C)	0.108	**0**	0.050	**0.010**	0.083	0.680
D_H	**0.023**	0.050	**0**	**0.024**	0.129	0.057
H_2O Melt (%)	**<0.0001**	**0.010**	**0.024**	**0**	**<0.0001**	**<0.0001**
log fH_2O (GPa)	**<0.0001**	0.083	0.129	**<0.0001**	**0**	**<0.0001**
H_2O in Ol (ppm)	**<0.0001**	0.680	0.057	**<0.0001**	**<0.0001**	**0**

Table A.4. Coefficients of determination for Figure 4.1 and Figure 4.2.

Variables	P (GPa)	T (°C)	D_H	H_2O Melt (%)	log fH_2O (GPa)	H_2O in Ol (ppm)
P (GPa)	**1**	0.042	0.082	0.295	0.962	0.841
T (°C)	0.042	**1**	0.061	0.104	0.048	0.003
D_H	0.082	0.061	**1**	0.081	0.037	0.058
H_2O Melt (%)	0.295	0.104	0.081	**1**	0.365	0.417
log fH_2O (GPa)	0.962	0.048	0.037	0.365	**1**	0.844
H_2O in Ol (ppm)	0.841	0.003	0.058	0.417	0.844	**1**

Table A.5. Goodness of fit statistics for model shown in Figure 4.4e.

Sum of weights	16
DF	14
R^2	0.945
Adjusted R^2	0.941
MSE	172.443
RMSE	13.132
MAPE	19.692
DW	1.040
Cp	2.000
AIC	84.265
SBC	85.810
PC	0.071

Table A.6. Residuals and predicted olivine H contents for Figure 4.3e

				Mean			Observation		
Experiment	Predicted Ol H (ppm)	Residual	Std. residual	Std. dev. on pred.	Lower bound 95%	Upper bound 95%	Std. dev. on pred.	Lower bound 95%	Upper bound 95%
C6a	89.22	9.28	0.71	3.43	81.87	96.57	13.57	60.11	118.33
C6b	68.23	10.57	0.81	3.3	61.14	75.31	13.54	39.18	97.27
C7a	68.23	-12.23	-0.93	3.3	61.14	75.31	13.54	39.18	97.27
C7b	93.42	-20.62	-1.57	3.52	85.88	100.96	13.59	64.26	122.57
C8a	194.18	-3.18	-0.24	8.45	176.06	212.3	15.62	160.69	227.67
Cb	152.2	0.6	0.05	6.04	139.25	165.14	14.45	121.2	183.19
C9a	57.73	-15.23	-1.16	3.45	50.33	65.13	13.58	28.61	86.85
C9b	57.73	-15.23	-1.16	3.45	50.33	65.13	13.58	28.61	86.85
B2	42.3	4.99	0.38	3.87	33.99	50.61	13.69	12.94	71.66
B19	38	-18	-1.37	4.03	29.36	46.64	13.74	8.54	67.46
B21a	49.39	6.61	0.5	3.65	41.56	57.22	13.63	20.16	78.62
B21b	59.86	5.15	0.39	3.41	52.54	67.17	13.57	30.76	88.95
B25a	-15.74	15.74	1.2	6.68	-30.07	-1.42	14.73	-47.34	15.85
B25b	3.11	-0.12	-0.01	5.65	-8.99	15.22	14.29	-27.54	33.77
B30b	107.19	15.82	1.2	3.92	98.77	115.6	13.71	77.79	136.58
B30a	119.18	15.82	1.21	4.4	109.75	128.61	13.85	89.48	148.88

Table A.7. Goodness of fit statistics for model shown in Figure 4.12e.

Sum of weights	81
DF	79
R^2	0.767
Adjusted R^2	0.764
MSE	9535.801
RMSE	97.651
MAPE	103.261
DW	0.999
Cp	2.000
AIC	744.162
SBC	748.951
PC	0.245

Table A.8. Goodness of fit statistics for Figure 4.13.

Observations	108.000
DF	103.000
R^2	0.909
SSE	4502420.751
MSE	43712.823
RMSE	209.076
AIC	1160.903
AICC	1161.735